Università degli Studi di Palermo

AREA RICERCA E TRASFERIMENTO TECNOLOGICO
SETTORE DOTTORATI E CONTRATTI PER LA RICERCA
U. O. DOTTORATI DI RICERCA

Dottorato in Scienze della Terra e del Mare

Dipartimento di Scienze della Terra e del Mare

Settore Scientifico Disciplinare (GEO/08)

A fluid and melt inclusion study of Fogo volcano, Cape Verde archipelago

IL DOTTORE

Francesco Maria Lo Forte

IL COORDINATORE

Prof. Alessandro Aiuppa

IL TUTOR

Prof. Alessandro Aiuppa

I CO-TUTORS

Prof. Silvio G. Rotolo

Dr. Vittorio Zanon

CICLO XXXVI

ANNO CONSEGUIMENTO TITOLO 2024

“L’amor che move il sole e l’altre stelle”

(Divina Commedia, Paradiso, XXXIII, v. 145)

Dante Alighieri

ACKNOWLEDGMENTS

This research received financial support from (i) the Deep Carbon observatory (Alfred P. Sloan Foundation, USA), the Ministero dell'Università e Ricerca (Italy, Grant n. 2017LMNLAW) and (ii) the research project MAGAT - From MAGma to the ATmosphere - a contribution to develop the next generation of geochemical sensors for realtime monitoring of magma movement at depth (CIRCNA/OCT/0016/2019), funded by the Fundação para a Ciência e Tecnologia, Portugal. I would like to thank the Instituto de Investigação em Vulcanologia e Avaliação de Riscos (IVAR), Ponta Delgada, Portugal; for providing a part of the samples, for the financial support for the field trip in Fogo Island, and for the hospitality received during the period spent for the analyses. I would like also the Laboratoire Magmas et Volcans (LMV), in Clermont-Ferrand, France, for the hospitality received during the period spent for the analyses. A thanks to the INGV- section of Palermo for the analysis carried out on the olivine samples, for the noble gases and carbon isotopes studies.

After the formal acknowledgments, it's time to express my gratitude in a more personal way. It is always difficult to delve into the drawer of feelings and open; however, I cannot help but say a few words for the people who have accompanied me on this long and intense journey, for which I already feel **"*SAUDADE*"**.

I am profoundly grateful to my supervisor, Professor Alessandro Aiuppa (Sandro), for his invaluable support and supervision throughout the duration of my doctoral studies. Thanks to his mentorship, I have gained significant insights into the research world. His sage advice and teachings have constituted one of the most cherished treasures that I shall carry with me always. He has taught me that not always when we have reason, we must be absolute; we must always seek to mediate and live in agreement with everyone, avoiding conflicts if we want to live into the world of research **"*Eh Ciccio, che ci vuoi fare.. Io quello che farei è..*"** I think that I will always carry this sentence with me.

I would also like to thank Dr. Vittorio Zanon and the Professor Andrea Luca Rizzo for the advice they have provided me and for the exceptional educational and scientific support extended to me. Another special thanks go to Professor Silvio G. Rotolo, who taught me that the most important thing of all is the passion, and that only with the passion you can one carry out a task.

Finally, I really appreciate the constant support and help of my lovely family (my two great and sweet angels (my grandparents) and my loving and supportive mum who has always helped me with the

phrase, "***Ce la farai come sempre***"), Alessandra, the girl to whom I wish immeasurable good, who has accompanied me on this journey and with whom, through ups and downs, I have spent an intense period of my life, and my friends (Antonio, Antonino, Ciro, Fabrizio, Gandolfo, Giovanni, and Michele). My gratitude extends to Dr. João Pedro Lages, Dr. Andrès Libardo Sandoval-Velasquez, and Dr. Marcello Bitetto who always offered me their unconditional help and advice during these three years. A particular thank to the Dr. Gabriele Carnevale (Coimbrinho), my friend and colleague, for sharing with me one of the most beautiful experiences of my life in the Azores, and for finding in him a scientific and convivial partner with whom a perfect synergy has been established.

I would like to express my gratitude to the two reviewers, Professor Rosario Esposito and Professor Paolo Fulignati, for giving their valuable advice and expressing a positive opinion regarding my PhD thesis.

INDEX

LIST OF FIGURES

LIST OF TABLES

ABSTRACT

Fogo volcano, in the Cape Verde Archipelago, is one of the most active ocean island basalts (OIBs) volcano on Earth. Previous independent studies have focused on reconstructing the magma plumbing system's architecture, the isotopic composition of the mantle source, and the geochemistry of volcanic gases. In this dissertation, through the study of fluid (FI) and melt (MI) inclusions hosted in olivine and clinopyroxene crystals from mafic products of the recent (<120 ka) activity period of Fogo, significantly advances the previous knowledges on the magma plumbing system and isotopic composition of the mantle source. Furthermore, we have quantified the parental melt volatile contents and the volatile evolution (degassing) throughout the different levels of the plumbing system during magma ascent. In addition, our investigation extends to investigating the presence of recycled crustal carbon within the mantle source, through carbon isotopes studies.

Our findings confirm the presence of a vertically elongated plumbing system with a deep-seated magma reservoir at depths of 27-36 km. This reservoir feeds the recent (<10 ka) alkali-rich magmatism of Fogo. We also identify a main magma storage zone at ~13-24 km depth and a magma stagnation zone at ~9-12 km depth. Furthermore, our research suggests a potential upward shift in pre-eruptive magma storage conditions since the 1951 eruption. Additionally, we highlight the volatile-rich nature of the Fogo parental melt, exhibiting elevated H_2O (up to 2.73 wt.%), CO_2 (up to 2.15 wt.%), S (up to 8200 ppm), Cl (up to 1400 ppm), and F (up to 2200 ppm) contents. The exceptionally high CO_2 content measured in the parental melt, up to 2.15 wt.%, reflects a carbon-rich signature in the mantle source (355-414 ppm). Our findings are consistent with recent observations indicating a carbon-rich nature in alkali-rich OIB magmas worldwide (e.g., El Hierro and La Palma in Canary Islands; Piton de la Fournaise in La Réunion Island).

Additionally, we have developed a carbon degassing model from mantle to crust. This model predicts a crustal signature for carbon, with a $\delta^{13}C$ value of ~ -0.4‰, in the primary melts (9.0 wt. % of CO_2) generated through upper mantle melting at ~ 2200 MPa (~ 77 km). This is interpreted as indicative of mantle metasomatism by melts/fluids enriched with a recycled crustal carbon component. Finally, through noble gases analyses, we constrain the Fogo $^3He/^4He$ signature (7.14-8.44 Rc/Ra) within the typical MORB-like mantle range.

CHAPTER 1.

INTRODUCTION

Volcanic degassing is one of the key geological processes that permit the exchange of volatiles (e.g., H_2O, CO_2, H_2S, SO_2, CH_4, Cl, F) between the Earth's interior and its surface (Oppenheimer et al., 2014; Aiuppa et al., 2017, 2019; Plank and Manning, 2019; Bekaert et al., 2021). The release of volcanogenic volatile species can drive change in the atmosphere over timescales of millions of years (Oppenheimer et al., 2014; Plank and Manning, 2019). A comprehensive understanding of the pre-eruptive volatile contents in magmas is also critical for volcano motoring, hazard assessment, and risk mitigation. Gas exsolution has been acknowledge as a critical driver of rapid magma ascent and eruptions (Edmonds and Wallace, 2017).

A proper understanding of initial dissolved volatile contents in mantle sourced magmas is challenged by degassing and differentiation experienced by magmas during their ascent to the surface (Lowenstern et al., 2003). Since erupted lavas/pyroclastic materials are then extremely volatile depleted upon eruption, one way to indirectly study the initial volatiles content in magmas is via the characterisation of fluid inclusions (FI), small volumes of fluid trapped within crystals during their growth from the fluid (Rodder, 1979), and silicate melt inclusions (MI), droplets of melt trapped during phenocrysts growth in the magma (Esposito, 2021), both the inclusions FI and MI, are entrapped in crystals from mafic volcanic rocks. Microthermometric analysis of CO_2-dominated FI provides valuable insights into the pressure, and hence depth, of pre-eruptive magma storage across multiple magma ponding levels (e.g., Hansteen et al., 1998; Zanon and Frezzotti, 2013; Zanon et al., 2020). Furthermore, noble gas and carbon isotope compositions of FI provide insights onto geodynamic evolution and composition of the source mantle, including the presence of mantle plumes (e.g., Gurenko et al., 2006; Day and Hilton, 2011, 2021; Rizzo et al., 2018, Sandoval-Velasquez et al., 2021a). On the other hand, MI are studied to quantify the dissolved volatile contents at the P-T-X conditions of entrapment. Additionally, they enable the determination of volatile contents in the parental melt if entrapment has occurred at or near the source (and before reaching volatile saturation) (e.g., Métrich and Wallace, 2008; Edmonds and Wallace, 2017).

MI studies have been critical to estimating the abundance and distribution of volatiles in the Earth's upper mantle. Recent studies have revealed a carbon-rich signature of the mantle source of Oceanic

Island Basalt (OIB) volcanoes (e.g., Longprè et al., 2017; Taracsák et al., 2019; Aiuppa et al., 2021). If the hypothesis suggesting the prevalence of carbon-rich OIBs globally holds true (e.g., El Hierro, Longpré et al., 2017; Taracsák et al., 2019; Piton de la Fournaise, Boudoire et al., 2018; Fogo, De Vitre et al., 2023), then OIB volcanism is expected to disproportionately contribute to the deep carbon flux into the atmosphere compared to volcanism in other setting, including Middle Oceanic Ridges (Dasgupta and Hirschmann, 2010; Hauri et al., 2019) and volcanic arcs (Plank and Manning, 2019). OIB volcanism opens a window into some of the more deeply explorable portions of the Earth's upper mantle (Hoffmann, 2003). Hence, quantifying the initial contents of volatile elements transported by such OIB magmas is crucial to understanding the cycling of volatiles from the deep planet interior (Hirschmann, 2006, 2018; Dasgupta and Hirschmann, 2010), and brings important clues on the roles of volatiles in mantle partial melting and magma generation and rise (Foley, 2011; Dasgupta, 2018). Unfortunately, however, the MI and FI dataset existing for OIB volcanoes is sparce and incomplete and biased toward a few better studied volcanic systems such as Kilauea, Hawaii (e.g., Moore et al., 2015; Tuohy et al., 2016), Iceland (e.g., Hartley et al., 2014; Bali et al., 2018), and the Canary Islands (Longpré et al., 2017; Taracsák et al., 2019).

One of the most active OIB volcanoes on the Earth is Fogo voclano, in the Cape Verde Archipelago (West Africa). Previous studies on this volcano have provided insights into (i) the architecture of the magma plumbing system (Hildner et al., 2011, 2012; Mata et al., 2017; Klügel et al., 2020); (ii) the isotopic (Sr-Nd-Pb-He) composition of the mantle source (e.g., Christensen et al., 2001; Doucelance et al., 2003; Mata et al., 2017); and (iii) the geochemistry of volcanic gases (Dionis et al., 2015; Aiuppa et al., 2020; Melián et al., 2021). In contrast, little information exists on the long-term stability or evolution of magma storage conditions (e.g., Hildner et al., 2011, 2012; Klügel et al., 2020) and on parental melt volatile contents and volatile evolution along the different regions of the magma plumbing system (DeVitre et al.,2023). Moreover, tittle is known on the factors that primarily control the isotopic diversity of the OIB mantle source, as well as the rates/modes of magma ascent prior and during eruption.

This thesis aims at filling this information gap, by investigating FI and MI hosted in olivine and clinopyroxene crystals of recent (<120 ka) products of Fogo. This information is vital for a more comprehensive understanding of volcano behaviours, and hence for assisting volcanic hazard mitigation programs in this populated island (~40,000 inhabitants).

1.1. Overview of developed research activities and structure of the dissertation

This doctoral dissertation arises from the need to (i) increase the actual limited knowledge on Fogo volcano and, more broadly, on the Cape Verde Archipelago and (ii) provide new constraints useful for future assessment of volcanic risk at Fogo, where the latest eruptions (1951, 1995 and 2014/15) have proven catastrophic for local communities. Our novel data provide new constraints on the (i) vertical arrangement of the magma plumbing system beneath Fogo Volcano, from the deep crust/upper mantle to the surface, and its evolution over the last 120 ka of activity; (ii) initial (parental melt) volatile contents, in the attempt to test the C-enriched source hypothesis and provide additional evidence for the C-enriched nature of alkali rich, OIB magmatism; (iii) evolution of the lithospheric mantle source beneath Cape Verde archipelago, as well as, the occurrence of mantle metasomatism and/or refertilization events, and the recycling into the mantle of noble gases due to recent or fossil subduction.

This PhD dissertation is structured in eight Chapters.

Chapter 2 offers a brief overview of OIB magmatism, with a specific emphasis on Cape Verde and Fogo volcano. In addition, I review examples of applications of fluid inclusions microthermometry, melt inclusions characterisation, and noble gases and carbon isotopes case studies in different OIB volcanoes. Chapter 3 discusses the methodological and analytical procedures used for the samples analysed, while Chapter 4 examines the geological setting of Cape Verde, and the volcanological history of Fogo. Chapters 5, 6 and 7 the form the core of the thesis, and report new geochemical results useful to better characterise the Fogo magma plumbing system and its mantle source, via (i) FI microthermometry (chapter 5); (ii) MI studies (chapter 6) and (iii) noble gases and carbon isotopes in FI and fumaroles (chapter 7).

The key findings of the FI microthermometry study (chapter 5) are: (i) a new conceptual model of the Fogo Volcano magma system, spanning the last 120 ka of activity; (ii) the identification of two stable magma accumulation zones are at ~25 km and ~13–21 km depth; (iii) the identification of a transient, pre-eruptive magma stagnation zone at 9–12 km depth for magmas involved in the recent (last century) eruptions; (iv) the rapid ascent, from 25 km depth, of magmas erupted in the early post-collapse phase (~60 ka), following a general reconfiguration of the plumbing system.

The main highlights of the MI study, carried out combining Raman Spectroscopy, Nano-SIMS, Electron microprobe, and LA-ICPMS (chapter 6) are: (i) mafic magmas feeding Fogo volcano are carbon-rich (2.1 wt. %); (ii) a degassing model can reproducing the behaviour of volatiles (H_2O,

CO_2, S, Cl, and F) during magma ascent/storage in the different magma plumbing system levels, and (iii) the mantle source beneath Fogo exhibit extremely high carbon contents (up to 400 ppm).

The characterization of the isotopic signature of carbon and noble gases in FI is discussed in Chapter 7. The first carbon isotopic measurements in FI in the Cape Verde archipelago are illustrated, and used to model the carbon isotopic evolution during degassing, from the mantle source to the surface. From this model, I predict a crustal signature for carbon in primary melts formed by upper mantle melting which is suggestive of mantle metasomatism by melts/fluids enriched in a crustal carbon component.

REFERENCES

Aiuppa, A., Bitetto, M., Rizzo, A.L., Viveiros, F., Allard, P., Frezzotti, M.L., Zanon, V., 2020. The fumarolic CO_2 output from Pico do Fogo Volcano (Cape Verde). Ital. J. Geosci. 139 (3), 325–340.

Aiuppa, A., Fischer, T.P., Plank, T., Bani, P., 2019. CO_2 flux emissions from the Earth's most actively degassing volcanoes, 2005–2015. Sci. Rep. 9, 5442.

Aiuppa, A., Fischer, T.P., Plank, T., Robidoux, P., Di Napoli, R., 2017. Along-arc, inter-arc and arc-to-arc variations in volcanic gas CO_2/St ratios reveal dual source of carbon in arc volcanism. Earth-Sci. Rev. 168, 24–47.

Aiuppa, A., Casetta, F., Coltorti, M., Stagno, V., Tamburello, G., 2021. Carbon concentration increases with depth of melting in Earth's upper mantle. Nat. Geosci. 14, 697–703.

Bali, E., Hartley, M.E., Halldórsson, S.A., Gudfinnsson, G.H., Jakobsson, S., 2018. Melt inclusion constraints on volatile systematics and degassing history of the 2014–2015 Holuhraun eruption, Iceland. Contrib. Mineral. Petrol. 173, 9.

Bekaert, D.V., Turner, S.J., Broadley, M.W., Barnes, J.D., Halldórsson, S.A., Labidi, J., Wade, J., Walowski, K.J., Barry, P.H., 2021. Subduction-Driven Volatile Recycling: A Global Mass Balance. Annu. Rev. Earth Planet. Sci. 49, 37–70.

Boudoire, G., Rizzo, A.L., Di Muro, A., Grassa, F., Liuzzo, M., 2018. Extensive CO_2 degassing in the upper mantle beneath oceanic basaltic volcanoes: First insights from Piton de la Fournaise volcano (La Réunion Island). Geochim. Cosmochim. Acta 235, 376–401.

Christensen, B.P., Holm, P.M., Jambon, A., Wilson, J.R., 2001. Helium, argon and lead isotopic composition of volcanics from Santo Antão and Fogo, Cape Verde Islands. Chem. Geol. 178, 127–142.

Day, J.M.D., Hilton, D.R., 2011. Origin of $^3He/^4He$ ratios in HIMU-type basalts constrained from Canary Island lavas. Earth Planet. Sci. Lett. 305, 226–234.

Day, J.M.D., Hilton, D.R., 2021. Heterogeneous mantle-derived helium isotopes in the Canary Islands and other ocean islands. Geology.

Dasgupta, R., 2018 Volatile-bearing partial melts beneath oceans and continents – where, how much, and of what compositions? Am. J. Sci. 318, 141–165.

Dasgupta, R., Hirschmann, M.M., 2010. The deep carbon cycle and melting in Earth's interior. Earth and Planet. Sci. Lett. 298, 1–13.

de Moor, J.M., Fischer, T.P., Sharp, Z.D., King, P.L., Wilke, M., Botcharnikov, R.E., et al., 2013. Sulfur degassing at Erta Ale (Ethiopia) and Masaya (Nicaragua) volcanoes: Implications for degassing processes and oxygen fugacities of basaltic systems. Geochem. Geophy. Geosy., 14(10), 4076-4108.

De Vitre, C.L., Gazel, E., Ramalho, R.S., Venugopal, S., Steele-MacInnis, M., Hua, J., et al., 2023. Oceanic intraplate explosive eruptions fed directly from the mantle. Proc. Natl. Acad. Sci. 120 (33), e2302093120.

Dionis S.M., Pérez N.M., Hernández P.A., Melián G., Rodríguez F., Padrón E., et al., 2015 - Diffuse CO_2 degassing and volcanic activity at Cape Verde Islands, West Africa. Earth, Planets and Space, 67 (1), 8.

Doucelance, R., Escrig, S., Moreira, M., Gariépy, C., Kurz, M.D., 2003. Pb-Sr-He isotope and trace element geochemistry of the Cape Verde Archipelago. Geochim. Cosmochim. Acta 67, 3717–3733.

Edmonds M., and Wallace P.J., 2017. Volatiles and Exsolved Vapor in Volcanic Systems. Elements, 13, 29–34.

Esposito, R., 2021. A protocol and review of methods to select, analyze and interpret melt inclusions to determine pre-eruptive volatile contents of magmas. In: Lecumberri-Sanchez, P., Steele-MacInnis, M., Kontak, D. (Eds.), Fluid and Melt Inclusions: Applications to Geologic Processes. Mineralogical Association of Canada, London, Ontario, 163–194.

Foley, S.F. 2011. A Reappraisal of Redox Melting in the Earth's Mantle as a Function of Tectonic Setting and Time, J. Petrol., 52, 7-8, 1363–1391.

Gurenko, A.A., Hoernle, K.A., Hauff, F., Schmincke, H.-U., Han, D., Miura, Y.N., Kaneoka, I., 2006. Major, trace element and Nd–Sr–Pb–O–He–Ar isotope signatures of shield stage lavas from the central and western Canary Islands: Insights into mantle and crustal processes. Chem. Geol. 233, 75–112. https://doi.org/10.1016/j.chemgeo.2006.02.016

Hansteen, T.H., Klügel, A., Schmincke, H.-U., 1998. Multi-stage magma ascent beneath the Canary Islands: evidence from fluid inclusions. Contrib. Mineral. Petrol. 132, 48–64.

Hartley, M.E., Maclennan, J., Edmonds, M., Thordarson, T., 2014. Reconstructing the deep CO_2 degassing behaviour of large basaltic fissure eruptions. Earth and Planet. Sci. Lett. 393, 120–131.

Hauri, E.H., Cottrell, E., Kelley, K.A., Tucker, J.M., Shimizu, K., Voyer, M.L., Marske, J., Saal, A.E., 2019. Carbon in the Convecting Mantle, in: Orcutt, B.N., Daniel, I., Dasgupta, R. (Eds.), Deep Carbon. Cambridge University Press, pp. 237–275.

Hildner, E., Klügel, A., Hauff, F., 2011. Magma storage and ascent during the 1995 eruption of Fogo, Cape Verde Archipelago. Contrib. Mineral. Petrol. 162, 751–772.

Hildner, E., Klügel, A., Hansteen, T.H., 2012. Barometry of lavas from the 1951 eruption of Fogo, Cape Verde Islands: Implications for historic and prehistoric magma plumbing systems. J. Volcanol. Geotherm. Res. 217–218, 73–90. https://doi.org/ 10.1016/j.jvolgeores.2011.12.014.

Hirschmann, M.M. 2006. Water, melting, and the deep Earth H_2O cycle Annu. Rev. Earth Planet. Sci. 629-653.

Hirschmann, M.M., 2018. Comparative deep Earth volatile cycles: The case for C recycling from exosphere/mantle fractionation of major (H_2O, C, N) volatiles and from H_2O/Ce, CO_2/Ba, and CO_2/Nb exosphere ratios. Earth and Planet. Sci. Lett. 502, 262–273.

Hofmann, A.W., 2003. Sampling mantle heterogeneity through oceanic basalts: isotopes and trace elements. In: Holland, Heinrich D., Turekian, Karl K. (Eds.), Treatise on Geochemistry, 2007. Pergamon, pp. 1–44. https://doi.org/10.1016/B0-08-043751- 6/02123-X.

Klügel, A., Day, S., Schmid, M., Faria, B., 2020. Magma plumbing during the 2014–2015 eruption of Fogo (Cape Verde Islands). Front. Earth Sci. 8, 157. https://doi.org/ 10.3389/feart.2020.00157.

Longpré, M.-A., Stix, J., Klügel, A., Shimizu, N., 2017. Mantle to surface degassing of carbon- and sulphur-rich alkaline magma at El Hierro, Canary Islands. Earth and Planet. Sci. Lett. 460, 268–280.

Lowenstern, J.B., 2003. Melt inclusions come of age: volatiles, volcanoes, and sorby's legacy. Develop. Volcanol. 5, 1–21.

Mata, J., Martins, S., Mattielli, N., Madeira, J., Faria, B., Ramalho, R.S., Silva, P., Moreira, M., Caldeira, R., Moreira, M., Rodrigues, J., Martins, L., 2017. The 2014–15 eruption and the short-term geochemical evolution of the Fogo volcano (Cape Verde): evidence for small-scale mantle heterogeneity. Lith. 288–289, 91–107.

Melián, G.V., Hernández, P.A., Pérez, N.M., Asensio-Ramos, M., Padrón, E., Alonso, M., et al., 2021. Insights from Fumarole Gas Geochemistry on the Recent Volcanic Unrest of Pico do Fogo, Cape Verde. Front. Earth Sci. 9, 631190.

Métrich, N., and Wallace, P.J., 2008. Volatile Abundances in Basaltic Magmas and Their Degassing Paths Tracked by Melt Inclusions. Reviews in Mineralogy and Geochemistry 69, 363–402.

Moore LR, Gazel E, Tuohy R, Lloyd AS, Esposito R, et al. 2015. Bubbles matter: an assessment of the contribution of vapor bubbles to melt inclusion volatile budgets. Am. Mineral. 100:806–23

Oppenheimer, C., Fischer, T.P., Scaillet, B., 2014. Volcanic Degassing: Process and Impact, in: Treatise on Geochemistry. Elsevier, pp. 111–179.

Plank, T., Manning, C.E., 2019. Subducting carbon. Nature 574, 343–352.

Rizzo, A.L., Pelorosso, B., Coltorti, M., Ntaflos, T., Bonadiman, C., Matusiak-Małek, M., Italiano, F., Bergonzoni, G., 2018. Geochemistry of Noble Gases and CO2 in Fluid Inclusions from Lithospheric Mantle Beneath Wilcza Góra (Lower Silesia, Southwest Poland). Front. Earth Sci. 6, 215. https://doi.org/10.3389/feart.2018.00215

Rodder, E. 1979a. Fluid inclusions as samples of ore fluids. In Geochemistry of Hydrotermal Ore Deposits, ed. H. L. Barnes, 684-737. New York: Wiley

Sandoval-Velasquez, A., Rizzo, A.L., Aiuppa, A., Remigi, S., Padrón, E., Pérez, N.M., Frezzotti, M.L., 2021a. Recycled crustal carbon in the depleted mantle source of El Hierro volcano, Canary Islands. Lithos 400–401, 106414.

Taracsák, Z., Hartley, M.E., Burgess, R., Edmonds, M., Iddon, F., Longpré, M.-A., 2019. High fluxes of deep volatiles from ocean island volcanoes: Insights from El Hierro, Canary Islands. Geochim Cosmochim. Acta 258, 19–36.

Tuohy RM, Wallace PJ, Loewen MW, Swanson DA, Kent AJ. 2016. Magma transport and olivine crystallization depths in Kilauea's east rift zone inferred from experimentally rehomogenized melt inclusions. Geochim. Cosmochim. Acta 185:232–50

Zanon, V., and Frezzotti, M.L., 2013. Magma storage and ascent conditions beneath Pico and Faial islands (Azores archipelago): a study on fluid inclusions. Geochem. Geophys. Geosyst. 14, 3494–3514. https://doi.org/10.1002/ggge.20221

Zanon, V., Pimentel, A., Auxerre, M., Marchini, G., Stuart, F.M., 2020. Unravelling the magma feeding system of a young basaltic oceanic volcano. Lith. 352–353, 105325.

CHAPTER 2.

STATE OF THE ART: OIB VOLCANISM

This chapter offers an overview of themes that have gained significant within the geochemical/volcanological community in recent decades, with special reference to the outgassing and carbon budget of the mantle, particularly in OIB setting (e.g., Dasgupta and Hirschmann, 2010; Anderson e Poland, 2017; Longpré et al., 2017; Boudoire et al., 2018; Hauri et al., 2019; Miller et al., 2019; Taracsák et al., 2019; Tucker et al., 2019; Aiuppa et al., 2021). Furthermore, a thorough overview is provided on the current knowledge of OIB volcanism, with a specific focus on the Cape Verde Archipelago and Fogo Volcano. A number of examples from literature are reviewed that have focused on a comprehensive characterisation of a OIB volcano plumbing system, spanning from the mantle source to the trans-crustal storage zone. This chapter also examines some key applications of the methodologies that have here been employed for studying Fogo volcano: (i) microthermometry of fluid inclusions (FI), (ii) analysis of volatile contents in melt inclusions (MI), and (iii) noble gases and carbon isotopes analyses in FI and fumaroles.

2.1. OIB volcanoes, mantle heterogeneities and evidence for a CO_2-rich OIB mantle source

The plate tectonic concept has explained the generation of magma and the geographic distribution of volcanic structures. Volcanism at mid-ocean ridges (MOR) is attributed to extension and decompressional melting due to passive upwelling of mantle materials in response to plate divergence (e.g., Langmuir et al., 1992). Conversely, volcanism at subduction zones is caused by the depression of melting temperatures caused by the influx of fluids released from the slab (e.g., Grove et al., 2006; Green et al., 2010). However, none of these processes can explain melting under ocean islands, which are away from plate boundaries (e.g., Hawaii and Galapagos Islands in the Pacific Ocean, La Réunion in the Indian Ocean, and the Azores, Cape Verde, and the Canary Islands in the Atlantic Ocean). One of the first modern solutions (i.e., after the establishment of plate tectonics theory) to explain their genesis was the mantle plume theory proposed by Morgan (1971). He suggested thermal plumes arising from the deeper mantle cause positive temperature anomalies and melting in the mantle under oceanic islands (Fig.1). In the last decades, considerable efforts have been spent to characterise the major element (Fig. 2), trace element (Fig.3), and isotopic compositions (Fig. 4) of magmas erupted

at oceanic islands in general (e.g., Staudacher et al., 1990; Weaver et al., 1991; Valbracht et al., 1997; Kurz et al., 2009; Métrich et al., 2014) and in the Cape Verde (Gerlach et al., 1988; Doucelance et al., 2003) and Canary archipelagos (Day and Hilton, 2011; Klügel et al., 2017) in particular. Figure 2 shows that, based on their alkalinity (Na_2O+K_2O) at a given SiO_2 content in the Total Alkali Silica (TAS) diagram, the OIBs products can be classified into alkaline and sub-alkaline/tholeiitic basalts. The alkalinity is generally correlated with degree of melting, tholeiitic basalts indicating a higher degree of melting at lower pressures, while alkaline basalts are associated with lower degrees of melting at higher pressures (e.g., Green and Ringwood, 1967; Frey et al., 1978; Garcia et al., 1993). In the course of their eruptive history, the Cape Verde archipelago has generated diverse volcanic products with a broad spectrum of chemical compositions, both inter- and intra-island, encompassing the entire range of the Total Alkali-Silica (TAS) diagram, as illustrated in Figure 2. All OIBs consistently display a trend in trace element composition characterized by an enrichment in High Field Strength Elements (HFSE) compared to Large Ion Lithophile Elements (LILE) and Light Rare Earth Elements (LREE), indicative of recycled basaltic ocean crust. In detail, HIMU (high-μ, a ^{206}Pb-rich) OIBs originate from a source with minimal contamination from other components. In contrast, EM-1 and EM-2 (Enriched Mantle 1 and 2) show contamination, with a significant presence (up to 5-10%) of sedimentary components derived from the continental crust. This includes ancient pelagic and terrigenous sediments for EM-1 (as evidenced by high Ba/Th and Ba/La ratios and low U/Pb) and EM-2 (characterised by high U/Pb and Rb/Sr ratios and no Ba enrichment), respectively (Weaver et al., 1991).

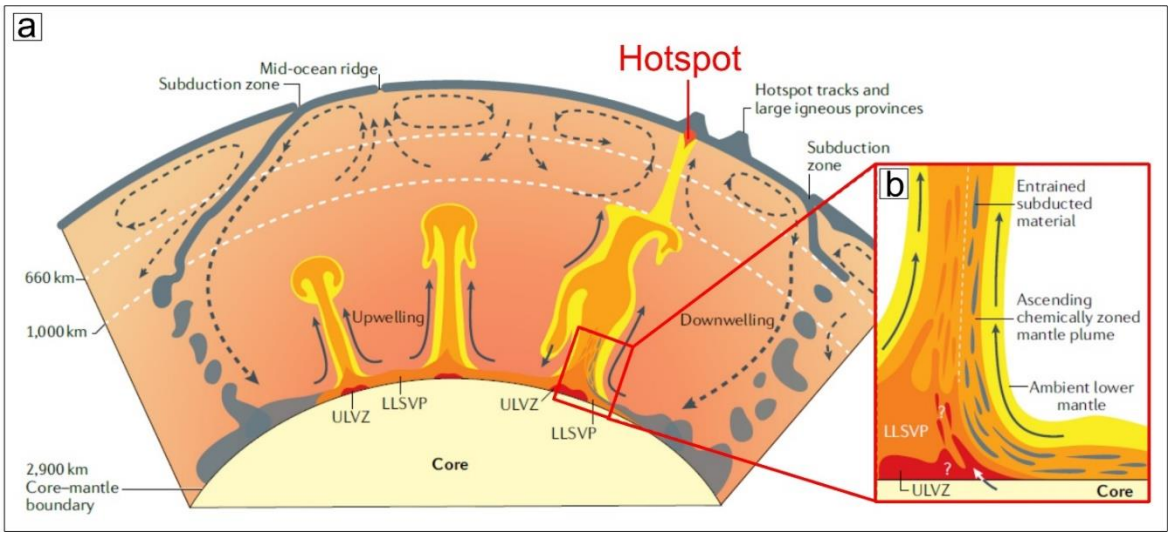

Figure 1 Earth's interior cross-section, illustrating mantle plume generation and upwelling in proximity to, above, and along the peripheries of a significant low-shear-velocity province (LLSVP)

and close to the core–mantle boundary. These LLSVPs may host localized ultra-low velocity zones (ULVZs), with subducted material accumulating along their edges potentially over hundreds of millions of years **(a)**. Schematic cross section of a plume root exhibiting the incorporation of subducted materials, LLSVP and ULVZ components, and potentially core materials at the periphery of an LLSVP and positioned directly above a ULVZ **(b)**. Modified from Koppers et al., 2021.

Geochemical investigations of OIB have especially benefited from the use of radiogenic isotopes (e.g., Sr, Nd, Pb) and noble gases (e.g., He, Ar, Ne). Radiogenic isotope compositions of OIB magmas are strikingly different from Mid-Ocean Ridge Basalts (MORBs), which are believed to originate from the melting of depleted upper mantle material. These distinct characteristics imply that the mantle is heterogeneous, and the source of this heterogeneity can be traced back to material being reintroduced into the deeper regions of the mantle through subduction zones (Hofmann and White, 1982). The recycled materials have been classified based on their radiogenic isotope composition (Zindler and Hart, 1986). As previously mentioned, two of these categories are EM-1 and EM-2, believed to represent recycled sedimentary material, and HIMU, often associated with recycled basaltic ocean crust (e.g., Day et al., 2010). However, the origin of this HIMU component is a matter of debate among researchers (e.g., Takamasa et al., 2009; Jackson et al., 2017a). These recycled components mix with the surrounding mantle, represented by the (Bulk Silicate Earth) BSE and the (Depleted MORB Mantle) DMM components. Within this wide range of distinct isotopic signatures, the Cape Verde archipelago occupies a unique position, sampling both extreme geochemical components (EM and HIMU, Jackson et al., 2018), exhibiting trends towards HIMU (Figure 4a) and towards EM (Figure 4b), as well as intermediate values (Figure 4c). This variability in radiogenic isotopes is present not only within the archipelago but also within the same island, as observed at Fogo (Mata et al., 2017).

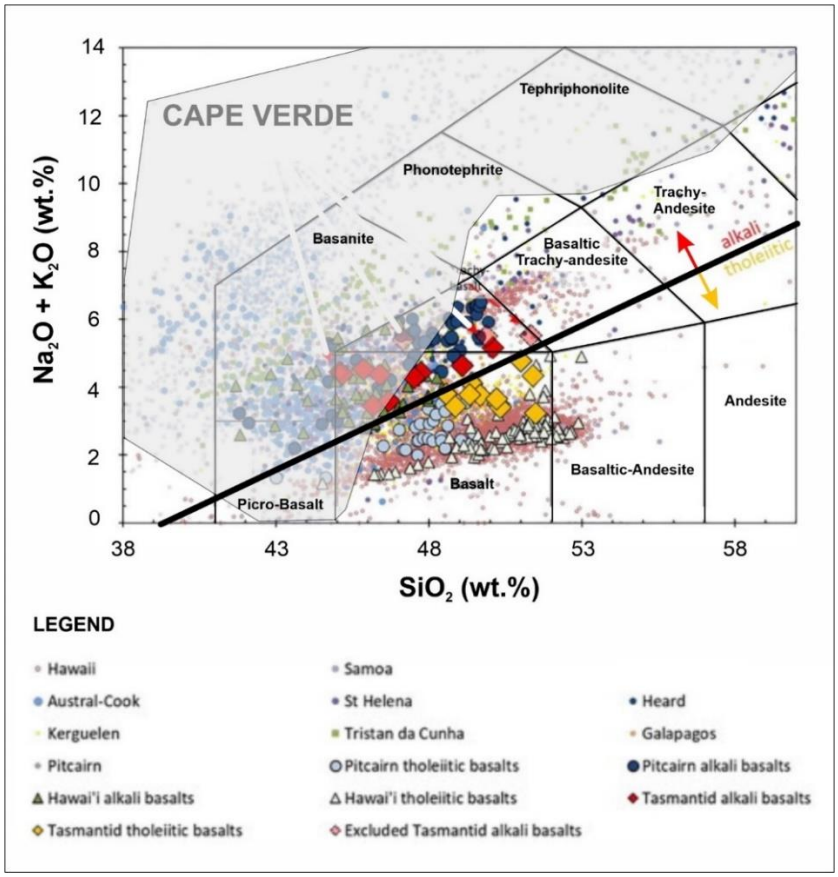

Figure 2 Total alkali-silica (TAS) diagram according to Le Bas et al. (1986) of samples from various OIB locations. Modified from Ruttor et al. (2021).

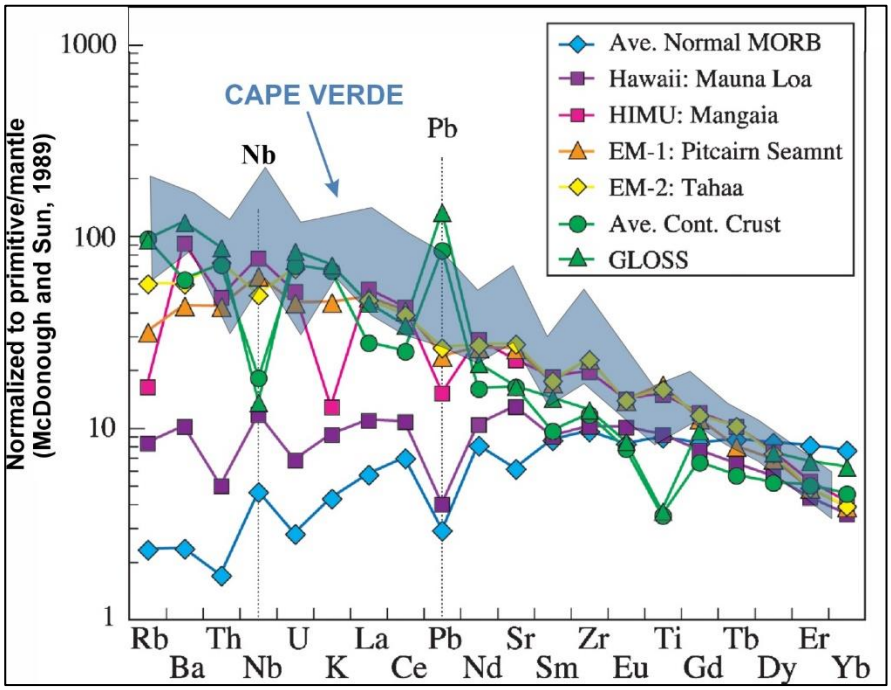

Figure 3 Plot of trace elements on a spider diagram illustrating the normalized abundance of trace elements for representative samples of HIMU, EM-1, EM-2; average Mauna Loa tholeiite, average continental crust, average subducting sediment, Global subducted sediments (GLOSS), and Average Normal MORB. All abundance values are standardized to the primitive/mantle values of McDonough and Sun (1995). Modified from Hofmann (2003).

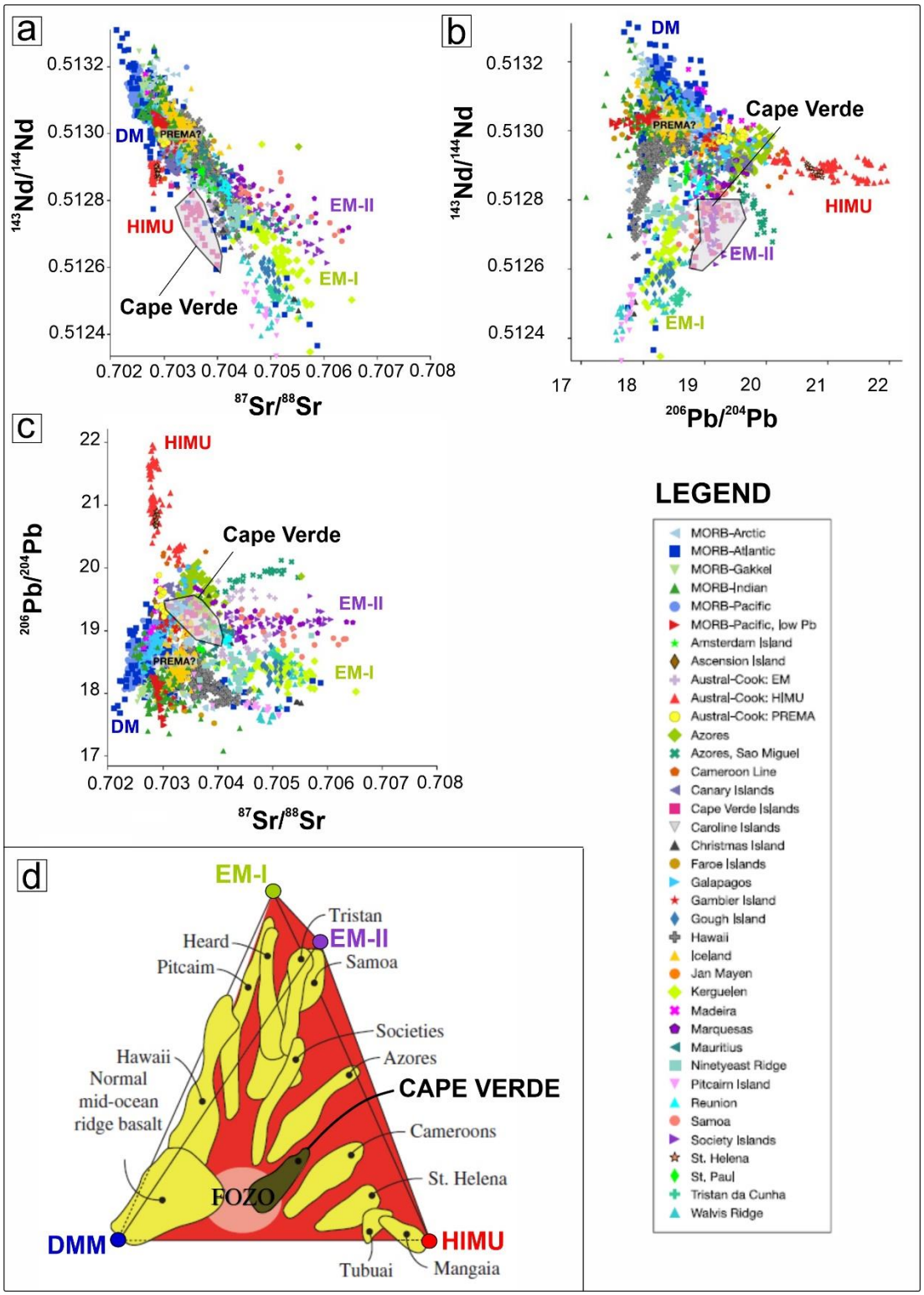

Figure 4 Plots of radiogenic isotopes (Sr-Nd-Pb) derived from MORBs and OIBs. The ratios are graphically represented using different combinations of $^{87}Sr/^{86}Sr$, $^{143}Nd/^{144}Nd$, and $^{206}Pb/^{204}Pb$. The plots also show the phenotypes, as defined by Zindler and Hart (1986): Depleted Mantle (DM), PREvalent MAntle (PREMA), high μ (HIMU), Enriched Mantle (EM) 1 and 2 **(a).** A three-dimensional projection of $^{87}Sr/^{86}Sr$, $^{143}Nd/^{144}Nd$, $^{206}Pb/^{204}Pb$ isotope arrays for various OIB groups (following Hart et al., 1992). The majority of OIBs, with Cape Verde more than others, appear to originate from a common region referred to as "FOZO" (Focal Zone), believed to represent the composition of the deep mantle **(b).** Modified from Stracke et al. (2022a)

Relative to the well-studied radiogenic isotopes, major volatile elements in OIB magmas are understudied. There are only a few available estimates for the contents of the main volatile species (e.g., H_2O, CO_2, and S) in oceanic island magmas; such as those for the Canary Islands (Longprè et al., 2017; Taracsák et al., 2019), the Azores (Métrich et al., 2014); the Galapagos (Koleszar et al., 2009), and Iceland (Bali et al., 2018; Hartley et al., 2014). Volatile elements, such as, carbon, sulphur, and halogens, play a critical role in discussions concerning mantle heterogeneity. However, compared to radiogenic isotopes, the study of volatiles in magmatic systems has been significantly challenged by factors that limit their direct measurement, notably their low solubility at low pressure (that cause erupted lavas to be severely degassed). Volatiles are important because they influence the physical properties of the mantle. Indeed, elevated volatile contents in the mantle lead to lower seismic velocities, reduced viscosity, and heightened electrical conductivity (e.g., Faccenda et al., 2012). One of the most notable effects of introducing volatiles into the mantle is the lowering of the solidus temperature, potentially by several hundred degrees (e.g., Hirschmann et al., 2009; Green et al., 2010). Moreover, volatile elements impact the chemical composition of mantle melts, giving rise to magmas with diverse chemical compositions erupting in various geodynamic settings (e.g., Dasgupta et al., 2007; Green et al., 2014). In recent years, researchers have extensively investigated whether volatile elements are recycled into the mantle during subduction (e.g., Kendrick et al., 2012; Jégo and Dasgupta, 2014; Plank and Manning, 2019; Walters et al., 2020). However, several questions remain unanswered, including whether these recycled volatiles, added to the mantle, undergo resurfacing at oceanic islands through the melting of heterogeneous mantle lithologies.

OIB, formed through partial melting in ascending mantle plumes represent a window into some of the more deeply explorable portions of the Earth's upper mantle (Hofmann, 2003). OIB, while accounting for only about 10% of the annual magma output on Earth, can be significantly enriched in volatiles, especially alkali-rich ones, with up to > 5% volume (Cabral et al., 2014; Boudoire et al., 2018; Longpré et al., 2017; Taracsák et al., 2019). As a result, OIB can disproportionately contribute

to the annual magmatic gas output compared to more voluminous but less volatile-enriched MORBs (Hauri et al., 2019). The silica-undersaturated alkaline lavas, exhibit significantly higher CO_2 enrichment compared to tholeiitic melts (Dixon et al., 1997; Dasgupta et al., 2007; Mallik and Dasgupta, 2014; Longpré et al., 2017). Thus, neglecting the study of alkaline OIB could potentially lead to an underestimation of CO_2 contents in OIB mantle sources, especially when they originate from the deep mantle.

The origin of alkaline OIB magmas is widely debated, and two distinct models have emerged to explain their petrogenesis. The first model suggests a low-degree partial melting of CO_2-bearing deep mantle sources in the asthenosphere (e.g., Gerbode and Dasgupta 2010; Davis et al., 2011; Mallik and Dasgupta, 2014; Sun and Dasgupta, 2023), while the second model proposes partial melting of metasomatised mantle in the lithosphere (Pilet et al., 2008; Pilet, 2015).

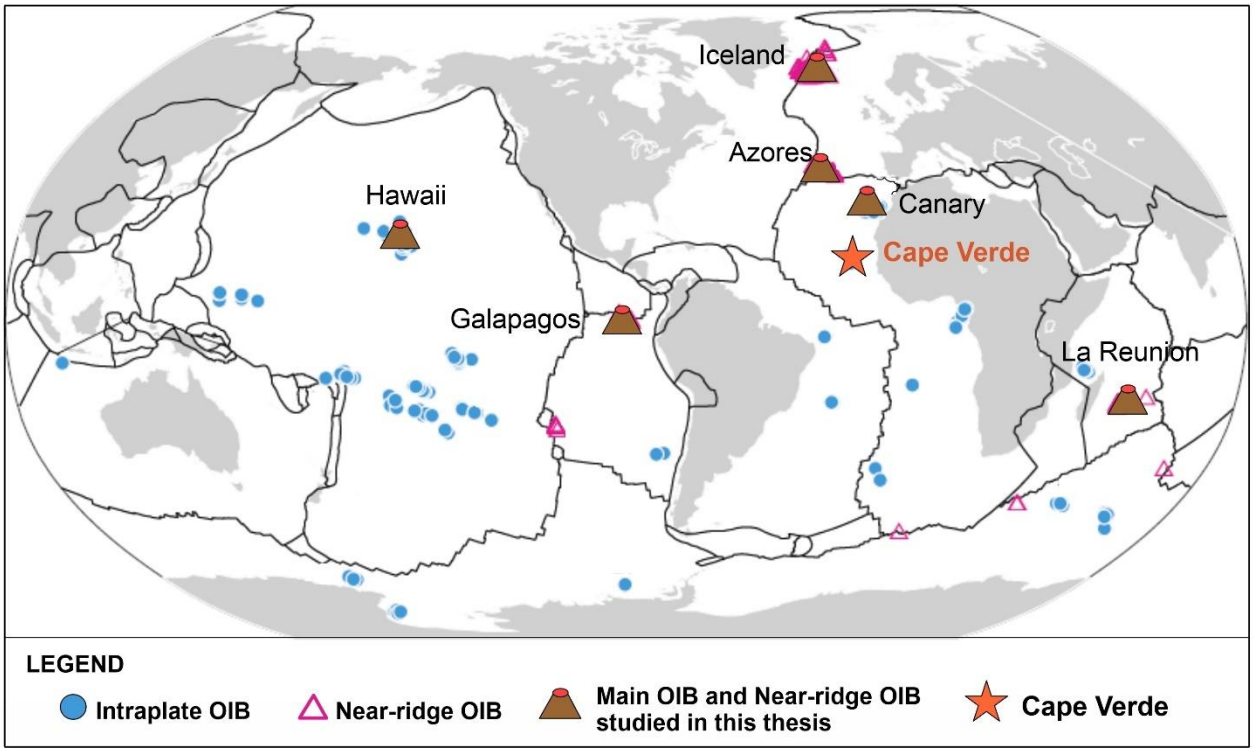

Figure 5 Global distribution of ocean island basalts (OIBs), modified by Sun and Dasgupta (2023)

2.3. FI microthermometry and magma plumbing system architecture at OIB volcanoes.

OIB volcanoes are indicators from the deep mantle, yet the filtering effect of the plumbing systems that bring OIB melts to the surface remains poorly assessed (Ubide et al., 2021). A robust

understanding of the magma plumbing system's architecture is key to modelling pre-eruptive magma storage conditions and timescales of magma ascent (Cashman et al., 2017; Pappalardo and Buono, 2021). Consequently, it is critical for volcano monitoring and the assessment and mitigation of volcanic hazards and risks.

Several studies on microthermometry analysis of CO_2-dominated FI have proved that this methodology is especially suited for this scope, as it can provide information on pressure, and hence depth, of pre-eruptive magma storage across multiple magma ponding levels (e.g., Canary Islands, Hasteen et al., 1998; Klugel et al., 2005, 2022; Oglialoro et al., 2017; Azores Islands, Zanon and Frezzotti, 2013; Métrich et al 2014; Zanon 2015; Zanon and Pimentel 2015; Zanon and Viveiros 2019; Zanon et al., 2020; Zanon et al., 2023). Fluid inclusions are "defects bubbles" trapped in crystals during their growth. In magmatic environments, fluid inclusions are bubbles of exsolved magmatic volatiles that are trapped in crystallographic defects during crystal growth, or during re-equilibration (Bodnar, 2003). The most frequently investigated minerals for FI studies, associated to mafic magmas, are olivine and pyroxenes, which are usually the first mineral phase to crystallize during magma fractionation (Bowen, 1922).

The complex interplay between local and regional stress fields, magma rheology and composition, and the sub-volcanic basement crustal structure collectively govern the conditions of pre-eruptive magma storage and ascent beneath intra-plate oceanic island volcanoes. These factors determine whether deep-seated (upper mantle; Longpré et al., 2008) or shallow stored (Garcia, 2003; Peltier et al., 2009; Di Muro et al., 2014; Bell et al., 2021) magma is activated prior to eruption (Zanon et al., 2020). The conditions of magma storage may also be influenced by mass loading and unloading during volcanic edifice growth or failure. Thus, the magma storage conditions of different oceanic island volcanoes range from shallow crustal [e.g., Kilauea (Hawaii), Wallace et al., 2021; Sierra Negra (Galapagos), Bell et al., 2021] to upper mantle [e.g., Fogo (Cape Verde), Hildner et al., 2011, 2012; Klügel et al., 2020; El Hierro (Canary) Klügel et al., 2022; Sao Miguel (Azores), Zanon, 2015]. This diversity is a function of the numerous parameters that govern magma ascent and storage at volcanoes. Crust thickness, ranging from ~27 to 29 km and ~12–15 km underneath São Miguel (Zanon et al., 2023) and Canary volcanoes (Ranero et al., 1995; D'Auria et al., 2022) respectively, and crust age, spanning from ~155 Ma below La Palma (Verhoef et al., 1991) to <5 Ma beneath the Galápagos (White et al., 1993), are two important parameters. Another important factor that influences the architecture of magma storage is the magma supply rate. This varies from 3 to 4 $m^3 \cdot s^{-1}$ at Kilauea (Poland, 2014), where more shallow storage conditions are established (in the crust,

Wallace et al., 2021), to 0.06 $m^3 \cdot s^{-1}$ at Fogo (Bagnardi et al., 2016), where deeper storage conditions exist (upper mantle, Hildner et al., 2011, 2012; Klügel et al., 2020).

2.4. Magma volatile budgets at oceanic islands volcanoes: insights from melt inclusions.

Silicate melt inclusions (MI) are small (1-100 μm) pockets of melts entrapped during host mineral growth (Sorby, 1858), and are studied to (i) quantify the budgets of volatiles in pre-eruptive magma conditions (e.g., Kovalenko et al., 2006; Hauri et al., 2011); (ii) reconstruct the magma degassing paths (e.g., Dixon and Stolper, 1995; Metrich and Wallace, 2008; Witham et al., 2012; Taracsák et al., 2019); (iii) constrain the magma plumbing system architecture (e.g., Wallace et al., 2021; Esposito, 2021). Upon rapid cooling into a glassy state, melt inclusions should, in theory, preserve the dissolved volatile contents at the specific pressure, temperature, and compositional conditions of entrapment. Moreover, they could offer perspectives into the volatile composition of the primary melt if entrapment occurred near the magma source (prior to reaching the saturation point) (e.g., Metrich and Wallace, 2008; Edmonds and Wallace, 2017). The volatile contents measured in melt inclusions are powerful tools to complement volcanic gas analysis (Aiuppa et al., 2022). When examined together, they provide a robust method for comprehending the history of gas exsolution from a magma (Métrich & Wallace, 2008).

Recent studies conducted on MI from alkaline-OIB volcanoes worldwide have highlighted the carbon-rich nature of these magmas, as demonstrated by El Hierro (up to 4 wt.% CO_2; Longpré et al., 2017; Moussallam et al., 2019; Taracsák et al., 2019) and La Palma (3-5 wt.% CO_2; Burton et al., 2023) in the Canary Archipelago, Piton de La Fournaise in Reunion Island (3.5 ± 1.4 wt.% CO_2; Boudoire et al., 2018), and Fogo in the Cape Verde Archipelago (De Vitre et al., 2023). These CO_2 levels fall at the lower range of measured or inferred CO_2-rich signatures of alkaline mafic melts from continental rift contexts (e.g., East African Rift system; Foley et al., 2012), and are significantly higher than those obtained at many other OIB localities worldwide, such as Erebus in Antarctica (Eschenbacher et al., 1998; Moussallam et al., 2014), Fernandina and Santiago in the Galapagos (Koleszar et al., 2009), Piton de la Fournaise in Reunion Island (Di Muro et al., 2014), Kilauea in Hawaii (Sides et al., 2014), Pico in the Azores (Métrich et al., 2014), and OIB localities near mid-ocean ridges, like Iceland (e.g., Bardabunga, Bali et al., 2018; Laki, Hartley, 2014) (Table 1). The MI volatile contents (H_2O-CO_2) combined with available saturation models are also employed to (i) estimate the entrapment pressures of MI, assuming melts are volatile-saturated at the time of

entrapment; (ii) gain insights into volatile degassing behaviour during magma storage and pre-eruptive ascent. The challenge lies in the conversion of volatile contents into pressures, necessitating the selection of one of several saturation models available in the literature [e.g., MagmaSat, Ghiorso and Gualda, (2015); Iacono-Marziano et al., (2012); D-Compress, Burgisser et al., (2015); Moretti et al., (2003); VolatileCalc, Newman and Lowenstern, (2002); Jiménez-Mejías et al., (2021); Shishkina et al., (2014)]. All of these models have been calibrated at relatively low pressures (the model of Eguchi and Desgupta, 2018, is the only exception) (< 800 MPa) and thus for lower CO_2 contents than those recently found in OIB context (e.g., El Hierro, Taracsák et al., 2019; La Reunion, Boudoire et al., 2018; Fogo, De Vitre et al., 2023). Therefore, the selection of a saturation model that accurately reproduces the volatile trends along the degassing paths, and providing valid MI saturation pressures is one of the challenges of recent studies have aimed to address.

Table 1. CO_2 content in different OIBs examined in this dissertation. (*) These data represent average values calculated within the MI samples

	CO_2 (wt.%)	**references**
Fogo	2.0	DeVitre et al., 2023
El Hierro	4.0	Longpré et al., 2017; Moussallam et al., 2019; Taracsák et al., 2019
La Palma	3.0-5.0	Burton et al., 2023
Piton de La Fournaise	3.5 ± 1.4	Boudoire et al., 2018
Erebus *	0.12	Eschenbacher et al., 1998; Moussallam et al., 2014
Fernandina *	0.06	Koleszar et al., 2009
Santiago *	0.03	Koleszar et al., 2010
Pico *	0.18	Métrich et al., 2014
Kilauea *	0.01	Sides et al., 2014
Bardabunga *	0.33	Bali et al., 2018
Laki *	0.13	Hartley, 2014

2.5 Mantle source signature, noble gases and carbon isotopes in fluid inclusions

The chemical inertness of the noble gases makes them valuable geochemical tools to characterise Earth's interior, from the deep mantle source to the surface (e.g., Dickin, 2018). Noble gases provide insights useful to understand the degassing history of the mantle, the relationship between different mantle components, and the nature and signature of metasomatic fluids in the mantle (Correale et al., 2012; Day and Hilton, 2011, 2021; Dunai and Porcelli, 2002; Gurenko et al., 2006; Rizzo et al., 2018; Sandoval-Velasquez et al., 2021a, 2021b).

Several studies have already used noble gases and CO_2 systematics in FI to understanding the primary processes that could modify the characteristics of the mantle both temporally and spatially (e.g., Deines, 2002; Gautheron et al., 2005; Martelli et al., 2011, 2014; Correale et al., 2012, 2016; Day et al., 2015; Gennaro et al., 2017, Rizzo et al., 2018; Carnevale et al., 2021; Sandoval-Velasquez et al., 2021a, 2021b). The ease of analysis and the radiogenic nature of the isotopes of Helium, Xenon, Argon, and Neon, compared to the remaining noble gases (Krypton and Radon), make them perfect for geochemical studies of OIB (Hennecke and Manuel, 1975; Kaneoka and Takaoka, 1978; Fisher, 1983; Sarda et al., 1988). In particular, the helium isotopes were exploited to determine the mantle structure (e.g., Williams et al., 2019; Day and Hilton, 2021). Noble gases measured in ultramafic xenoliths, lavas and volcanic gases across the globe suggest the existence of at least four main volatile reservoirs in the mantle (e.g., Burnard et al., 1997; Dunai and Porcelli, 2002; Graham, 2002; Day et al., 2022): (i) low-$^3He/^4He$ OIB (< 7 Ra) (e.g., São Miguel, Azores, Moriera et al., 2012; St. Helena, Hanyu et al., 2011; Mangaia, Parai et al., 2009); (ii) MORB-like $^3He/^4He$ OIB (8 ± 2 RA) (e.g., Ascension Island, Ammon et al., 2009; Canary Islands, Hilton et al., 2000; Day and Hilton, 2011; the Comoros, Class et al., 2005; Mount Erebus, Day et al., 2019); (iii) intermediate-$^3He/^4He$ OIB group (~10 - ~20 RA) (e.g., Azores (although there are exceptions), Madureira et al., 2005; Cape Verde (although there are exceptions), Doucelance et al., 2003; Pitcairn Island, Garapìc et al., 2015; Reunion Island, Staudacher et al., 1990; Füri et al., 2011); (iv) high-$^3He/^4He$ OIB group (>25 RA) (Iceland, Hilton et al., 1999; Hawaii, Valbracht et al., 1997; Galapagos, Kurz et al., 2009; Samoa, Jackson et al., 2009).

Similar to noble gases, carbon isotopes serve as unique geochemical tracers. Insight from FI in mantle xenoliths (Deines, 2002) has revealed a highly diverse range of carbon isotope signatures within the mantle, encompassing $\delta^{13}C$ values spanning from -29.9‰ in Hawaii (Pineau and Mathez, 1990) to +0.9‰ at El Hierro (Canary Islands, Sandoval-Velasquez et al., 2021a). This wide range of carbon

isotopic compositions strongly indicates the involvement of various crustal carbon components, varying from organic crustal carbon (-30‰ to -10‰) to limestone carbon (from -1‰ to +1‰), possibly intermingling in different proportions with a deep Depleted MORB (Middle Oceanic Ridge Basalt) mantle (DMM) carbon ($\delta^{13}C$ of -4 to -8 ‰) (Sano and Marty, 1995; Deines, 2002). Alkaline-OIB, are carbon-rich (Boudoire et al., 2018; Sun and Dasgupta, 2023 and references therein), indicating these magmas do form by low-degree of melting of carbon-enriched (metasomatised) mantle sources. Measuring the carbon isotope signature of alkaline OIB is thus critical to testing models (Dasgupta et al., 2019) that see these metasomatic agents (carbonatitic to carbonated silicate melts) to derive from melting of deeply subducted, carbon enriched crustal lithologies.

REFERENCES

Aiuppa, A., Allard, P., Bernard, B., Lo Forte, F.M., Moretti, R., Hidalgo, S., 2022. Gas Leakage from Shallow Ponding Magma and Trapdoor Faulting at Sierra Negra Volcano (Isabela Island, Galápagos). Geochem. Geophys. Geosyst. 23.

Ammon, K., Dunai, T.J., Stuart, F.M., Meriaux, A.S., Gayer, E., 2009. Cosmogenic ^{3}He exposure ages and geochemistry of basalts from Ascension Island, Atlantic Ocean. Quat. Geochronol. 4, 525–532.

Anderson, K.R, Poland, M.P., 2017. Abundant carbon in the mantle beneath Hawaii. Nat. Geosci. 10: 704-708

Bali, E., Hartley, M.E., Halldórsson, S.A., Gudfinnsson, G.H., Jakobsson, S., 2018. Melt inclusion constraints on volatile systematics and degassing history of the 2014–2015 Holuhraun eruption, Iceland. Contrib. Mineral. Petrol. 173, 9.

Bell, A.F., La Femina, P.C., Ruiz, M., Amelung, F., Bagnardi, M., Bean, C.J., et al., 2021. Caldera resurgence during the 2018 eruption of Sierra Negra volcano, Galapagos Islands. Nat. Commun. 12, 1397.

Boudoire, G., Rizzo, A.L., Di Muro, A., Grassa, F., Liuzzo, M., 2018. Extensive CO_2 degassing in the upper mantle beneath oceanic basaltic volcanoes: First insights from Piton de la Fournaise volcano (La Réunion Island). Geochim. et Cosmochim. Acta 235, 376–401.

Burgisser, A., Alletti, M., Scaillet, B., 2015. Simulating the behavior of volatiles belonging to the C–O–H–S system in silicate melts under magmatic conditions with the software D-Compress. Comput. Geosci. 79, 1–14.

Burnard, P., Graham, D., Turner, G., 1997. Vesicle-Specific Noble Gas Analyses of "Popping Rock": Implications for Primordial Noble Gases in Earth. Science 276, 568–571.

Burton, M., Aiuppa, A., Allard, P., Asensio-Ramos, M., Confrades, A.P., La Spina., A., et al., 2023. Exceptional eruptive CO_2 emissions from intra-plate alkaline magmatism in the Canary volcanic archipelago. Commun. Earth Environ. 4, 467.

Cabral, R. A., Jackson, M. G., Koga, K. T., Rose-Koga, E. F., Hauri, E. H., M. J. Whitehouse et al., 2014. Volatile cycling of H_2O, CO_2, F, and Cl in the HIMU mantle: A new window provided by melt inclusions from oceanic hot spot lavas at Mangaia, Cook Islands, Geochem. Geophys. Geosyst., 15, 4445–4467

Carnevale, G., Caracausi, A., Correale, A., Italiano, L., Rotolo, S., 2021. An Overview of the Geochemical Characteristics of Oceanic Carbonatites: New Insights from Fuerteventura Carbonatites (Canary Islands). Minerals 11, 203. https://doi.org/10.3390/min11020203

Christensen, B.P., Holm, P.M., Jambon, A., Wilson, J.R., 2001. Helium, argon and lead isotopic composition of volcanics from Santo Antão and Fogo, Cape Verde Islands. Chem. Geol. 178, 127–142.

Class, C., Goldstein, S.L., Stute, M., Kurz, M.D., Schlosser, P., 2005. Grand Comore Island: a well-constrained "low $^3He/^4He$" mantle plume. Earth Planet. Sci. Lett. 233, 391–409.

Correale, A., Martelli, M., Paonita, A., Rizzo, A., Brusca, L., Scribano, V., 2012. New evidence of mantle heterogeneity beneath the Hyblean Plateau (southeast Sicily, Italy) as inferred from noble gases and geochemistry of ultramafic xenoliths. Lith. 132–133, 70–81.

Correale, A., Rizzo, A.L., Barry, P.H., Lu, J., Zheng, J., 2016. Refertilization of lithospheric mantle beneath the Yangtze craton in south-east China: Evidence from noble gases geochemistry. Gondwana Res. 38, 289–303. https://doi.org/10.1016/j.gr.2016.01.003

Davies, G.F., 2011. Mantle Convection for Geologists. Cambridge University Press, Cambridge.

Day, J.M.D., Barry, P.H., Hilton, D.R., Burgess, R., Pearson, D.G., Taylor, L.A., 2015. The helium flux from the continents and ubiquity of low-$^3He/^4He$ recycled crust and lithosphere. Geochim. Cosmochim. Acta 153, 116–133.

Day, J.M.D., Harvey, R.P., Hilton, D.R., 2019. Melt-modified lithosphere beneath Ross Island and its role in the tectono-magmatic evolution of the West Antarctic Rift System. Chem. Geol. 518, 45–54. https://doi.org/10.1016/j.chemgeo.2019.04.012

Day, J.M.D., and Hilton, D.R., 2011. Origin of $^3He/^4He$ ratios in HIMU-type basalts constrained from Canary Island lavas. Earth Planet. Sci. Lett. 305, 226–234.

Day, J.M.D., Hilton, D.R., 2021. Heterogeneous mantle-derived helium isotopes in the Canary Islands and other ocean islands. Geology.

Day, J.M.D., Jones, T.D., Nicklas, R.W., 2022. Mantle sources of ocean islands basalts revealed from noble gas isotope systematics. Chem. Geol. 587, 120626.

Day, J.M.D., Pearson, D.G., Macpherson, C.G., Lowry, D., Carracedo, J.C., 2010. Evidence for distinct proportions of subducted oceanic crust and lithosphere in HIMU-type mantle beneath El Hierro and La Palma, Canary Islands. Geochim. Cosmochim. Acta 74, 6565–6589.

Dasgupta, R., Grewal, D.S., 2019. Origin and early differentiation of carbon and associated life-essential volatile elements on Earth. In: Orcutt, B., Daniel, I., Dasgupta, R. (Eds.), Deep Carbon: Past to Present. Cambridge University Press, Cambridge, pp.4–39. https://doi .org /10 .1017 /9781108677950.

Dasgupta, R., Hirschmann, M.M., 2010. The deep carbon cycle and melting in Earth's interior. Earth and Planet. Sci. Lett. 298, 1–13. https://doi.org/10.1016/j.epsl.2010.06.039

Dasgupta, R., Hirschmann, M.M., Smith, N.D., 2007. Partial melting experiments of peridotite + CO_2 at 3 GPa and genesis of alkalic ocean island basalts. J. Petrol.48, 2093–2124. https://doi .org /10 .1093 /petrology /egm053

Deines, P., 2002. The carbon isotope geochemistry of mantle xenoliths. Earth-Sci. Rev. 58, 247–278. https://doi.org/10.1016/S0012-8252(02)00064-8

Dickin, A.P., 2018. Radiogenic Isotope Geology, 3rd ed. Cambridge University Press.

Di Muro, A., Metrich, N., Vergani, D., Rosi, M., Armienti, P., Fougeroux, T., Deloule, E., Arienzo, I., Civetta, L., 2014. The Shallow Plumbing System of Piton de la Fournaise Volcano (La Reunion Island, Indian Ocean) Revealed by the Major 2007 Caldera-Forming Eruption. J. Petrol. 55, 1287–1315.

Dixon, J.E., Clague, D.A., Wallace, P., Poreda, R., 1997. Volatiles in alkalic basalts from the North Arch volcanic field, Hawaii: extensive degassing of deep submarine-erupted alkalic series lavas. J. Petrol.38, 911–939. https://doi .org /10 .1093 /petroj /38 .7.911.

Doucelance, R., Escrig, S., Moreira, M., Gariépy, C., Kurz, M.D., 2003. Pb-Sr-He isotope and trace element geochemistry of the Cape Verde Archipelago. Geochim. Cosmochim. Acta 67, 3717–3733.

Dunai, T.J., Porcelli, D., 2002. Storage and Transport of Noble Gases in the Subcontinental Lithosphere. Rev. Mineral. Geochem. 47, 371–409. https://doi.org/10.2138/rmg.2002.47.10

Eguchi, J. and Dasgupta, R., 2018. A CO_2 solubility model for silicate melts from fluid saturation to graphite or diamond saturation, Chem. Geol., 487, 23–38.

Eschenbacher, A. 1998. Open-system degassing of a fractionating, alkaline magma, Mount Erebus, Ross Island, Antarctica. Unpublished Master's Thesis, New Mexico Institute of Mining and Technology, Socorro.

Esposito, R., 2021. A protocol and review of methods to select, analyze and interpret melt inclusions to determine pre-eruptive volatile contents of magmas. In: Lecumberri-Sanchez, P., Steele-MacInnis, M., Kontak, D. (Eds.), Fluid and Melt Inclusions: Applications to Geologic Processes. Mineralogical Association of Canada, London, Ontario, 163–194.

Faccenda, M., Gerya, T.V., Mancktelow, N.S., Moresi, L., 2012. Fluid flow during slab unbending and dehydration: implications for intermediate-depth seismicity, slab weakening and deep water recycling. Geochem. Geophys. Geosyst. 13 (1).

Fisher, D.E., 1983. Rare gases from the undepleted mantle? Nature 305, 298–300.

Foley, S. F., Link, K., Tiberindwa, J. V. & Barifaijo, E. 2012. Patterns and origin of igneous activity around the Tanzanian craton. J. Afr. Earth Sci. 62, 1–18.

Frey, F.A., Garcia, M.O., Roden, M.F., 1994. Geochemical characteristics of Koolau Volcano: Implications of intershield geochemical differences among Hawaiian volcanoes. Geochim. Cosmochim. Acta, 58, 1441-1462.

Füri, E., Hilton, D.R., Murton, B.J., Hemond, C., Dyment, J., Day, J.M.D., 2011. Helium isotope variations between Réunion Island and the Central Indian Ridge (17°-21°S): new evidence for ridge-hotspot interaction. J. Geophys. Res. Solid Earth. https://doi. org/10.1029/2010JB007609.

Garapìc, G., Mallik, A., Dasgupta, R., Jackson, M.G., 2015. Oceanic lavas sampling the high-$^{3}He/^{4}He$ mantle reservoir: Primitive, depleted, or re-enriched? Am. Mineral. 100, 2066–2081.

Garcia, M.O., Jorgenson, B.A., Mahoney, J.J., Ito, E., Irving, A.J., 1993. An evaluation of temporal geochemical evolution of Loihi Summit Lavas: Results from Alvin submersible dives. J. Geophys. Res. Solid Earth, 98, 537-550.

Gautheron, C., Moreira, M., Allègre, C., 2005a. He, Ne and Ar composition of the European lithospheric mantle. Chem. Geol. 217, 97–112.

Gennaro, M.E., Grassa, F., Martelli, M., Renzulli, A., Rizzo, A.L., 2017. Carbon isotope composition of CO_2 -rich inclusions in cumulate-forming mantle minerals from Stromboli volcano (Italy). J. Volcanol. Geotherm. Res. 346, 95–103. https://doi.org/10.1016/j.jvolgeores.2017.04.001

Gerbode, C., Dasgupta, R., 2010. Carbonate-fluxed melting of MORB-like pyroxenite at 2 ·9GPa and genesis of HIMU ocean island basalts. J. Petrol.51, 2067–2088. https://doi .org /10 .1093 /petrology /egq049.

Gerlach, D.C., Cliff, R.A., Davies, G.R., Norry, M., Hodgson, N., 1988. Magma sources of the Cape Verdes archipelago: Isotopic and trace element constraints. Geochim. Cosmochim. Acta 52, 2979–2992.

Ghiorso, M.S., and Gualda, G.A.R., 2015. An H_2O–CO_2 mixed fluid saturation model compatible with rhyolite-MELTS. Contrib. Mineral. Petrol. 169, 53.

Graham, D.W., 2002. Noble Gas Isotope Geochemistry of Mid-Ocean Ridge and Ocean Island Basalts: Characterization of Mantle Source Reservoirs. Rev. Mineral. Geochem. 47, 247–317.

Green, D. H., Hibberson, W. O., Kovacs, I., and Rosenthal, A. 2010. Water and its influence on the lithosphere-asthenosphere boundary. Nature, 467(7314):448–451.

Green, D. H., Hibberson,W. O., Rosenthal, A., Kovács, I., Yaxley, G. M., Falloon, T. J., et al., 2014. Experimental study of the influence of water on melting and phase assemblages in the upper mantle. J. Petrol., 55(10):2067–2096

Green, D., and Ringwood, A., 1967. The genesis of basaltic magmas. Contrib. Miner. Petrol., 15, 103-190.

Grove, T. L., Chatterjee, N., Parman, S. W., and Médard, E. 2006. The influence of H_2O on mantle wedge melting. Earth and Planet. Sci. Lett., 249(1):74–89.

Gurenko, A.A., Hoernle, K.A., Hauff, F., Schmincke, H.-U., Han, D., Miura, Y.N., et al., 2006. Major, trace element and Nd–Sr–Pb–O–He–Ar isotope signatures of shield stage lavas from the central and western Canary Islands: Insights into mantle and crustal processes. Chem. Geol. 233, 75–112.

Hanyu, T., Tatsumi, Y., Kimura, J.I., 2011. Constraints on the origin of the HIMU reservoir from He–Ne–Ar isotope systematics. Earth Planet. Sci. Lett. 307, 377–386.

Hart, S. R., Hauri, E. H., Oschmann, L. A., Whitehead, J. A. 1992. Mantle plumes and entrainment: isotopic evidence. Science 256, 517–520.

Hartley, M.E., Maclennan, J., Edmonds, M., Thordarson, T., 2014. Reconstructing the deep CO_2 degassing behaviour of large basaltic fissure eruptions. Earth and Planet. Sci. Lett. 393, 120–131.

Hauri, E.H., Cottrell, E., Kelley, K.A., Tucker, J.M., Shimizu, K., Voyer, M.L., Marske, J., Saal, A.E., 2019. Carbon in the Convecting Mantle, in: Orcutt, B.N., Daniel, I., Dasgupta, R. (Eds.), Deep Carbon. Cambridge University Press, 237–275.

Hennecke, E.W., Manuel, O.K., 1975. Noble gases in an Hawaiian xenolith. Nature 257, 778–780.

Hilton, D.R., Grönvold, K., Macpherson, C.G., Castillo, P.R., 1999. Extreme $^{3}He/^{4}He$ ratios in Northwest Iceland: constraining the common component in mantle plumes. Earth Planet. Sci. Lett. 173, 53–60.

Hilton, D.R., Macpherson, C.G., Elliott, T.R., 2000. Helium isotope ratios in mafic phenocrysts and geothermal fluids from La Palma, the Canary Islands (Spain): implications for HIMU mantle sources. Geochim. Cosmochim. Acta 64, 2119–2132.

Hirschmann, M. M., Tenner, T., Aubaud, C., and Withers, A. C. 2009. Dehydration melting of nominally anhydrous mantle: The primacy of partitioning. Phys. Earth and Planet. Inter. 176(1–2):54–68.

Hofmann, A.W., 2003. Sampling mantle heterogeneity through oceanic basalts: isotopes and trace elements. In: Holland, Heinrich D., Turekian, Karl K. (Eds.), Treatise on Geochemistry, 2007. Pergamon, pp. 1–44.

Hofmann, A.W., 2003. Sampling mantle heterogeneity through oceanic basalts: isotopes and trace elements. In: Holland, Heinrich D., Turekian, Karl K. (Eds.), Treatise on Geochemistry, 2007. Pergamon, pp. 1–44.

Hofmann, A.W. 2003 Sampling mantle heterogeneity through oceanic basalts: isotopes and trace elements. Treatise on geochemistry. Volume 2; 61–101.

Hofmann, A. W. and White, W. M. 1982. Mantle plumes from ancient oceanic crust. Earth and Planet. Sci. Lett., 57(2):421–436.

Iacono-Marziano, G., Morizet, Y., Le Trong, E., Gaillard, F., 2012. New experimental data and semi-empirical parameterization of H_2O–CO_2 solubility in mafic melts. Geochim. Cosmochim. Acta 97, 1–23.

Jackson, M.G., Becker, T.W., Konter, J.G., 2018. Evidence for a deep mantle source for EM and HIMU domains from integrated geochemical and geophysical constraints. Earth Planet. Sci. Lett. 484, 154–167.

Jackson, M. G., Konter, J.G., Becker, T.W., 2017a. Primordial helium entrained by the hottest mantle plumes. Nature 542, 340–343.

Jackson, M.G., Kurz, M.D., Hart, S.R., 2009. Helium and neon isotopes in phenocrysts from Samoan lavas: evidence for heterogeneity in the terrestrial high $^{3}He/^{4}He$ mantle. Earth Planet. Sci. Lett. 287, 519–528.

Jégo, S. and Dasgupta, R., 2014. The fate of sulfur during fluid-present melting of subducting basaltic crust at variable oxygen fugacity. J. Petrol., 55(6):1019– 1050.

Jiménez-Mejías, M., Andújar, J., Scaillet, B., Casillas, R., 2021. Experimental determination of H_2O and CO_2 solubilities of mafic alkaline magmas from Canary Islands. Comptes Rendus. Géoscience 353, 289–314.

Jørgensen, J.Ø., Holm, P.M., 2002. Temporal variation and carbonatite contamination in primitive ocean island volcanics from S. Vicente, Cape Verde Islands. Chem. Geol. 192, 249–267.

Kaneoka, I., Takaoka, N., 1978. Excess ^{129}Xe and high $^{3}He/^{4}He$ ratios in olivine phenocrysts of Kapuho lava and xenolithic dunites from Hawaii. Earth Planet. Sci. Lett. 39, 382–386.

Kendrick, M. A., Woodhead, J. D., and Kamenetsky, V. S., 2012. Tracking halogens through the subduction cycle. Geol., 40(12):1075–1078.

Koleszar, A.M., Saal, A.E., Hauri, E.H., Nagle, A.N., Liang, Y., Kurz, M.D., 2009. The volatile contents of the Galapagos plume; evidence for H_2O and F open system behavior in melt inclusions. Earth and Planet. Sci. Lett. 287, 442–452.

Koppers, A.A.P., Becker, T.W., Jackson, M.G., Konrad, K., Müller, R.D., Romanowicz, B., et al. 2021. Mantle plumes and their role in Earth processes. Nat Rev Earth Environ. 2, 382–401.

Klügel, A., Galipp, K., Hoernle, K., Hauff, F., and Groom, S. 2017. Geochemical and Volcanological Evolution of La Palma, Canary Islands. J. Petrol. 58, 1227–1248. doi:10.1093/petrology/egx052

Kurz, M. D., Curtice, J., Fornari, D., Geist, D. J., & Moreira, M. 2009. Primitive neon from the center of the Galápagos hotspot. Earth Planet. Sci. Lett., 286 (1-2), 23–34.

Langmuir, C. H., Klein, E. M., & Plank, T., 1992. Petrological systematics of mid-ocean ridge basalts: Constraints on melt generation beneath ocean ridges. In J. P. Morgan, D. K. Blackman, & J. M. Sinton (Eds.), Mantle flow and melt generation at mid-ocean ridges, Geophysical monograph series (71, 183–280). AGU.

Le Bas, M.J.L., Maitre, R.W.L., Streckeisen, A., Zanettin, B., 1986. IUGS Subcommission on the Systematics of Igneous Rocks. A Chemical Classification of Volcanic Rocks Based on the Total Alkali-Silica Diagram. J. Petrol. 27,3, 745–750.

Longpré, M.-A., Stix, J., Klügel, A., Shimizu, N., 2017. Mantle to surface degassing of carbon- and sulphur-rich alkaline magma at El Hierro, Canary Islands. Earth and Planet. Sci. Lett. 460, 268–280.

Madureira, P., Moreira, M., Mata, J., Allègre, C.J., 2005. Primitive neon isotopes in Terceira Island (Azores archipelago). Earth Planet. Sci. Lett. 233, 429–440.

Mallik, A., Dasgupta, R., 2014. Effect of variable CO_2 on eclogite-derived andesite and lherzolite reaction at 3 GPa -implications for mantle source characteristics of alkalic ocean island basalts. Geochem. Geophys. Geosyst.15, 1533–1557. https://doi .org /10 .1002 /2014GC005251.

Martelli, M., Bianchini, G., Beccaluva, L., Rizzo, A., 2011. Helium and argon isotopic compositions of mantle xenoliths from Tallante and Calatrava, Spain. J. Volcanol. Geotherm. Res. 200, 18–26. https://doi.org/10.1016/j.jvolgeores.2010.11.015

Martelli, M., Rizzo, A.L., Renzulli, A., Ridolfi, F., Arienzo, I., Rosciglione, A., 2014. Noble-gas signature of magmas from a heterogeneous mantle wedge: The case of Stromboli volcano (Aeolian Islands, Italy). Chem. Geol. 368, 39–53.

Mata, J., Martins, S., Mattielli, N., Madeira, J., Faria, B., Ramalho, R.S., et al., 2017. The 2014–15 eruption and the short-term geochemical evolution of the Fogo volcano (Cape Verde): Evidence for small-scale mantle heterogeneity. Lith. 288–289, 91–107.

Métrich, N., Zanon, V., Créon, L., Hildenbrand, A., Moreira, M., Marques, F.O., 2014. Is the 'Azores Hotspot' a Wetspot? Insights from the Geochemistry of Fluid and Melt Inclusions in Olivine of Pico Basalts. J. Petrol. 55, 377–393.

Miller, W.G.R., Maclennan, J., Shorttle, O., Gaetani, G.A., Le Roux, V., Klein, F., 2019. Estimating the carbon content of the deep mantle with Icelandic melt inclusions. Earth Planet. Sci. Lett. 523, 115699.

Morgan, W. J. 1971. Convection plumes in the lower mantle. Nature, 230(5288):42–43.

Moretti, R., Papale, P., Ottonello, G., 2003. A model for the saturation of C-O-H-S fluids in silicate melts. SP 213, 81–101.

Moriera, M., Kanzari, A., Madureira, P., 2012. Helium and neon isotopes in São Miguel Island basalts, Azores Archipelago: new constraints on the "low ^{3}He" hotspot origin. Chem. Geol. 322-323, 91–98.

Moussallam, Y., Oppenheimer, C., Scaillet, B., Gaillard, F., Kyle, P., Peters, N., et al., 2014. Tracking the changing oxidation state of Erebus magmas, from mantle to surface, driven by magma ascent and degassing. Earth and Planet. Sci. Lett. 393, 200–209.

Moussallam, Y., Longpré, M.-A., McCammon, C., Gomez-Ulla, A., Rose-Koga, E.F., Scaillet, B., Peters, N., Gennaro, E., Paris, R., Oppenheimer, C., 2019. Mantle plumes are oxidised. Earth and Planet. Sci. Lett. 527, 115798.

Newman, S., Lowenstern, J.B., 2002. VolatileCalc: a silicate melt–H_2O–CO_2 solution model written in Visual Basic for excel. Computers & Geosciences 28, 597–604.

Pilet, S., 2015. Generation of low-silica alkaline lavas: petrological constraints, mod-els, and thermal implications. Spec. Pap., Geol. Soc. Am.514, 281–304. https://doi .org /10 .1130 /2015 .251417.

Parai, R., Mukhopadhyay, S., Lassiter, J.C., 2009. New constraints on the HIMU mantle from neon and helium isotopic compositions of basalts from the Cook-Austral Islands. Earth Planet. Sci. Lett. 277, 253–261.

Pilet, S., Baker, M.B., Stolper, E.M., 2008. Metasomatized lithosphere and the ori-gin of alkaline lavas. Science80 (320), 916–919. https://doi .org /10 .1126 /science .1156563.

Pineau, F., and Mathez, E.A., 1990. Carbon isotopes in xenoliths from tha Hualalai Volcano, Hawaii, and the generation of isotopic variability. Geochim. Cosmochim. Acta 54, 217-227.

Plank, T., Manning, C.E., 2019. Subducting carbon. Nature 574, 343–352.

Rizzo, A.L., Pelorosso, B., Coltorti, M., Ntaflos, T., Bonadiman, C., Matusiak-Małek, M., Italiano, F., Bergonzoni, G., 2018. Geochemistry of Noble Gases and CO_2 in Fluid Inclusions from Lithospheric Mantle Beneath Wilcza Góra (Lower Silesia, Southwest Poland). Front. Earth Sci. 6, 215.

Ruttor, S., Nebel, O., Nebel-Yacobsen, Y., Cohen, B.E., Eggins, S., 2021. Alkalinity of ocean island lavas decoupled from enriched source components: a case study from EM1-PREMA Tasmantid mantle plume. Geochim. Cosmochim. Acta 314, 140-158.

Sandoval-Velasquez, A., Rizzo, A.L., Aiuppa, A., Remigi, S., Padrón, E., Pérez, N.M., Frezzotti, M.L., 2021a. Recycled crustal carbon in the depleted mantle source of El Hierro volcano, Canary Islands. Lithos 400–401, 106414.

Sandoval-Velasquez, A., Rizzo, A.L., Frezzotti, M.L., Saucedo, R., Aiuppa, A., 2021b. The composition of fluids stored in the central Mexican lithospheric mantle: Inferences from noble gases and CO_2 in mantle xenoliths. Chem. Geol. 576, 120270.

Sano, Y., and Marty, B., 1995. Origin of carbon in fumarolic gas from island arcs. Chem. Geol. 119, 265–274.

Sarda, P., Staudacher, T., Allegre, C., 1988. Neon isotopes in submarine basalts. Earth Planet. Sci. Lett. 91, 73–88. https://doi.org/10.1016/0012-821X(88)90152-5

Sides, I.R., Edmonds, M., Maclennan, J., Swanson, D.A., Houghton, B.F., 2014. Eruption style at Kīlauea Volcano in Hawai'i linked to primary melt composition. Nature Geosciences 7, 464–469.

Shishkina, T.A., Botcharnikov, R.E., Holtz, F., Almeev, R.R., Jazwa, A.M., Jakubiak, A.A., 2014. Compositional and pressure effects on the solubility of H_2O and CO_2 in mafic melts. Chemical Geology 388, 112-129.

Staudacher, T., Sarda, P., Allègre, C.J., 1990. Noble gas systematics of Réunion island, Indian Ocean. Chem. Geol. 89, 1–17.

Stracke, A., Willig, M., Genske, F., Béguelin, P., & Todd, E., 2022a. Chemical geodynamics insights from a machine learning approach. Geochem. Geophys. Geosystems, 23 (10), e2022GC010606.

Sun, C. and Dasgupta, R., 2023. Carbon budget of Earth's deep mantle constrained by petrogenesis of silica-poor ocean island basalts. Earth and Planet. Sci. Lett. 611, 118135.

Takamasa, A., Nakai, S., Sahoo, Y., Hanyu, T., and Tatsumi, Y. 2009. W isotope compositions of oceanic islands basalts from French Polynesia and their meaning for core–mantle interaction. Chem. Geol. 260(1):37–46.

Taracsák, Z., Hartley, M.E., Burgess, R., Edmonds, M., Iddon, F., Longpré, M.-A., 2019. High fluxes of deep volatiles from ocean island volcanoes: Insights from El Hierro, Canary Islands. Geochim Cosmochim. Acta 258, 19–36.

Tucker, J.M., Hauri, E.H., Pietruszka, A.J., Garcia, M.O., Marske, J.P., Trusdell, F.A., 2019. A high carbon content of the Hawaiian mantle from olivine-hosted melt inclusions. Geochim Cosmochim. Acta 254, 156–172.

Valbracht, P.J., Staudacher, T., Malahoff, A., Allegre, C.J., 1997. Noble gas systematics of deep rift zone glasses from Loihi Seamount, Hawaii. Earth Planet. Sci. Lett. 150, 399–411.

Walters, J., Cruz-Uribe, A., and Marschall, H., 2020. Sulfur loss from subducted altered oceanic crust and implications for mantle oxidation. Geochem. Persp. Let., 13:36–41.

Weaver, B.L., 1991. The origin of ocean island basalt end-member compositions: trace element and isotopic constraints. Earth and Planet. Sci. Lett. 104, 381–397.

Williams, C.D., Mukhopadhyay, S., Rudolph, M.L., Romanowicz, B., 2019. Primitive helium is sourced from seismically slow regions in the lowermost mantle. Geochem. Geophys. Geosyst. 20, 4130–4145.

Zanon, V., 2015a. Conditions for mafic magma storage beneath fissure zones at oceanic islands. The case of São Miguel Island (Azores archipelago). In: Caricchi, L., Blundy, J.D. (Eds.), Chemical, Physical and Temporal Evolution of Magmatic Systems. The Geological Society of London, Special Publications, pp. 85–104, 422. https://doi.org/10.1144/SP422.4.

Zanon, V., and Frezzotti, M.L., 2013. Magma storage and ascent conditions beneath Pico and Faial islands (Azores archipelago): a study on fluid inclusions. Geochem. Geophys. Geosyst. 14, 3494–3514. https://doi.org/10.1002/ggge.20221

Zanon,V., Pimentel, A. 2015. Spatio-temporal variations of magma storage and ascent conditions in an extensional tectonic setting. The case of the Terceira Island, Azores (Portugal). Am Mineral 100:795–805

Zanon, V., Viveiros, M. 2019. A multi-methodological re-evaluation of the volcanic events during the 1580 CE and 1808 eruptions at São Jorge Island (Azores Archipelago, Portugal). J Volcanol Geotherm Res 373:51–67

Zanon, V., Pimentel, A., Auxerre, M., Marchini, G., Stuart, F.M., 2020. Unravelling the magma feeding system of a young basaltic oceanic volcano. Lithos 352–353, 105325.

Zanon, V., Silva, R., Goulart, C., 2023. The crust-mantle transition beneath the Azores region (central-north Atlantic Ocean). Contrib. Mineral. Petrol, 178, 8, 50.

Zindler, A., Hart, S., 1986. Chemical Geodynamics. Annu. Rev. Earth Planet. Sci. 14, 493–571.

CHAPTER 3.

MATERIALS AND METHODS

3.1. Sampling sites

The selection of samples for the thesis analysis is motivated by the necessity (i) to characterise the products which were not considered in the previous literature and (ii) to further investigate eruptions that have already been examined in previous literature works (e.g., 1951, Hildner et al., 2012; 1995, Hildner et al., 1995; 2014/15, Mata et al., 2017, Klügel et al., 2020). A significant portion of the samples was already available in the Instituto de Investigação em Vulcanologia e Avaliação de Riscos (IVAR), Ponta Delgada, Azores, Portugal and in the Laboratoire Magmas et Volcans (LMV), in Clermont-Ferrand, France. Whereas some of them were collected during the field trip on Fogo Island from November 12th to 19th, 2021. Six pyroclastic and five lava rocks were sampled specifically for melt inclusion, fluid inclusion microthermometry, and noble gases analyses. The field work involved the collection of intra- and extra-caldera samples representing of the last 120 ka of activity of Fogo volcano. More specifically, the intra-caldera samples span from 10 ka to the last eruption (2014/15), while the extra-caldera samples span from 120 ka to 10 ka of activity. The samples, of these samples, was made to enable a comparison between the older (pre-Mt. Amarelo collapse;~123/73 ka) and the actual magma plumbing system (post-Mt. Amarelo collapse). Additionally, a portion of the samples analysed for noble gases and carbon isotopes was supplied by Professor Andrea Luca Rizzo and Dr. Giullaume Boudoire. These samples, namely mafic enclaves (FG1-A, FG2-A1, FG2-A3, FG3-A, FG4-A, FG4-B, FG4-D, and FG4-E), were embedded within lava flows, and their crystals were embedded in lava flows and crystals were extracted by scraping. Further details regarding the sample locations are provided in Table 2.

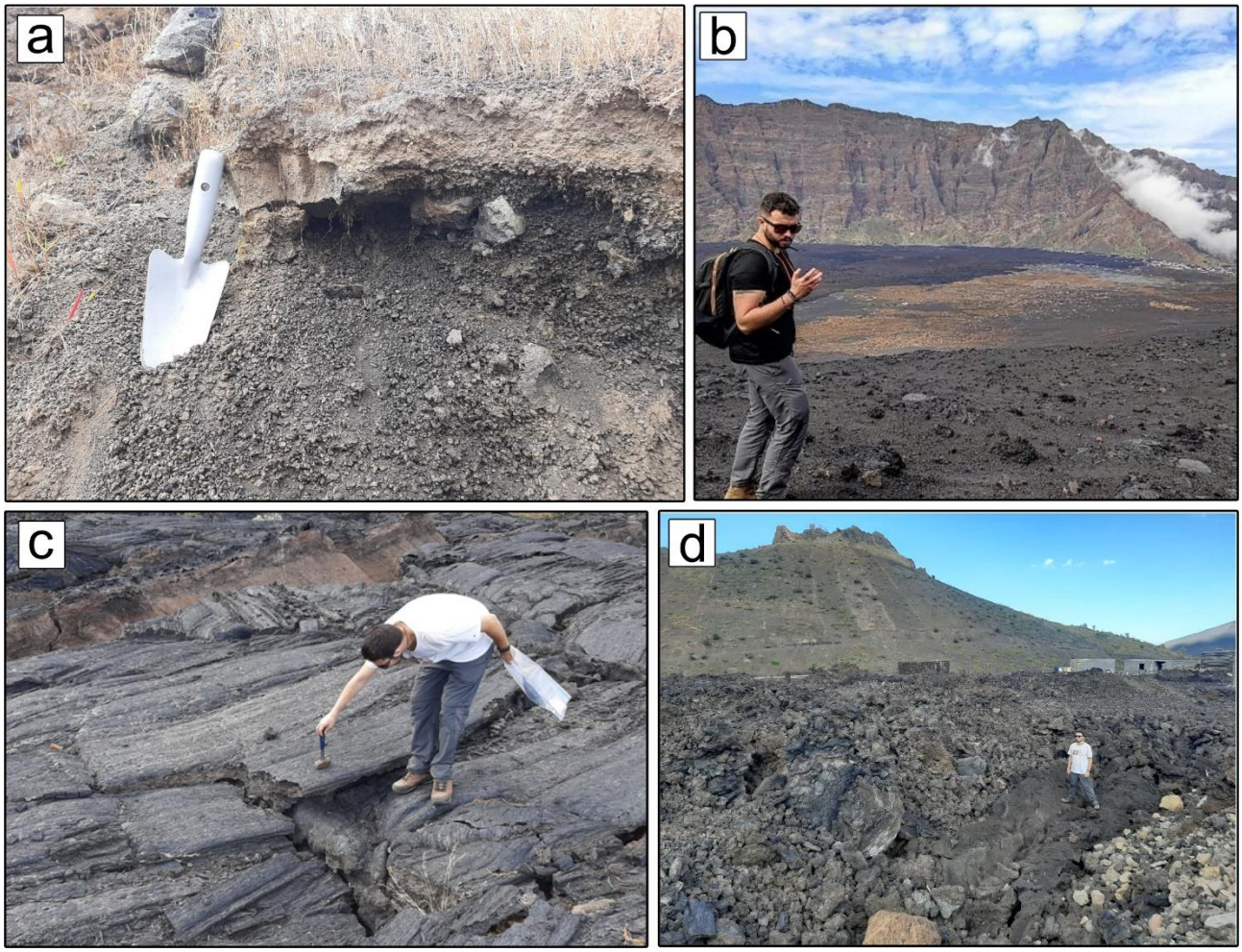

Figure 6 Pyroclastic samples from Sao Jõrge (Fog 43, er.~10 ka) (a); sampling on Pico do Fogo volcano (b); lava samples of the 1995 eruption (Fog 10) (c); lava flow of the 2014-15 eruption (Fog 6) (d).

TABLE 2. Samples location, elevation, and typology of rock materials

Sample	Rock type	Eruption	Latitude (N)	Longitude (W)	Elevation (m a.s.l.)	Materials
Fog 1	Basanite	1852	14° 58’ 24.8”	-24° 20’ 39.5”	1656	Lava
Fog 2	Basanite	1721-25	14° 58’ 23.5”	-24° 20’ 35.7”	1713	Lava
Fog 4	Basanite	1400s-1800s	14° 58’ 21.1”	-24° 20’ 48.5”	1723	Lava
Fog 5	/	1951	14° 57’ 59.5”	-24° 21’ 21.8”	1776	Tephra
Fog 6	Basanite	2014-15	14° 58’ 1.3”	-24° 21’ 58.8”	1728	Lava
Fog 8	Basanite	1951	14° 55’ 51.8”	-24° 20’ 49.8”	1840	Tephra
Fog 9	Basanite	~10 ka	14° 55’ 35.1”	-24° 21’ 5.5”	1799	Tephra
Fog 10	Basanite	1995	14° 56’ 48.0”	-24° 23’ 10.8”	1748	Lava
Fog 11	/	2014-15	14° 56’ 35.1”	-24° 21’ 6.1”	2018	Tephra
Fog 13	Basanite	1769	14° 55’ 44.8”	-24° 20’ 25.7”	1858	Tephra
Fog 16	Foidite	~10 ka	14° 52’ 2.2”	-24° 20’ 36.4”	771	Lava
Fog 17	Basanite	1857	14° 55’ 12.9”	-24° 17’ 40.6”	332	Lava
Fog 18	Foidite	1769	14° 55’ 20.1”	-24° 17’ 43.2”	343	Lava
Fog 19	Basanite	1799	14° 57’ 43.7”	-24° 17’ 39.1”	162	Lava
Fog 20	Basanite	1799	14° 57’ 41.5”	24° 17’ 39.6”	164	Lava
Fog 21	Basanite	1847	14° 57’ 58.2”	24° 17’ 36.5”	154	Lava
Fog 22	Foidite	1816	14° 59’ 24.5”	24° 17’ 38.9”	81	Lava
Fog 23	Basanite	1664	15° 0’ 24.9”	24° 18’ 19.2”	148	Lava
Fog 24	Basanite	1852	15° 0’ 40.1”	24° 18’ 22.8”	109	Lava
Fog 25	Basanite	1785	15° 1’ 51.5”	24° 18’ 55.5”	31	Lava
Fog 26	Ankaramite	~120 ka	14° 53’ 23.4”	24° 29’ 5.6”	173	Lava
Fog 27	Basanite	~60 ka	14° 52’ 13.0”	24° 22’ 7.5”	874	Lava
Fog 28	/	~10 ka	14° 58’ 11.8”	24° 20’ 59.5”	1750	Lava
Fog 29	Basanite	~10 ka	14° 52’ 1.7”	24° 19’ 26.3”	656	Tephra
Fog 31	/	1951	14° 55’ 1.2”	24° 17’ 45.7”	370	Lava
Fog 33	Basanite	1400s-1800s	14° 57’ 3.7”	24° 20’ 30.9”	2758	Lava
Fog 43	/	~10 ka	15° 0’ 53.6”	24° 24’ 34.7”	1000	Tephra
FG1-A	/	~10 ka	14° 58’ 50.9”	24° 22’ 11.4”	1665	Mafic Enclaves
FG2-A1	/	1951	14° 58’ 50.0”	24° 21’ 20.3”	1651	Mafic Enclaves
FG2-A3	/	1951	14° 58’ 50.0”	24° 21’ 20.3”	1651	Mafic Enclaves

FG3-A	/	1400s-1800s	14° 57’ 6.10”	24° 20’ 33.45”	2707	Mafic Enclaves
FG4-A	/	~10 ka	14° 58’ 14.1”	24° 22’ 05.4”	1702	Mafic Enclaves
FG4-B	/	~10 ka	14° 58’ 14.1”	24° 22’ 05.4”	1702	Mafic Enclaves
FG4-D	/	~10 ka	14° 58’ 14.1”	24° 22’ 05.4”	1702	Mafic Enclaves
FG4-E	/	~10 ka	14° 58’ 14.1”	24° 22’ 05.4”	1702	Mafic Enclaves

3.2. Analytical methods

3.2.1 Thin section modal analysis

Petrographic study and modal analysis were conducted on 21 thin sections, representative for 16 eruptions with a semi-automated digital point counter at the IVAR.

3.2.2. Fluid inclusions

3.2.2.1. Electron Microprobe Analyses (EMPA)

Electron microprobe analyses were conducted on olivine and clinopyroxene crystals as well as the groundmass, at the CAMPARIS center (University of Paris La Sorbonne, France). The analyses were carried out using a CAMECA SX-Five electron microprobe, which is equipped with five WDS spectrometers and an EDS detector. Seventeen olivine crystals, fourteen pyroxene crystals, and sixteen fragments of the groundmass were analysed. The measurements were performed at a 15-kV accelerating voltage and a 20 nA current beam, with counting times ranging from 10 to 20 seconds on the peak. The accuracy of the results was verified against the San Carlos Olivine international standard. The relative errors: <6.5% for Ni and Mn, <5% for Fe and Ca, and <1% for Si and Mg.

3.2.2.2. Microthermometry

Microthermometry data were measured on ~ 2700 FI (founded in 15 different samples from 11 eruptions; Table 3) using a Linkam MDSG600 heating-cooling stage, at the Instituto de Investigação em Vulcanologia e Avaliação de Riscos (IVAR), Ponta Delgada, Portugal. The calibration of the stage involved the use of a crystal of quartz with synthetic fluid inclusions containing pure CO_2 and

H_2O. A heating rate ranging from 0.2 to 0.5 °C/min was applied, achieving an accuracy of ±0.1 °C during both melting and homogenization phases. The determination of density values for pure-CO_2 fluid inclusions was carried out through the derivation of homogenization temperatures (Th), employing equations 3.14 and 3.15 as outlined in Span and Wagner (1996). To calculate the densities of fluid inclusions, the Sterner and Bodnar (1991) equation was utilized, incorporating the correction proposed by Hansteen and Klügel (2008). This correction accounts for the original presence of a maximum 10% molar volume of H_2O in the fluid inclusions during their formation, reflecting CO_2: H_2O ratios of 9:1. This correction is necessary to consider the potential presence of H_2O in the fluid at the time of trapping, with subsequent water loss upon cooling through diffusion (Barth et al., 2019; Frezzotti et al., 2012). Isochores, based on fluid density, composition, and hosted mineral composition, were employed to derive fluid trapping pressure at assumed or calculated temperatures. The FLUIDS software (Bakker, 2003) was utilized for isochore calculations.

Figure 7 Microthermometric analysis of fluid inclusions conducted at the laboratory of the Instituto de Investigação em Vulcanologia e Avaliação de Riscos (IVAR), Ponta Delgada, Portugal. In the picture, the Linkam MDSG600 heating-cooling stage.

3.2.3 Melt inclusions

3.2.3.1. Electron Microprobe Analyses (EMPA)

Electron microprobe analyses were conducted utilizing a Cameca SxFiveTactis instrument equipped with a LaB6 source and five wavelength-dispersive spectrometers (WDS) at the Laboratoire Magmas et Volcans (LMV) in Clermont-Ferrand, France. Major elements and volatiles were examined during the same analytical session, employing an accelerating voltage of 15 kV, an 8 nA beam current, and a 20 µm defocused beam for major elements. Chlorine, sulfur, and fluorine analyses were executed with an accelerating voltage of 15 kV, a 40 nA beam current, and a 20 µm defocused beam, following the acquisition program outlined in the Cameca Peak Sight software. The olivine were analysed with an accelerating voltage of 15 kV and 15 nA beam current. The total concentration of volatiles was determined by summing the counts from multiple iterations. Total counting times were 100 s for F and Cl peaks. The detection limits for Cl and F were 150 and 300 ppm, respectively. Calibration of various elements utilized a substantial set of standards. In details, for MI analyses, three different glasses were employed: KE12 LMV, ALV-98I R23, and CFA47. For olivine analyses, five olivine samples from San Carlos were used. Typical errors on the samples (1σ error of the mean) are less than 10% for all elements analysed in both MI and olivine samples.

3.2.3.2. Nano-SIMS Analyses

High spatial resolution measurements of volatiles in minor and trace amounts in MI were conducted using the CAMECA NanoSIMS50 of the Muséum National d'Histoire Naturelle de Paris. All measurements were carried using a focussed Cs+ primary ion beam accelerated to 16 keV in high vacuum conditions (< $8x10^{-10}$ mbar). Prior to acquisition, a 5 x 5 µm² region was pre-sputtered with a 280 pA primary beam for 2 minutes to remove the Au coat and ensure the signal stability. The current was then reduced to 20 pA and the inner 3 x 3 µm² were rastered over a 32 x 32 pixels matrix with a 1 ms/px dwell time during 100 cycles (~2 min). A numerical blanking was applied to 32 x 32 px matrix to consider only the innermost 1 x 1 µm² region, this in order to limit the contribution of potential contamination. A cloud of electron was generated above the sample' surface to avoid the accumulation of positive charges induced by the implantation of the Cs+ beam. ^{12}C, $^{16}O^{1}H$, ^{28}Si, ^{32}S, and ^{35}Cl were acquired simultaneously in multicollection mode on 5 electron multipliers (EMs). Each

measurement was corrected for the 44 ns of the EMs deadtime. We used a 20 x 140 µm entrance slit (#3) with a 200 µm diameter aperture slit (#2) and a 10% energy slit to optimize our mass-resolving power without compromising our transmission. This setting enabled a MRP > 8000 which ensured the distinction between 16O1H and its isobaric interference 17O. An extensive set of standards were used for the calibration of the different elements: Two glass NIST 610 and 612; A Suprasil crystal; two basaltic glass MRN-G1 and IND-G2 (Shimizu et al., 2017) and three internal standards STR 10-11-13. All of this enable to achieve statistically robust linear regression spanning a range of concentrations from the wt% to the hundreds of ppm (Figure S1 in the Supplementary Material S2). Errors were estimated as the quadratic sum of the measured 1σ Poisson ratio error and the 1σ prediction/confidence interval local estimation and were subsequently reported as 2σ errors.

3.2.3.3. Raman Spectroscopy

Raman spectra were obtained using an inVia confocal Raman micro-spectrometer produced by Renishaw. The system was equipped with a diode-pulsed solid-state laser with a wavelength of 532.1 ± 0.3 nm and an output power of 200 mW. A Peltier-cooled CCD detector with a resolution of 1040 × 256 pixels was employed, along with a Leica DM 2500 M optical microscope featuring a motorized XYZ stage. The measurements were conducted at the Laboratoire Magmas et Volcans (LMV) using a back-scattered geometry for collecting scattered light. The laser power applied to the sample surface was approximately 10 mW. A 100x microscope objective, a grating with 2400 grooves mm^{-1}, and a 20-µm slit aperture (high confocality setting) were utilized, resulting in a spectral resolution better than 0.4 cm^{-1}. The vertical and horizontal spatial resolutions near the sample surface were approximately 2-3 µm and 1 µm, respectively. Peak position calibration was performed based on the 520.5 cm-1 peak of silicon and the 1331.5 cm^{-1} peak of a diamond standard. Two Neon emission bands with wavelengths of 568.98163 and 576.44188 nm were employed to assess the linearity of the spectrometer. For CO_2 measurements in melt inclusion bubbles, spectra were recorded in the 725-1880 cm^{-1} range using WiRETM 4.4 software. Subsequently, spectra were acquired in the 60-1320 cm^{-1} wavenumber range to identify the presence of mineral phases (e.g., carbonates, sulfates) or fluid SO_2. Finally, spectra were collected in the 2800-3900 cm^{-1} region to detect H_2O and/or OH^- molecules. The acquisition time for a single CO_2 analysis was fixed at 60 s. Spectra underwent initial treatment for the removal of cosmic rays, followed by the application of an appropriate polynomial baseline correction. A combined Gaussian-Lorentzian curve was fitted to the CO_2 Fermi dyad (e.g.

Esposito et al., 2011; Hartley et al., 2014, Moore et al., 2015). The analytical uncertainty associated with CO_2 density measurements is < 0.05 g/cm^3 (Boudoire et al., 2023).

3.2.3.4. Laser Ablation-ICPMS (LA-ICPMS)

Trace-element (Li, Al, Ca, Sc, V, Co, Ni, Rb, Sr, Zr, Nb, Ba, La, Ce, Nd, Sm, Hf, Ta, Pb, Th, U) analyses on melt inclusions (MI) were conducted employing a laser ablation system (193 nm Excimer Resonetics M-50E) coupled with an inductively coupled plasma mass spectrometer (Agilent 7500 cs LA–ICP–MS) at the Laboratoire Magmas et Volcans, Clermont-Ferrand. The analytical procedure followed established methods outlined in previous studies (e.g., Le Voyer et al. 2010; Rose-Koga et al. 2012). The laser system operated with a pulse energy of approximately 3 mJ, a spot diameter ranging from 15 to 33 µm, and a laser pulse frequency of 2–3 Hz. These parameters varied based on the inclusion size to maintain a fluence at the sample surface of approximately 4 J/cm^{-2}. A background measurement was conducted for 30–40 s before ablation, and the analysis time was approximately 100 s. Data reduction was accomplished using the GLITTER software, employing CaO (measured by EMP) as an internal standard. To ensure the reproducibility and accuracy of the analysis, systematic analyses of two standards, BCR2-G and SRM NIST 612, were performed at the beginning, middle, and end of the session. The typical errors on the samples (1σ error of mean) are less than 10% for all trace elements analysed.

3.2.3. Noble gases and Carbon isotopes analyses

Noble gases (He, Ne, and Ar) as well as CO_2 concentrations and isotopic compositions in both (i) fluid inclusions (cf. 3.2.4.1 for further details) and fumaroles (cf. 3.2.4.2 for further details) were analysed at the INGV, Section of Palermo isotopic laboratories, Italy.

3.2.3.1. Isotope compositions of He, Ne, Ar, and CO_2 in fluid inclusions

The crystals were separeted into two aliquots: the first one was used for noble gas isotopes measurement, while the second one to determine the concentration and isotope composition of CO_2. Either noble gases or CO_2 underwent extraction through a single-step crushing under vacuum at

approximately 200 bars. The procedures applied for FI purification before mass spectrometric measurements of noble gases and carbon are consistent with those detailed in Rizzo et al. (2018, 2021) and Sandoval-Velasquez et al. (2021a, 2021b, 2023). Helium isotopes (^{3}He and ^{4}He) and ^{20}Ne were individually assessed using two distinct split-flight-tube mass spectrometers (Helix SFT, Thermo Scientific). $^{3}He/^{4}He$ ratios are presented in units of R/Ra, where Ra signifies the $^{3}He/^{4}He$ ratio of air, equivalent to 1.39 × 10-6. The analytical uncertainty of the He-isotope ratio (1σ) typically remained below 1.6%. The ^{20}Ne values were corrected for isobaric interferences at m/z values of 20 ($^{40}Ar^{2+}$). The ^{36}Ar, ^{38}Ar, and ^{40}Ar were analyzed through a multi-collector mass spectrometer (Argus, GVI) with an analytical uncertainty (1σ) of less than 0.5%. Additional details regarding analytical procedures, adopted standards, and their precision over time are available in Rizzo et al. (2018, 2021) and in Sandoval-Velasquez et al. (2021a, 2021b, 2023). The ^{40}Ar was corrected for air contamination ($^{40}Ar^{*}$) using the following formula:

$$^{40}Ar^{*} = {}^{40}Ar_{sample} - [{}^{36}Ar_{sample} \cdot ({}^{40}Ar/{}^{36}Ar)_{air}]$$

The $^{3}He/^{4}He$ ratio was corrected for contamination (Rc/Ra) by utilizing the measured $^{4}He/^{20}Ne$ ratio, as follows:

$$Rc/Ra = ((R_M/Ra)(He/Ne)_M - (He/Ne)_A)/((He/Ne)_M - (He/Ne)_A)$$

Here, Rc denotes the air-corrected $^{3}He/^{4}He$ ratios, and subscripts M and A denote measured and atmospheric theoretical values, respectively. Following the noble gas analysis, seven aliquots with the highest CO_2 concentrations (2 olivines, Fog33 and FG3A, and 1 clinopyroxene FG1A) were chosen to determine the carbon isotopic composition of FI ($^{13}C/^{12}C$), reported as δ13C in parts per mil (‰) relative to the Vienna Pee Dee Belemnite international standard (V-PDB). The CO2 extraction and purification protocol mirrors that reported in Correale et al. (2015), Gennaro et al. (2017), and Rizzo et al. (2018). The analytical error, estimated as 2σ, consistently remained below 0.3‰. Noble gas and carbon isotope results are documented in Table S1 of Supplementary Material

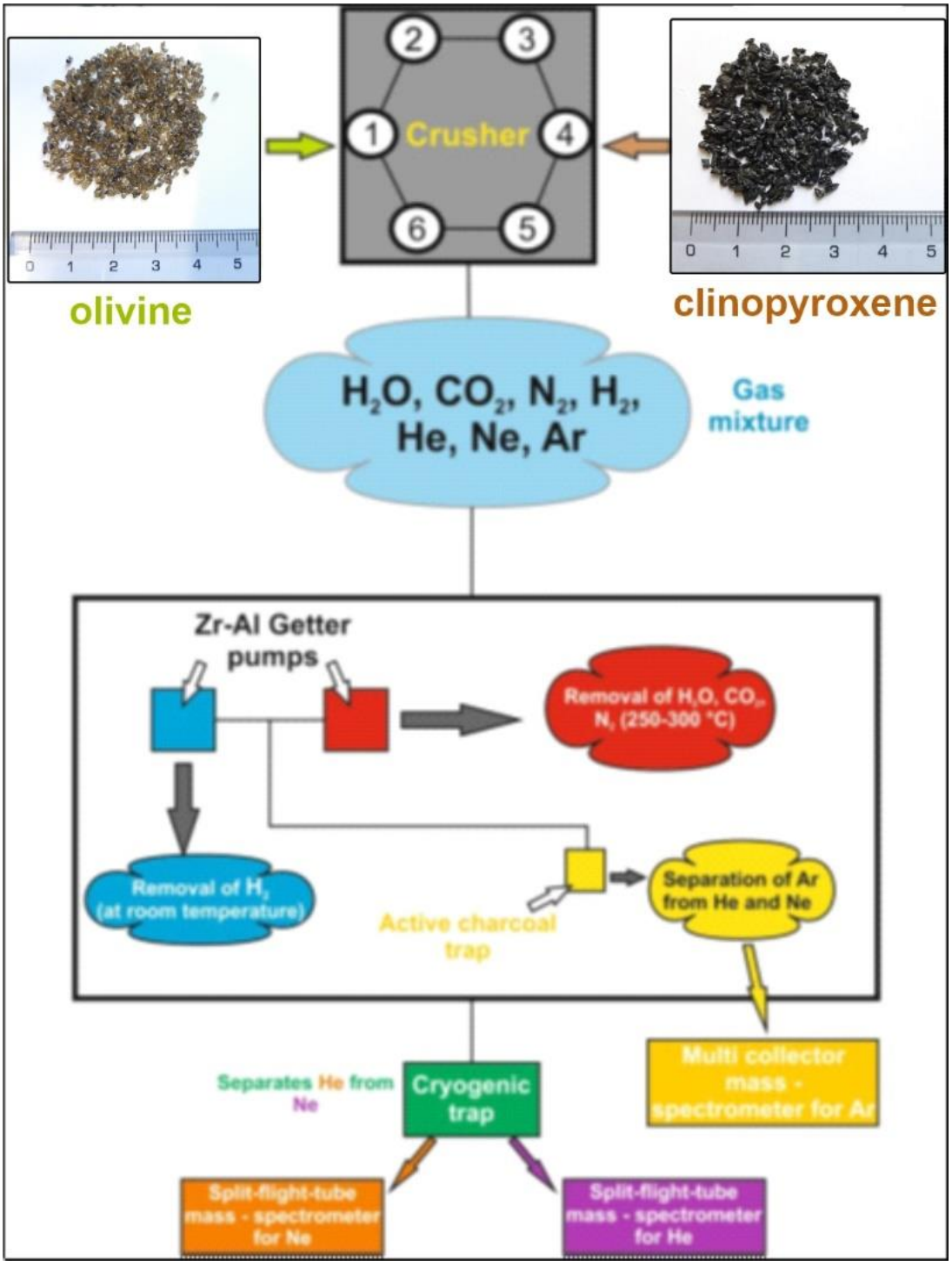

Figure 8 Schematic diagram that represents the crushing system and the purification line used for the analysis of noble gases. Modified from Sandoval Velasquez (2022).

3.2.3.2. Isotope compositions of He, Ne, Ar, and CO_2 in fumaroles

Fumarole gas samples were collected as "dry gas" in glass and stainless-steel containers with two stopcocks, employing the methodology detailed in, for example, Rizzo et al. (2015). Concentrations of major gases were assessed using a gas chromatograph (Clarus 500, Perkin Elmer) featuring a 30-meter column (inner diameter = 0.32 mm; Poraplot-Q). The chromatograph operated at a constant temperature of 50°C with helium serving as the carrier gas. The analyses were conducted at the laboratory of INGV, Sezione di Palermo, Italy. Measurements of ^{3}He, ^{4}He, and ^{20}Ne, along with the $^{4}He/^{20}Ne$ ratios, were conducted by separately introducing helium and neon into a split-flight tube mass spectrometer (GVI-Helix SFT, for He analysis) and a multi-collector mass spectrometer (Thermo-Helix MC plus, for Ne analysis) following standard purification protocols.The carbon isotope composition of CO_2, expressed as $\delta^{13}C$ vs. V-PDB (Vienna Pee Dee Belemnite), was determined using a continuous-flow isotope-ratio mass spectrometer (Thermo Delta Plus XP, Finnigan) connected to a gas chromatograph (Trace GC) and interface (Thermo GC/C III, Finnigan). The standard deviation for $\delta^{13}C$ was below 0.2‰. Further details on the analytical procedure and adopted standards are the same reported in Rizzo et al. (2015, 2016, 2019). The chemical and isotopic compositions of dry gases are reported in Table S1 of Supplementary Material.

3.2.3.3. Electron Microprobe Analyses (EMPA)

Electron microprobe analyses on mineral phases were performed by using a CAMECA SX5 (LMV, Clermont-Ferrand, France) set with 15 kV potential, 20 nA focused beam coupled with a counting time varying from 10 to 50s depending on the element. Analytical error (as 3σ) was lower than 2% of the measurement for Si-Mg-Ca (12% for Ca in clinopyroxene), lower than 4% for Fe-Al; lower than 13 % for Ti-Na in clinopyroxene and lower than 40 % and 70 % for Cr in clinopyroxene and Ni in olivine, respectively.

3.2.3.4. Raman Spectroscopy

Fluid inclusions in clinopyroxene and olivine crystals were analysed by Raman at the Laboratoire Magmas et Volcans (LMV, Clermont-Ferrand, France) using an InVia confocal Raman micro-spectrometer manufactured by Renishaw and equipped with a 532 nm diode laser, a Peltier-cooled CDD detector of 1040x256 pixels, a motorized XY stage, and a Leica DM 2500 M optical

microscope. Laser power was reduced to 10% of the nominal output power (200 mW) using filters. A 2400 grooves/mm was used for the analysis resulting in a spectral resolution better than 1 cm^{-1}. Calibration of the spectrometer was performed on a Si 520.5 cm^{-1} standard.

REFERENCES

Bakker, R.J., 2003. Package FLUIDS 1. Computer programs for analysis of fluid inclusion data and for modelling bulk fluid properties. Chem. Geol. 194, 3–23.

Barth, A., Newcombe, M., Plank, T., Gonnermann, H., Hajimirza, S., Soto, G.J., Saballos, A., Hauri, E., 2019. Magma decompression rate correlates with explosivity at basaltic volcanoes — Constraints from water diffusion in olivine. J. Volcanol. Geotherm. Res. 387, 106664.

Boudoire G., Pasdeloup G., Schiavi F**.**, Cluzel N., Rafflin V., Grassa F., et al., 2023. Magma storage and degassing beneath the youngest volcanoes of the Massif Central (France): lessons for the monitoring of a dormant volcanic province. Chem Geol., 634, 121603.

Correale, A., Paonita, A., Rizzo, A., Grassa, F., Martelli, M., 2015. The carbon-isotope signature of ultramafic xenoliths from the Hyblean Plateau (southeast Sicily, Italy): Evidence of mantle heterogeneity. Geochem. Geophys. Geosystems 16, 600–611.

Esposito, R., Bodnar, R.J., Danyushevsky, L., De Vivo, B., Fedele, L., Hunter, J., Lima, A., and Shimizu, N. 2011. Volatile evolution of magma associated with the Solchiaro Eruption in the Phlegrean Volcanic District (Italy). Journal of Petrology. 52, 2431–2460.

Frezzotti, M.L., Tecce, F., Casagli, A., 2012. Raman spectroscopy for fluid inclusion analysis. J. Geochem. Explor. 112, 1–20.

Gennaro, M.E., Grassa, F., Martelli, M., Renzulli, A., Rizzo, A.L., 2017. Carbon isotope composition of CO_2 -rich inclusions in cumulate-forming mantle minerals from Stromboli volcano (Italy). J. Volcanol. Geotherm. Res. 346, 95–103. https://doi.org/10.1016/j.jvolgeores.2017.04.001

Hansteen, T.H., Klugel, A., 2008. Fluid inclusion thermobarometry as a tracer for magmatic processes. Rev. Mineral. Geochem. 69, 143–177. https://doi.org/ 10.2138/rmg.2008.69.5.

Hartley, M.E., Maclennan, J., Edmonds, M., Thordarson, T., 2014. Reconstructing the deep CO_2 degassing behaviour of large basaltic fissure eruptions. Earth and Planet. Sci. Lett. 393, 120–131.

Hildner, E., Klügel, A., Hauff, F., 2011. Magma storage and ascent during the 1995 eruption of Fogo, Cape Verde Archipelago. Contrib. Mineral. Petrol. 162, 751–772.

Hildner, E., Klügel, A., Hansteen, T.H., 2012. Barometry of lavas from the 1951 eruption of Fogo, Cape Verde Islands: Implications for historic and prehistoric magma plumbing systems. J. Volcanol. Geotherm. Res. 217–218, 73–90. https://doi.org/ 10.1016/j.jvolgeores.2011.12.014.

Klügel, A., Day, S., Schmid, M., Faria, B., 2020. Magma plumbing during the 2014–2015 eruption of Fogo (Cape Verde Islands). Front. Earth Sci. 8, 157. https://doi.org/ 10.3389/feart.2020.00157.

Le Voyer, M., Rose-Koga, E. F., Shimizu, N., Grove, T. L., Schiano, P. 2010. Two Contrasting H_2O-rich Components in Primary Melt Inclusions from Mount Shasta, J. Petrol. 51, 7, 1571–1595. https://doi.org/10.1093/petrology/egq030

Mata, J., Martins, S., Mattielli, N., Madeira, J., Faria, B., Ramalho, R.S., Silva, P., Moreira, M., Caldeira, R., Moreira, M., Rodrigues, J., Martins, L., 2017. The 2014–15 eruption and the short-term geochemical evolution of the Fogo volcano (Cape Verde): evidence for small-scale mantle heterogeneity. Lith. 288–289, 91–107.

Moore, L.R., Gazel, E., Tuohy, R., Lloyd, A.S., Esposito, R., Steele-MacInnis, M., et al., 2015. Bubbles matter: An assessment of the contribution of vapor bubbles to melt inclusion volatile budgets. Am. Mineral. 100, 806–823.

Rizzo, A.L., Barberi, F., Carapezza, M.L., Di Piazza, A., Francalanci, L., Sortino, F., D'Alessandro, W., 2015. New mafic magma refilling a quiescent volcano: Evidence from He-Ne-Ar isotopes during the 2011-2012 unrest at Santorini, Greece. Geochem. Geophys. Geosyst. 16, 798–814.

Rizzo, A. L., Caracausi, A., Chavagnac, V., Nomikou, P., Polymenakou, P. N., Mandalakis, M., et al., 2016. Kolumbo submarine volcano (Greece): an active window into the Aegean subduction system. Sci. Rep. 6:28013. doi: 10.1038/srep28013

Rizzo, A. L., Caracausi, A., Chavagnac, V., Nomikou, P., Polymenakou, P. N., Mandalakis, M., et al., 2019. Geochemistry of CO_2-Rich Gases Venting from Submarine Volcanism: The Case of Kolumbo (Hellenic Volcanic Arc, Greece). Front. Earth Sci. 7:60. doi: 10.3389/feart.2019.00060

Rizzo, A.L., Faccini, B., Casetta, F., Faccincani, L., Ntaflos, T., Italiano, F., et al., 2021. Melting and metasomatism in West Eifel and Siebengebirge Sub-Continental Lithospheric Mantle: Evidence from concentrations of volatiles in fluid inclusions and petrology of ultramafic xenoliths. Chem. Geol. 581, 120400. https://doi.org/10.1016/j.chemgeo.2021.120400

Rizzo, A.L., Pelorosso, B., Coltorti, M., Ntaflos, T., Bonadiman, C., Matusiak-Małek, M., Italiano, F., Bergonzoni, G., 2018. Geochemistry of Noble Gases and CO_2 in Fluid Inclusions from Lithospheric Mantle Beneath Wilcza Góra (Lower Silesia, Southwest Poland). Front. Earth Sci. 6, 215.

Rose-Koga, E.F., Koga, K., Schiano, P., Le Voyer, M., 2012. Mantle source heterogeneity for South Tyrrhenian magmas revealed by Pb isotopes and halogen contents of olivine-hosted melt inclusions. Chem. Geol. 334, 266–279.

Sandoval-Velasquez, A., 2022. Noble gas and CO_2 isotopic signatures of the lithospheric mantle underneath Mexico and the Canary Islands: clues from mantle xenoliths and arc lavas. PhD Thesis, Università degli Studi di Palermo.

Sandoval-Velasquez, A., Rizzo, A.L., Aiuppa, A., Remigi, S., Padrón, E., Pérez, N.M., Frezzotti, M.L., 2021a. Recycled crustal carbon in the depleted mantle source of El Hierro volcano, Canary Islands. Lithos 400–401, 106414.

Sandoval-Velasquez, A., Rizzo, A.L., Casetta, F., Ntaflos, T., Aiuppa, A., Alonso, M., et al., 2023. The noble gas signature of the 2021 Tajogaite eruption (La Palma, Canary Islands). J. Volcanol. Geotherm. Res. 443, 107928.

Sandoval-Velasquez, A., Rizzo, A.L., Frezzotti, M.L., Saucedo, R., Aiuppa, A., 2021b. The composition of fluids stored in the central Mexican lithospheric mantle: Inferences from noble gases and CO_2 in mantle xenoliths. Chem. Geol. 576, 120270.

Shimizu, K., Ushikubo, T., Hamada, M., Itoh, S., Higashi, Y., Takahashi, E., et al., 2017. H_2O, CO_2, F, S, Cl, and P_2O_5 analyses of silicate glasses using SIMS: Report of volatile standard glasses. Geochem. J., 51(4), 299-313.

Span, R., Wagner, W., 1996. A new equation of state for carbon dioxide covering the fluid region from the triple-point temperature to 1100 K at pressures up to 800 MPa. J. Phys. Chem. Ref. Data 25, 1509–1596.

Sterner, S.M., Bodnar, R.J., 1991. Synthetic fluid inclusions; X, experimental determination of P-V-T-X properties in the CO_2-H_2O system to 6 kb and 700 degrees C. Am. J. Sci. 291, 1–54. https://doi.org/10.2475/ajs.291.1.1.

CHAPTER 4.

GEOLOGICAL SETTING OF CAPE VERDE

4.1. Cape Verde Archipelago

The Cape Verde archipelago, in the North Atlantic Ocean, consists of ten major islands divided into northern (Santo Antão, São Vicente, Santa Luzia, São Nicolau, Sal and Boa Vista), and southern (Maio, Santiago, Fogo and Brava) (Fig. 9, inset) islands. The origin of Cape Verde is attributed to a deep mantle plume, with hotspot-related volcanism starting ~26 Ma (Torres et al., 2010), as supported by previous studies (e.g., Zhao et al. 2013, Liu & Zhao 2014, French & Romanowicz 2015, Saki et al. 2015, Lodhia et al. 2018, and Carvalho et al. 2019). The archipelago stands on the Cape Verde Rise, the largest oceanic intraplate bathymetric anomaly on Earth (Wilson et al., 2013). The oldest exposed hotspot-related volcanism is ~26 Ma (Torres et al., 2010)

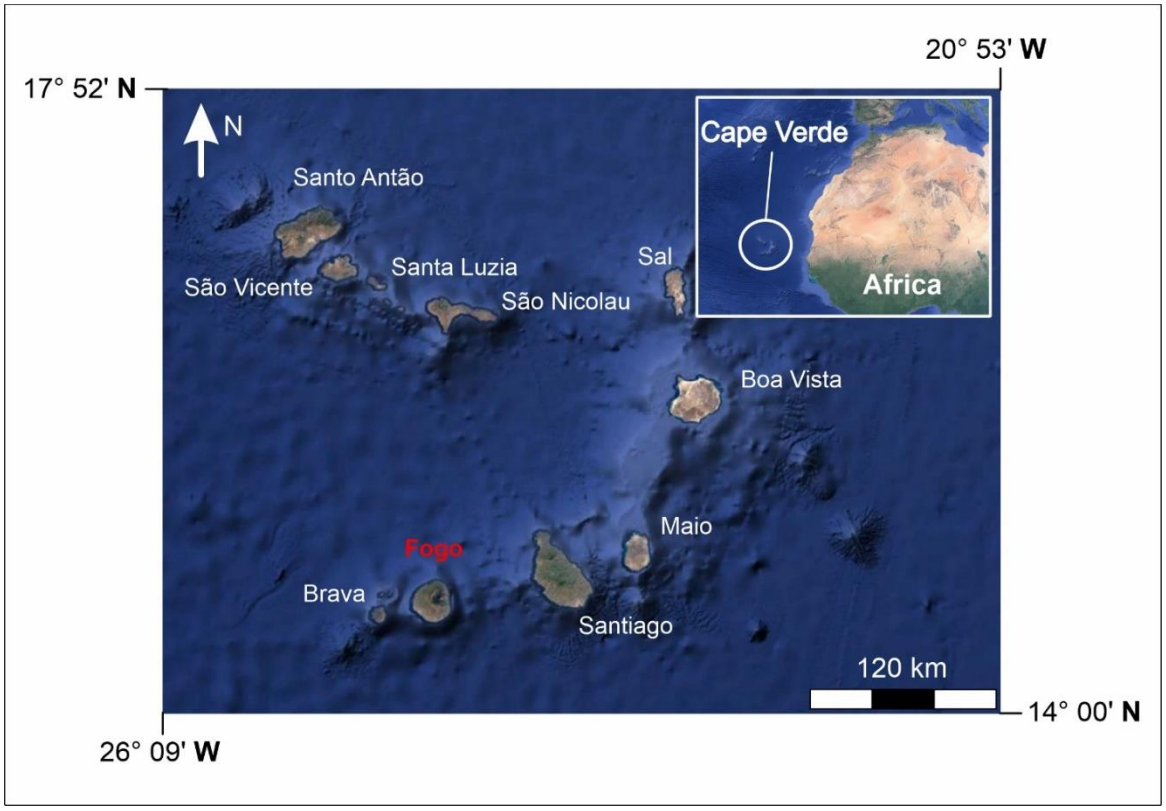

Figure 9 Map of Cape Verde Archipelago, constructed using Google Earth, showing the position of Fogo Island, inset show the location of the Cape Verde (top right).

The Cape Verde rise is interpreted as the result of the interaction between the mantellic plume localized under the archipelago and the quasi-stationary (<10 mm yr^{-1}, Morgan 1983; Pollitz 1991) oceanic lithosphere (110-150 Ma) beneath the Atlantic Ocean, on the Nubian plate (Pollitz, 1991; Holm et al., 2008). The Cape Verde Rise marks an area of significant gravity (Fig. 10 c) (Ali et al., 2003a,b), heat flow (~61 mW m^{-2}; Courtney & White 1986), geoid (Fig. 10b) (~8 m; Monnereau & Cazenave 1990), and seismic anomaly (Fig. 10 c) (Dash et al., 1976; Wilson et al., 2013), interpreted as the surface expression of an hot-spot mantle swell (Holm et al., 2008; Liu and Zhao, 2014). High-resolution seismic images reveal a clearly identifiable zone of low-Vs in the lower mantle extending down to the core-mantle boundary (French & Romanowicz 2015). Additionally, significant depressions are observed in the 410-km and shallower 660-km discontinuities (Saki et al. 2015), along with a distinct column-like low-velocity anomaly in the upper mantle (Liu & Zhao 2014).

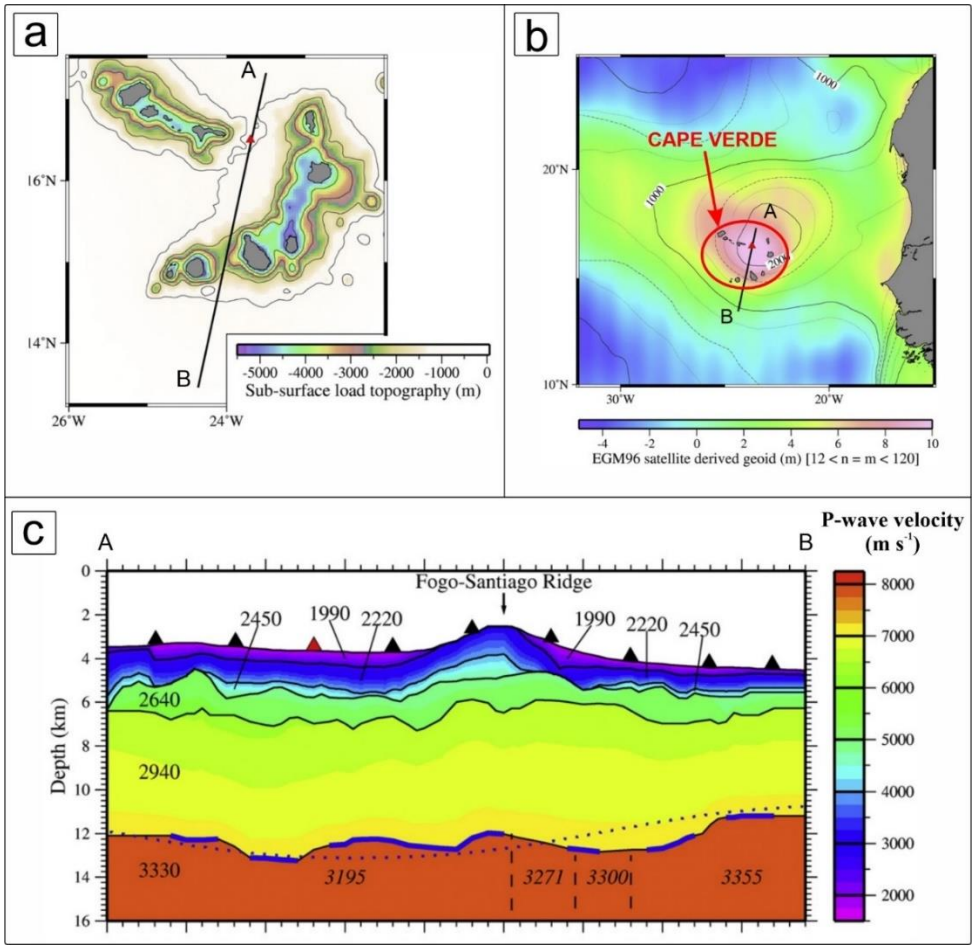

Figure 10 The sub-surface load topography, required to explain the correlation between the free-air gravity anomaly and topography concerning wavelength in the Cape Verde islands region (Ali et al., 2003a) **(a)**. Geoid anomaly obtained by subtracting the EGM96 satellite-derived geoid (Lemoine et al., 1998) **(b)**. Velocity-depth model, incorporating layer boundaries for both seismic and gravity

modelling, is indicated by solid lines. The black triangles are the ocean-bottom seismographs (OBS), with OBS 30 denoted by the red triangle. Solid blue lines illustrate the seismic control on the Moho, and the densities are the number annotated in kg m^{-3} **(c)**. All the panels (a,b,c) are modified from Pim et al., 2008.

Among the various OIB and near-ridge OIB locations, Cape Verde represents with the Canaries (Hansteen et al., 1998; Klügel et al., 2005; Longpré et al., 2017; Taracsák et al., 2019; Sandoval-Velasquez et al., 2021), Hawaii (e.g., Sides et al., 2014; Tucker et al., 2019), Azores (e.g., Zanon and Frezzotti, 2013; Métrich et al., 2014; Zanon, 2015; Zanon et al., 2020), La Réunion (Di Muro et al., 2014; Boudoire et al., 2018), Galapagos (Koleszar et al., 2009; Bell et al., 2021; Aiuppa et al., 2022) and Iceland (Hartley et al., 2014; Bali et al., 2018), one of the most studied in recent years, particularly due to the presence of one of the planet's most active volcanoes and the most active within the Cape Verde archipelago, Fogo (Hildner et al., 2011, 2012; Mata et al., 2017; Klügel et al., 2020).
Volcanism in the archipelago began at ~ 26 Ma (Torres et al., 2010), and is largely dominated by silica undersaturated melts of basanitic to phonolitic compositions (Gerlach et al., 1988). Rare carbonatites are also present in both southern and northern islands (Hoernle et al., 2002; Mourão et al., 2012). The eastern region is home to the oldest islands (Sal, Boa Vista, and Maio), estimated to be ≤30 Ma. Moving northwest, the islands of Santo Antão, São Vicente, and São Nicolau, which have intermediate ages, are estimated to be ≤11 Ma. The young island of Santiago, located to the south, is estimated to be ≤10 Ma, while the southwestern islands of Fogo and Brava potentially experienced the most recent volcanism, estimated to be ≤6 Ma (Ramalho et al., 2011). The presence of highly alkaline silicate rocks (nephelinitic, melanephelinitic, and melilititic rocks), along with carbonatites (e.g., Bonadiman et al., 2005), provides evidence for a diverse and potentially carbon-rich mantle source. This is further supported by the CO_2-rich signature of fumaroles (Aiuppa et al., 2020; Melián et al., 2021) and the high CO_2 content (up to 2.0 wt.%) measured in MI samples (De Vitre et al., 2023). Recent studied conducted by Sun and Dasgupta (2023) provide evidence for this carbon-rich signature of Cape Verde volcanism, with CO_2 content in the parental melt up to~9 wt.% and up to ~ 400 ppm of C in the mantle source. In the Cape Verde islands of of Fogo (Foeken et al., 2007), Brava (Mourão et al., 2010), and Santiago (Martins et al., 2010), carbonatite eruptions have occurred, supporting the presence of a carbon-rich metasomatized mantle source beneath the archipelago. The occurrence of metasomatism, involving carbonatitic to carbonated-silicate melts within the archipelago, is suggested to be a result of a subcontinental lithospheric mantle beneath Cape Verde (e.g., Bonadiman et al., 2005). This phenomenon might potentially reflect the deep recycling of

crustal carbonate back into the mantle (Dasgupta and Hirschmann, 2010; Dorfman et al., 2018). This phenomenon has been suggested as potentially linked to past subduction processes of oceanic slabs in the region (e.g., Hoernle et al., 2002; Mourão et al., 2010).

The nature of the mantle source beneath the Cape Verde Archipelago is still debated due to the complexity of mantle isotopic signatures displayed by Cape Verde. This complexity makes it one of the most challenging hotspots to characterise from a geochemical perspective. This hotspot records all extreme isotopic signatures (HIMU, EM-I), and high $^{3}He/^{4}He$ (>12.6 Ra) in the northern islands (at São Nicolau the $^{3}He/^{4}He$ ratio is up to 16 Ra) suggest a possible lower mantle plume contributiom (Jackson et al., 2017a). A primary unresolved issue regarding the Cape Verde archipelago revolves around the location of the mantle plume (e.g., Civiero et al., 2023), further compounded by the isotopic dichotomy (Sr-Nd-Pb) that emerges between the northern and southern islands. The northern islands - Santo Antão, São Vicente, Santa Luzia, São Nicolau, Sal, and Boa Vista - originate from a HIMU ($^{206}Pb/^{204}Pb$=20.25, Jackson et al., 2017a) mantle source. Conversely, the southern islands - Maio, Santiago, Fogo, and Brava - exhibit characteristics of an EM-I ($^{143}Nd/^{144}Nd$= 0.512606, Jackson et al., 2017a) mantle source (Gerlach et al., 1988; Escrig et al., 2005; Doucelance et al., 2010; Mata et al., 2017). The same isotopic dichotomy (Sr-Nd-Pb), present in the Cape Verde Archipelago mantle source, is equally apparent in the erupted products from Fogo. Indeed, erupted rocks have isotopic affinities spanning from HIMU to EM (Mata et al., 2017) as reported in Figure 11.

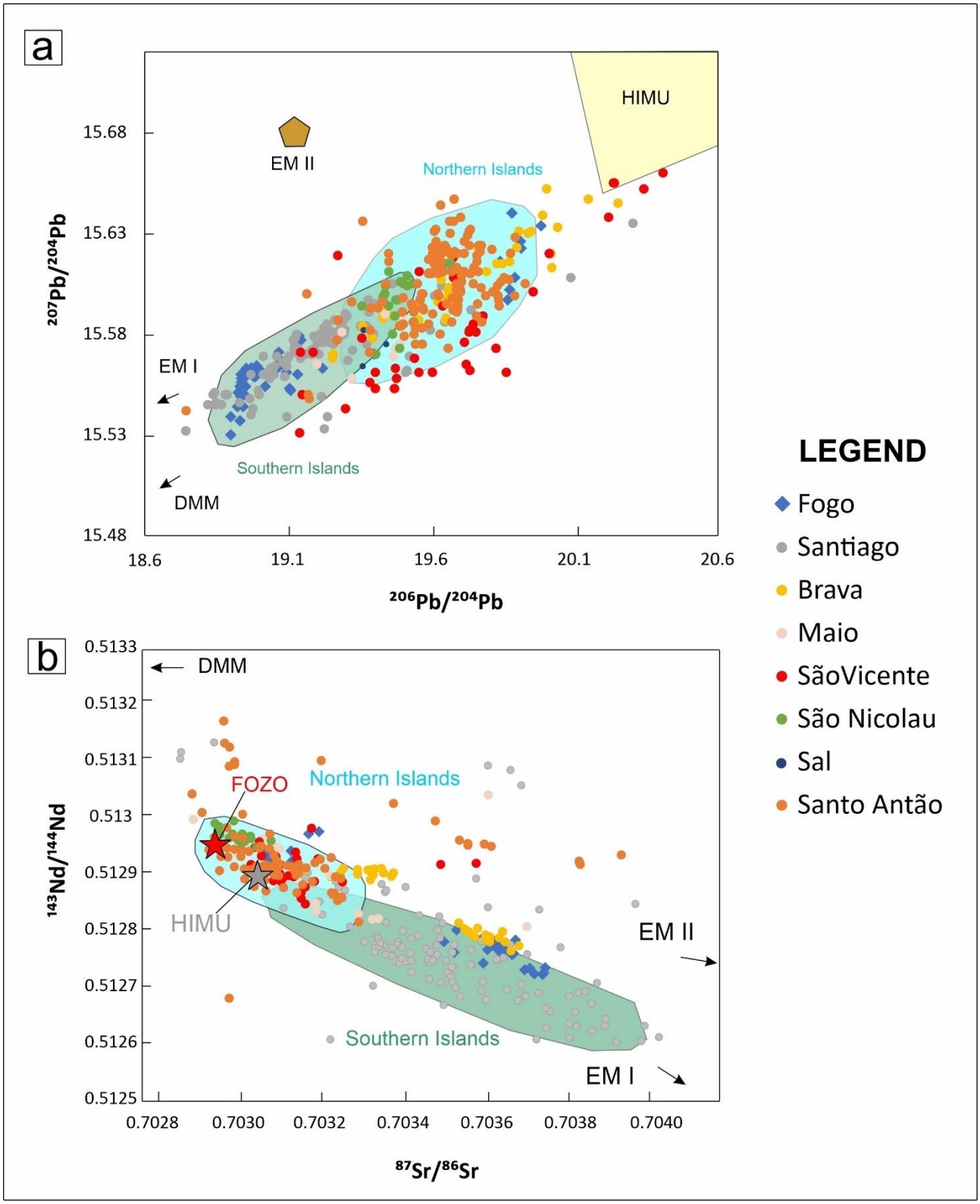

Figure 11 Pb, Sr and Nd isotope compositions of Cape Verde Archipelago. Northern Islands (Santo Antão, São Nicolau, São Vicente, and Sal) data are from (Gerlach et al., 1988; Hoernle et al. 2002; Jorgensen et al., 2002; Holm et al., 2006; Doucelance et al., 2003; Millet et al., 2008; Mata et al., 2017); Southern Islands (Fogo, Santiago, Maio, and Brava) data are from (Gerlach et al., 1988; Hoernle et al. 2002; Doucelance et al., 2003; Escrig et al., 2005; Holm et al., 2006; Martins et al.,

2010; Mourao et al. 2012a; Mata et al., 2017). Plotted mantle components are from Iwamori and Nakamura (2015).

This dichotomy is similarly highlighted by helium isotopic analysis ($^{3}He/^{4}He$). Notably, the southern islands, including Fogo and Santiago, exhibit more radiogenic signatures (Fogo, 7-9 Ra; Santiago 8-9 Ra) compared to the northern islands (Santo Antão 9-10 Ra, São Vicente 9-11 Ra, São Nicolau 10-16, Sal 9-10) (Christensen et al., 2001; Doucelance et al., 2003). The southern island of Brava, is the only exception, recording He isotope ratio signature ($^{3}He/^{4}He$= 10-12 Ra) similar to those observed in the northern islands of the archipelago (Mourão et al., 2012). The presence of a hot, volatile-rich plume beneath the Cape Verde archipelago is corroborated by both geochemical (above mentioned) and geophysical data. Indeed, Liu et al. (2021) recently identified a column-shaped low-Vs zone within the asthenosphere, extending down to a depth of 400 km (Fig. 12).

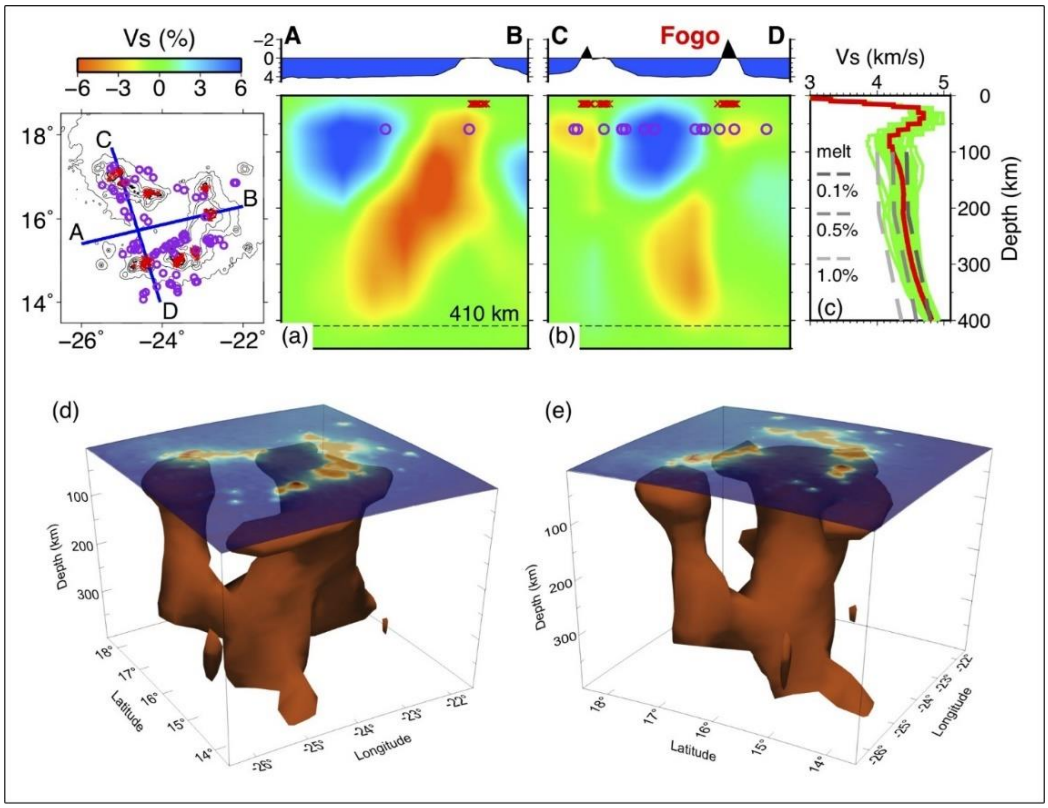

Figure 12 Vertical cross-sections of Vs tomography beneath Cape Verde, determined through a joint inversion of teleseismic S-wave traveltime data, Rayleigh-wave phase-velocity data, and receiver functions, from in Liu et al. (2021). The purple circles on the inset mand and in the (a) and (b) panels, highlighted the piercing points at 60 km depth. In panel (c), the 1-D Vs model used is represented by the red line, while the green lines depict the obtained 3-D Vs model. Additionally, three grey dashed lines in panel (c) illustrate synthetic Vs models obtained with melt fraction values of 0.1, 0.5, and 1.0

per cent, respectively. Panels (d) and (e) present 3-D views of the Vs tomography, with the iso-surface of velocity anomalies rendered where Vs perturbation is -1 per cent.

4.2. Fogo Volcano

4.2.1. Volcano-tectonic structures

Fogo has experienced numerous explosive eruptions in prehistoric times (Eisele et al., 2015), and there have been 28 eruptions in the last 500 years (Ribeiro, 1954; Torres et al., 1997), three of which occurred within a span of only 63 years (1951, 1995, and 2014-15). The currently active volcanic structure is the Pico do Fogo (h = 1100 m) strato-volcano (Fig. 13), which brings the current altitude of the island of Fogo to 2898 m a.s.l. Pico do Fogo has originated inside Chã das Caldeira, a depression of~8 km in diameter, 1/3 of the diameter of the entire islands (Figs. 14, 15, 16a).

Figure 13 Pico do Fogo volcano, and the intra-caldera village of Portela

The caldera itself is the product of a massive flank collapse (Fig. 14) of the precedent volcanic structure, Mt. Amarelo, which is thought to have caused a mega-tsunami in the island of Santiago circa 73 ka ago (Day et al., 1999; Martínez-Moreno et al., 2018). The results of this collapse are (i)

the accumulation of a large debris fan between Fogo and Santiago islands (Martínez-Moreno et al., 2018), (ii) the Chã das Caldeira depression (iii), the wall Bordeira, around the caldera, and (iv) the tsunamites founded in the neighbouring island of Santiago (Paris et al., 2011; Ramalho et al., 2015; Martínez-Moreno et al., 2018).

The Mt. Amarelo massive flank collapse involved significant volumes of rock, with estimates varying among different studies. Madeira et al. (2008) proposed a volume of 70 km^3 based on the multibeam survey conducted by Masson et al. (2008), while Day et al. (1999) estimated a range of 150–200 km^3. Martinez-Moreno et al. (2018) provided intermediate values, suggesting a displaced volume of ~110 km^3. This value closely aligns with those employed by Paris et al. (2011) when generating seven scenarios for tsunami simulations, ranging from 121 to 124 km^3. Figure 14 shows an interpretive profile derived from geophysical data and geological observations. The profile delineates the geometry of the collapsed area at depth, as proposed by the geological interpretation of Magneto Telluric (MT) profiles (Martinez-Moreno et al., 2018).

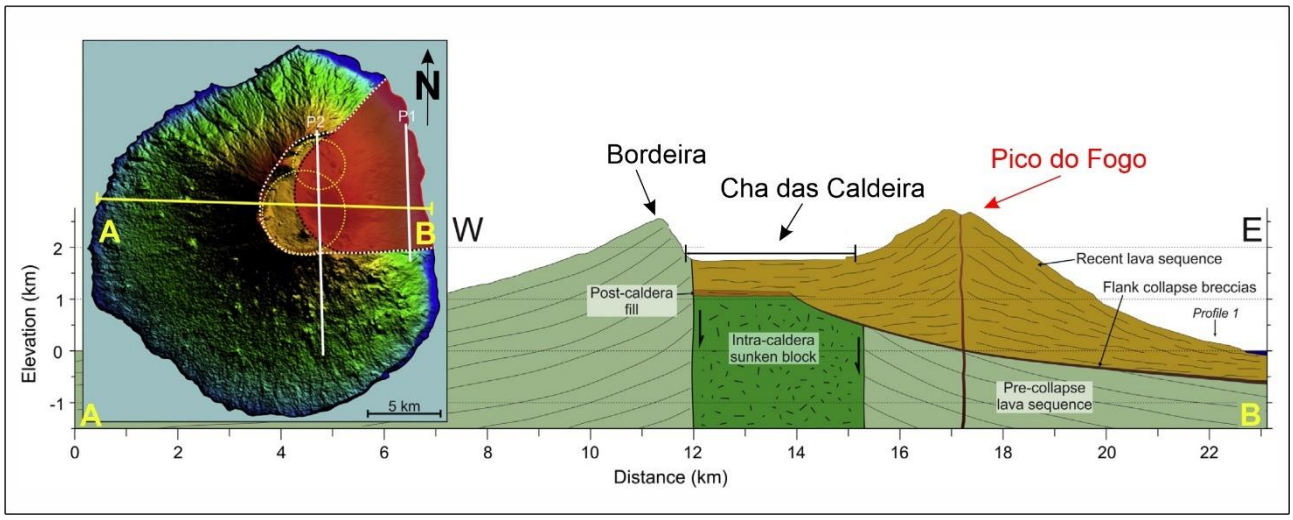

Figure 14 Profile representing the geometry of the collapsed flank at depth of Mt. Amarelo, modified from Martinez-Moreno et al., 2018

The main volcano-tectonic structures, which have strongly influenced the volcanic activity of Fogo, are the rift zones (Day et al., 1999). They are widely recognised as the most prominent and persistent structures in the evolution of mature oceanic volcanic islands. Indeed, they determine the formation of volcanic edifices, concentrate eruptive events, and often play a crucial role in triggering flank collapses (McGuire & Pullen 1989). This phenomenon is likely responsible for the clustering of volcanism within the collapse scars on Fogo (Carracedo et al., 2015).

The most active zones align along approximate bearings of 030°, 150°, and 240-270°, closely corresponding to the rift zones of the Monte Amarelo volcano, as indicated by the locations and elongation trends of post-collapse monogenetic scoria cones (Fig. 15). From the 18th century onward, eruptions clustered along N-S trending fissures/fractures, except for the 1995 and 2014–15 eruptions that occurred on Pico do Fogo's southwestern flank, along the 240°-trending rift system. However, the most recent eruptions (post-1785) are confined within the Monte Amarelo collapse structures and align along N-S-trending fissures, often arranged in en-echelon systems. The sense of offset within these en echelon sets indicates that the dykes feeding these systems lie along the old 030°- and 150°-trending swarms at depth but rotate as they propagate upwards, conforming to an east-west extensional stress system (Day et al., 1999).

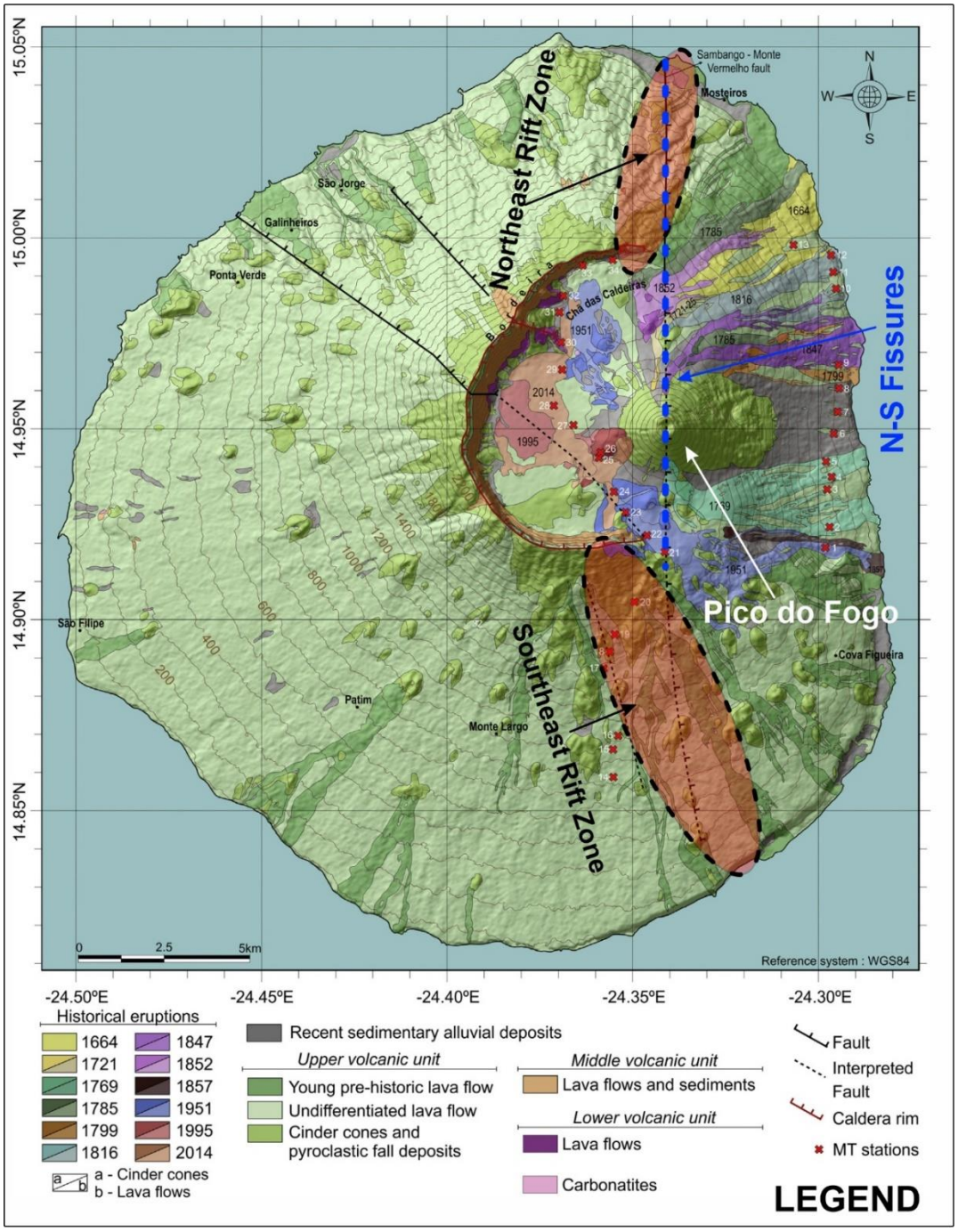

Figure 15 Geological map of Fogo, with the main volcano-tectonic structures, modified form Martinez-Moreno et al., 2018.

4.2.2. Volcano stratigraphy and eruptive history

Fogo volcano erupted approximately 30 times since the 1400s and some of these eruptions were destructive, severely impacting the local populations (e.g., the 1951, 1995, and 2014-15 eruptions; Ribeiro, 1954; Torres et al., 1997). Eruptions are believed to be sourced by a complex, vertically elongated magma plumbing system (Hildner et al., 2011, 2012; Klügel et al., 2020; Lo Forte et al., 2023). The volcanological evolution of Fogo includes four eruptive phases:

(i) The Ribeira de Almada Group: carbonatitic and alkali-rick mafic submarine lavas from the uplifted Seamount Series dated at ~4.5 Ma (Foeken et al., 2007, 2009).

(ii) The Monte Barro Group: the first sub-aerial lavas of unknown age.

(iii) The Monte Amarelo Group (no absolute chronology): a ~2-3 km thick succession of highly alkaline mafic to intermediate lavas, emplaced before the lateral collapse of the volcano. The main products are highly alkaline basic to intermediate lavas, featuring numerous scoria and spatter cones, lapilli and epiclastic breccia units, and occasional felsic elements. The Monte Amarelo Group is divided into two sub-unit: the Bordeira and Ribeira Aguadinha Formations. The Ribeira Aguadinha Formation, consisting of ankaramitic rocks, marks the onset of an eastward migration of volcanic activity and the development of dominant N–S trending dike swarms in the pre-collapse Monte Amarelo volcano. The upper member (Fernao Gomes Member) of the Ribeira Aguadinha Formation is characterised by pyroxene and olivine-phyric ankaramite lavas.

(iv) The Chã das Caldeira Group: the youngest eruptive phase, subdivided into the Pico do Fogo and Monte Orlando formations (Foeken et al., 2009). The former includes the volcanic products emplaced during protracted summit/central activity at Pico do Fogo, in between the Monte Amarelo collapse and the 1785 eruption (Ribeiro, 1954). The Monte Orlando formation includes fissure-fed effusive eruptions concentrating along the Pico do Fogo flanks, from the 1700s century onward (Day et al., 2000). These eruptions clustered along N-S trending fissures/fractures, except for the 1995 and 2014-15 eruptions, that occurred on Pico do Fogo's south-western flank.

Eruptions during the period from 1500 to 1785 were frequent, with intermittent periods of rest or relative quiet. Notably, strong earthquakes in 1680 were associated with a significant eruption, leading to the emigration of some Fogo residents to Brava. During this period, the activity was predominantly associated with explosive events at Pico do Fogo's summit. According to testimonies and descriptions, these events are likely to have been of strombolian style, as typical of Fogo and similar to the most recent eruptions (Day et al., 2000). The last eruption involving the volcano's

summit at Pico do Fogo occurred in 1785 and was extensively documented by Feijo (1786). This fissure eruption involved up to nine vents along the SW-NE-trending volcanic rift zone, with three vents located north of the older collapse structure's northern boundary. Despite being the most recent eruption involving vents beyond this structure, the summit activity during the 1785 eruption appeared relatively minor, generating a small, dark (non-incandescent) eruption column that deposited fine ash at the onset. However, no recognizable deposits from this activity remain at the summit, likely due to the covering by fresh lapilli from subsequent eruptions, especially those in 1951 and 1995. Subsequent eruptions in 1799, 1816, 1847, 1852, and 1857 involved relatively small groups or single vents, mainly located north of Pico do Fogo. The only exception was the 1857 eruption, which occurred southeast of Pico do Fogo. Identifying precise vent locations is challenging due to the proximity of different vents and a thick layer of lapilli from the 1951 and 1995 eruptions.

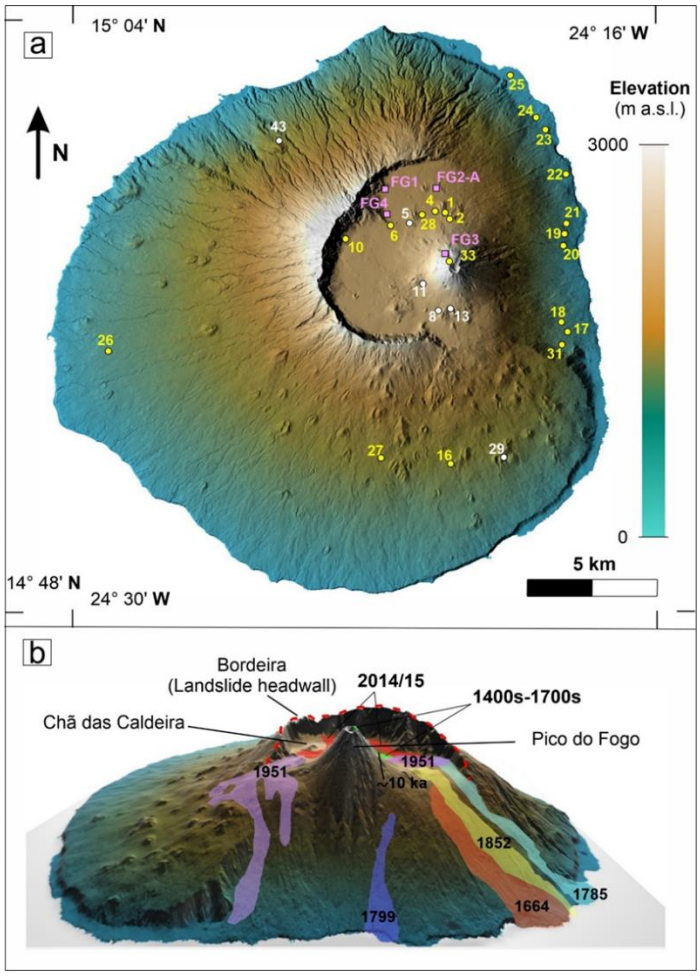

Figure 16 Elevation map of Fogo Island (adapted from: Official SketchFab website, administered by the Volcanology and Petrology Lab's 3D models, Department of Geology and Geography, West Virginia University), indicating locations for collecting lava (yellow numbers), tephra (white

numbers), and mafic enclave (pink numbers) samples used in this thesis **(a)**. The main eruptions are mapped using satellite imagery sourced from Google Earth and existing geological maps (Torres et al., 1997; Carracedo et al., 2015) **(b)**.

The latest eruptions have been extensively studied in the literature, focusing on both the chemistry of the products and the characterisation of the magma plumbing system (e.g., Hildner et al., 2011, 2012; Mata et al., 2017; Klugel et al., 2020). Additionally, volcanic monitoring has been conducted through studies of gas geochemistry, seismic activity, satellite geodetic modeling, and InSAR observations (e.g., Amelung et al., 2002; Cappello et al., 2016; Dionis et al., 2015; Gonzàlez et al., 2015). In detail, the 1951 eruption lasted 70 days (June 12th – August 21st) and produced ~1.1×10^7 m^3 of lava (Siebert and Simkin, 2002), and alternated strombolian and hawaiian phases (Hildner et al., 2012). The 1995 eruption lasted 56 days (April 2nd – May 26th) and emitted $2.9 \pm 0.7 \times 10^6$ m^3 lava (Siebert and Simkin, 2002). Eruptive style and chemistry of the erupted lavas evolved throughout the eruption, from strombolian to hawaiian and from phonotephrites to tephrites, respectively (Hildner et al., 2011). The most-recent eruption in 2014-15 lasted 77 days (November 23rd – February 7th), with an estimated erupted volume of ~45×10^6 m^3 (Bagnardi et al., 2016; Richter et al., 2016). Likewise the 1995 eruption, eruption style evolved from strombolian to hawaiian (Mata et al., 2017).

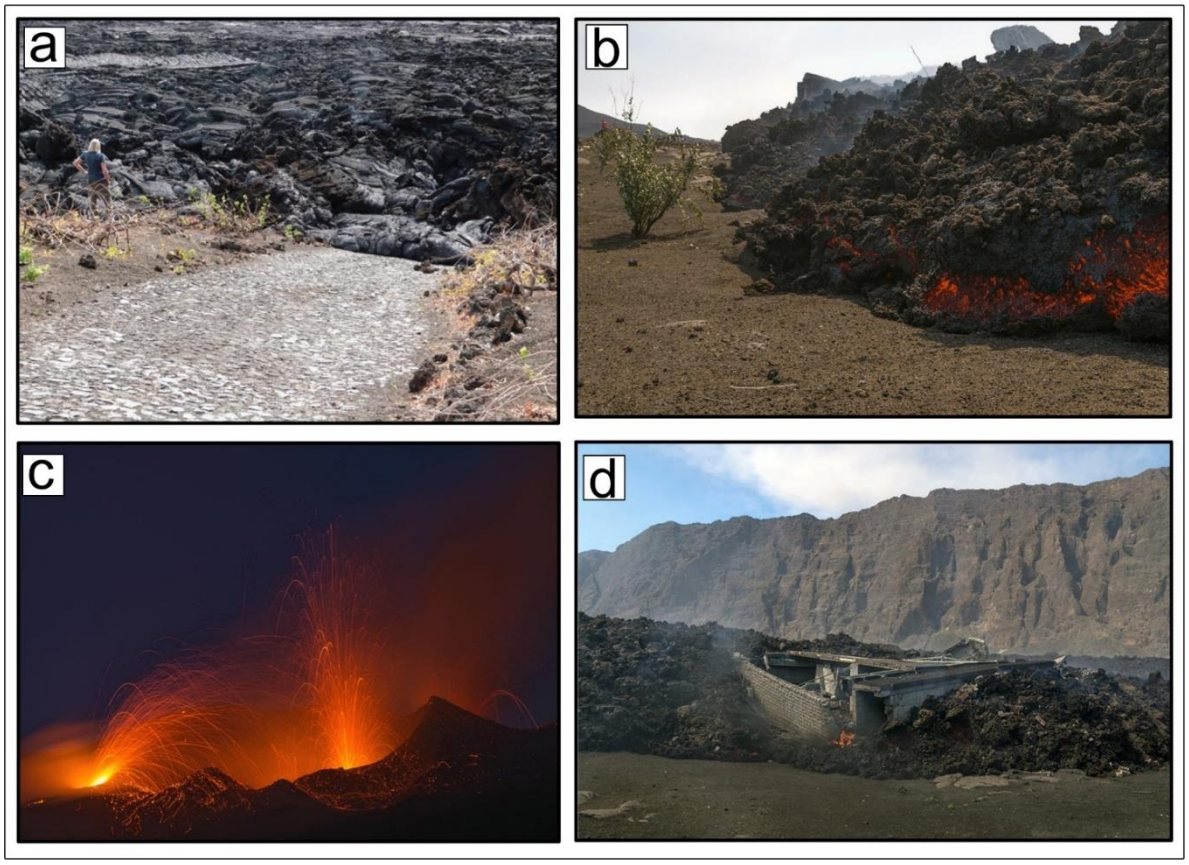

Figure 17 The former 'escape' road was cut by the still-active pahoehoe flow near the site of Ilhéu de Losna following the 2014-15 eruption, from "John Wiley & Sons Ltd, The Geologists' Association & The Geological Society of London, Geology Today, Vol. 31, No. 4, July–August 2015" **(a)**. Lava flow (aa) at Fogo during 30 November-3December 2014. From: https://volcano.si.edu/volcano.cfm?vn=384010 **(b)**. Strombolian activity during 2014-15 eruption. From: https://volcano.si.edu/volcano.cfm?vn=384010 **(c)**. Lava flow during the 2014-15 eruption, resulting in the destruction of a house in Portela village. From: https://volcano.si.edu/volcano.cfm?vn=384010 **(d)**.

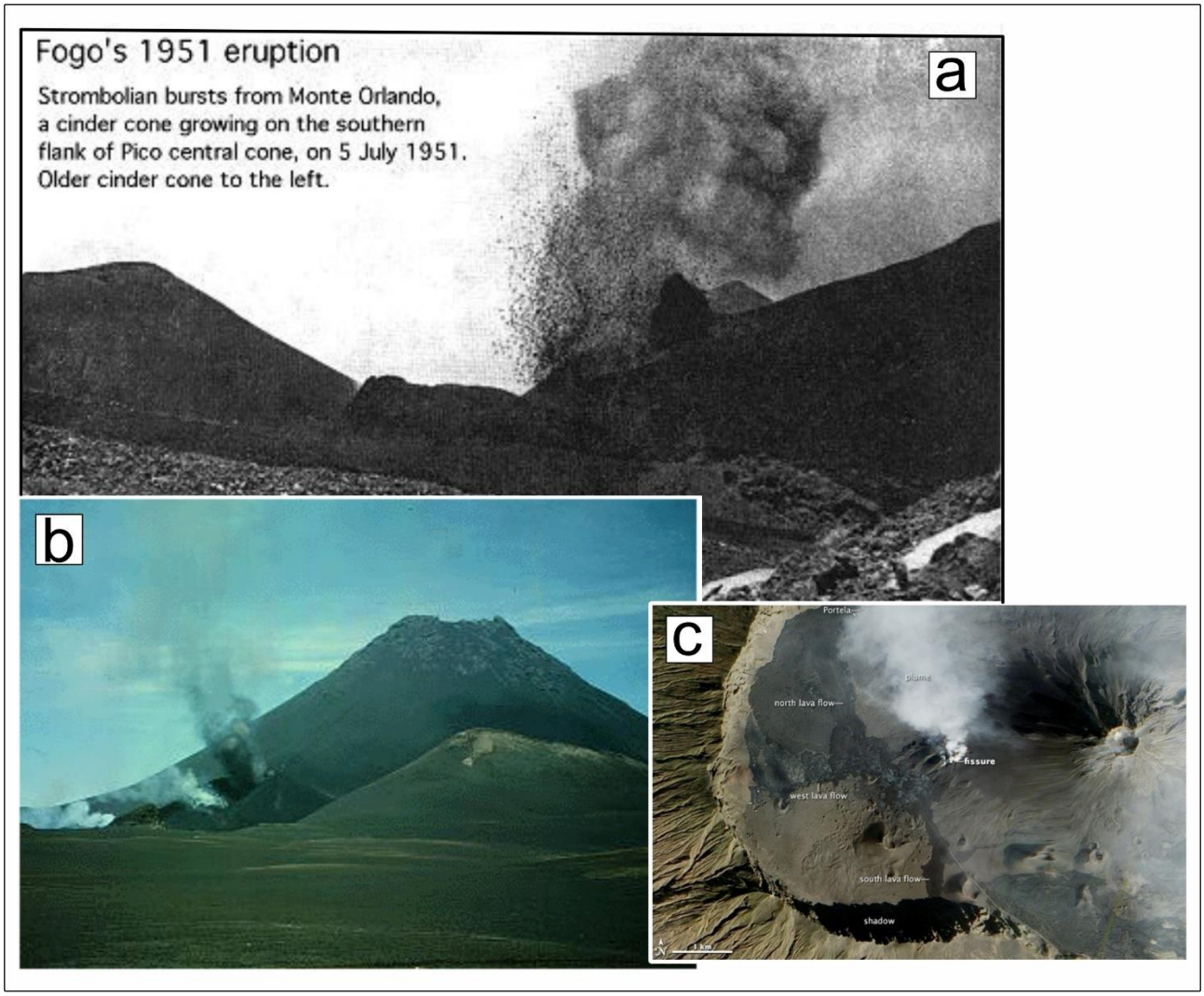

Figure 18 Monte Orlando during a violent Strombolian burst, during the 1951 eruption. Explosion occurs from a vent on the SW side of the main vent which is on the right of the image. Photo taken by Orlando Ribeiro. Credit: https://www.italysvolcanoes.com/FOGO-images.html **(a)**. Photograph of the 1995 eruption. From: https://volcano.oregonstate.edu/fogo **(b)**.Satellite image of the 2014-15 eruption. The image offers a broad view of the volcanic plume streams from a fissure at the SW base of Pico de Fogo. From: https://volcano.si.edu/volcano.cfm?vn=384010 **(c)**.

4.2.3. Magma plumbing system architecture and geochemical characterisation of the erupted products

Recent studies provide new findings on the architecture of the plumbing system and on magma dynamics during its ascent prior to reaching the surface on Fogo. These studies, which include FI microthermometry (Hildner et al., 2012, 2011; Klügel et al., 2020), clinopyroxene-liquid geothermobarometry (Hildner et al., 2011, 2012; Klügel et al., 2020), and MI saturation pressures

(De Vitre et al., 2023), have revealed a vertically elongated magma feeding system, characterised by the presence of interconnected magma lenses within the plumbing system. The plumbing system's architecture includes (i) a deep magma accumulation zone at 31.5 ± 4.3 km depth within the lithospheric mantle; (ii) a main magma storage zone at of 17–25 ± 5 km depth, and (iii) a magma stagnation zone at 9–12 ± 2 km depth, where magma temporarily stagnates, facilitating differentiation processes before and during eruptions, giving rise to phonotephritic melts, as exemplified by those erupted in the 1951, 1995, and 2014-2015 events (Hildner et al., 2011, 2012; Klügel et al., 2020; DeVitre et al., 2023). Other peculiarities of Fogo include (i) the high CO_2 content in the melts, which is up to a factor of 10 higher than observed at other OIB and near-ridge OIB localities (e.g., Erebus in Antarctica, Eschenbacher et al., 1998; Fernandina and Santiago in the Galapagos, Koleszar et al., 2009; Bardabunga in Iceland, Bali et al., 2018; Piton de la Fournaise in Reunion Island, Di Muro et al., 2014; Kilauea in Hawaii, Sides et al., 2014; Laki in Iceland, Hartley et al., 2014; Pico in the Azores, Métrich et al., 2014), being only comparable to the nearby island of El Hierro, in the Canary Archipelago (Taracsák et al., 2019). Consequently, (ii) the presence of a carbon-rich mantle source, previously inferred from the occurrence of carbonatites found in the islands of Sal (Bonadiman et al., 2005), Fogo (Foeken et al., 2007), Brava (Mourão et al., 2010), and Santiago (Martins et al., 2010), and recently substantiated by the elevated CO_2 values (up to 2 wt.%) identified in melt inclusion studies De Vitre et al. (2023). In its brief eruptive history (~4.5 million of years, Foeken et al., 2007, 2009), relative to the age of the entire archipelago ~26 Ma (Torres et al., 2010), Fogo has erupted a wide geochemical compositional range of products, ranging from picro-basalts to phonolites. The most recent eruptions have yielded, respectively: basanitic to tephritic magma during the 1951 eruption (Hildner et al., 2012); phonotephrites to tephrites during the 1995 eruption (Hildner et al., 2011); and compositions ranging from basanitic/tephritic to phonolite for the 2014-2015 eruption, covering a broad spectrum on the TAS diagram.

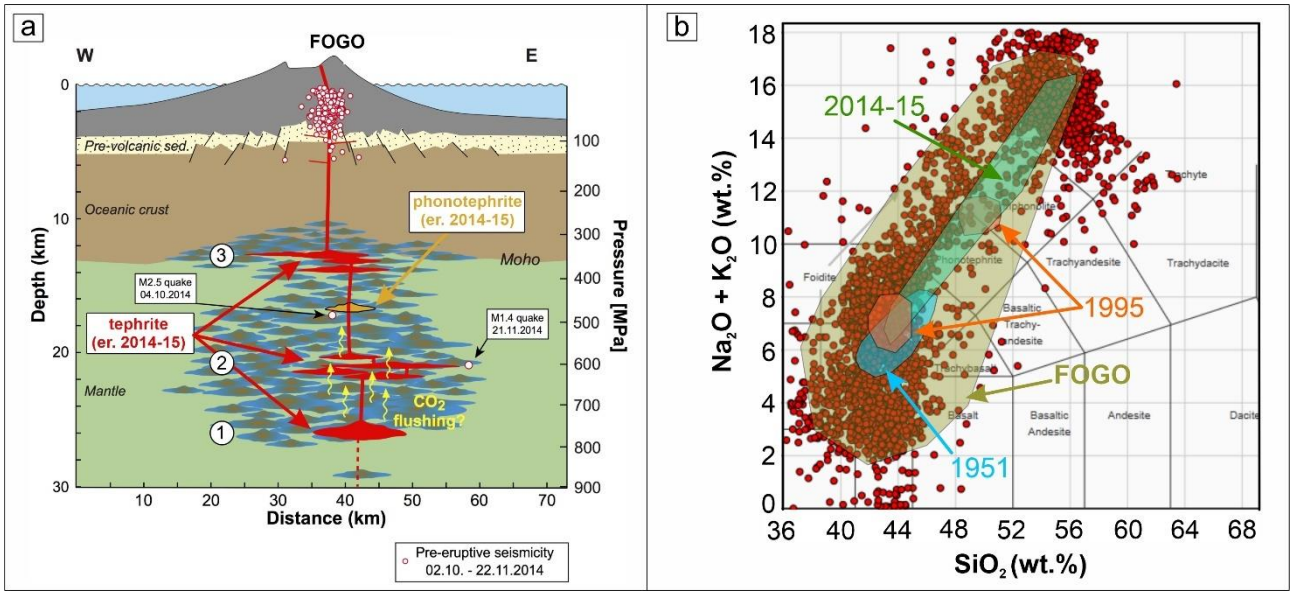

Figure 19 Magma plumbing system of Fogo, shows the: 1) main magma storage zone and crystal fractionation before eruption, 2) temporary stalling in complex ponding zone, 3) magma stagnation zone near the Moho. The cross-section is modified from Klügel et al. (2020) **(a)**. Total Alkali-Silica (TAS) diagram following Le Bas et al. (1986). The red dots represent all Cape Verde samples, while the blue-shaded area represents all Fogo samples. Data sourced from GEOROC database (https://georoc.eu/georoc/new-start.asp) **(b)**.

REFERENCES

Aiuppa, A., Allard, P., Bernard, B., Lo Forte, F.M., Moretti, R., Hidalgo, S., 2022. Gas Leakage from Shallow Ponding Magma and Trapdoor Faulting at Sierra Negra Volcano (Isabela Island, Galápagos). Geochem. Geophys. Geosyst. 23.

Aiuppa, A., Bitetto, M., Rizzo, A.L., Viveiros, F., Allard, P., Frezzotti, M.L., Zanon, V., 2020. The fumarolic CO_2 output from Pico do Fogo Volcano (Cape Verde). Ital. J. Geosci. 139 (3), 325–340. Aiuppa, A., Casetta, F., Coltorti, M., Stagno, V., Tamburello, G., 2021. Carbon concentration increases with depth of melting in Earth's upper mantle. Nat. Geosci. 14, 697–703.

Ali, M.Y., Watts, A.B., Hill, I., 2003a. A seismic reflection profile study of lithospheric flexure in the vicinity of the Cape Verde islands. J. Geophys. Res. 108, 2239.

Amelung, F., Day, S., 2002. InSAR observations of the 1995 Fogo, Cape Verde, eruption: Implications for the effects of collapse events upon island volcanoes. Geophys. Res. Lett. 29, 1606

Ali, M.Y.,Watts, A.B., Hill, I., 2003b. Structure of Mesozoic oceanic crust in the vicinity of the Cape Verde islands from seismic reflection profiles. Mar. Geophys. Res. 24, 329–343.

Bagnardi, M., González, P.J., Hooper, A., 2016. High-resolution digital elevation model from tri-stereo Pleiades-1 satellite imagery for lava flow volume estimates at Fogo Volcano. Geophys. Res. Lett. 43 (12), 6267–6275.

Bali, E., Hartley, M.E., Halldórsson, S.A., Gudfinnsson, G.H., Jakobsson, S., 2018. Melt inclusion constraints on volatile systematics and degassing history of the 2014–2015 Holuhraun eruption, Iceland. Contrib. Mineral. Petrol. 173, 9.

Bell, A.F., La Femina, P.C., Ruiz, M., Amelung, F., Bagnardi, M., Bean, C.J., et al., 2021. Caldera resurgence during the 2018 eruption of Sierra Negra volcano, Galapagos Islands. Nat. Commun. 12, 1397.

Bonadiman, C., Beccaluva, L., Coltorti, M., Siena, F., 2005. Kimberlite-like Metasomatism and 'Garnet Signature' in Spinel-peridotite Xenoliths from Sal, Cape Verde Archipelago: relics of a subcontinental mantle domain within the atlantic oceanic lithosphere? J. Petrol. 46, 2465–2493.

Boudoire, G., Rizzo, A.L., Di Muro, A., Grassa, F., Liuzzo, M., 2018. Extensive CO_2 degassing in the upper mantle beneath oceanic basaltic volcanoes: First insights from Piton de la Fournaise volcano (La Réunion Island). Geochim. et Cosmochim. Acta 235, 376–401.

Cappello, A., Ganci, G., Calvari, S., Pérez, N. M., Hernández, P. A., Silva, S. V., et al., 2016. Lava flow hazard modeling during the 2014–2015 Fogo eruption, Cape Verde, J. Geophys. Res. Solid Earth, 121, 2290–2303.

Carracedo, J.C., Perez-Torrado, F.J., Rodriguez-Gonzalez, A., Paris, R., Troll, V.R., Barker, A.K., 2015. Volcanic and structural evolution of Pico do Fogo, Cape Verde. Geol. Today 31, 146–152.

Carvalho, J., Bonadio, R., Silveira, G., Lebedev, S., Mata, J., Arroucau, P., et al., 2019. Evidence for high temperature in the upper mantle beneath Cape Verde archipelago from Rayleighwave phase-velocity measurements, Tectonophysics, 770, 228225.

Civiero, C., Carvalho, J., Silveira, G., 2023. Mantle structure beneath the Macaronesian volcanic islands (Cape Verde, Canaries, Madeira and Azores): A review and future directions. Front. Earth Sci. 11:1126274. doi: 10.3389/feart.2023.1126274

Dasgupta, R., Hirschmann, M.M., 2010. The deep carbon cycle and melting in Earth's interior. Earth and Planet. Sci. Lett. 298, 1–13. https://doi.org/10.1016/j.epsl.2010.06.039

Dash, B.P., Ball, M.M., King, G.A., Butler, L.W., Rona, P.A., 1976. Geophysical investigation of the Cape Verde Archipelago. J. Geophys. Res. 81, 5249–5259.

Day, S.J., Carracedo, J.C., Guillou, H., Pais Pais, F.J., Badiola, E.R., Fonseca, J.F.B.D., et al., 2000. Comparison and cross-checking of historical, archaeological and geological evidence for the dilocation and type of historical and sub-historical eruptions of multiple-vent oceanic island volcanoes. Geol. Soc. Lond. Spec. Publ. 171, 281–306.

Day, S.J., Heleno da Silva, S.I.N., Fonseca, J.F.B.D., 1999. A past giant lateral collapse and present-day flank instability of Fogo, Cape Verde Islands. J. Volcanol. and Geother. Res. 94, 191–218.

DeVitre, C.L., Gazel, E., Ramalho, R.S., Venugopal, S., Steele-MacInnis, M., Hua, J., Allison, C.M., Moore, L.R., Carracedo, J.C., Monteleone, B., 2023. Oceanic intraplate explosive eruptions fed directly from the mantle. Proc. Natl. Acad. Sci. 120 (33), e2302093120.

Di Muro, A., Metrich, N., Vergani, D., Rosi, M., Armienti, P., Fougeroux, T., Deloule, E., Arienzo, I., Civetta, L., 2014. The Shallow Plumbing System of Piton de la Fournaise Volcano (La Reunion Island, Indian Ocean) Revealed by the Major 2007 Caldera-Forming Eruption. J. Petrol. 55, 1287–1315.

Dionis S.M., Pérez N.M., Hernández P.A., Melián G., Rodríguez F., Padrón E., et al., 2015 - Diffuse CO_2 degassing and volcanic activity at Cape Verde Islands, West Africa. Earth, Planets and Space, 67 (1), 8.

Dorfman, S.M., Badro, J., Nabiei, F., Prakapenka, V.B., Cantoni, M., Gillet, P., 2018. Carbonate stability in the reduced lower mantle. Earth and Planet. Sci. Lett. 489, 84–91.

Doucelance, R., Escrig, S., Moreira, M., Gariépy, C., Kurz, M.D., 2003. Pb-Sr-He isotope and trace element geochemistry of the Cape Verde Archipelago. Geochim. Cosmochim. Acta 67, 3717–3733.

Doucelance, R., Hammouda, T., Moreira, M., Martins, J.C., 2010. Geochemical constrains on depth of origin of oceanic carbonatites: the Cape Verde case Geochim. Cosmochim. Acta, 74, 7261-7282.

Eschenbacher, A. 1998. Open-system degassing of a fractionating, alkaline magma, Mount Erebus, Ross Island, Antarctica. Unpublished Master's Thesis, New Mexico Institute of Mining and Technology, Socorro.

Escrig, S., Doucelance, R., Moreira, M., Allègre, C.J., 2005. Os isotope systematics in Fogo Island: Evidence for lower continental crust fragments under the Cape Verde Southern Islands. Chem. Geol. 219, 93–113.

Eisele, S., Reißig, S., Freundt, A., Kutterolf, S., Nürnberg, D., Wang, K.L., et al., 2015. Pleistocene to Holocene offshore tephrostratigraphy of highly explosive eruptions from the southwestern Cape Verde Archipelago. Mar. Geol. 369, 233–250.

Feijo, J. S., 1786. Memoria sobre a nova irrupcao volcanica do Pico da ilha do Fogo que deve servir de Suplemento a Letra Filosofica No. 5 sobre o mesmo objecto. Archivo Historico Ultramarino, Lisboa, Cabo Verde." Cartografia - mapas nao catalogados (Memoir on the new volcanic eruption of the Pico of the Island of Fogo, supplementary to the 5th Philosophical Letter on the same subject. Overseas Historical Archive, Lisbon: Cape Verde Cartography Section- unserialized maps) (complete transcript, with original diagrams, has been given by Ribeiro (1960)).

Foeken, J., Stuart, F., Day, S., Wall, F., 2007. Carbonatite seamount formation and first subaerial exposure of Fogo (Cape Verde Islands): results from apatite and pyrochlore (U–Th)/He dating. Geophys. Res. Abstr. 9. EGU2007-A-09688.

Foeken, J.P.T., Day, S., Stuart, F.M., 2009. Cosmogenic ^{3}He exposure dating of the Quaternary basalts from Fogo, Cape Verdes: implications for rift zone and magmatic reorganisation. Quat. Geochronol. 4, 37–49.

French, S., and Romanowicz, B., 2015. Broad plumes rooted at the base of the Earth's mantle beneath major hotspots, Nature, 525, 95–99.

Gerlach, D.C., Cliff, R.A., Davies, G.R., Norry, M., Hodgson, N., 1988. Magma sources of the Cape Verdes archipelago: Isotopic and trace element constraints. Geochim. Cosmochim. Acta 52, 2979–2992.

González, P. J., Bagnardi, M., Hooper, A. J., Larsen, Y., Marinkovic, P., Samsonov, S. V., et al., 2015. The 2014–2015 eruption of Fogo volcano: Geodetic modeling of Sentinel-1 TOPS interferometry, Geophys. Res. Lett., 42, 9239–9246.

Hansteen, T.H., Klügel, A., Schmincke, H.-U., 1998. Multi-stage magma ascent beneath the Canary Islands: evidence from fluid inclusions. Contrib. Mineral. Petrol. 132, 48–64.

Hartley, M.E., Maclennan, J., Edmonds, M., Thordarson, T., 2014. Reconstructing the deep CO_2 degassing behaviour of large basaltic fissure eruptions. Earth and Planet. Sci. Lett. 393, 120–131.

Hildner, E., Klügel, A., Hauff, F., 2011. Magma storage and ascent during the 1995 eruption of Fogo, Cape Verde Archipelago. Contrib. Mineral. Petrol. 162, 751–772.

Hildner, E., Klügel, A., Hansteen, T.H., 2012. Barometry of lavas from the 1951 eruption of Fogo, Cape Verde Islands: Implications for historic and prehistoric magma plumbing systems. J. Volcanol. Geotherm. Res. 217–218, 73–90.

Hoernle, K., Tilton, G., Le Bas, M.J., Duggen, S., Garbe-Schönberg, D., 2002. Geochemistry of oceanic carbonatites compared with continental carbonatites: mantle recycling of oceanic crustal carbonate. Contrib. Mineral. Petrol. 142, 520–542.

Holm, P. M., Wilson, J.R., Christensen B.P., Hansen, L., Hansen, S. L., Hein, K.M., et al., 2006, Sampling the Cape Verde Mantle Plume: Evolution of Melt Compositions on Santo Antão, Cape Verde Islands, J. Petrol., 47, 1, 145–189.

Holm, P.M., Grandvuinet, T., Friis, J., Wilson, J.R., Barker, A.K., Plesner, S., 2008. An ^{40}Ar-^{39}Ar study of the Cape Verde hot spot: temporal evolution in a semistationary plate environment. J. Geophy. Res. 113, B08201.

Iwamori, H., Nakamura, H., 2015. Isotopic heterogeneity of oceanic, arc and continental basalts and its implications for mantle dynamics. Gondwana Res. 27, 1131–1152.

Jackson, M. G., Konter, J.G., Becker, T.W., 2017a. Primordial helium entrained by the hottest mantle plumes. Nature 542, 340–343.

Koleszar, A.M., Saal, A.E., Hauri, E.H., Nagle, A.N., Liang, Y., Kurz, M.D., 2009. The volatile contents of the Galapagos plume; evidence for H_2O and F open system behavior in melt inclusions. Earth and Planet. Sci. Lett. 287, 442–452.

Klügel, A., Day, S., Schmid, M., Faria, B., 2020. Magma plumbing during the 2014–2015 eruption of Fogo (Cape Verde Islands). Front. Earth Sci. 8, 157.

Klügel, A., Hansteen, T.H., Galipp, K., 2005. Magma storage and underplating beneath Cumbre Vieja volcano, La Palma (Canary Islands). Earth Planet. Sci. Lett. 236, 211–226.

Lemoine, F.G., Kenyon, S.C., Factor, J.K., Timmer, R.G., Pavlis, N.K., Chinn, D.S., et al., 1998. EGM96: The NASA GSFC and NIMA Joint Geopotential Model, NASA technical report, TP-1998-206861

Liu, X., and Zhao, D., 2014. Seismic evidence for a mantle plume beneath the Cape Verde hotspot, Int. Geol. Rev., 56, 1213–1225.

Liu, X., Zhao, D., 2021. Seismic evidence for a plume-modified oceanic lithosphere–asthenosphere system beneath Cape Verde. Geophys. J. Int.225, 872–886.

Longpré, M.-A., Stix, J., Klügel, A., Shimizu, N., 2017. Mantle to surface degassing of carbon- and sulphur-rich alkaline magma at El Hierro, Canary Islands. Earth and Planet. Sci. Lett. 460, 268–280.

Lodhia, B., Roberts, G., Fraser, A., Fishwick, S., Goes, S., Jarvis, J., 2018. Continental margin subsidence from shallow mantle convection: example from West Africa, Earth planet. Sci. Lett., 481, 350–361.

Lo Forte, F.M., Aiuppa, A., Rotolo, S.G., Zanon, V., 2023. Temporal evolution of the Fogo Volcano magma storage system (Cape Verde Archipelago): a fluid inclusions perspective. J. Volcanol. Geotherm. Res. 433, 107730.

Madeira, J., Brum da Silveira, A., Mata, J., Mourão, C., Martins, S., 2008. The role of mass movements on the geomorphologic evolution of island volcanoes: examples from Fogo and Brava in the Cape Verde archipelago. Comunicações Geológicas 95, 93–106.

Martínez-Moreno, F.J., Monteiro Santos, F.A., Madeira, J., Pous, J., Bernardo, I., Soares, A., et al., 2018. Investigating collapse structures in oceanic islands using magnetotelluric surveys: The case of Fogo Island in Cape Verde. J. Volcanol. and Geother. Res. 357, 152–162.

Martins, S., Mata, J., Munhá, J., Mendes, M.H., Maerschalk, C., Caldeira, R., et al., 2010. Chemical and mineralogical evidence of the occurrence of mantle metasomatism by carbonate-rich melts in an oceanic environment (Santiago Island, Cape Verde). Miner. Petrol. 99, 43–65.

Masson, D., Le Bas, T., Grevemeyer, I., Weinrebe, W., 2008. Flank collapse and large-scale landsliding in the Cape Verde Islands, off West Africa. Geochem. Geophys. Geosyst. 9 (7).

Mata, J., Martins, S., Mattielli, N., Madeira, J., Faria, B., Ramalho, R.S., et al., 2017. The 2014–15 eruption and the short-term geochemical evolution of the Fogo volcano (Cape Verde): Evidence for small-scale mantle heterogeneity. Lithos 288–289, 91–107.

McGuire, W.J., and Pullen, A.D. 1989. Location and orientation of eruptive fissures and feeder-dykes at Mount Etna; influence of gravitational and regional tectonic stress regimes. J. Volcanol. Geotherm. Res., 38, 325-344.

Melián, G.V., Hernández, P.A., Pérez, N.M., Asensio-Ramos, M., Padrón, E., Alonso, M., Padilla, G.D., Barrancos, J., Sortino, F., Sumino, H., Rodríguez, F., Amonte, C., Silva, S., Cardoso, N., Pereira, J.M., 2021. Insights from Fumarole Gas Geochemistry on the Recent Volcanic Unrest of Pico do Fogo, Cape Verde. Front. Earth Sci. 9, 631190.

Métrich, N., Zanon, V., Créon, L., Hildenbrand, A., Moreira, M., Marques, F.O., 2014. Is the 'Azores Hotspot' a Wetspot? Insights from the Geochemistry of Fluid and Melt Inclusions in Olivine of Pico Basalts. J. Petrol. 55, 377–393.

Millet, M.A., Doucelance, R., Schiano, P., David, K., Bosq, C., 2008. Mantle plume heterogeneity versus shallow-level interactions: a case study, the São Nicolau Island, Cape Verde archipelago. J. Volcanol. Geotherm. Res.176, 265–276.

Monnereau, M., and Cazenave, A. 1990. Depth and geoid anomalies over oceanic hotspot swells: A global survey. J. Geophys Res. 95, 15429.

Morgan, P., 1983. Constraints on rift thermal processes from heat flow and uplift. Tectonophysics

Mourão, C., Moreira, M., Mata, J., Raquin, A., Madeira, J., 2012. Primary and secondary processes constraining the noble gas isotopic signatures of carbonatites and silicate rocks from Brava Island: evidence for a lower mantle origin of the Cape Verde plume. Contrib. Mineral. Petrol. 163, 995–1009.

Mourão, C., Mata, J., Doucelance, R., Madeira, J., da Silveira, A.B., Silva, L.C., et al., 2010. Quaternary extrusive calciocarbonatite volcanism on Brava Island (Cape Verde): a nephelinite-carbonatite immiscibility product. J. Afr. Earth Sci. 56 (2), 59-74.

Paris, R., Giachetti, T., Chevalier, J., Guillou, H., Frank, N., 2011. Tsunami deposits in Santiago Island (Cape Verde archipelago) as possible evidence of a massive flank failure of Fogo volcano. Sediment. Geol. 239, 129–145.

Pollitz, F., 1991. Two-stage model of African absolute motion during the last 30 million years. Tectonophysics 194, 91–106.

Ramalho, R., 2011. Building the Cape Verde Islands. Springer Theses (207 pp.).

Ramalho, R., Winckler, G., Madeira, J., Helffrich, G., Hipólito, A., Quartau, R., et al., 2015. Hazard potential of volcanic flank collapses raised by new megatsunami evidence. Sci. Adv.

Ribeiro O., 1954. A Ilha do Fogo e as suas erupções, Memórias da Junta de Investigação Científica do Ultramar, Série Geográfica, I, Lisboa, 327.

Richter, N., Favalli, M., Dalfsen, E.Z., Fornaciai, A., Fernandes, R.M.S., Rodriguez, N.P., et al., 2016. Lava flow hazard at Fogo volcano, Cape Verde, before and after the 2014–2015 eruption. Nat. Hazards and Earth Syst. Sci. 16,1925–1951.

Saki,M., Thomas, C., Nippress, S., and Lessing, S., 2015. Topography of upper mantle seismic discontinuities beneath the North Atlantic: the Azores, Canary and Cape Verde plumes, Earth planet. Sci. Lett., 409, 193–202.

Sandoval-Velasquez, A., Rizzo, A.L., Aiuppa, A., Remigi, S., Padrón, E., Pérez, N.M., Frezzotti, M.L., 2021a. Recycled crustal carbon in the depleted mantle source of El Hierro volcano, Canary Islands. Lithos 400–401, 106414.

Sides, I.R., Edmonds, M., Maclennan, J., Swanson, D.A., Houghton, B.F., 2014. Eruption style at Kīlauea Volcano in Hawai‘i linked to primary melt composition. Nature Geosciences 7, 464–469.

Siebert, L., Simkin, T., 2002. Volcanoes of the World: An Illustrated Catalog of Holocene Volcanoes and their Eruptions. In: Global Volcanism Program Digital Information Series. Smithsonian Institution.

Sun, C. and Dasgupta, R., 2023. Carbon budget of Earth’s deep mantle constrained by petrogenesis of silica-poor ocean island basalts. Earth and Planet. Sci. Lett. 611, 118135.

Taracsák, Z., Hartley, M.E., Burgess, R., Edmonds, M., Iddon, F., Longpré, M.-A., 2019. High fluxes of deep volatiles from ocean island volcanoes: Insights from El Hierro, Canary Islands. Geochim Cosmochim. Acta 258, 19–36.

Torres, P., Madeira, J., Silva, L., Brum da Silveira, A., Serraheíro, A., Mota Gomes, A., 1997. Carta Geologica das Erupç˜oes Hist´oricas da Ilha do Fogo (Cabo Verde): revisão e actualização Comn. Inst. Geol. Mine. 84, A193–A196.

Torres, P., Silva, L.C., Munhá, J., Caldeira, R., Mata, J., Tassinari, C., 2010. Petrology and geochemistry of lavas from Sal Island: implication for the variability of the Cape Verde magmatism. Comun. Geol. 97, 35–62.

Tucker, J.M., Hauri, E.H., Pietruszka, A.J., Garcia, M.O., Marske, J.P., Trusdell, F.A., 2019. A high carbon content of the Hawaiian mantle from olivine-hosted melt inclusions. Geochim Cosmochim. Acta 254, 156–172.

Wilson, D.J., Peirce, C., Watts, A.B., Grevemeyer, I., 2013. Uplift at lithospheric swells–II: is the Cape Verde mid-plate swell supported by a lithosphere of varying mechanical strength? Geophys. J. Int. 193, 798–819.

Zanon, V., 2015a. Conditions for mafic magma storage beneath fissure zones at oceanic islands. The case of São Miguel Island (Azores archipelago). In: Caricchi, L., Blundy, J.D. (Eds.), Chemical, Physical and Temporal Evolution of Magmatic Systems. The Geological Society of London, Special Publications, pp. 85–104, 422. https://doi.org/10.1144/SP422.4.

Zanon, V., and Frezzotti, M.L., 2013. Magma storage and ascent conditions beneath Pico and Faial islands (Azores archipelago): a study on fluid inclusions. Geochem. Geophys. Geosyst. 14, 3494–3514. https://doi.org/10.1002/ggge.20221

Zanon, V., Pimentel, A., Auxerre, M., Marchini, G., Stuart, F.M., 2020. Unravelling the magma feeding system of a young basaltic oceanic volcano. Lithos 352–353, 105325. https://doi.org/10.1016/j.lithos.2019.105325.

Zhao, D., Yamamoto, Y., and Yanada, T., 2013. Global mantle heterogeneity and its influence on teleseismic regional tomography, Gondwana Res., 23, 595–616.

WEB REFERENCES

https://georoc.eu/georoc/new-start.asp

https://sketchfab.com/WVUpetrology

https://volcano.oregonstate.edu/fogo

https://volcano.si.edu/volcano.cfm?vn=384010.

https://www.italysvolcanoes.com/FOGO-images.html

CHAPTER 5.

TEMPORAL EVOLUTION OF THE FOGO VOLCANO MAGMA STORAGE SYSTEM (CAPE VERDE ARCHIPELAGO): A FLUID INCLUSIONS PERSPECTIVE

Published in Journal of Volcanology and Geothermal Research:
https://doi.org/10.1016/j.jvolgeores.2022.107730

(Lo Forte et al., 2023)

ABSTRACT

The architecture of the magma storage system underneath Fogo Volcano (Cape Verde archipelago) is characterised using novel fluid inclusion results from fifteen basanites, spanning the last 120 thousand years of volcanic activity, and encompassing a major flank collapse event at ~73 ka. Fluid inclusions, hosted in olivine and clinopyroxene, are made of pure CO_2, and based on their textural characteristics, are distinguished in early (Type I) and late (Type II) stage. Inclusions homogenise to a liquid phase in the 2.8 to 30.8 °C temperature range. Densities values, recalculated assuming an original 10% H_2O content at the time of trapping, range from 543 to 952 $kg \cdot m^{-3}$, and correspond to entrapment or re-equilibration pressure ranges of 500-595 MPa, 700-740 MPa, and 245-610 MPa respectively for pre-collapse, early post-collapse, and Holocene/historical eruptions. These entrapment pressures are interpreted as reflecting the existence of two main magma ponding zones at ~25 km and ~13-21 km depth, and a zone of fluid inclusion re-equilibration at 9-12 km depth. There is evidence of a complex temporal evolution of the plumbing system. Historical eruptions, and especially the three most recent ones (occurred in 1951, 1995 and 2014-25), bring fluid inclusion evidence for transient, pre-eruptive shallow (9-17 km depth) magma ponding. Early post-collapse (60 Ka) volcanics, in contrast, document fast magma transport from ~25 km, and suggest a reconfiguration of the magma plumbing system after the Monte Amarelo collapse event.

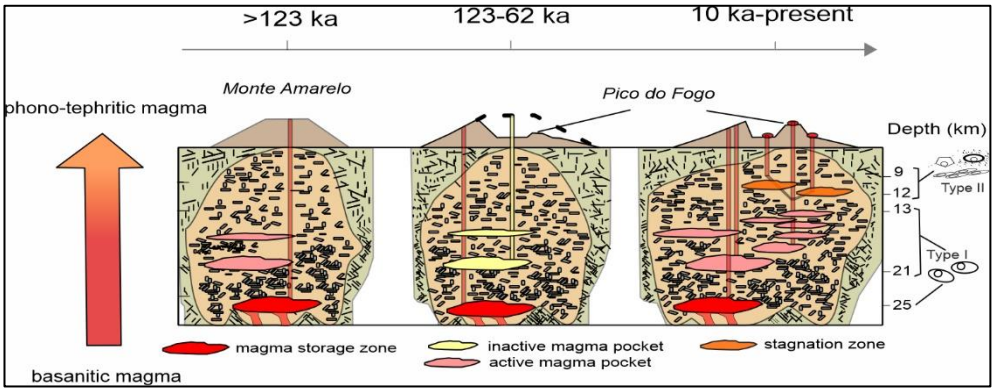

Keywords: *oceanic island volcanism, magma ascent path, basanites, magmatic system.*

5.1.Introduction

Recent geophysical, mineralogical, and geochemical results have reshaped our understanding of the trans-crustal magmatic systems below active volcanoes. The emerging view of the subsurface structures of oceanic island volcanoes is that of complex, vertically extended magma systems with multiple levels of magma storage (e.g., Cashman and Giordano, 2014; Cashman et al., 2017; Cashman and Edmonds, 2019; Edmonds et al., 2019; Sparks et al., 2019). While thermal and rheological conditions in the lower crust favour melt segregation and fractionation, upper crustal magma systems are thought to take the form of non-eruptible mushes, separated by crystallised bodies and small magma lenses (Menand, 2011). This is remarkable in case of shallow-level magma intrusions, such as those at oceanic island volcanoes (e.g., Schwarz et al., 2004; Klügel et al., 2005; Stroncik et al., 2009; Zanon et al., 2020). Under these circumstances, the lifetime of a magma system is strictly linked to magma supply rate and composition, and the stress field (Holtzman and Kohlstedt, 2007; Cooper and Kent, 2014; Parmigiani et al., 2014). In addition, the architecture of the magma system and ascent rates can vary from one eruption to another.

Understanding the architecture of a magma system is, therefore, key to modelling pre-eruptive storage conditions and ascent timescales (Cashman et al., 2017; Pappalardo and Buono, 2021), and it is of paramount importance for volcanic hazard assessment and risk mitigation. In the mush-dominated reservoir view, geophysical methods and satellite-based observations may lack the required spatial

resolution to identify melts stored in the crust (Foroozan et al., 2010; Mattioli et al., 2010; Voight et al., 2010; Biggs et al., 2014). Petrological methods, based on the post-hoc analysis of erupted rocks, are therefore invaluable in the definition of the pre-eruptive magma storage conditions and mechanisms/timescales of magma ascent. They can also be applied to probe the past temporal evolution of the plumbing system over the lifetime of the volcanic system. Fluid inclusions microthermometry is especially suited for this scope, as it provides information on pressure of fluid trapping and/or re-equilibration, which occurs during magma ponding, and hence the depths of pre-eruptive magma storage across multiple ponding levels (Hansteen et al., 1998). The concept of fluid inclusion assemblages (Goldstein, 2003) is useful, as it includes in the interpretation a large population of inclusions with the same composition, which have been trapped at the same environmental conditions. The interpretation of single fluid inclusion might be biased by a complicated post-entrapment history.

In magmatic environments, fluid inclusions are bubbles of exsolved magmatic volatiles that are trapped in crystallographic defects during crystal growth, or during re-equilibration (Bodnar, 2003). Upon cooling, these fluids can undergo phase separation to vapour or liquid (Bodnar, 2003). The analysis of their composition and texture reveals different periods of formation and/or re-equilibration, which are barometrically constrained by the microthermometric study of phase changes of the fluid trapped.

Here, the fluid inclusion microthermometry has been used to characterise the crustal magma system of Fogo Volcano (Cape Verde archipelago), one of the most frequently erupting intraplate volcanic systems on Earth (Siebert and Simkin, 2002). Previous petrological works (Hildner et al., 2011, 2012; Mata et al., 2017; Klügel et al., 2020) have used the fluid inclusions microthermometry and the clinopyroxene-melt barometry to the three most recent eruptions (1951, 1995 and 2014-15), but little information exists on the long-term stability or evolution of magma storage conditions. Our aim is to complement these previous studies by presenting new petrological, geochemical, and fluid inclusions results for lavas erupted during 11 eruptions spanning in age from ~120 ka to 2014-15. This temporal window encompasses the Monte Amarelo flank collapse, the major structural collapse event of the volcanic edifice. The architecture of the magma system of Fogo Volcano is re-evaluated through a fine-tuned study of fluid inclusions following the approach suggested by Zanon et al. (2020), that was applied to Pico Volcano in the Azores. This methodology combines the different densities (and,

hence, entrapment pressures and depths) of fluid inclusion assemblages in the hosted phenocrysts to identify the different magma ponding levels during the magma ascent.

Our novel results provide new constraints on (i) the vertical arrangement of the plumbing system beneath Fogo Volcano (e.g., the different magma storage and stagnation levels, from the deep crust/upper mantle to the surface), and (ii) the temporal evolution of plumbing system in the last 120 thousand years.

5.2.Geological setting and volcanic history

The Cape Verde archipelago (Fig. 20, inset), in the central Atlantic Ocean, stands on the Cape Verde Rise, the largest oceanic intraplate bathymetric anomaly on Earth (Wilson et al., 2013). The Cape Verde Rise marks an area of significant gravity, heat flow and anomalous seismic velocities at depth (Dash et al., 1976; Courtney and White, 1986; Wilson et al., 2013), interpreted as the surface expression of a hot-spot mantle swell (Liu and Zhao, 2014). Volcanism in the archipelago began ~26 Ma (Torres et al., 2010), and is dominated by silica-undersaturated melts of basanitic to phonolitic compositions (Gerlach et al., 1988), with rare carbonatites (Hoernle et al., 2002; Mourão et al., 2012).

Fogo Island (Fig. 20) formed and developed during the last 3-4.5 Ma, and has been the only site of volcanism since the first historical report in the 1400s century, with at least 28 recorded eruptions (Ribeiro, 1954; Torres et al., 1997). Historic activity concentrated on and around Pico do Fogo (Fig. 1), a steep cone formed inside Chã das Caldeira, a ~8 km wide semi-circular depression resulting from the flank collapse event of the Monte Amarelo Volcano, which has been dated at ~73 ka (Day et al., 1999) to 62-123 ka (Foeken et al., 2009). The volcanological evolution of Fogo includes four eruptive phases:

1. The Ribeira de Almada Group: carbonatitic and alkali-rich mafic submarine lavas dated at ~4.5 Ma (Foeken et al., 2007, 2009);
2. The Monte Barro Group: the first sub-aerial lavas of unknown age;
3. The Monte Amarelo Group (no absolute chronology): a ~2-3 km thick succession of highly alkaline mafic to intermediate lavas, emplaced before the lateral collapse of the volcano;
4. The Chã das Caldeira Group: the youngest eruptive phase, subdivided into the Pico do Fogo and Monte Orlando formations (Foeken et al., 2009). The former includes the volcanic products emplaced during protracted summit/central activity at Pico do Fogo, in between the

Monte Amarelo collapse and the 1785 eruption (Ribeiro, 1954). The Monte Orlando formation includes fissure-fed effusive eruptions concentrating along the Pico do Fogo flanks, from the 1700s century onward (Day et al., 2000). These eruptions clustered along N-S trending fissures/fractures, except for the 1995 and 2014-15 eruptions, that occurred on Pico do Fogo's south-western flank.

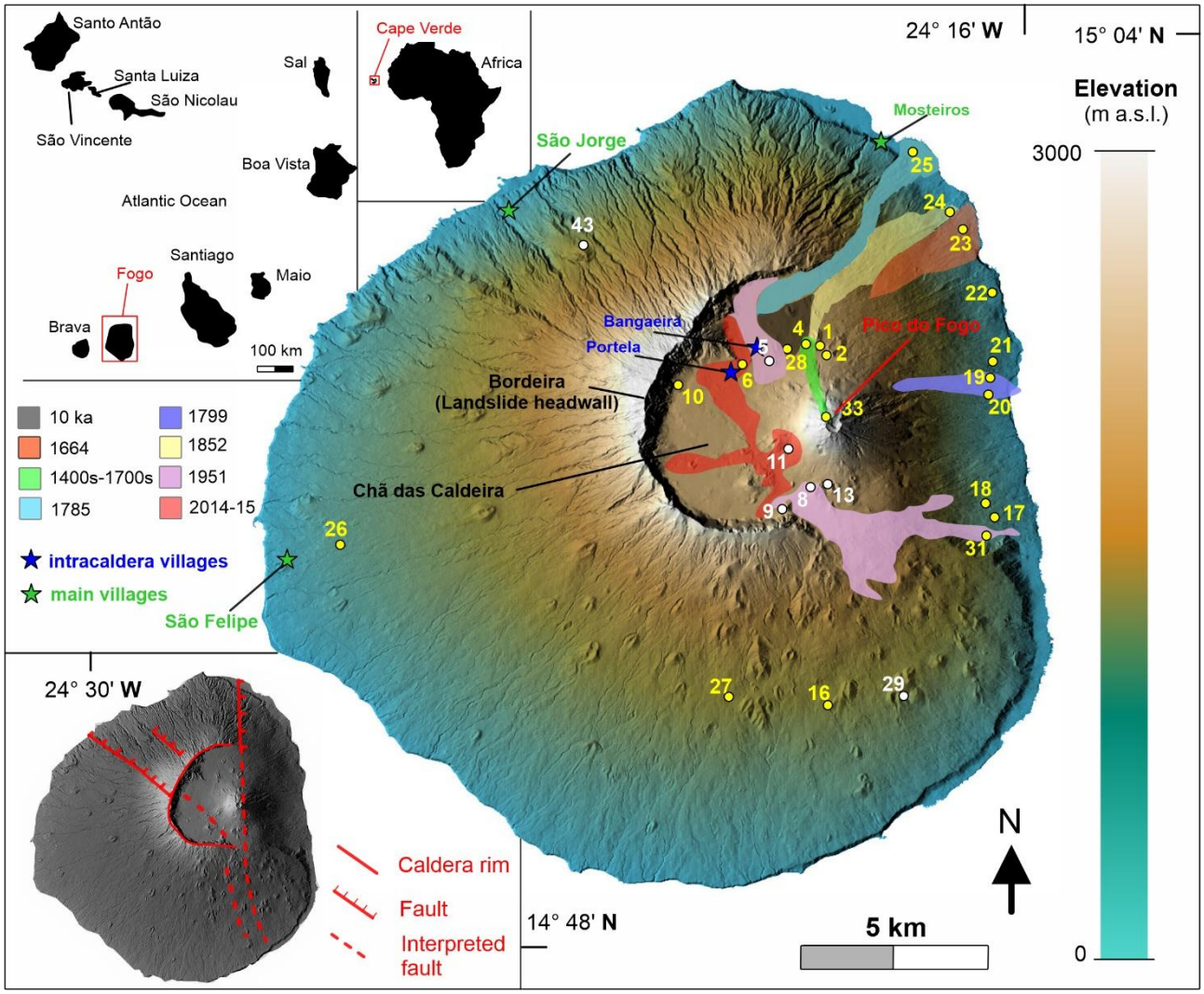

Figure 20 Digital elevation map of Fogo Island (modified from: Official SketchFab internet site, managed by the Volcanology and Petrology lab's 3D models, Department of Geology and Geography, West Virginia University), showing sampling sites of lavas (yellow numbers) and pyroclastic deposits (white numbers). The studied eruptions are mapped from satellite images available from Google Earth and existing geological maps (Torres et al., 1997; Carracedo et al., 2015). Insets show the position of the Cape Verde archipelago (top, right), Fogo Island (top, left) and the main fault systems (bottom, left) (Day et al., 1999; Martínez-Moreno et al., 2018).

5.3.Materials and methods

Twenty-seven rock samples spanning the last 120 ka of volcanic activity, were studied (Figure 20, Supplementary Data Table 1). Five of them are extra-caldera lavas and proximal tephra fall deposits with ages from ~120 to ~10 ka (Foeken, 2009; Carracedo et al., 2015), and 22 are Holocene-historical intra-caldera samples (17 lava flows and 5 tephra deposits).

Whole-rock major element compositions were measured in 21 samples (Supplementary data 2) with a Perkin Elmer 9000 inductively coupled plasma-mass spectrometer (ICP-MS) at Activation Laboratories (Actlabs), Ontario, Canada. Alkaline dissolution with lithium metaborate/tetraborate, followed by nitric acid, was used on 1 g of rock powders before fusion in an induction furnace. The melt was poured into a solution of 5% nitric acid containing cadmium as an internal standard and stirred until complete dissolution. The analytical precision is better than 5% for all major elements.

Petrographic study and modal analysis were conducted on 21 thin sections, representative for 16 eruptions (Supplementary data 3) with a semi-automated digital point counter at the Instituto de Investigação em Vulcanologia e Avaliação de Riscos (IVAR), Ponta Delgada, Portugal.

For the study of fluid inclusions assemblages (FIAs), rocks were coarsely crushed and then sieved to separate grainsize populations in the 250-4000 μm range. For each sample, about 200 olivine and 200 clinopyroxene phenocrysts were hand-picked from the grainsize fractions. Crystals were doubly polished with silica carbide paper and alumina to attain a maximum thickness of 80-100 μm for olivine and 60-70 μm for pyroxenes. About 0.7 % of investigated olivine and 0.3 % of clinopyroxene contain FIAs, these were separated for a microtextural study, inclusions mapping and microthermometry analysis.

Electron microprobe analyses on olivine and pyroxene crystals and groundmass were carried at the CAMPARIS centre (University of Paris La Sorbonne, France), using a CAMECA SX-Five electron microprobe, equipped with five WDS spectrometers and an EDS detector. Seventeen olivine crystals, 14 pyroxenes crystals and 16 fragments of groundmass were analysed, with a 15-kV accelerating voltage and a 20 nA current beam, with counting times from 10 to 20 s on the peak. We checked the accuracy against the San Carlos Olivine international standard. The relative errors are <6.5% for Ni and Mn, <5% for Fe and Ca, and <1% for Si and Mg.

Two olivine and two clinopyroxene compositional data (Supplementary data 4) coupled with groundmass electron microprobe analysis were used to estimate the magma temperature by applying the olivine-liquid geothermobarometer of Putirka et al. (2007) (eq. 4) and the clinopyroxene-liquid geothermobarometer of Putirka (2008) (eq. 33). We tested the chemical equilibrium hypothesis using the Rhodes diagram (Rhodes et al., 1979) and the observed (Kd $(Fe\text{-}Mg)_{ol\text{-}liq}$ = 0.26 ±0.02; Kd $(Fe\text{-}Mg)_{cpx\text{-}liq}$ = 0.27 ±0.01) and equilibrium (Kd $(Fe\text{-}Mg)_{cpx/olv\text{-}liq}$ = 0.27 ±0.03) Fe-Mg exchange coefficients were in close agreement.

Microthermometry data were measured on 2691 inclusions (from a selection of 15 samples from 11 eruptions; Table 3) using a Linkam MDSG600 heating-cooling stage, at the Instituto de Investigação em Vulcanologia e Avaliação de Riscos (IVAR), Ponta Delgada, Portugal. The stage was calibrated using synthetic fluid inclusions of pure CO_2 and H_2O. A heating rate of 0.2-0.5 °C/min was used, resulting in a ±0.1 °C accuracy during melting and homogenisation. Density values for pure-CO_2 fluid inclusions were derived from measured homogenisation temperatures (Th) using equations 3.14 and 3.15 in Span and Wagner (1996). The equation of Sterner and Bodnar (1991) was used to calculate the densities of fluid inclusions, after the correction suggested by Hansteen and Klügel (2008) that accounts for the pristine presence of a maximum 10% molar volume of H_2O in the fluid inclusions during their formation (CO_2:H_2O ratios of 9:1). We use this correction to account for the fact that, at the time of trapping, the fluid may also have contained some H_2O (Hansteen and Klügel, 2008). This water was lost upon cooling by diffusion (Barth et al., 2019; Frezzotti et al., 2012). Previous work in intraplate magmatism context (Dixon and Stolper, 1995; Hansteen and Klügel, 2008) supports this 10 mol% H_2O upper limit for the FIAs trapped at upper mantle conditions.

Isochores, which are based on fluid density and composition, and hosted mineral composition, allows the derivation of fluid trapping pressure at assumed or calculated temperature. The FLUIDS software (Bakker, 2003) was used for isochores calculation.

5.4.Results

All studied samples are nepheline-normative (8.4 - 25.4 %) basanites (SiO_2 = 41.08-44.26 wt%; K_2O + Na_2O= 2.99-9.35 wt%), forming an evolution trend towards the foidite field in the TAS diagram (Fig. 21a). A single lava contains up to 45 vol% of mafic phenocrysts as cumulate phases and, therefore, plot close to the boundary with picrites (SiO_2 = 41.53 wt%; K_2O + Na_2O = 2.99 wt%).

Basanites are porphyritic (vesicle-free, average 67.8 vol% phenocrysts), with the common mineral assemblage represented by clinopyroxene, olivine, plagioclase, and Fe-Ti oxides. Amphibole is rare, but it is present in the last three eruptions and has decomposition rims of variable thickness (from 100 μm to amphibole total decomposition). The microcrystalline groundmass (<50 μm) is intergranular and is made up of dominant plagioclase, with lesser olivine and clinopyroxene. The two alkali-rich lavas are poorly porphyritic (13.3 and 4.1 vol%), with microphenocrysts (in the 50-500 μm size range) of clinopyroxene, olivine, plagioclase, and Fe-Ti oxide. The crystal-rich lava (vesicle-free, ~37.3 vol% phenocrysts) is characterised by 10.8 vol% clinopyroxene phenocrysts that occur as pinkish, Ti-rich, patchy zoned phenocrysts (and pale green phenocrysts), set in a groundmass of plagioclase, olivine, and Fe-Ti oxides.

The studied clinopyroxene are compositionally diopside (Wo_{49} En_{32} Fs_{11} to Wo_{52} En_{40} Fs_{15}) except a single augite crystal (Wo_{33} En_{42} Fs_{26}) (Fig. 21b). Clinopyroxene phenocrysts show a wide Al_2O_3 range (5.64-14.19 wt%), while TiO_2 (2.44-5.89 wt%) and Na_2O (0.37-2.38 wt%) are somewhat less variable. The Mg# ranges from 62 to 79. Olivine phenocrysts have forsterite contents ranging from Fo_{77} to Fo_{84}. Olivine are low in CaO (0.28-0.38 wt%), and NiO varies from 0.04 – 0.13 wt.%, (Supplementary data 4).

Table 3. Summary of microthermometry results for FIAs in olivine (top) and clinopyroxene (bottom). Owing to the large microthermometric dataset results are presented as ranges for individual eruptions, rather than data for individual inclusions. The calculation of isochores used a magmatic temperatures of 1133 °C and 1134 °C from clinopyroxene and olivine thermometry respectively. Corresponding depths are derived using a reference crustal model (see text). Uncertainties on individual calculations of densities are ±1 kg·m^{-3}, for Th < 25 °C and ±2 kg·m-3, for Th >25 °C. Whereas for the derived pressures, uncertainties are ±5-8 MPa, for fluid densities in the 500-700 kg·m^{-3} range and ±8-15 MPa in the 700 to 900 kg·m^{-3} density range.

olivine

Sample ID	eruption	Number of analysed crystals	Number of measurements	Homogenization temperature Th_L (°C)	Density (kg·m^{-3})		Density H_2O-corrected (kg·m^{-3})		Pressure (Mpa)	depth (km)
					Type I	*Type II*	*Type I*	*Type II*		
Fog 26	120 ka	2	85	15.6-22.6	744-814	/	778-853	/	497-595	16.2-19.5

Fog 27	60 ka	3	73	2.8-3.7	904-910	/	946-952	/	700-740	23.0-24.3
Fog 28	10ka intracaldera	2	125	21.6 – 27.1	675-755	/	706-790	/	405-510	13.1-16.7
Fog 43	10ka extracaldera	2	198	13.4-30.8	802-835	537-651	839-873	561-680	260-625	9.8-20.5
Fog 23	1664	3	238	11.9-20.6	767-847	/	802-886	/	540-640	17.7-21.0
Fog 4, 33	1400s-1700s	5	370	16.5-23.1	672-808	659-665	702-845	689-696	390-585	12.8-19.2
Fog 25	1785	1	20	29.9-30.9	/	520-600	/	543-627	245-315	9.2-10.3
Fog 19, 20	1799	7	191	18.8- 30.8	667-787	596-659	698-822	623-689	311-554	11.7-18.2
Fog 24	1852	2	61	15.2-29.9	799-825	598-668	836-863	625-699	315-600	11.8-19.7
Fog 5,8,31	1951	7	587	21.9-30.8	656-753	537-647	686-787	561-676	305-510	11.5-16.7
Fog 11	2014-15	2	169	26.6 – 30.2	663-689	586-647	693-721	613-676	305-425	11.5-13.9

clinopyroxene

Sample ID	**eruption**	**Number of analysed crystals**	**Number of measurements**	**Homogenization temperature Th_L (°C)**	**Density H_2O-uncorrected (kg·m^{-3})**		**Density H_2O-corrected (kg·m^{-3})**		**Pressure (Mpa)**	**depth (km)**
					Type I	*Type II*	*Type I*	*Type II*		
Fog 23	1664	2	55	26.9-29.5	672-679	615-647	703-710	643-676	340-420	11.9-14.7
Fog 4,33	1400s-1700s	2	90	30.2-30.7	/	554-583	/	579-610	280-308	9.8-10.8
Fog 25	1785	3	177	29.6-30.2	/	583-611	/	610-639	308-340	10.8-11.9
Fog 19,20	1799	2	151	28.8-30.8	/	537-636	/	561-665	265-366	9.3-12.8
Fog 5, 31	1951	2	188	29.8-30.9	/	520-604	/	543-631	248-330	8.7-11.5

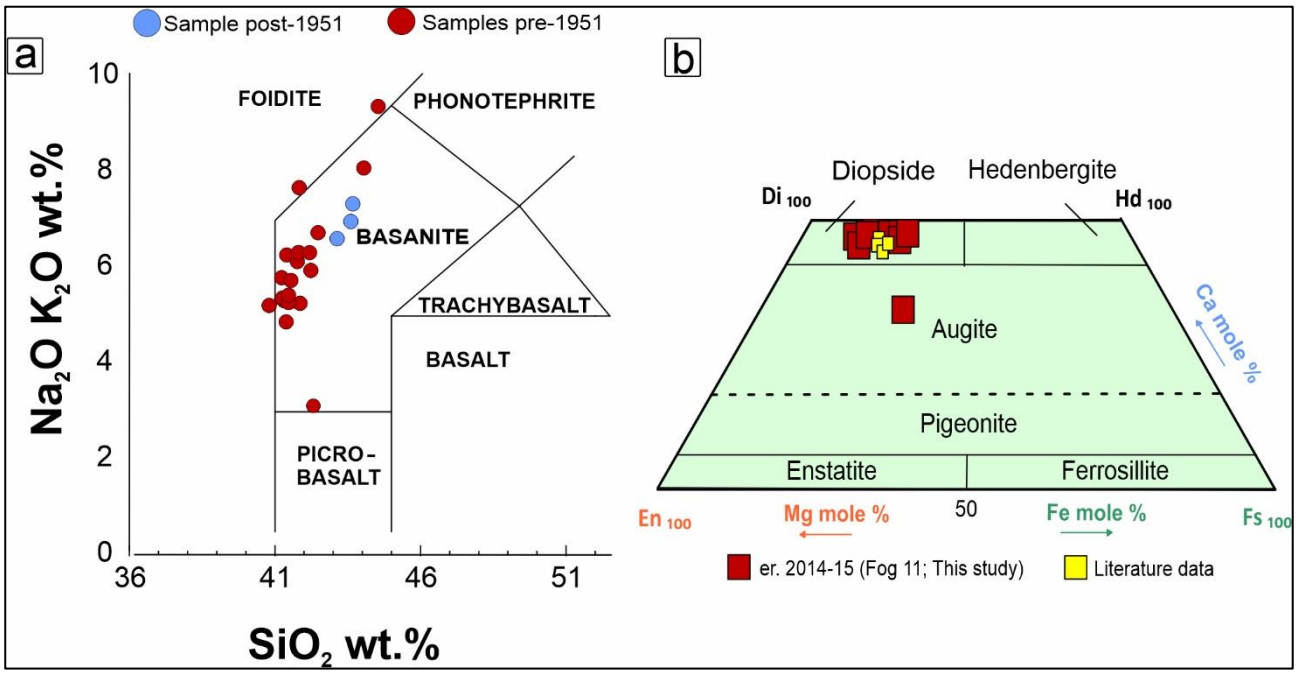

Figure 21 Total alkali-silica (TAS) diagram (a) and pyroxene quadrilateral classification (b). Literature data are from Mata et al., (2017). All pyroxene analyses were conducted on sample Fog 11 from the 2014-2015 eruption.

5.4.1. Petrography of FIAs

Both olivine and pyroxene phenocrysts trapped FIAs, while megacrysts (> 1000 μm) are devoid. Fluid inclusion diameters are variable (up to 41 μm) and commonly around 5–10 μm. Below the temperature of homogenisation (Th= 2.8-30.8 °C) all fluid inclusions are two-phase (L + V), with liquid volume being more abundant than vapour (L_V). Fluid inclusions do not contain visible daughter minerals or co-trapped minerals.

Shapes range from negative-crystal to elliptic as a function of their formation dynamics; the early-stage fluid inclusions, entrapped during crystal formation and growth, exhibit rounded/semi-rounded shapes, whereas late-stage inclusions, which result from re-equilibration processes of the fluid, have elliptic shapes. Here, we follow the textural criteria in Zanon and Frezzotti (2013) to distinguish between early (Type I) and late (Type II) stage inclusions. Type I inclusions (Fig. 22a) are isolated or occur in small clusters, and their texture shows no evidence of decrepitation. Type II inclusions (Fig. 22b) are present in linear trails along healed fractures and have likely experienced volume stretching and/or leaking. Evidence of partial or total density re-equilibration includes a visible black border surrounding the inclusions, and radial short cracks, generated by decrepitation near the

inclusion (Fig. 22c). Type II fluid inclusions are more abundant, with Type II to Type I proportions of about 4:1 in olivine phenocrysts and 5:1 in clinopyroxene phenocrysts.

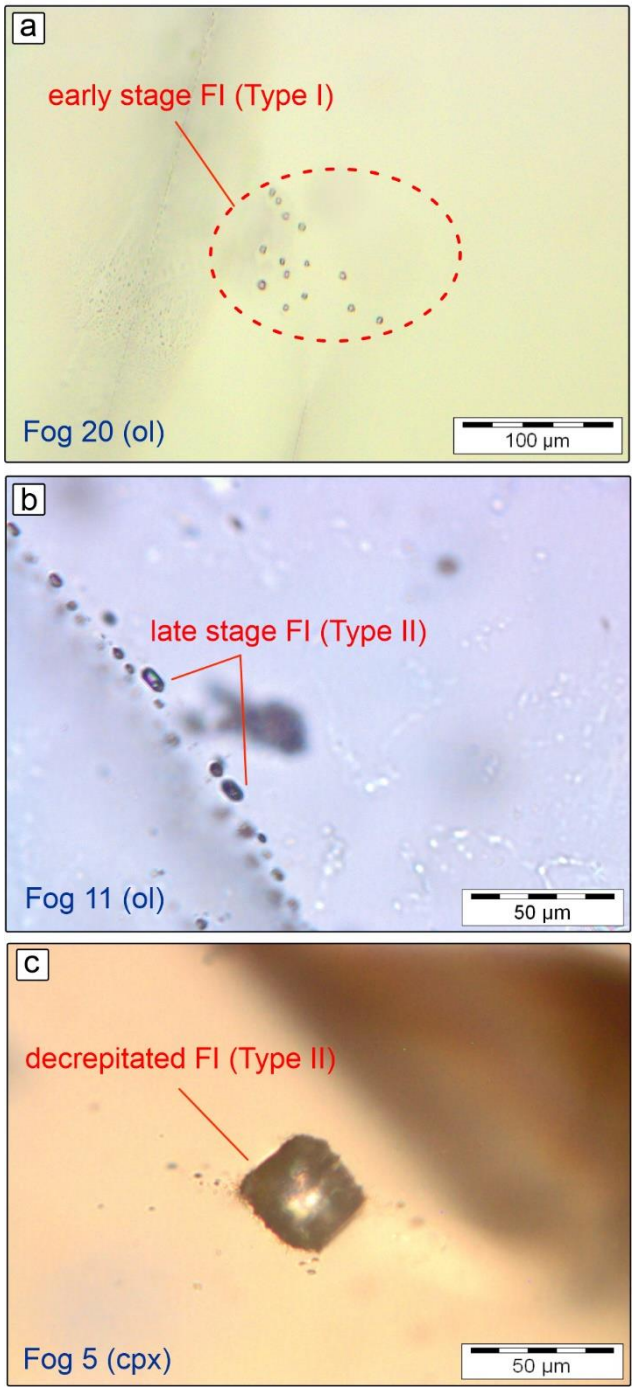

Figure 22 Photomicrographs of texturally different fluid inclusions hosted in olivine and clinopyroxene. (a) Cluster of Type I rounded fluid inclusions. (b) Type II elliptic fluid inclusions along trails. (c) Isolated decrepitated fluid inclusion with squared/irregular shape, surrounded by visible microfractures.

5.4.2. Microthermometry of FIAs

About 2700 fluid inclusions (an average of 68 fluid inclusions for each olivine and 51 for each clinopyroxene), hosted in 36 olivines and 11 clinopyroxenes, were analysed. On cooling, nearly all inclusions froze between -80 and -105 °C, and melted at T_m = -56.6 ±0.1 °C, which characterises a pure CO_2 fluid composition (Wilmart et al., 1991). Upon heating, inclusions homogenised to the liquid phase in a range of temperatures (Th_L) from 2.8 to 30.8 °C, corresponding to densities between 952 and 543 kg·m^{-3} (uncertainty in density calculation, is on average 5.0%). No inclusion homogenising to the vapour phase has been found, indicating a lack of low CO_2 density inclusions. 136 inclusions in two olivine of sample Fog 20, melted between -58.1 and -56.8 °C, showing micromole amounts of other volatile species. These inclusions homogenized to a liquid phase in the range 19.2 to 20.3 °C and represent only a small (<5%) fraction of the analysed inclusions; for this reason, they will not be further considered.

Table 3 lists both raw (uncorrected for H_2O content) and H_2O-corrected density values. We report density ranges for individual eruptions, noting that densities values measured within individual mineral grains vary within a narrow range (± 5.0 % of the average), implying relatively homogeneous trapping histories. The analysed samples cover a prolonged temporal interval of volcanic activity that encompasses the Monte Amarelo collapse. This event marks a major turning point in the morphological evolution of Fogo Island; therefore, the following description will follow a temporal sequence, corroborated by the histograms of density distribution of Figure 23.

Pre-collapse period sample (120 ka) - Fog 26 is the only sample representative of volcanic activity before the Monte Amarelo collapse. The derived fluid inclusion densities for this eruption, as inferred from the analysis of Type I inclusions only, show a bimodal distribution, with H_2O-corrected densities ranging from 778 to 853 kg·m^{-3}.

Early post-collapse phase sample (60 ka) – The sample Fog 27 represents volcanic activity in the period immediately after the Monte Amarelo collapse. Type I inclusions show a unimodal distribution of densities (ranging from 946 to 952 kg·m^{-3}).

Holocene/historical eruptions (10 ka – 2014/15) - The density populations show polymodal and skewed distributions. Olivine and clinopyroxene trap both Type I and Type II inclusions. Densities of Type I inclusions in olivine range from as low as 686 kg·m^{-3} (1951 eruption) to as high as 886

kg·m^{-3} (1664 eruption). Type I inclusions are present in clinopyroxene from only a single sample (Fog 23; 1664 eruption) and inclusion densities are 703-710 kg·m^{-3}. Type II inclusions show densities ranging from 543 to 699 kg·m^{-3} in olivine and from 543 to 676 kg·m^{-3} in clinopyroxene.

5.5.Discussion

5.5.1. Interpretation of histograms of FIAs density populations

The frequency distribution of inclusion densities, as recorded in crystals of each eruption, reflects the conditions of magma storage/ascent before that specific event (Zanon and Frezzotti, 2013).

We have identified two texturally distinct FIAs Types (Fig. 22).

Rounded/semi-rounded, isolated Type I FIAs (Fig. 22) are commonly interpreted (Bodnar, 2003; Frezzotti and Zanon, 2013) to form in response to slow crystal growth during magma storage. The modern view of vertically extensive, complex magmatic systems (Cashman et al., 2017) imposes a heterogeneous distribution of gas bubbles and of (different populations of) crystals in a magma storage zone. Notably, a magma system can be fluxed by CO_2-rich fluids released from a deep source (Caricchi et al., 2018) which could be a possible responsible for fluid inclusions. Since gas bubbles are likely to distribute heterogeneously (and accumulate at local geometrical/rheological discontinuities; Edmonds et al., 2022), Type I FIAs are hence expected to be entrapped over a range of P-T-X conditions. This is due to the fact that magma slowly rises through the multiple (staked) magma lenses that make a vertically extensive magma system, Type I FIAs can undergo re-equilibration (to lower densities) due to decompression, generating internal fluid overpressures (non isochoric ascent path; Frezzotti et al., 2004). During prolonged magma ponding this re-equilibration process involves all the FIAs which are now reset to the new pressure conditions of the shallower magma storage zone, thus loosing memory of deeper entrapment conditions. Ultimately, several distinct populations of Type I FIAs can be found in different mineral grains of a sample, whose density distributions reflect the multiple, over-imposed regions of magma storage. The depth interval recorded by each Type I FIA populations has a geo-volcanological meaning (e.g., it corresponds to specifics level of transient magma storage) if it is recurrently observed in several eruptions.

The second typology of FIAs – Type II – are texturally identified as trails of inclusions aligned along crystal fractures. At Fogo, these Type II FIAs record lower densities (Fig. 23). They therefore form upon further magma ascent and decompression, as large fluid overpressures develop in Type I inclusions, causing them to decrepitate and fail. Healing of microcracks caused by fluid overpressure

during magma decompression is therefore the dominant mode of Type II fluid inclusion formation (Roedder, 1984). Crystal fracturing/regrowth during decompression-driven magma ascent and degassing, and/or during magma mixing, inherently contribute to Type II FIA formation.

The ultimate effect of the multiple events of fluid redistribution (described above) is the generation of several FIA populations, as evidenced by complex polymodal density curves (Fig. 23). Joint interpretation of a set of polymodal density distributions, obtained for several eruptions which occurred over short activity periods (Fig. 23), potentially offer the opportunity to identify geological discontinuities at depth (Zanon et al., 2020).

The density distributions for the Fogo eruptions studied are variable, and range from (i) sharp, narrow, and unimodal (e.g., ~60 ka eruption), to (ii) broad, negatively skewed, and unimodal (e.g., 1799 eruption), and (iii) complex and polymodal (e.g., ~120 ka eruption). These observations suggest that the conditions of magma storage, and the rates and modes of magma ascent (that control FIAs re-equilibration), are distinct for each eruption. Overall, the highest density values are observed for the early post-collapse (~60 ka) eruption (Fog 27; 946-952 $kg \cdot m^{-3}$), and lowest for the 2014-15 eruption (693-721 $kg \cdot m^{-3}$).

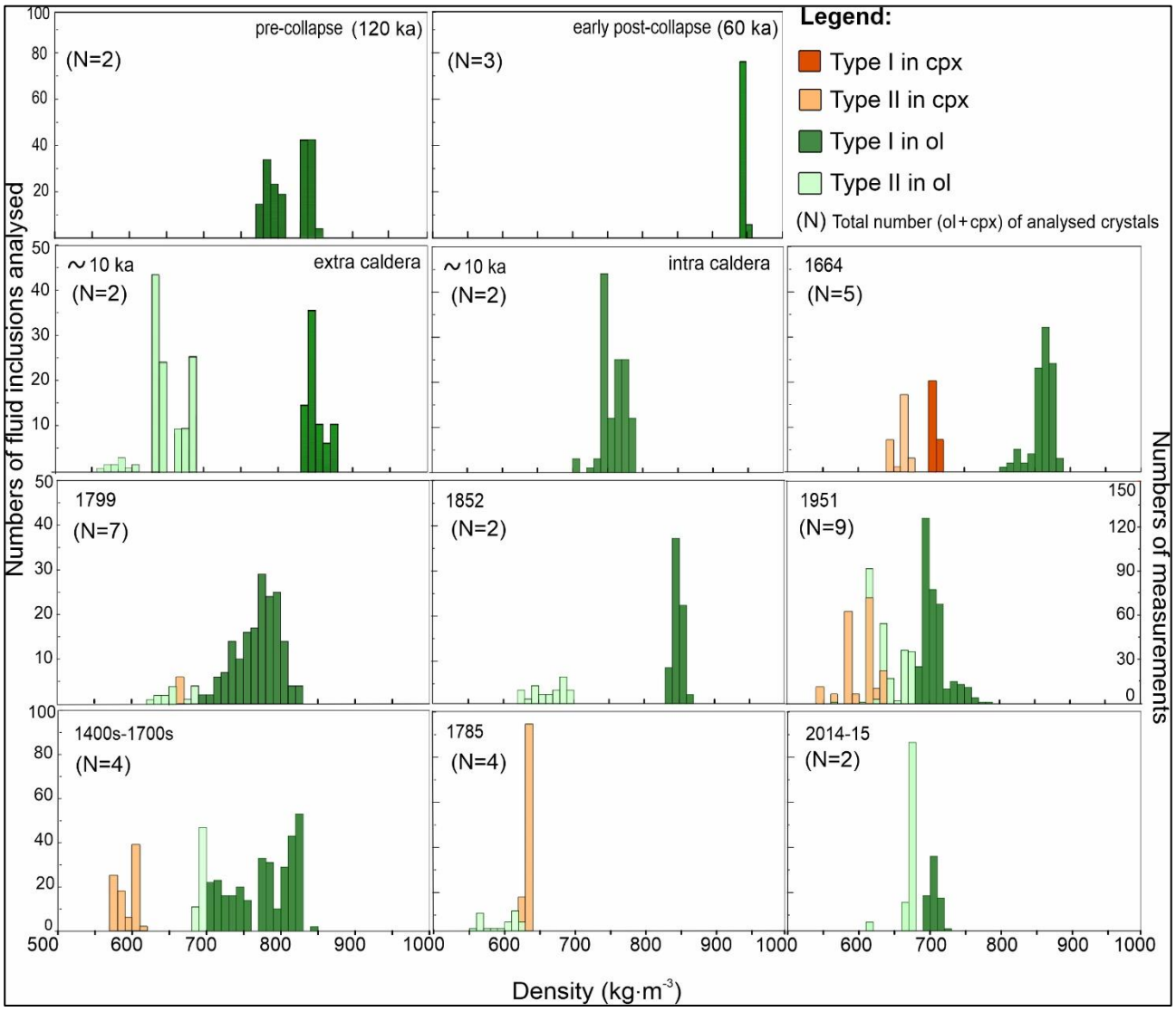

Figure 23 Histograms of fluid inclusion densities (H_2O-corrected) for the eruptions studied. Barometric results for olivine-hosted fluid inclusions (dark green: Type I; light green: Type II) and clinopyroxene-hosted fluid inclusions (red: Type I; orange: Type II) are shown. These histograms show variable density frequency distributions, ranging from sharp and unimodal (e.g., the ~60 ka early post-collapse eruption) to complex and polymodal (e.g., pre-collapse, ~120 ka), implying distinct conditions of magma storage and ascent. The highest density values are observed for the Monte Amarelo post-collapse eruption (~60 ka) and the lowest for Fogo's most recent eruption (2014-15).

We additionally find the densities of FIAs trapped in clinopyroxene are always lower than in olivine. This is consistent with the common observation (Hansteen et al., 1998; Galipp et al., 2006) that FIAs in clinopyroxene undergo faster re-equilibration (than olivine), potentially in response to the presence of two planes of weakness (cleavage). We cannot exclude, however, that the lower densities recorded by FIAs in clinopyroxene merely reflect a late (and shallower) crystallization of this mineral phase.

The only exception is represented by the 1785 eruption, whose lavas carry frequent but (dominantly) fluid inclusion-free olivine.

5.5.2. Entrapment pressures and depths

The H_2O-corrected densities have been converted into pressures (Table 3) of inclusion entrapment and/or re-equilibration (Fig. 24) from isochore calculations at the temperature of olivine and pyroxene crystallisation. These temperatures have been obtained using the olivine-liquid and clinopyroxene-liquid geothermometers (Putirka, 2008, eq. 33 and Putirka et al., 2007, eq. 21). The two geothermometers provide the same temperature ranges (i.e., 1133 ±26 °C for the clinopyroxene-melt and 1134 ±10 °C for the olivine-melt geothermobarometer). We note that uncertainties on temperature estimation have a minor influence on calculated pressures: a ±20 °C temperature uncertainty converts into 1-2% change in calculated fluid inclusion pressures.

Converting pressures into depths (Table 3) requires a reference model for the crustal structure, including the location of the upper mantle-crust transition underneath the volcano. Here, the interpretation of geophysical data generated contrasting models. Large changes in V_P/V_S have been recognized at depths of 12±1 km (Vinnik et al., 2012; Pim et al., 2008; Wilson et al., 2013) and 30 km (Vinnik et al., 2012). Basing upon these depths, it is possible to hypothesize that the first 12 km consists of lavas and small intrusive bodies being part of the oceanic crust with a density of 2700 $kg \cdot m^{-3}$ (Carlson and Raskin, 1984). The rocks up to 30 km depth should be part of the deeper magma system of the volcano, formed by ultramafic cumulates, crystal mushes and/or mantle lithologies (Cooper et al., 1992; Tenzer et al., 2013). For these rocks a general density of 3100 $kg \cdot m^{-3}$ was assumed. The Figure 24 shows the resulting pressure estimates. The entrapment pressures from 248 to 740 MPa suggests that Fogo magmas coexist with a CO_2-dominated fluid phase throughout their entire ascent path, in agreement with the low CO_2 solubility in silicate melts (Métrich and Wallace, 2008). There is a good matching with literature data for the last three eruptions for the shallow magma systems (Fig. 24). However, there is also a deep level of entrapment of FIAs (>500 MPa), providing independent support for a deep magma storage zone (at 17-25 km) that had so far been only identified by cpx-melt geothermobarometry (Hildner et al., 2011, 2012; Klügel et al., 2020).

The following paragraphs describe the distinct entrapment conditions for pre-collapse, early post-collapse and Holocene-historical eruptions.

5.5.2.1.Pre-collapse phase (~120 ka eruption)

There are two narrow FIAs entrapment pressure intervals at 557-595 MPa and 497-529 MPa, corresponding to olivine growth. These data therefore show the existence of magma storage areas at depth of ~19±0.9 km and ~17±0.7 km. These depths closely match the shallowest to intermediate portions of the 17-25 km deep magma storage zone identified in the literature. Notably, there is no evidence FIAs entrapment/re-equilibration at depths less than 17 km, suggesting a rapid magma ascent through the upper crust.

5.5.2.2.Early post-collapse phase (~60 ka eruption)

The FIAs in olivine record entrapment pressures from 700 to 740 MPa, the deepest so far obtained for this volcano using fluid inclusions. These correspond to inferred entrapment depths of 23.7 ±0.9 km, and therefore to the roots of the 17-25 km deep magma storage zone already identified in literature.

5.5.2.3.Holocene/historical activity (≤ 10 ka to 2014-2015 eruption)

The FIAs in olivine record a range of entrapment pressures from 245 to 640 MPa which are lower than those of the early post-collapse (Fig. 24). Type I FiAs provided entrapment pressures between 384 and 640 MPa, suggesting that these recent eruptions have been fed by magma which ascended from a depth of ~13 to ~21 km. Type II FIAs in clinopyroxene (Fig. 24) record shallower entrapment conditions of 248 to 380 MPa, corresponding to depths from 9.4 to 12.5 km.

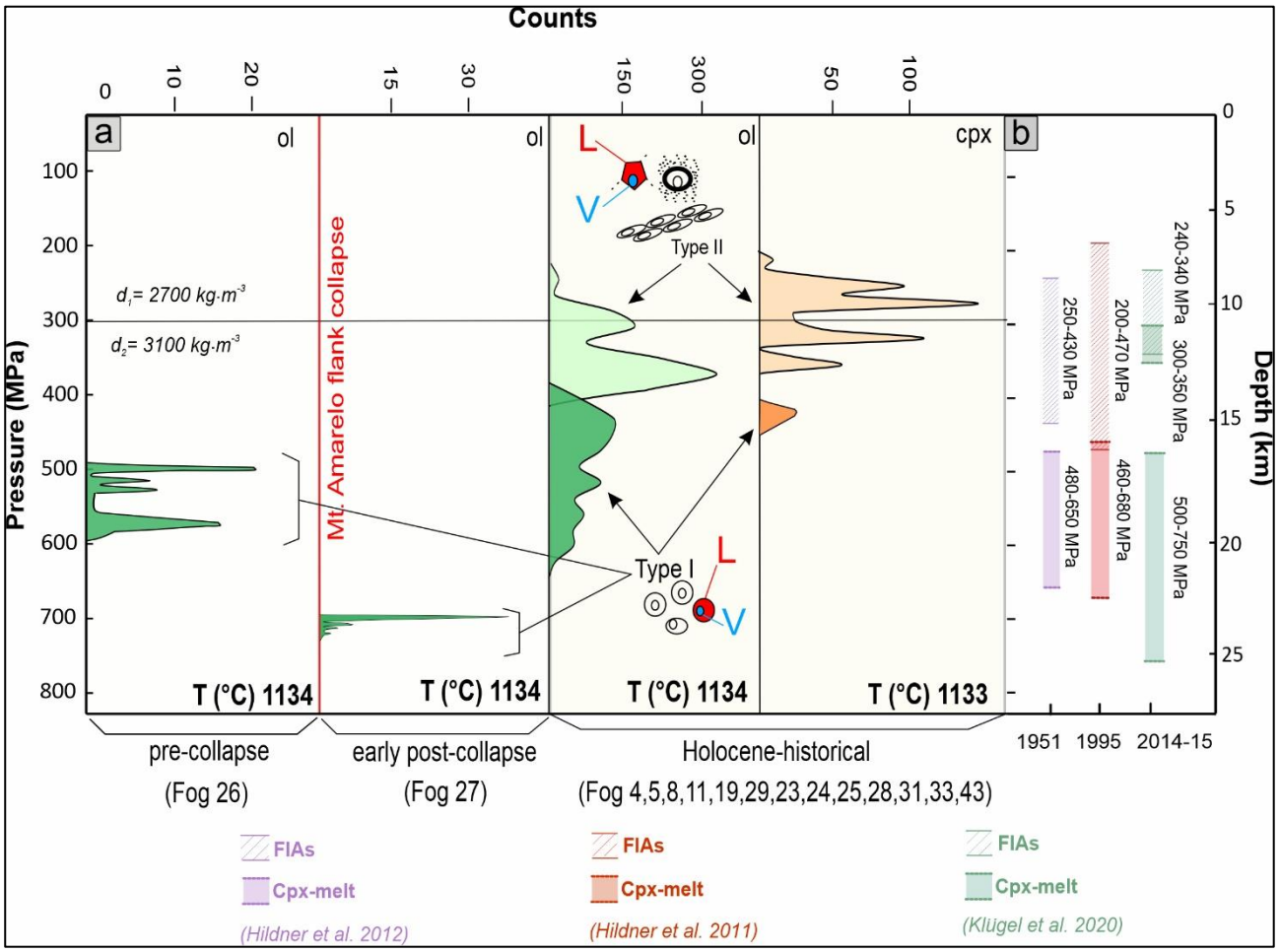

Figure 24 (a) FIAs entrapment/re-equilibration pressures (and corresponding depths). (left), pre-collapse eruption; (centre), early post-collapse eruption; (right) Holocene-historical eruptions (green, olivine-hosted; orange, clinopyroxene-hosted; dark tones, Type I fluid inclusions; light tones, Type II fluid inclusions; schematic representations of Type I and Type II fluid inclusions, in both the two different fluid phases (Liquid, L and Vapour, V) are signed by red (L) and light blue (V) colours). The melt temperatures are derived with different geothermobarometers (see text) and are used to convert density values in trapping pressures. The highest pressures are recorded in an early post-collapse eruption (~60 ka). Type II fluid inclusions identify a low-pressure region where magma ponded for a short time and where inclusions re-equilibrated before the final ascent to the surface and is only detected Holocene-historical eruption. The thin horizontal black line shows the boundary between two layers of the stratigraphic model underneath Fogo (see text) characterised by different densities (d_1 and d_2). (b) Comparison with literature data (Hildner et al., 2011, 2012; Klugel et al. 2020).

5.5.3. Temporal evolution of the magma plumbing system

These results help refining the current understanding of the architecture of the magma system underneath Fogo Volcano. This large fluid inclusion dataset can help to better understand if, and to

what extent, such conditions of pre-eruptive magma storage and ascent have evolved through time at this volcano.

Some FIAs entrapment pressure/depth intervals recur in distinct eruptions spanning thousands of years (Fig. 25). These depth intervals are interpreted as magma accumulation zones in the inner structure of the volcano which are stable through time. The deepest of these magma storage regions (23.7 ±0.9 km) is only recorded by the olivine-hosted FIAs in the ~60 ka early post-collapse lavas. The difference with the pre-collapse lava sample suggests some re-organisation of the magma system after the Monte Amarelo collapse event, as previously found (Hildner et al. 2012). We argue that the formation of deep faults, as commonly observed in response to lateral collapse events (Amelung and Day, 2002), may have contributed to a fast withdrawal of deeply stored magmas. Rapid magma ascent (in addition to the possible disruption of any existing shallow magma reservoirs) would have reduced the possibility for further FIAs entrapment/re-equilibration, ultimately determining the absence of shallow pressure records in fluid inclusions for this eruption (Fig. 25). Post-collapse re-activation of deep reservoirs is indeed not unique to Fogo, but rather a recurrent feature at other oceanic volcanoes, such as El Hierro (Carracedo et al., 1999; Manconi et al., 2009) and La Palma (Galipp et al, 2006) in the Canary Islands, and Piton de la Fournaise at La Reunion island (Lénat and Bàchelery et al., 1990). The lack of lower pressure entrapment conditions in the FOG 27 olivine confirms little or no shallow crustal processing/stalling of magma in the early post-collapse phase (at ~60 ka eruption). This contrasts with the more recent historical eruptions that have more shallow crustal stalling/processing (see below).

Type I inclusions in olivine from the pre-collapse eruption and from Holocene-historical eruptions identify two major magma ponding regions (dark to light-dark green areas in Fig. 25) in the ~13 to ~19 km depth interval. The deepest level (dark green) is recorded in the Monte Amarelo products and in four Holocene-historical eruptions. The shallower ponding region begins at a depth of ~17 ±0.7 km for the eruption of 120 ka; at ~15.5 ±2.9 km depth in Holocene-historical eruptions (~10 ka intra caldera, 1400s-1700s, and 1799); and at ~15 ±2.4 km depth in the 1951 and 2014-15 eruptions. This latter depth (~14 ±0.3 km) is also shown by data in clinopyroxene phenocrysts. These two regions are interpreted as portions of a vertically extended magma system, in which multiple, distinct magma ponding zones exist that are repeatedly tapped/re-activated during individual eruptions (Fig. 26). As cpx-melt geothermobarometry shows a deeper (17-25 km) source for the most recent historical eruptions, these levels from ~13 to ~19 km should be interpreted as intermediate regions where

magmas undergo prolonged ponding, crystallization and degassing, thus entrapping fluid inclusions in a exsolved fluid-rich magmatic environment. We cannot exclude that deeply formed (> 21 km) fluid inclusions exist whose density resets to lower values during decompression/temporal storage in the ~13-19 km depth range. Notably, these magma processes, absent in the early post-collapse ~60 ka eruption, have been at work since ~10 ka at least, and have remained a recurrent feature of Fogo activity from there onward.

Type II inclusions, both in olivine and clinopyroxene phenocrysts in all Holocene-historical eruptions, record depths of 9-12 km (light green in Fig. 25). We interpret this region as a portion of the magma system where the originally trapped fluid inclusions (Type I) undergo density re-equilibration, leading to fluid redistribution along crystal fractures, ultimately forming trails of (Type II) fluid inclusions. There are multiple causes that can determine such re-equilibration, including crystal fracturing and re-growth driven by de-compressional degassing during magma ascent, and/or by mixing of chemically/thermally distinct magma batches/lenses (Neave et al., 2021). Ultimately, re-equilibration takes place in response to crystals experiencing (upon ascent) lower external pressures relative to the initial fluid internal isochoric conditions (Frezzotti et al., 2004). Whatever the cause, the presence of Type II FIAs in Holocene/historic eruption – and their absence in older ones - reflects slower magma ascent rates, as longer residence times in the 9-12 km region are necessary for inclusion re-equilibration to occur (Zanon et al., 2020). At the very end of the spectrum of possible processes, formation of Type II FIAs may reflect short-lived stagnation events at 9-12 km depth taking place during magma ascent. In any case, our results would suggest that the growth of the Pico do Fogo cone, during protracted historical activity, has been associated with less direct ascent from the deep- to mid-crust than in the early post-collapse phase. There is no evidence for magma stagnation at depths <9 km (Fig. 24,25), excluding any role played by shallow sin-eruptive magmatic processes in FIAs re-equilibration.

Overall, the 1951, 1995 and 2014-2015 eruptions show an apparent upward migration of magma storage regions (Fig. 25). These three eruptions additionally show more prolonged re-equilibration events at <12 km than in older analysed samples (as indicated the relatively abundant Type II inclusions). Assuming, from literature data (Klügel et al., 2020), that the erupted magmas were initially sourced in reservoirs at 17-25 km, our results concur to suggest pre-eruptive prolonged stalling of magmas starting from 17 km. Such longer residence times in the oceanic crust would be

consistent with the slightly evolved nature (SiO_2 > 42 wt%; FeO/MgO > 2.0) of the erupted lavas relative to 1600s-1800s volcanics.

Pico do Fogo has been frequently active since the 1400s (Ribeiro, 1954; Siebert and Simkin, 2002; Bagnardi et al., 2016; Richter et al., 2016), and it is therefore possible that such repeated pulses of magma ascent through the central feeding system have locally altered the thermal properties of the ocean crust, causing magma stalling at progressively shallower depths over time. Magma mixing during prolonged shallow magma residence would also fit with clinopyroxene textural features (e.g., rounded or embayed cores overgrown by euhedral and zoned clinopyroxene, that show disequilibrium; Hildner et al., 2012) and with the recurrent eruption of upper crustal xenoliths by lavas (Hildner et al., 2012).

Our data suggests the magmatic system is evolving toward a state in which magma is drained from the uppermost portion of the 17-25 km source area, but then stalls at ~9-17 km depth shortly before eruption. In any future unrest, this process should be traceable as a progressive escalation of increasingly shallow seismicity, as seen elsewhere (D'Auria et al., 2022).

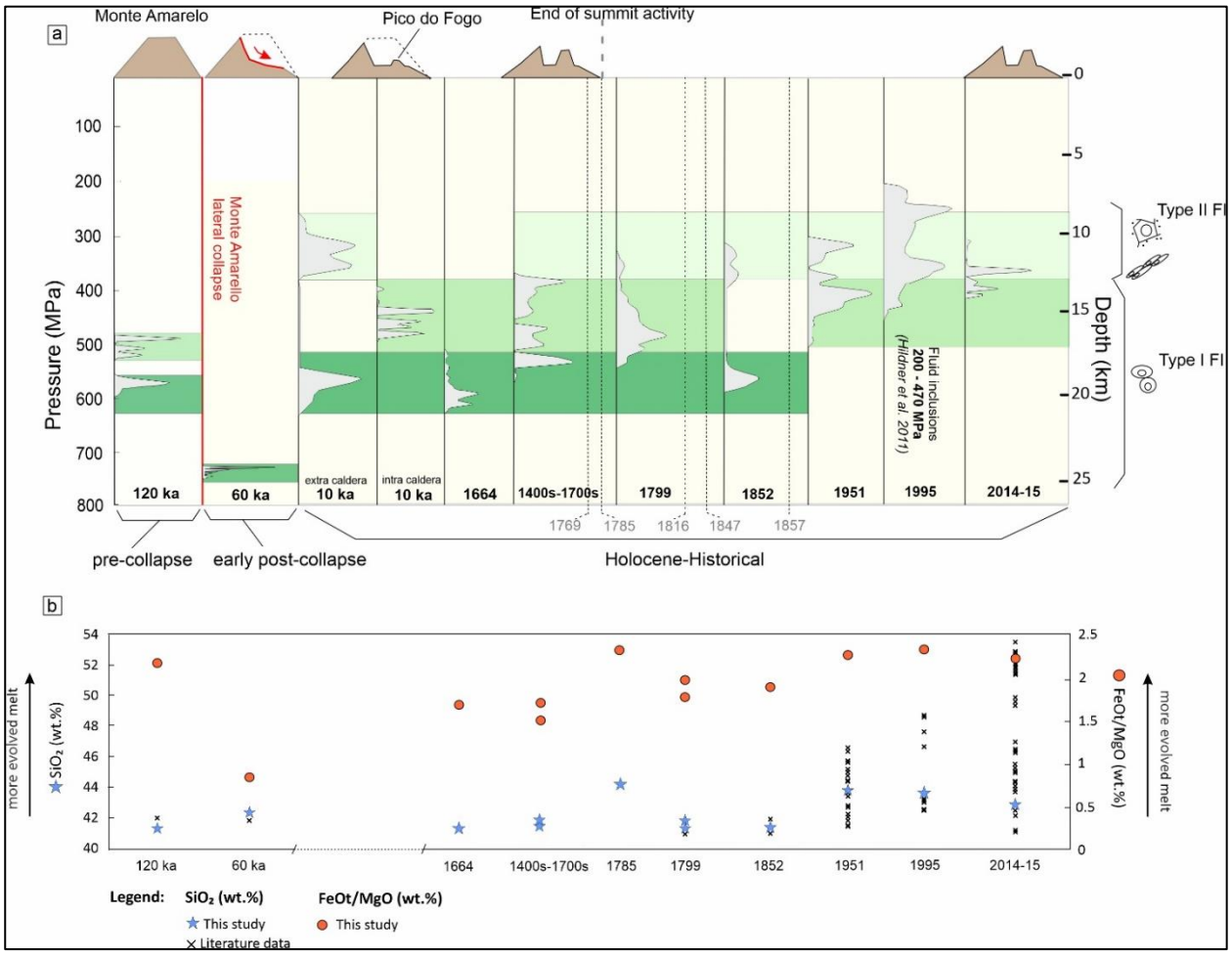

Figure 25 (a) Temporal evolution of entrapment/re-equilibration pressures/depths for the studied Fogo eruptions, based on FIAs in olivine phenocrysts only. The coloured bands mark regions of magma ponding that recur in several eruptions. Key magma storage areas are observed at ~22-25 km, ~19 km and ~15-17 km. Type II inclusions indicate FIA re-equilibrations at ~9-12 km. Low-density inclusions (of both types) suggest that deep crustal (9-17 km) magma ponding has been recurrent in historical time, and especially before the 1951, 1995 and 2014-2015 eruptions, during which more evolved lavas have consistenty been erupted, as shown by (b), temporal plots of bulk-rock SiO_2 contents and FeO_t/MgO ratios in the studied eruptions (data from the georoc database (Hildner et al. 2011,2012; Magnusson et al. 2016; Mata et al. 2017), https://georoc.eu/georoc/new-start.asp, and from this study, Table A1). Grey numbers mark the dates of non-studied eruptions.

5.5.4. Comparison with the magma system at other ocean island volcanoes

During the last two decades, fluid inclusions microthermometry has been applied to many oceanic island volcanic systems to define the architecture of their magma system. These data are compared with our Fogo results in Figure 26. The figure includes examples of oceanic volcanism in the Pacific

Ocean (Kilauea, Hawaii Archipelago; Sierra Negra, Galápagos Archipelago), in the Indian Ocean (Piton de La Fournaise, Réunion Island) and in the Atlantic Ocean (El Hierro and La Palma in the Canary Islands; Pico, Faial, Terceira, and São Miguel, in the Azores). For each volcanic system, we use literature data derived from fluid inclusions microthermometry, but also combine other sources of (petrological/geophysical) information where fluid inclusion results are unavailable.

Figure 26 demonstrates a large variety of magma storage conditions at ocean island volcanoes worldwide, ranging from shallow crustal (e.g., Kilauea) to upper mantle (e.g., El Hierro). This diversity is not unexpected considering our compilation includes volcanoes spanning a large range of key parameters that govern magma ascent and storage, including: (i) thickness (from ~27-29 km underneath São Miguel, in the Azores, to ~12-15 km underneath Canary volcanoes) and age (from ~155 Ma below La Palma; Verhoef et al., 1991 to <5 Ma beneath the Galápagos; White et al., 1993) of the underlying oceanic crust, (ii) magma supply rate (from 3-4 $m^3 \cdot s^{-1}$ at Kilauea; Poland, 2014; to 0.06 $m^3 \cdot s^{-1}$ at Fogo; Bagnardi et al., 2016), (iii) magma geochemistry (from MOR-type basalts in the Azores to alkali-rich basanites at Cape Verde and in the Canary), (iv) volcano/eruption type (central vs. fissural; e.g., Fogo vs. Cumbre Vieja at La Palma), and (v) tectonic setting (e.g., presence of regional transestive systems – such as in the Azores and Canary – that favour tapping and rapid ascent of deeply stored magma). The effect of central vs. fissural activity is, for example, evident at the scale of a single volcano, as demonstrated by heterogenous (shallow vs. deep) FI entrapping conditions at Pico and Faial in the Azores (Fig. 26e).

These complexities considered, we note that the oceanic volcanoes of Figure 26 broadly fall into two main categories. A first class of volcanoes exhibit a magma storage conditions near the Moho, as inferred from dominant FI entrapment conditions at ~10-12 km depth at El Hierro (Oglialoro et al., 2017) and 9-12 km depth at Cumbre Vieja (Klügel et al., 2022), in the Canary. Rapid (weeks) magma transfer from upper mantle reservoirs into the upper crust shortly prior/during eruption is strongly supported by seismic tomography results obtained during the 2021 Cumbre Vieja eruption (D'Auria et al., 2022). Similarly, at São Miguel volcano in the Azores, FIs testify for magma ponding in the upper mantle at ~24-29 km depth (Zanon, 2015), and magmas stored in the ~16-21 km depth interval (e.g., at the moho transition) are though to feed volcanism at Pico, Faial and Terceira in the Azores (Zanon et al., 2020).

A second class of ocean island volcanoes is exemplified by Kilauea, Sierra Negra and Piton de la Fournaise (Fig. 26), where pre-eruptive magma storage in the upper crust is suggested by data. At Kilauea, melt inclusion results clearly point to shallow magma storage conditions, ranging from 1-5

km depth (Lerner et al., 2021) to 2-3 km depth (Wieser et al., 2021). Volcanic rock geochemistry, seismic and geodetic evidence (Bell et al. 2021), and volcanic gas compositions (Aiuppa et al., 2022), likewise indicate shallow magma ponding at ~2 km depth below Sierra Negra caldera (Galápagos Archipelago) during volcano repose. At Piton de la Fournaise, FIs reveal a dominant entrapment pressure mode at ~12 km (e.g., close to the moho), but also indicate shallow entrapment (storage) conditions in the upper crust (Boudoire et al., 2019).

Ultimately, this comparison demonstrates that Fogo volcano exhibits storage conditions that closely resemble those observed at La Palma in the Canary (Fig. 26), and that therefore fall in the first category of ocean island volcanoes. The lack of shallow (< 200 MPa) magma storage at Fogo (in contrast to the persistently active Kilauea; Fig. 26) is consistent with geophysical data recorded before and during more recent eruptions, including: (i) the absence of volcano-wide deformation (inflation/deflation cycles) prior, during and after the 1995 and 2014-15 eruptions (Amelung et al., 2002 González et al., 2015), and (ii) the deep nature (hypocentres at ~17 km b.s.l.) of precursor seismicity observed before the 2014-15 eruption (Mata et al. 2017). Overall, these results are geophysical evidence of the relatively deep (deep crustal or upper mantle) source of magmas. We propose that a combination of (i) low magma supply rates (0.06 $m^3 \cdot s^{-1}$, Bagnardi et al., 2016; or 1-2 orders of magnitude lower than observed at Kilauea) and (ii) a relatively "cold" nature of the old (~125 Ma, Courtney, and White, 1986) oceanic crust beneath Fogo, concur to cause cooling, crystallization and stalling of magmas in the deep crust, and/or at the crust/mantle interface (Hildner et al. 2012), and prevent from shallow magma reservoirs to stably form. At Kilauea, in contrast, the low trapping pressures in olivines are interpreted to reflect high magma supply rate (3-4 $m^3 \cdot s^{-1}$; Poland, 2014) that allow primitive magmas to ascend with ease through the "hot" crustal section, to only stall in a shallow magma storage zone (Lerner, 2020; Wallace et al. 2021).

While persistent shallow magma storage at Fogo is inconsistent with micro-thermometric results (Fig. 24-26) and with the geophysical record, we cannot exclude that magma temporarily stalls, shortly prior to eruption, is a shallow (< 8-9 km) magma stagnation zone (Mata et al. 2017). For example, reaction edges on amphiboles are often observed, consisting in decomposition rims of variable thickness consisting of aggregates of rhönite, clinopyroxene, +/- Fe-Ti oxides (Mata et al., 2017). These relatively thick (> 500 µm) reaction rims testify for the instability of deeply formed (600-660 MPa pressure) amphibole upon ascent and residence in a low pH_2O environment (at total pressures <100 MPa; Pompilio and Rutherford, 2002; Alletti et al., 2005; Browne and Gardner, 2006), and have been taken as evidence for transient (30-50 days) stagnation zone in the shallow crust at ~2-7 km

depth (Mata et al., 2017). Such shallow pre-eruptive magma stalling could be favoured by the presence of intrusive bodies (e.g., dykes; Amelung et al., 2002) that would inhibit magma ascent to the surface, and is consistent with the recurrent recovery of crustal xenoliths in the Fogo recent lavas (Hildner et al. 2012).

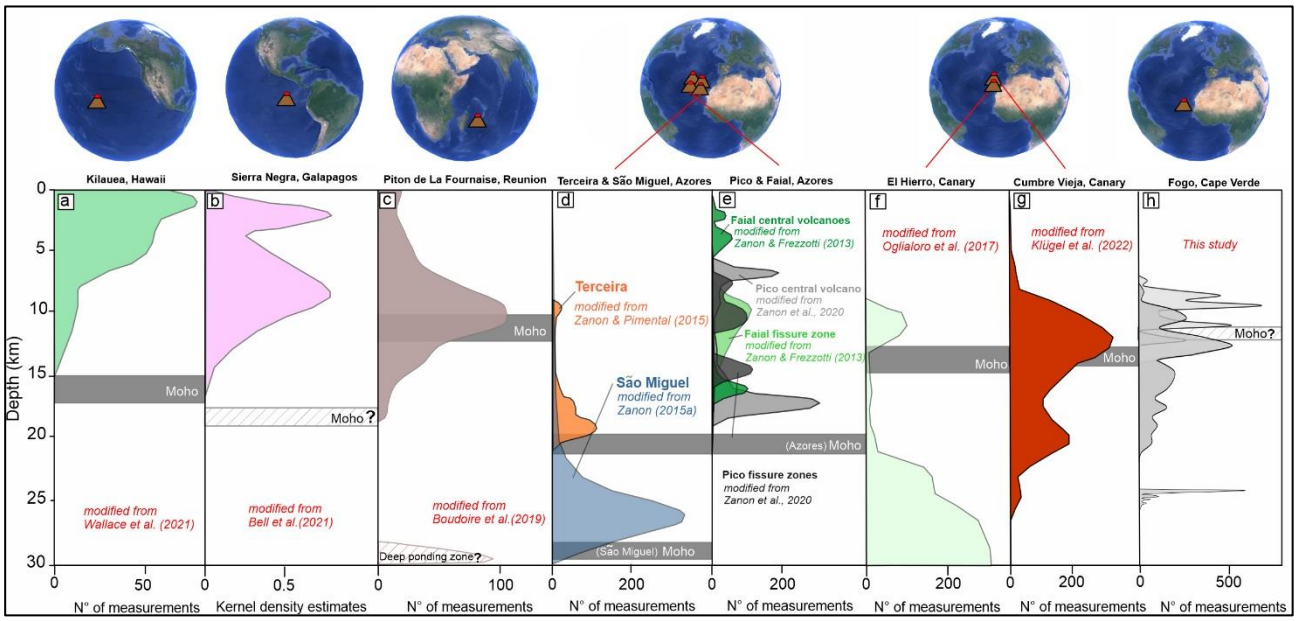

Figure 26 Plumbing systems barometric studies for contrasting types of mafic volcanoes (Analytics method: melt inclusions entrapment pressure, a; olivine-augite-plagioclase-melt (OPAM) barometer, b; fluid inclusions Raman densimeter and clinopyroxene-melt barometer, c; fluid inclusions microthermometry, d,e,f,g,h). The two volcanoes Kilauea (a) and Sierra Negra (b), in the Pacific Ocean, and Piton de La Fournaise (c) in the Indian Ocean, record barometric ranges that show a shallow storage zone <6 km depth. Contrary, Terceira, São Miguel, Pico and Faial (d,e) (Azores Archipelago), El Hierro (f) and La Palma (g) (Canary Islands), and Fogo (h) (Cape Verde), have in common the presence of a deepest magma zone at~15-30 km depth.

5.5.5. Caveats and limitations

Our results have provided some advance in the understanding of magma feeding processes at Fogo - yet we acknowledge several limitations still exist that prevent us from obtaining a comprehensive and unitary view of the plumbing system.

One main concern arises from the representativity of data. Despite ~2700 fluid inclusions were analysed from 11 eruptions, only 1-3 crystals per eruption were studied. Therefore, the extent to which the relatively few mineral grains analysed are representative of the fluid entrapment conditions

of the entire population of crystals (all/most containing FIAs) of a given eruption remains uncertain. Additionally, while we have characterised crystals from some historical eruptions, many others remain unstudied (Fig. 25). Therefore, further studies are required before the structure and temporal evolution of the magma system can be fully understood.

One additional source of uncertainty is the assumption that the inclusions contain 10 mol. % H_2O (cfr. 3). Clearly, if deep fluids did not contain 10 mol% H_2O, then pressure/depth estimates would be ~10% lower than reported here (Figs. 24,25). However, we observe that the Fogo basanites are relatively hydrous (up to > 2.5 wt.% H_2O measured in deeply trapped melt inclusions; Moussallam et al., 2019) relative to other hot-spot localities (e.g., Kilauea; Lerner et al., 2020; Wallace et al., 2021). At such conditions, degassing model calculations, performed by initialising the Moretti et al. (2003) saturation code with parental melt compositions appropriate for Fogo (e.g., using the melt inclusion results of Moussallam et al., 2019), indicate that the magmatic fluid phase in equilibrium with the melt in the 250-400 MPa pressure range contains from ~5 to ~10 mol.% H_2O, overall justifying our correction methodology.

Finally, Type II FIAs are here interpreted as the result re-equilibration of Type I inclusions upon ascent, in which the fluid delivered by Type I inclusions is re-entrapped as trails of lower density bubbles along crystal fractures. We caution that such re-equilibration, and density resetting to the new (lower) external pressures, may only be partial and not complete, in which case our inferred pressures for Type II FIAs would in fact over-estimate the real depths at which re-equilibration takes place.

5.6.Conclusions

The evolution of magma system underneath Fogo Volcano has been previously characterised by fluid inclusions microthermometry and clinopyroxene–melt-barometry (Hildner et al., 2011, 2012; Klügel et al., 2020), only for a limited dataset of recent eruptions. The barometric results presented here extends this analysis to ~120 ka and helps reconstruct the temporal history of the Fogo magma system, which, according to the resulting conceptual model (Fig. 27), evolved over the last 120 ka.

We propose that the ~120 ka eruption, pre-dating the Monte Amarelo collapse event, emitted basanite magma stored at a depth of ~19-22 km (Fig. 26a). Results for the ~60 ka early post-collapse eruption bring evidence for the direct magma withdrawal from the deepest storage system at ~24 km (Fig.

26b), suggesting that after the collapse, magma extraction bypassed the shallower magma system. FIAs in Holocene/historical eruptions indicate, instead, slower magma ascent rates, and more prolonged magma storage in the 13-17 km depth range (as indicated by Type I fluid inclusions). Shallow re-equilibration of FIAs takes place at 9-12 km depth, as indicated by Type II FIAs (Fig. 23, 24).

The picture that emerges from our study reinforces earlier conclusions (Hildner et al., 2012) for the recent (< 10 ka) activity being modulated by dynamics of magma stored at ~13-25 km. The geometry of this ~13-25 km magma storage zone is unconstrained, but the diverse entrapment and re-equilibration events identified for the various historical Fogo eruptions (Fig. 24a), and the relatively small erupted volumes, concur to suggest the existence of small-volume magma pockets interspersed within a well-established crystal mush zone, overall giving rise to a vertically extended trans-crustal magmatic system (Fig. 27c). Our results suggest the magma storage conditions and ascent pathways at Fogo are eruption-specific, suggesting the plumbing system is made of several relatively small, interconnected magma lenses, rather than by a single melt-dominated reservoir. We thus provide additional support to modern views (Cashman and Blundy, 2013; Cashman et al., 2017; Ruprecht and Bachmann, 2010) of magma systems that suggest the existence of multiple, superimposed ponding levels in which magma is only temporarily stored during its journey towards the surface.The magma system of Fogo would therefore share features with many oceanic volcanoes in which a series of small magma lenses at deep crustal to upper mantle depths feed transient crustal magma ponding zones during rapid (days/weeks) pre-eruptive emplacement (Klügel et al., 2005; Boudoire et al., 2019; Zanon et al., 2020). Notably, in contrast to some ocean island volcanoes with persistent shallow magma storage regions (e.g., Kilauea, Poland et al., 2014, Lerner et al., 2021, Wieser et al 2021; Sierra Negra, Bell et al., 2021), the lack of Type I inclusions at depths < 13 km points against any long-lived magma storage at shallow crustal levels. However, the apparent upward migration of magma storage conditions observed since the 1951 eruption (Figs. 25,27), if corroborated by additional results, may suggest a tendency toward a more mature, central-volcano activity phase, in which shallow crustal processing of magma is becoming more important with time. The fluid inclusion results provide a guide to the relatively deep depths of magma storage at Fogo and the potentially short transit time to the surface. This information aids the interpretation of earthquake locations and other monitoring information. Our study thus contributes crucial information for future assessment of volcanic risk and hazard mitigation at Fogo, where recent eruptions (1995 and 2014-15) have proven catastrophic for local communities.

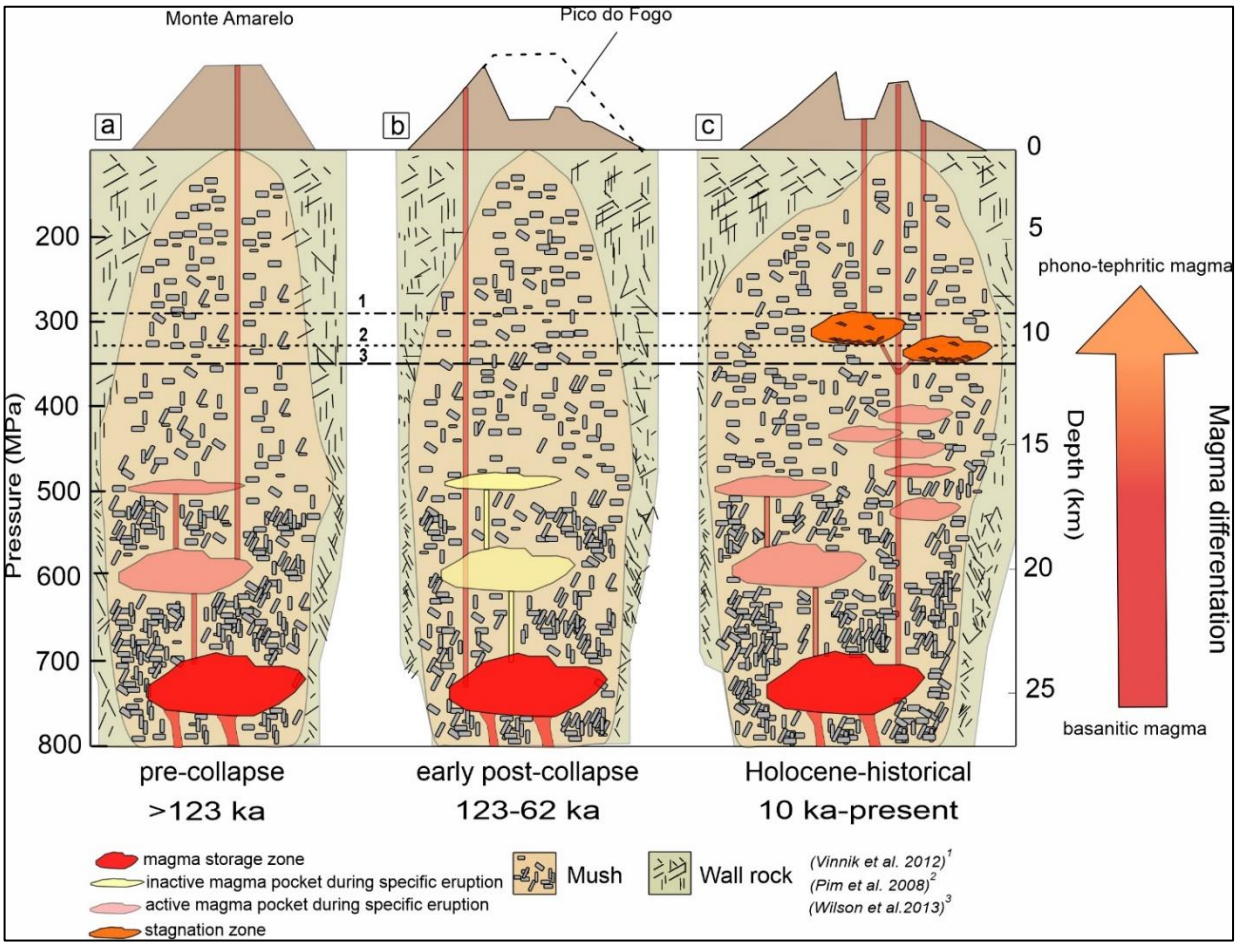

Figure 27 Schematic cross-sections of Fogo Island (not to scale), showing the temporal evolution of the magma feeding system during (a) pre-collapse, (b) early post-collapse and (c) Holocene-historical activity. FIAs in Holocene-historical eruptions suggest longer residence in a shallower magma ponding zone prior to eruption, at the inferred fossil Moho (1, Vinnik et al., 2012) and/or at the upper mantle-crust transition (2, Pim et al., 2008; 3, Wilson et al., 2013). More evolved melts (e.g., phono-tephrites) may form in this region by fractional crystallisation. The ~19 km and ~15-17 km regions are interpreted as parts of a vertically extended magma system, in which several interconnected ponding zones exist that are periodically refilled during specific eruptions. The main region of magma storage is at ~23.7 ±0.9 km.

REFERENCES

Aiuppa, A., Allard, P., Bernard, B., Lo Forte, F. M., Moretti, R., & Hidalgo, S. (2022). Gas leakage from shallow ponding magma and trapdoor faulting at Sierra Negra volcano (Isabela Island, Galápagos). Geochemistry, Geophysics, Geosystems, 23, e2021GC010288.

Alletti, M., Pompilio, M., Rotolo, S., 2005. Mafic and ultramafic enclaves in Ustica Island lavas: Inferences on composition of lower crust and deep magmatic processes. Lithos 84, 151–167.

Amelung, F., Day, S., 2002. InSAR observations of the 1995 Fogo, Cape Verde, eruption: Implications for the effects of collapse events upon island volcanoes. Geophysical Research Letters 29, 1606.

Bagnardi M., González P.J., Hooper A., 2016. High-resolution digital elevation model from tri-stereo Pleiades-1 satellite imagery for lava flow volume estimates at Fogo Volcano Geophysical Research Letters, 43 (12), pp. 6267-6275.

Bakker, R.J., 2003. Package FLUIDS 1. Computer programs for analysis of fluid inclusion data and for modelling bulk fluid properties. Chemical Geology 194, 3–23.

Barth, A., Newcombe, M., Plank, T., Gonnermann, H., Hajimirza, S., Soto, G.J., Saballos, A., Hauri, E., 2019. Magma decompression rate correlates with explosivity at basaltic volcanoes — Constraints from water diffusion in olivine. Journal of Volcanology and Geothermal Research 387, 106664.

Bell, A.F., La Femina, P.C., Ruiz, M., Amelung, F., Bagnardi, M., Bean, C.J., Bernard, B., Ebinger, C., Gleeson, M., Grannell, J., Hernandez, S., Higgins, M., Liorzou, C., Lundgren, P., Meier, N.J., Möllhoff, M., Oliva, S.-J., Ruiz, A.G., Stock, M.J., 2021. Caldera resurgence during the 2018 eruption of Sierra Negra volcano, Galápagos Islands. Nature Communications 12, 1397.

Biggs, J., Ebmeier, S.K., Aspinall, W.P., Lu, Z., Pritchard, M.E., Sparks, R.S.J., Mather, T.A., 2014. Global link between deformation and volcanic eruption quantified by satellite imagery. Nature Communications. 5, 3471.

Bodnar R.J., 2003. Introduction to fluid inclusions, in: Fluid Inclusions: Analysis and Interpretation., Assoc. Canada, Short Course 32. Samson I., Anderson A. and Marshall D. (Eds.), pp. 1–8.

Boudoire, G., Brugier, Y.-A., Di Muro, A., Wörner, G., Arienzo, I., Metrich, N., Zanon, V., Braukmüller, N., Kronz, A., Le Moigne, Y., Michon, L., 2019. Eruptive Activity on the Western Flank of Piton de la Fournaise (La Réunion Island, Indian Ocean): Insights on Magma Transfer, Storage and Evolution at an Oceanic Volcanic Island. Journal of Petrology 60, 1717–1752.

Caricchi, L., Sheldrake, T.E., Blundy J., 2018. Modulation of magmatic processes by CO2 flushing. Earth Planetary Science Letters, 491, pp. 160-171.

Carlson, R.L., Raskin, G.S., 1984. Density of the ocean crust. Nature 311, 555–558.

Carracedo, J.C., 1999.Growth, structure, instability and collapse of Canarian volcanoes and comparisons with Hawaiian volcanoes, Journal of Volcanology and Geothermal Research, 94(1-4), 1-19.

Carracedo, J.-C., Perez-Torrado, F.J., Rodriguez-Gonzalez, A., Paris, R., Troll, V.R., Barker, A.K., 2015. Volcanic and structural evolution of Pico do Fogo, Cape Verde. Geol. Today 31, 146–152.

Cashman, K., Blundy, J., 2013. Petrological cannibalism: the chemical and textural consequences of incremental magma body growth. Contributions to Mineralogy and Petrology. 166, 703–729.

Cashman, K.V., Giordano, G., 2014. Calderas and magma reservoirs. Journal of Volcanology and Geothermal Research. 288, 28–45.

Cashman, K.V., Sparks, R.S.J., Blundy, J.D., 2017. Vertically extensive and unstable magmatic systems: A unified view of igneous processes. Science 355, eaag3055.

Cashman, K.V., Edmonds, M., 2019. Mafic glass compositions: a record of magma storage conditions, mixing and ascent. Philos. Trans. R. Soc. Math. Phys. Eng. Sci. 377, 20180004.

Cooper, A.K., Marlow, M.S., Scholl, D.W., Stevenson, A.J., 1992. Evidence for Cenozoic crustal extension in the Bering Sea region. Tectonics 11, 719–731.

Cooper, K.M., Kent, A.J.R., 2014. Rapid remobilization of magmatic crystals kept in cold storage. Nature 506, 480–483.

Courtney, R.C., White, R.S., 1986. Anomalous heat flow and geoid across the Cape Verde Rise: evidence for dynamic support from a thermal plume in the mantle. Geophys. J. Int. 87, 815–867.

D'Auria, L., Koulakov, I., Prudencio, J., Cabrera-Perez, I., Ibáñez, J., Barrancos, J., Hernandez R.G., Van Dorth D. M., Hernandez G.P., Przeor M., Ortega V.,Perez P.H., Rodriguez N.P, 2022. Voluminous storage and Rapid magma ascent beneath La Palma revealed by seismic Tomography. Research Square preprint.

Dash, B.P., Ball, M.M., King, G.A., Butler, L.W., Rona, P.A., 1976. Geophysical investigation of the Cape Verde Archipelago. Journal of Geophysical Research, 81, 5249–5259.

Day, S.J., Heleno da Silva, S.I.N., Fonseca, J.F.B.D., 1999. A past giant lateral collapse and present-day flank instability of Fogo, Cape Verde Islands. Journal of Volcanology and Geothermal Research 94, 191–218.

Day, S.J., Carracedo, J.C., Guillou, H., Pais Pais, F.J., Badiola, E.R., Fonseca, J.F.B.D., Heleno, S.I.N., 2000. Comparison and cross-checking of historical, archaeological and geological evidence for the dilocation and type of historical and sub-historical eruptions of multiple-vent oceanic island volcanoes. Geologial Society London Special Publications 171, 281–306.

Dixon J.E., Stolper E.M., 1995. An Experimental Study of Water and Carbon Dioxide Solubilities in Mid-Ocean Ridge Basaltic Liquids. Part II: Applications to Degassing. Journal of Petrology

Edmonds, M., Cashman, K.V., Holness, M., Jackson, M., 2019. Architecture and dynamics of magma reservoirs. Philos. Trans. R. Soc. Math. Phys. Eng. Sci. 377, 20180298.

Foeken, J., Stuart, F., Day, S., Wall, F., 2007. Carbonatite seamount formation and first subaerial exposure of Fogo (Cape Verde Islands): results from apatite and pyrochlore (U–Th)/He dating. Geophysical Research Abstracts 9 EGU2007-A-09688.

Foeken, J.P.T., Day, S., Stuart, F.M., 2009. Cosmogenic 3He exposure dating of the Quaternary basalts from Fogo, Cape Verdes: Implications for rift zone and magmatic reorganisation. Quat. Geochronology 4, 37–49.

Foroozan, R., Elsworth, D., Voight, B., Mattioli, G.S., 2010. Dual reservoir structure at Soufrière Hills Volcano inferred from continuous GPS observations and heterogeneous elastic modeling. Geophysical Research Letters, 37.

Frezzotti, M.L., Tecce, F., Casagli, A., 2012. Raman spectroscopy for fluid inclusion analysis. Journal of Geochemical Exploration 112, 1–20.

Galipp, K., Klügel, A., Hansteen, T.H., 2006. Changing depths of magma fractionation and stagnation during the evolution of an oceanic island volcano: La Palma (Canary Islands). Journal of Geophysical Research .155, 285–306.

Gerlach, D.C., Cliff, R.A., Davies, G.R., Norry, M., Hodgson, N., 1988. Magma sources of the Cape Verdes archipelago: Isotopic and trace element constraints. Geochimica et Cosmochimica Acta 52, 2979–2992.

Goldstein RH, Samson I, Anderson A, Marshall D (2003) Petrographic analysis of fuid inclusions. Fluid Inclusions: Analysis and Interpretation 32:9–53.

Hansteen, T.H., Klügel, A., Schmincke, H.-U., 1998. Multi-stage magma ascent beneath the Canary Islands: evidence from fluid inclusions. Contributions to Mineralogy and Petrology. 132, 48–64.

Hansteen, T.H., Klugel, A., 2008. Fluid Inclusion Thermobarometry as a Tracer for Magmatic Processes. Reviews in Mineralogy and Geochemistry 69, 143–177.

Hildner, E., Klügel, A., Hauff, F., 2011. Magma storage and ascent during the 1995 eruption of Fogo, Cape Verde Archipelago. Contributions to Mineralogy and Petrology 162, 751–772.

Hildner, E., Klügel, A., Hansteen, T.H., 2012. Barometry of lavas from the 1951 eruption of Fogo, Cape Verde Islands: Implications for historic and prehistoric magma plumbing systems. Journal of Volcanology and Geothermal Research 217–218, 73–90.

Hoernle, K., Tilton, G., Le Bas, M.J., Duggen, S., Garbe-Schönberg, D., 2002. Geochemistry of oceanic carbonatites compared with continental carbonatites: mantle recycling of oceanic crustal carbonate. Contributions to Mineralogy and Petrology. 142, 520–542.

Holtzman, B.K., Kohlstedt, D.L., 2007. Stress-driven Melt Segregation and Strain Partitioning in Partially Molten Rocks: Effects of Stress and Strain. Journal of Petrology 48, 2379–2406.

Klügel, A., Hansteen, T.H., Galipp, K., 2005. Magma storage and underplating beneath Cumbre Vieja volcano, La Palma (Canary Islands). Earth and Planetary Science Letters 236, 211–226.

Klügel, A., Day, S., Schmid, M., Faria, B., 2020. Magma Plumbing During the 2014–2015 Eruption of Fogo (Cape Verde Islands). Frontiers in Earth Science 8, 157.

Klügel, A., Albers, E., and Hansteen, T.H., 2022. Mantle and Crustal Xenoliths in a Tephriphonolite From La Palma (Canary Islands): Implications for Phonolite Formation at Oceanic Island Volcanoes. Frontiers in Earth Science 10:761902.

Lénat, J.-F., and P. Bàchelery, 1990. Structure et fonctionnement de la zone centrale du Piton de la Fournaise, in Le volcanisme de la Reunion, Monographie, 257 – 296, Cent. Rech. Volc., Clermont-Ferrand.

Lerner A. H., O'Hara D., Karlstrom L., Ebmeier S. K., Anderson K. R., Hurwitz S., 2020. The prevalence and significance of offset magma reservoirs at arc volcanoes. Geophysical Research Letters 47, e2020GL087856 (2020).

Lerner, A. H., Wallace, P., & Shea, T. (2021). The petrologic and degassing behavior of sulfur and other magmatic volatiles from the 2018 erup-tion of Kīlauea, Hawai'i: Melt concentrations, magma storage depths, and magma recycling. Bulletin of Volcanology, 83(43), 1–32.

Liu, X., Zhao, D., 2014. Seismic evidence for a mantle plume beneath the Cape Verde hotspot. International Geology Review 56, 1213–1225.

Maclennan, J., McKenzie, D., Gronvöld, K., Slater, L., 2001. Crustal accretion under northern Iceland. Earth Planetary Science Letters 191, 295–310.

Maclennan, J., 2019. Mafic tiers and transient mushes: evidence from Iceland. Philos. Trans. R. Soc.Math. Phys. Eng. Sci. 377, 20180021.

Magnusson, E. (2016). Temporal Evolution of Historic Mafic Lavas from Fogo , Cape Verde. MSc Thesis, Uppsala University, Uppsala, Sweden.

Manconi, A., Longpre, M.-A., Walter, T.R., Troll, V.R., Hansteen, T.H., 2009. The effects of flank collapses on volcano plumbing systems. Geology 37, 1099–1102.

Martínez-Moreno, F.J., Monteiro Santos, F.A., Madeira, J., Pous, J., Bernardo, I., Soares, A., Esteves, M., Adão, F., Ribeiro, J., Mata, J., Brum da Silveira, A., 2018. Investigating collapse structures in oceanic islands using magnetotelluric surveys: The case of Fogo Island in Cape Verde. Journal of Volcanology and Geothermal Research 357, 152–162.

Mata, J., Martins, S., Mattielli, N., Madeira, J., Faria, B., Ramalho, R.S., Silva, P., Moreira, M., Caldeira, R., Moreira, M., Rodrigues, J., Martins, L., 2017. The 2014–15 eruption and the short-term geochemical evolution of the Fogo volcano (Cape Verde): Evidence for small-scale mantle heterogeneity. Lithos 288–289, 91–107.

Mattioli, G.S., Herd, R.A., Strutt, M.H., Ryan, G., Widiwijayanti, C., Voight, B., 2010. Long term surface deformation of Soufrière Hills Volcano, Montserrat from GPS geodesy: Inferences from simple elastic inverse models. Geophysical Research Letters 37.

Menand, T., 2011. Physical controls and depth of emplacement of igneous bodies: a review. Tectonophysics, 500(1-4), 11-19.

Moretti, R., Papale, P., & Ottonello, G. (2003). A model for the saturation of C-H-O-S fluids in silicate melts. In C. Oppenheimer, D. M. Pyle, & J. Barclay (Eds.), (Vol. 213, pp. 81–101). Geological Society of London Special Publication. Volcanic Degassing.

Mourão, C., Moreira, M., Mata, J., Raquin, A., Madeira, J., 2012. Primary and secondary processes constraining the noble gas isotopic signatures of carbonatites and silicate rocks from Brava Island: evidence for a lower mantle origin of the Cape Verde plume. Contributions to Mineralogy Petrology 163, 995–1009.

Neave, D.A., Beckmann, P., Behrens, H., Holtz, F., 2021. Mixing between chemically variable primitive basalts creates and modifies crystal cargoes. Nature Communications 12, 5495.

Oglialoro, E., Frezzotti, M., Ferrando, S., Tiraboschi, C., Principe, C., Groppeli, G., Villa, I.M., 2017. Lithospheric magma dynamics beneath the El Hierro Volcano, Canary Islands: insights from fluid inclusions. Bulletin of Volcanology 79, 70.

Pappalardo, L., Buono, G., 2021. Insights Into Processes and Timescales of Magma Storage and Ascent From Textural and Geochemical Investigations: Case Studies From High-Risk Neapolitan Volcanoes (Italy), in: Masotta, M., Beier, C., Mollo, S. (Eds.), Geophysical Monograph Series. Wiley, pp. 213–235.

Parmigiani, A., Huber, C., Bachmann, O., 2014. Mush microphysics and the reactivation of crystal-rich magma reservoirs. Journal of Geophysical Research: Solid Earth 119, 6308–6322.

Pim, J., Peirce, C., Watts, A.B., Grevemeyer, I., Krabbenhoeft, A., 2008. Crustal structure and origin of the Cape Verde Rise. Earth Planetary Science Letters 272, 422–428.

Poland, M. P., 2014. Time-averaged discharge rate of subaerial lava at Kīlauea Volcano, Hawai'i, measured from TanDEM-X interferometry: Implications for magma supply and storage during 2011–2013, Journal of Geophysical Research: Solid Earth, 119, 5464–5481.

Poland, M.P., Takahashi, T.J., Landowski, C.M., 2014. Characteristics of Hawaiian Volcanoes. Government Print Office.

Pompilio, M., Rutherford, M.J., 2002. Pre-eruption Conditions and Magma Dynamics of Recent Amphibole-Bearing Etna Basalt, in: AGU Fall Meeting Abstracts. pp. V61A-1354.

Putirka, K.D., Perfit, M., Ryerson, F.J., Jackson, M.G., 2007. Ambient and excess mantle temperatures, olivine thermometry, and active vs. passive upwelling. Chemical Geology. 241, 177–206.

Putirka, K.D., 2008. Thermometers and Barometers for Volcanic Systems. Reviews in Mineralogy and Geochemistry 69, 61–120.

Rhodes, J.M., Dungan, M.A., Blanchard, D.P., Long, P.E., 1979. Magma mixing at mid-ocean ridges: Evidence from basalts drilled near 22° N on the Mid-Atlantic Ridge. Tectonophysics 55, 35–61.

Ribeiro, O., 1954. A Ilha Do Fogo e as suas erupções. Junta de Investigações do Ultramar., Lisbon.

Richter, N., Favalli, M., de Zeeuw-van Dalfsen, E., Fornaciai, A., da Silva Fernandes, R.M., Pérez, N.M., Levy, J., Victória, S.S., Walter, T.R., 2016. Lava flow hazard at Fogo Volcano, Cabo Verde, before and after the 2014–2015eruption. Natural Hazards and Earth System Sciences. 16, 1925–1951.

Ruprecht, P., Bachmann, O., 2010. Pre-eruptive reheating during magma mixing at Quizapu volcano and the implications for the explosiveness of silicic arc volcanoes. Geology 38, 919–922.

Schwarz, S., Klügel, A., Wohlgemuth-Ueberwasser, C., 2004. Melt extraction pathways and stagnation depths beneath the Madeira and Desertas rift zones (NE Atlantic) inferred from barometric studies. Contribution to Mineralogy and Petrology. 147, 228–240.

Siebert, L., Simkin, T., 2002. Volcanoes of the World: an illustrated catalog of Holocene volcanoes and their eruptions. Smithsonian Institution, Global Volcanism Program Digital Information Series.

Span, R., Wagner, W., 1996. A New Equation of State for Carbon Dioxide Covering the Fluid Region from the Triple-Point Temperature to 1100 K at Pressures up to 800 MPa. Journal of Physical and Chemical Reference Data 25, 1509–1596.

Sparks, R.S.J., Annen, C., Blundy, J.D., Cashman, K.V., Rust, A.C., Jackson, M.D., 2019. Formation and dynamics of magma reservoirs. Philos. Trans. R. Soc. Math. Phys. Eng. Sci. 377, 20180019.

Sterner, S.M., Bodnar, R.J., 1991. Synthetic fluid inclusions; X, Experimental determination of P-V-T-X properties in the CO2-H2O system to 6 kb and 700 degrees C. American Journal of Science 291, 1–54.

Stroncik, N.A., Klügel, A., Hansteen, T.H., 2009. The magmatic plumbing system beneath El Hierro (Canary Islands): constraints from phenocrysts and naturally quenched basaltic glasses in submarine rocks. Contributions to Mineralogy and Petrology. 157, 593–607.

Tenzer, R., Bagherbandi, M., Vajda, P., 2013. Global model of the upper mantle lateral density structure based on combining seismic and isostatic models. Geosciences Journal 17, 65–73.

Torres, P., Madeira, J., Silva, L., Brum da Silveira, A., Serraheíro, A., Mota Gomes, A., 1997. Carta Geológica das Erupções Históricas da Ilha do Fogo (Cabo Verde): revisão e actualização Comn. Instit. Geol. Mine. 84, A193–A196.

Torres, P., Silva, L.C., Munhá, J., Caldeira, R., Mata, J., Tassinari, C., 2010. Petrology and geochemistry of lavas from Sal Island: implication for the variability of the Cape Verde magmatism. Comunicaçõe Geológicas 97, 35–62.

Verhoef, J., Collette, B.J., Dañobeitia, J.J., Roeser, H.A., Roest, W.R., 1991. Magnetic anomalies off West-Africa (20–38°N). Marine Geophysical Research 13 (2), 81–103.

Vinnik, L., Silveira, G., Kiselev, S., Farra, V., Weber, M., Stutzmann, E., 2012. Cape Verde hotspot from the upper crust to the top of the lower mantle. Earth Planetary Science Letters 319–320, 259–268.

Voight, B., Widiwijayanti, C., Mattioli, G., Elsworth, D., Hidayat, D., Strutt, M., 2010. Magma-sponge hypothesis and stratovolcanoes: Case for a compressible reservoir and quasi-steady deep influx at Soufrière Hills Volcano, Montserrat. Geophysical Research Letters 37.

Wallace, P. J., Plank, T., Bodnar, R. J., Gaetani, G. A., & Shea, T. (2021). Olivine-hosted melt inclusions: A microscopic perspective on a complex magmatic world. Annual Review of Earth and Planetary Sciences, 49, 465–494.

White, W.M., McBirney, A.R., Duncan, R.A., 1993. Petrology and geochemistry of the Galápagos Islands: portrait of a pathological mantle plume. Journal of Geophysical Research 98 (B11), 19533–19563.

Wilmart, E., Clocchiatti, R., Duchesne, J.-C., Touret, J.L.R., 1991. Fluid inclusions in charnockites from the Bjerkreim-Sokndal massif (Rogaland, southwestern Norway): fluid origin and in situ evolution. Contributions to Mineralogy and Petrology 108, 453–462.

Wilson, D.J., Peirce, C., Watts, A.B., Grevemeyer, I., 2013. Uplift at lithospheric swells--II: is the Cape Verde mid-plate swell supported by a lithosphere of varying mechanical strength? Geophysical Journal International 193, 798–819.

Wieser, P. E., Lamadrid, H., Maclennan, J., Edmonds, M., Matthews, S., Iacovino, K., et al. (2021). Reconstructing magma storage depths for the 2018 Kīlauean eruption from melt inclusion CO_2 contents: The importance of vapor bubbles. Geochemistry, Geophysics, Geosystems, 22.

Zanon, V., Frezzotti, M.L., 2013. Magma storage and ascent conditions beneath Pico and Faial islands (Azores archipelago): A study on fluid inclusions. Geochemistry, Geophysics, Geosystems, 14, 3494–3514.

Zanon, V., Pimentel, A., 2015. Spatio-temporal constraints on magma storage and ascent conditions in a transtensional tectonic setting: The case of the Terceira Island (Azores). American Mineralogist. 100, 795–805.

Zanon, V., 2015b. Conditions for mafic magma storage beneath fissure zones at oceanic islands. The case of São Miguel Island (Azores archipelago). In: Caricchi, L., Blundy, J.D. (Eds.), Chemical, Physical and Temporal Evolution of Magmatic Systems. The Geological Society of London, Special Publications, pp. 85–104 422.

Zanon, V., Pimentel, A., Auxerre, M., Marchini, G., Stuart, F.M., 2020. Unravelling the magma feeding system of a young basaltic oceanic volcano. Lithos 352–353, 105325

Web references

https://georoc.eu/georoc/new-start.asp

https://sketchfab.com/WVUpetrology

CHAPTER 6.

HIGH CO_2 IN THE MANTLE SOURCE OF OCEAN ISLAND BASANITES

Published in Geochimica et Cosmochimica Acta:
https://doi.org/10.1016/j.gca.2024.01.016

(Lo Forte et al., 2024)

ABSTRACT

Some of the most CO_2-rich magmas on Earth are erupted by intraplate ocean island volcanoes. Here, we characterise olivine-hosted melt inclusions from recent (< 10 ky) basanitic tephra erupted by Fogo, the only active volcano of the Cape Verde Archipelago in the eastern Atlantic Ocean. We determine H2O, S, Cl, F in glassy melt inclusions and recalculate the total (glass+shrinkage bubbles) CO_2 budget by three independent methodologies. We find that the Fogo parental basanite, entrapped as melt inclusion in forsterite-rich (Fo_{80-85}) olivines, contains up to~ 2.1 wt% CO_2, 3-47% of which is partitioned in the shrinkage bubbles. This CO_2 content is among the highest ever measured in melt inclusions in OIBs. In combination with~ 2 wt.% H_2O content, our data constrain an entrapment pressure range for the most CO_2-rich melt inclusion of 648-1430 MPa, with a most conservative estimate at 773-1020 MPa. Our results therefore suggest the parental Fogo melt is stored in the lithospheric mantle at minimum depths of ~27 to ~36 km, and then injected into a vertically stacked magma ponding system. Overall, our results corroborate previous indications for a CO_2-rich nature of alkaline ocean island volcanism. We propose that the Fogo basanitic melt forms by low degrees of melting (F=0.06-0.07) of a carbon-enriched mantle source, containing up to 355-414 ppm C. If global OIB melts are dominantly as carbon-rich as our Fogo results suggest, then OIB volcanism may cumulatively outgas as high as ~16-21 Tg of carbon yearly, hence substantially contributing to the global deep carbon cycle.

Keywords: alkaline ocean islands, intraplate volcanism, Fogo volcano, melt inclusions, Cape Verde.

6.1. Introduction

Quantifying the initial amount of volatile elements (H_2O, CO_2, S, Cl, and F) transported by OIB magmas is essential for understanding the cycling of volatiles from Earth's deep interior (e.g., Hirschmann, 2006, 2018; Dasgupta and Hirschmann, 2010), and their role for mantle melting, and magma generation and extraction (e.g., Foley, 2011; Dasgupta, 2018). Although sustaining only ~10% of the annual magma output on Earth, OIB magmas can contain more than 5% volatiles, and therefore significantly contribute to the annual magmatic gas output (e.g., Cabral et al., 2014; Longpré et al., 2017; Boudoire et al., 2018; Taracsák et al., 2019; Burton et al., 2023), especially if compared to more voluminous - but less volatile rich - Mid Ocean Ridge Basalts (MORBs) (e.g., Hauri et al., 2019). Oceanic intra-plate magmas have some of the most CO_2-enriched magmas on Earth (Longpré et al., 2017; Taracsák et al., 2019), likely reflecting their derivation from low melting degree of a metasomatised (C-enriched) mantle source (Foley et al., 2009, 2011; Dasgupta et al., 2013; Foley and Fischer, 2017; Dasgupta, 2018; Aiuppa et al., 2021).

Glassy melt inclusions (MI), small droplets of silicate melt entrapped in crystals during their growth in magmas or during episodes of crystal fracturation, are - at least in principle - physically and chemically isolated systems shielded from the surrounding environment by the host crystal (e.g., Lowenstern 1995; Danyushevsky et al. 2002; Schiano 2003; Wallace 2005; Cannatelli et al. 2016; Wallace et al., 2021; Rose-Koga et al., 2021). As such, the entrapped melt should escape extensive volatile loss upon magma ascent/storage in the crust prior/during eruption. Upon quenching as glass, MI should allow recording the dissolved volatile contents at the P-T-X conditions of entrapment, and eventually the parental melt volatile contents if entrapment has occurred at/near source (and before volatile saturation is reached) (e.g., Métrich and Wallace, 2008; Edmonds and Wallace, 2017). However, the task is complicated by a range of processes that can potentially modify MI composition after it is entrapped in the crystal (e.g., Anderson 1974; Roedder 1979; Danyushevsky et al., 2002; Wallace et al., 2021), including post-entrapment crystallization at the MI-host crystal interface (e.g., Danyushevsky et al., 2000), diffusive exchanges of major, trace and volatile (H^+) elements (e.g., Gaetani and Watson, 2000, 2002; Danyushevsky, 2001; Cottrell et al., 2002; Gaetani et al. 2012) and – above all – shrinkage bubble formation (Anderson, 1974; Roedder, 1979; Maclennan, 2017). This latter process is especially relevant for volatile species, as it leads to partitioning of poorly soluble CO_2 from the melt inclusion glass into the shrinkage bubble. Shrinkage bubbles can contain up to >90% of the bulk MI CO_2 content (e.g., Esposito et al., 2011; Mironov and Portnyagin, 2011; Hartley

et al., 2014; Mironov et al., 2015; Moore et al., 2015; Esposito et al., 2016; Aster et al., 2016; Rasmussen et al., 2018, 2020), demonstrating the caveats of traditional approaches (Lowenstern, 2015) that focus on measuring volatiles in glass only. Still, accurately quantifying the shrinkage bubble CO_2 content is technically challenging (e.g., Naumov et al., 2003), and few examples are available of reconstructions of the total (bubble+glass) MI CO_2 budget in OIB context (e.g., Taracsák et al., 2019; Tucker et al., 2019, Burton et al., 2023).

Some of the most alkali-rich OIB magmas are erupted in the Cape Verde Archipelago, in the central eastern Atlantic Ocean. This archipelago lies on the largest intraplate bathymetric anomaly in the Earth's oceans – the Cape Verde Rise - interpreted as the surface expression of a hotspot sustained by the ascent of a deeply-rooted mantle plume (Holm et al., 2006; French and Romanowicz, 2015). The presence of highly alkaline silica undersaturated rocks (nephelinites, melanephelinites, and melilitites), as well as carbonatites (Hoernle et al., 2002; Bonadiman et al., 2005), are evidence for a heterogeneous, oxidized (Moussallam et al., 2019), potentially C-enriched mantle source, as also indicated by the CO_2-rich signature of fumaroles (Aiuppa et al., 2020; Melián et al., 2021).

In this study we use primitive MI composition to confirm the carbon-rich signature of the Cape Verde magma source. We report on the major, trace, and volatile composition of olivine-hosted MI from basanitic tephra erupted at Fogo, the youngest active volcano of the Cape Verde Archipelago. Our goal is to determine the initial (parental melt) volatile contents, in the attempt to (i) test the carbon-enriched source hypothesis, (ii) refine our understanding of the architecture of the magma system, and (iii) more broadly, provide additional evidence for the carbon-enriched nature of alkali rich, OIB magmatism.

6.2. Volcanological Background

Fogo is the only active volcano in the Cape Verde Archipelago, in the central eastern Atlantic ocean, West of Africa coasts (Figure 28). Volcanic activity on the islands started ~26 Ma (Torres et al., 2010), and is dominated by silica-undersaturated alkaline melts (e.g., Gerlach et al., 1988), and rarer carbonatites (Hoernle et al., 2002; Mourão et al., 2012). Subaerial volcanic activity has been divided into four eruptive phases: (i) The Ribeira de Almada Group (~4.5 Ma, Foeken et al., 2009); (ii) The Monte Barro Group (of unknown age); (iii) The Monte Amarelo Group, whose activity preceded the lateral collapse of Monte Amarelo at circa 62 to 123 ka (Day et al., 1999; Foeken et al., 2009; Martínez-Moreno et al., 2018); and (iv) The Chã das Caldeira Group (Foeken et al., 2009) related to

the recent growth of Pico do Fogo central volcano. Pico do Fogo volcano erupted 28 times since the 1500s. Eruptions are sourced by a complex, vertically elongated magma plumbing system, with main magma storage/stagnation zones at ~24, ~13-19 and ~9-12 km depth (Hildner et al., 2011, 2012; Klügel et al., 2020; Lo Forte et al., 2023).

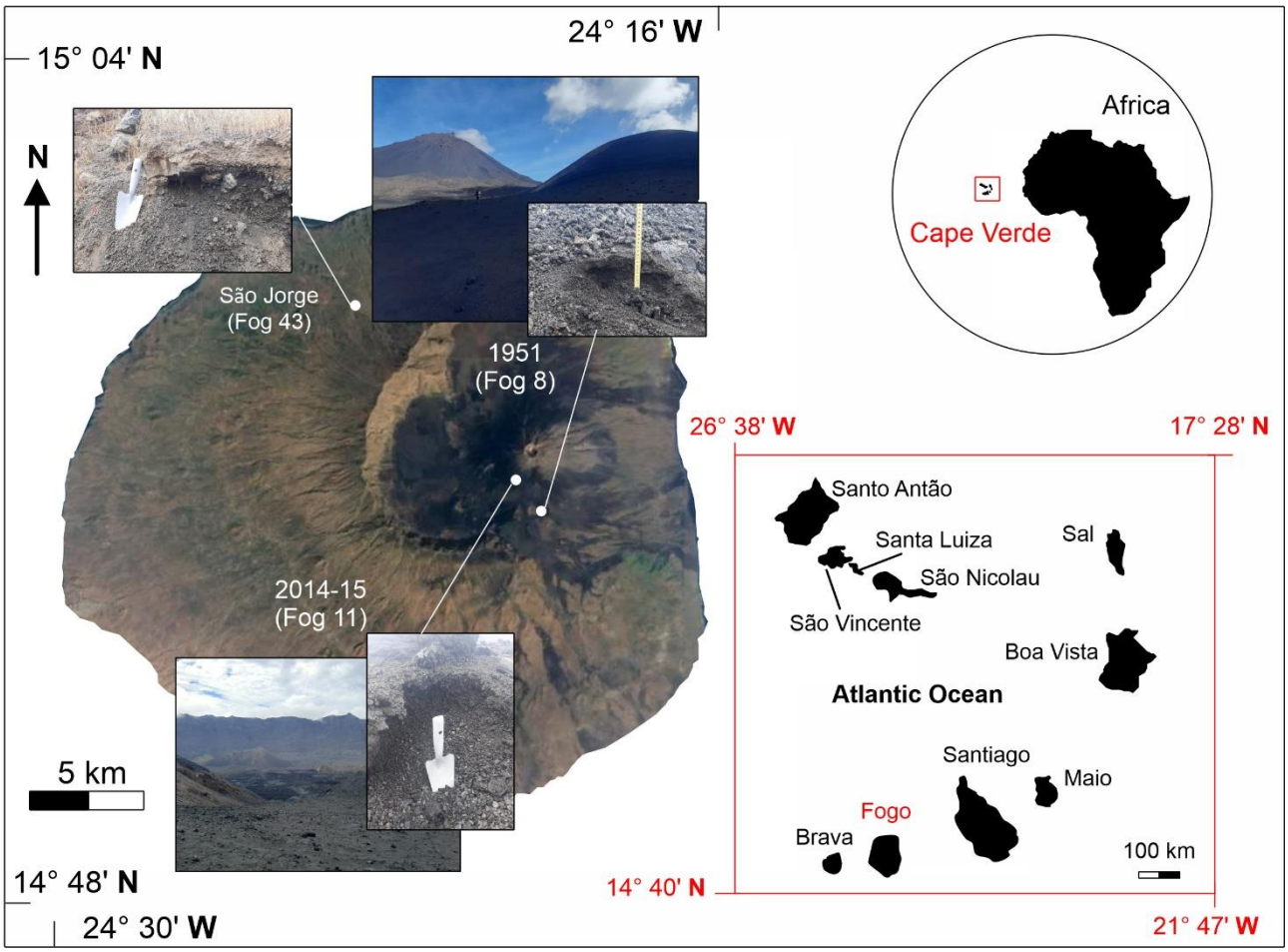

Figure 28 Modified Satellite map of Fogo Island from Google Earth, showing sampling sites with their relative pictures. Insets show the location of the Cape Verde archipelago (top right), and Fogo Island (bottom right).

6.3. Materials and Methods

6.3.1. Sample preparation

We report data for 18 MI hosted in 12 olivine phenocrysts from three different tephra samples representative for the last eruptive phase of Fogo volcano (see tables S1 and S2 of Supplementary Material S1, for further details). In detail, we analysed (i) 8 MI hosted in 5 olivines from the clinopyroxene- and olivine-rich tephra samples of São Jorge (SJ), of the early Holocene period of

activity (~10 ka), and (ii) 10 MI hosted in 7 olivines from the recent basanitic tephra samples of the 1951 and 2014/15 eruptions. Samples were prepared according to the methodology described by Rose-Koga et al., (2021). Tephra samples were initially sieved to separate grain size populations in the 250–4000 μm range. For each sample, about 400 olivine phenocrysts were hand-picked from these grain size fractions. Olivine crystals were mounted on glass slides using Crystal Bond 509®, subsequently they were doubly polished with silicon carbide paper and alumina powders to attain a maximum thickness of 80–100 μm. Twenty phenocrysts, containing 26 MIs with size greater than 25 μm were selected for analysis.

6.3.2. Analytical techniques

Electron microprobe analysis (EMPA) was used to determine the major element compositions of both host olivines and melt inclusions, as well as Cl, and F concentrations in glasses. Volatile element concentrations (H_2O, CO_2, S, and Cl) in glasses were measured by nano-SIMS. The CO_2 concentration in shrinkage bubbles in MI was determined by Raman micro-spectroscopy. Finally, Laser Ablation-ICPMS was utilized for trace element analysis. The full compositional dataset is listed in tables S3, S4, S5, S5.1, and S5.2 of Supplementary Material S1.

6.3.2.1. Electron microprobe analysis (EMPA)

Electron microprobe analyses were performed with a Cameca SxFiveTactis with a LaB6 source equipped with five wavelength-dispersive spectrometers at the Laboratoire Magmas et Volcans (LMV), in Clermont-Ferrand, France. Major elements and volatiles were analysed in the same analytical session, with an accelerating voltage of 15 kV, an 8 nA beam current, and a 20 μm defocused beam for major elements. Chlorine, sulphur, and fluorine analyses were conducted using an accelerating voltage of 15 kV, a 40 nA beam current and a 20 μm defocused beam, following the acquisition program outlined in the Cameca Peak Sight software (see Rose-Koga et al., 2020 for more details). The olivines were analysed with an accelerating voltage of 15 kV and 15 nA beam current. The total concentration of volatiles was determined by summing the counts from multiple iterations. Total counting times were 100 s for F and Cl peaks. The detection limits for F and Cl were 300 and 150 ppm, respectively. KE12 LMV, CFA47 (Spilliaert et al., 2006), and ALV-98I R23 (Hekin and

Walker, 1987) glasses and the San Carlos olivine were used as standards. Typical errors on the samples (1σ error of mean) are less than 10% for all elements analysed both in MI and in olivines.

6.3.2.2. Nano-SIMS analysis

High spatial resolution measurements of volatiles in minor and trace amounts in MI were conducted using the CAMECA nanoSIMS50 of the Muséum National d'Histoire Naturelle de Paris. All measurements were carried using a focussed Cs^+ primary ion beam accelerated to 16 keV in high vacuum conditions (< $8x10^{-10}$ mbar). Prior to acquisition, a 5 × 5 µm² region was pre-sputtered with a 280 pA primary beam for 2 minutes to remove the Au coat and ensure a clean surface. The current was then reduced to 20 pA and the inner 3 × 3 µm² were rastered over a 32 × 32 pixels matrix with a 1 ms/px dwell time during 100 cycles (~2 min). A numerical blanking was applied to 32 × 32 px matrix to consider only the innermost 1 × 1 µm² region, this in order to limit the contribution of potential contamination. A cloud of electron was generated above the sample's surface to avoid the accumulation of positive charges induced by the implantation of the Cs^+ beam. ^{12}C, $^{16}O^1H$, ^{28}Si, ^{32}S, and ^{35}Cl were acquired simultaneously in multicollection mode on 5 electron multipliers (Ems). Each measurement was corrected for the 44 ns of the detector's deadtime. We used a 20 × 140 µm entrance slit (#3) with a 200 µm diameter aperture slit (#2) and a 10% energy slit to optimize the Mass-Resolving Power (MRP) without compromising our transmission. This setting enabled a MRP > 8000 which ensured the separation of $^{16}O^1H$ and its isobaric interference ^{17}O. The standards used for the calibration of the different elements were: two glasses NIST 610 and 612; a Suprasil crystal; two basaltic glasses MRN-G1 and IND-G2 (Shimizu et al., 2017) and three internal standards STR 10-11-13 (Créon et al., 2018). All of this enables to achieve a statistically robust linear regression spanning a range of concentrations from wt% (H_2O) to hundreds of ppm (CO_2, S, Cl) (Figure S1 in the Supplementary Material S2). The nano-SIMS technique is typically associated with higher analytical precision (< 5%) and lower detection limits (< 10 ppm typically) for Cl (Rose-Koga et al., 2021) relative to electron probe (Rose-Koga et al., 2020). The Suprasil standards is a synthetic crystal known for its purity. It has been extensively used alongside Herasil crystal to assess the blank values for H_2O and CO_2 (e.g., Shimizu et al., 2021). By setting their concentrations at 0 in our calibrations we systematically subtract these blank contributions. Errors were estimated as the quadratic sum of the measured 1σ Poisson ratio error and the 1σ prediction/confidence interval local estimation and were subsequently reported as 2σ errors. For each measurement corrected by our determined linear

regression we can extract an error associated with the estimation through the 95% confidence interval. This error is then quadratically added to the error on the measurement itself (poissonian error on ratios).

6.3.2.3. Raman Spectroscopy

Raman spectra were collected using an inVia confocal Raman micro-spectrometer manufactured by Renishaw and equipped with a 532.1 ± 0.3 nm diode-pulsed solid state laser (200 mW output power), a Peltier-cooled CCD detector of 1040 × 256 pixels, and a Leica DM 2500 M optical microscope with a motorised XYZ stage, at the LMV. Scattered light was collected via a back-scattered geometry. Laser power was about 10 mW on the sample surface. A 100x microscope objective, a grating of 2400 grooves mm^{-1}, and a 20-μm slit aperture (high confocality setting) were used, which resulted in spectral resolution better than 0.4 cm^{-1} and in vertical and horizontal spatial resolutions of approximately 2-3 and 1 μm, respectively, near the surface of the sample. Calibration of peak positions was performed at room temperature, based on the 520.5 cm^{-1} peak of silicon and the 1331.5 cm^{-1} peak of a diamond standard; two Neon emission bands of 568.98163 and 576.44188 nm wavelengths were used to check the linearity of the spectrometer. For CO_2 measurements in MI bubbles, the spectra were recorded from 725 to 1880 cm^{-1} using the WiRE™ 4.4 software. Then, spectra were acquired in the 60-1320 cm^{-1} wavenumber range to detect presence of mineral phases (e.g., carbonates, sulphates) or fluid SO_2. Finally, spectra were collected in the 2800-3900 cm^{-1} region to detect H_2O and/or OH^- molecules. Acquisition time for a single CO_2 analysis was fixed at 60 s. Spectra were initially treated for removal of cosmic rays, and then an appropriate polynomial baseline correction was applied before fitting a combined Gaussian-Lorentzian curve to the CO_2 Fermi diad (e.g., Moore et al., 2015; Mironov et al., 2020; Schiavi et al., 2020). The analytical uncertainty associated with CO_2 density measurements is < 0.05 g/cm^3 (Boudoire et al., 2023). We used the densimeter of Wang et al. (2011) for the calculation of the bubble CO_2 density. Examples of Raman spectra acquired on shrinkage bubbles in melt inclusion are shown in Figure 29. In all shrinkage bubbles, only CO_2 was detected as fluid phase (Figure 29a).

6.3.2.4. Laser Ablation-ICPMS (LA-ICPMS)

Trace-element measurements on melt inclusions were carried out using a laser ablation system (193 nm Excimer Resonetics M-50E) associated with an inductively coupled plasma mass spectrometer (Agilent 7500 cs LA–ICP–MS at the LMV). Analysis was performed following classical procedures outlined in the previous studies (e.g., Rose-Koga et al., 2012). We used a pulse energy of about 3 mJ, a spot diameter between 15 and 33 µm, and a laser pulse frequency of 2–3 Hz, depending in the inclusion size to keep a fluence at sample surface of about 4 J/cm^{-2}. The background was measured for 30–40 s before ablation and analysis time was approximately 100 s. Data reduction was performed using the GLITTER software (Van Achterbergh et al., 2001). This technique uses CaO (measured by electron probe) as an internal standard. Reproducibility and accuracy of the analysis were constrained by systematic analysis of two standards BCR2-G and SRM NIST 612 at the beginning, in the middle and at the end of the session. Typical errors on the samples (1σ error of mean) are less than 10% for all trace elements analysed.

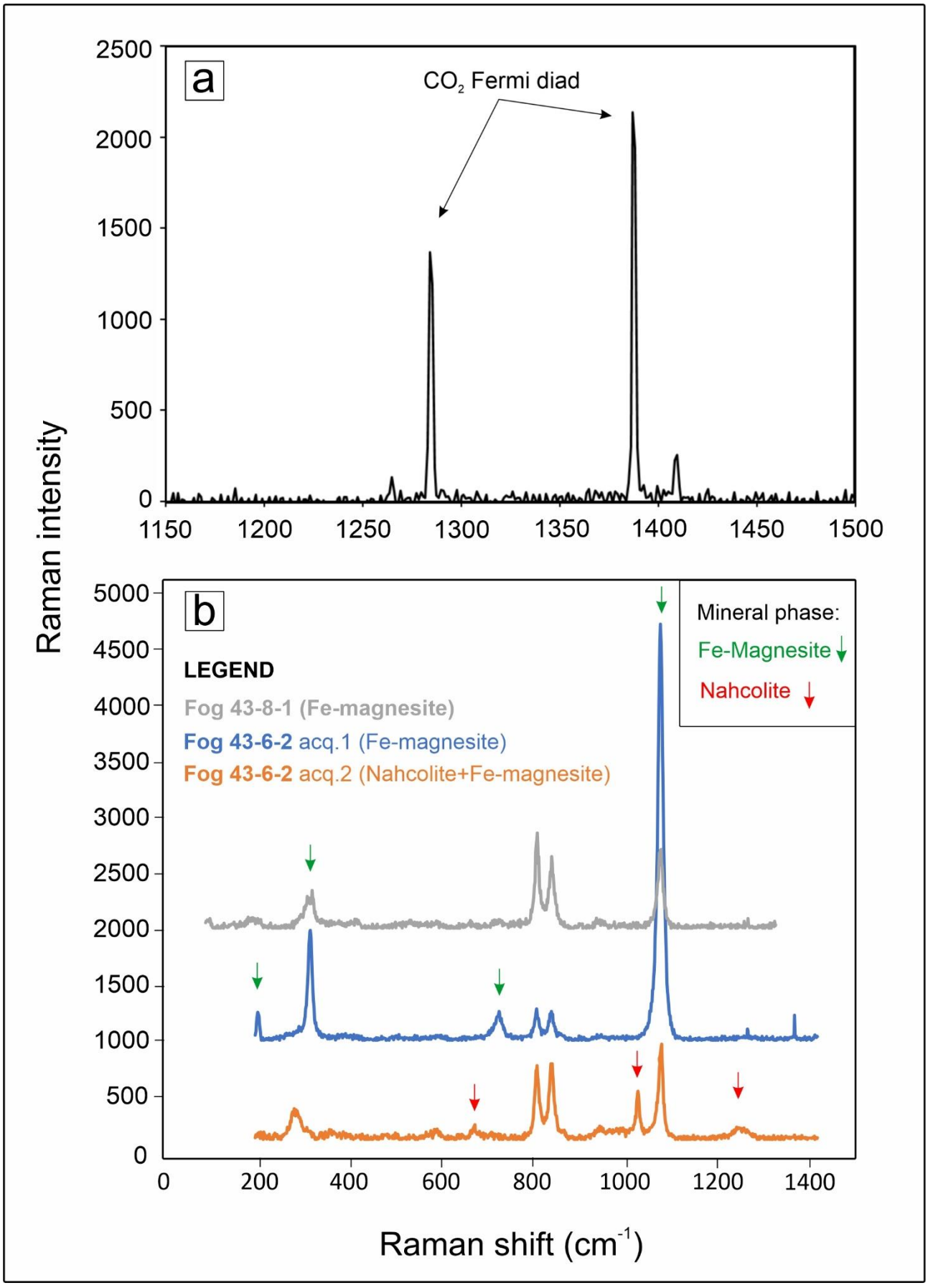
a
CO_2 Fermi diad
2500
2000
1500
1000
500
0
1150
1200
1250
1300
1350
1400
1450
1500
b
Mineral phase:
Fe-Magnesite
Nahcolite
LEGEND
Fog 43-8-1 (Fe-magnesite)
Fog 43-6-2 acq.1 (Fe-magnesite)
Fog 43-6-2 acq.2 (Nahcolite+Fe-magnesite)
5000
4500
4000
3500
3000
2500
2000
1500
1000
500
0
0
200
400
600
800
1000
1200
1400
Raman intensity
Raman shift (cm^{-1})

Figure 29 (a) Raman spectrum of melt inclusion shrinkage bubble (sample Fog 43-8-1). The bubble is made of pure CO_2, as revealed by the two strong peaks at 1284 and 1387 cm^{-1}, identified as Fermi diad (Kawakami et al., 2003). The separation between the two Raman bands of CO_2 is a reliable densimeter for the CO_2 fluid. **(b)** Raman spectra collected from the shrinkage bubble of Fog 43-8-1 (grey spectrum) and Fog 43-6-2 (orange and light blue spectra, acquired during tomographic analysis) MI samples. In the bubble, minerals such as Fe-magnesite and nahcolite were identified, as evidenced by peaks at 318, 737, and 1092 cm^{-1} for Fe-magnesite, $(Mg,Fe)CO_3$ (Boulard et al., 2012) and the peaks at 685, 1045, and 1266 cm^{-1} for nahcolite, $NaHCO_3$ (Fall et al., 2007). Both spectra also exhibit the characteristic olivine peaks at ~822 e 854 cm^{-1}.

6.4. Results

6.4.1. Whole-rock and mineral chemistry

The studied tephra samples are nepheline-normative (Ne= 17.6–21.2 wt.%) basanites (SiO_2 = 41.73–43.78 wt.%; $K_2O + Na_2O$ = 6.69-7.68 wt.%) (table 1 of Supplementary Data S1), with a common mineral assemblage represented by clinopyroxene, olivine, plagioclase, and Fe-Ti oxides. These tephra samples are part of the same suite analysed (for major elements and fluid inclusions) by Lo Forte et al. (2023). The olivine grains have euhedral shapes and exhibit a narrow range of compositions (forsterite mol% Fo_{80-85}) (table S3 of Supplementary Material S1). The olivine phenocrysts of sample SJ (Fog 43) are slightly more forsteritic (Fo_{83-85}) than the 1951 (Fog 8) and 2014/15 (Fog 11) olivines (Fo_{80-84}). The same SJ olivines exhibit higher CaO (0.34–0.40 wt%) and NiO (0.13–0.15 wt%) contents than the 1951 and 2014/2015 olivines (CaO, 0.31-0.39 wt.%; NiO, 0.03-0.15 wt.%). Mineral chemistry results are detailed in table S3 of Supplementary Material S1.

6.4.2. Melt inclusions: size and morphology

Olivines contain abundant MI, but only 13 % of them were large enough (> 25 μm) for trace element analyses. All studied inclusions are perfectly glassy, and elliptical in shape (Figure 30), with the long axis (a) ranging between 17.0 μm and 94.0 μm (mean, 49.6 μm) and the short axis (b) between 11.3 μm and 83.1 μm (mean, 40.7 μm). Different criteria are used in the literature to determine the size of the third semi-axis c (e.g., axis a > b =c, Hauri et al., 2018; Shaw et al., 2008, 2010; Wanless et al., 2014, 2015 ; geometric mean, Ni et al., 2017); direct measurements can be used to test different assumptions (Mironov et al., 2020). Here we use the criteria of Moore et al. (2015) that assumes axis

(c) equals to the arithmetic mean of axes (a) and (b) of the ellipsoid. Semi-axis (c) is therefore estimated at between 14.2 µm and 88.5 µm (mean, 37.8 µm). Shrinkage bubbles were observed inside all the MI (table S7 of Supplementary Material S1). However, in 31 % of the selected MI the bubbles were lost during the polishing process as the MI surface was exposed for analysis. The MI in which bubbles were lost are not considered further (except samples Fog 43-3-1 for which we report glass CO_2 contents only). There is no textural evidence of MI decrepitation. Roughly half of the shrinkage bubbles contain mineral phases such as Fe-magnesite, nahcolite, and sulphates (Figure 29b).

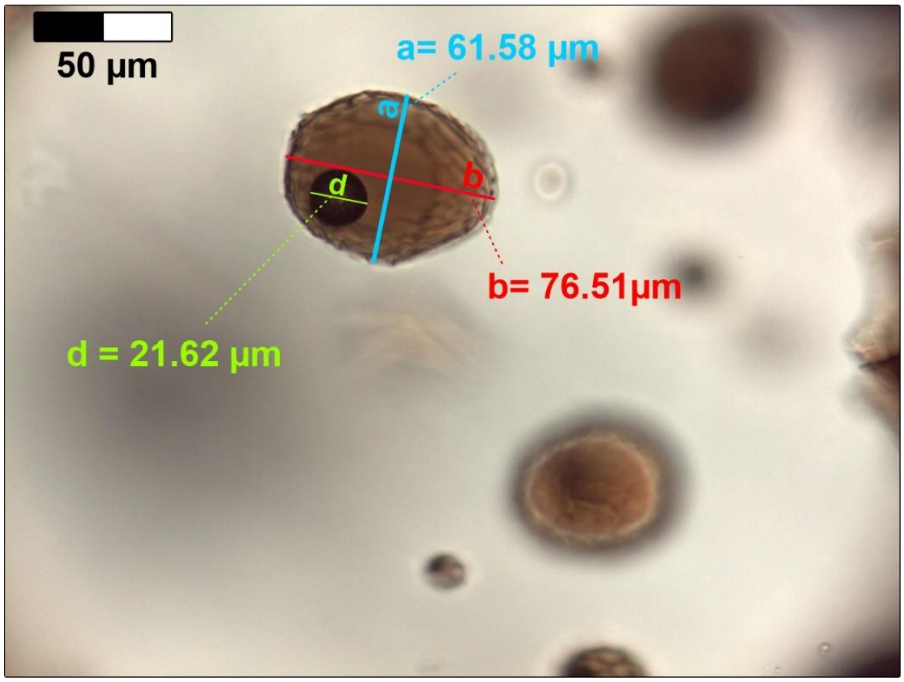

Figure 30 Measurements of the major (a) and minor (b) axes of the MI (Fog 43-6-3) for the determination of the melt volume and measurement of the diameter (d) of the shrinkage bubble for the calculation of its volume.

6.4.3. Melt inclusion major element compositions and post-entrapment correction (PEC)

Melt inclusion glasses are foiditic to basanitic and compositionally overlap with bulk rocks (Fig. 31a). They typically contain 39.89-45.95 wt.% SiO_2, 3.15-5.85 wt.% MgO, 3.13-5.32 wt.% Na_2O, and 8.07-10.74 wt.% FeO_t (Fig. 31). A variety of processes are known to potentially alter the melt composition after entrapment (see review in Wallace et al., 2021), including: (i) post-entrapment crystallization (PEC) of olivine at the MI-host mineral interface during slow cooling (Kent et al., 2008); (ii) volatile loss from the melt to the shrinkage bubbles (Wallace et al., 2015) or due to

inclusion decrepitation (e.g., Maclennan, 2017); (iii) hydrogen ('water') diffusive loss (Hauri, 2002; Massare et al. 2002; Portnyagin et al. 2008, 2019; Chen et al. 2011; Gaetani et al. 2012); (iv) iron, magnesium diffusive exchange between the inclusion and its host mineral (e.g., Danyushevsky et al., 2000; Cottrell et al., 2002; Gaetani and Watson, 2000, 2002). We correct the composition of olivine-hosted MI for PEC using MIMiC (Rasmussen et al., 2020). The code employs the (KD^{Fe-Mg}) model of Toplis (2005) and the olivine-melt thermometer of Putirka et al. (2007) to calculate the Fe-Mg olivine-melt partitioning (at redox conditions estimated by Moussallam et al., 2019) and to estimate magma temperature, respectively. Melt inclusion compositions, both pre- and post- MIMiC correction, are provided in tables S5 and S6 of Supplementary Material S1. PEC correction requires the addition of 0.03 to 9.28 % olivine to restore melt inclusion compositions to equilibrium with their hosts. The average PEC correction is 3.85 % for São Jorge (SJ) MI and 2.17 % for the two recent eruptions. Following PEC correction, melt inclusion compositions range 39.87-45.74 wt.% SiO_2, 4.00-7.36 wt.% MgO, 3.02-5.20 wt.% Na_2O, and 8.36-11.57 wt.% FeO_t. On the total alkali-silica diagram (Figure 20a), the PEC-corrected MI span the foidite to basanite compositional fields, with the most SiO_2-rich MI (41.74-45.74 wt.%) overlapping the range of the whole-rocks (compositions given in Lo Forte et al., 2023) and of bulk rocks from the literature (Hildner et al., 2011, 2012; Mata et al., 2017). These MI have MgO contents varying from 4.00 to 5.76 wt.%, TiO_2 from 2.44 to 3.06 wt.%, and P_2O_5 from 0.84 to 1.36 wt.%. The CaO/Al_2O_3 ratios vary between 0.88 and 0.97 for SJ MI, and between 0.44 and 0.84 for the 1951 and 2014/15 MI (Figure 31b).

We model fractional crystallisation (FC) (Figures 31b-d) to determine the extent of crystallisation at the time of entrapment, and to test if the melt follows the liquid line of descent (LLD) prior to be entrapped, or if instead points to some Fe-Mg diffusive exchange during crystallisation (Figure 31b, c). We start our simulations with a hypothetic parental melt composition corresponding to the primitive lava Fogo 16 from Hildner et al. (2012) (MgO = 9.79 wt.%; FeO = 12.03 wt.%). We assume an initial H_2O content of 2.0 wt.% (see below) and an oxygen fugacity of 1.5 log units above the Fayalite-Magnetite-Quartz buffer (ΔFMQ +1.5; Moussallam et al., 2019). Starting from this parental melt composition and an initial temperature of 1150 °C, we simulate the cooling-crystallisation trajectory using Petrolog3 (Danyushevsky and Plechov, 2011), using the melt-mineral equilibrium models of Danyushevsky, (2001) for olivine, clinopyroxene, and plagioclase, and Ariskin and Barmina, (1999) for magnetite. Results (Fig. 31b,c,d) show that the modelled LLD accurately reproduces the whole-rock compositional trend. After PEC correction, MI also match more closely the LLD and the bulk rocks trend (Figure 31b,c,d), implying diffusive Fe loss was minor (if any). No

correction was therefore applied. All raw and corrected MI compositions are listed in Tables S5 and S6 of Supplementary Material S1.

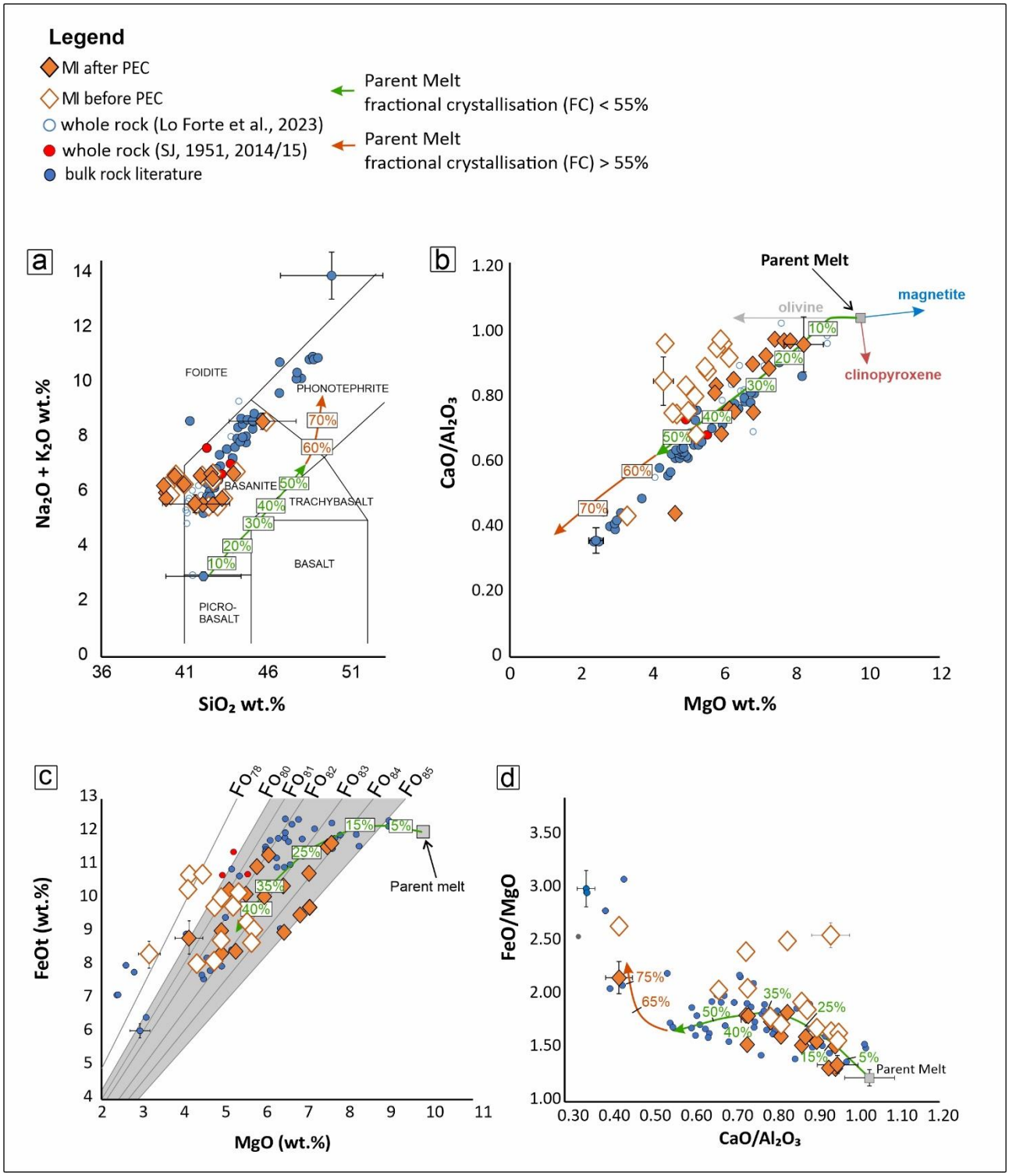

Figure 31 Total alkali-silica diagram (**a**) and major element compositions of melt inclusions (**b, c, d**) together with whole-rock compositions from Hildner et al. (2011, 2012), Lo Forte et al. (2023) and Mata et al. (2017). The solid lines are liquid lines of descent (LLD), calculated from a primitive parent melt (SiO_2 42.14 wt.%, MgO 9.79 wt.%, FeO 12.03 wt.%, Al_2O_3 12.41 wt.%, CaO 12.96 wt.%) using

Petrolog3 (Danyushevsky and Plechov, 2011). The LLD are calculated assuming initial H_2O content of 2 wt.% and oxygen fugacity of ΔFMQ +1.5 (Moussallam et al., 2019). We used the melt-mineral equilibrium models of Danyushevsky (2001) for olivine, clinopyroxene and plagioclase, and of Ariskin and Barmina (1999) for magnetite. The orange LLD was calculated for FC > 55%, to fit the more evolved MI (**d**). The grey area represents the range of forsterite component (Fo80-85) in the analysed olivines hosting MI (**a**).

6.4.4. Trace element composition

Table S5.2 of Supplementary Material S1 reports the concentrations of a selected suite of trace elements in the studied MI. The primitive mantle normalised trace element patterns (Fig. 32) (this study) match those of the bulk-rocks (Hildner et al., 2011, 2012; Mata et al., 2017). No negative Hf anomaly is observed, and the Zr/Hf ratios (averaging at 39) are comparable to the typical primitive mantle value (~36; Palme and O'Neil, 2003). The LILE (Large Ion Lithophile Elements)-enriched composition of Fogo melts is additionally corroborated by elevated Ba/La (15.0-20.3), Rb/Sr (0.05-0.07) and Rb/La (0.98-1.54) ratios (Weaver, 1991).

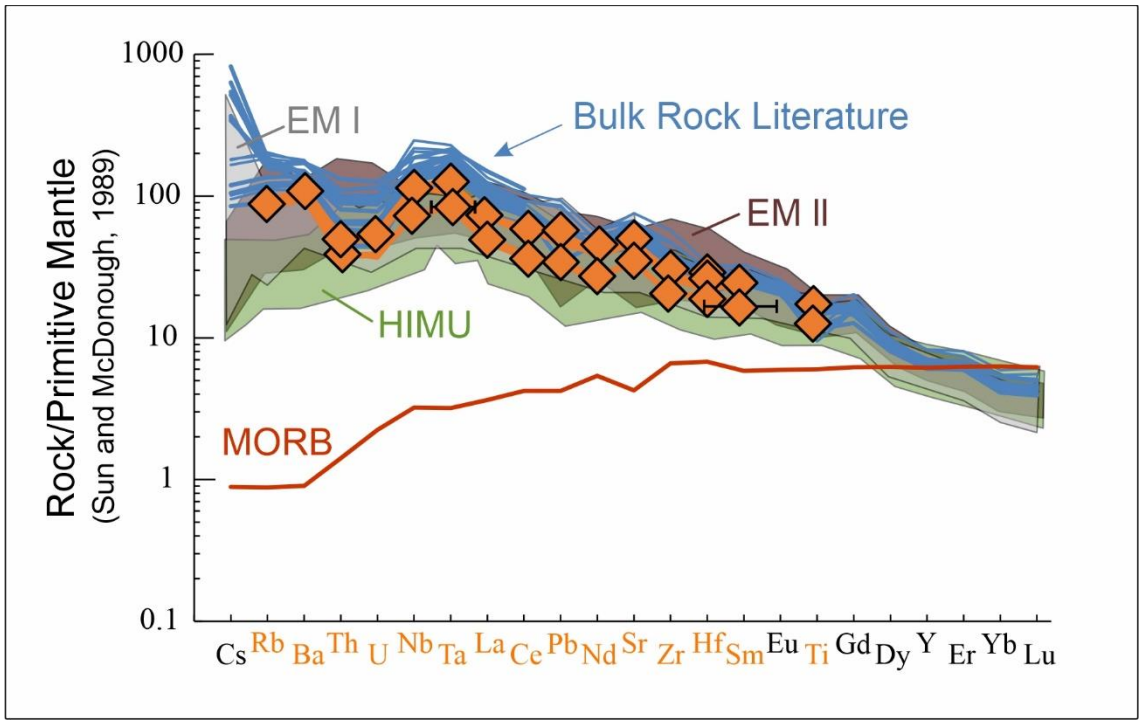

Figure 32 Primitive mantle-normalised (Sun and McDonough, 1989) trace element patters in MI samples (orange patterns; average values from all samples are used). The trace element patterns are intermediate between the compositional ranges of enriched mantle sources (EM-I and EM-II; data from Willbold and Stracke, 2006) and the HIMU mantle source (Willbold and Stracke, 2006). Note the significant Nb and Ta enrichment relative to the light REE. The red line identifies the compositions of Mid-Oceanic Ridge Basalts (MORB; Sun and McDonough, 1989).

6.4.5. Volatiles

All the melt inclusion glasses are volatile-rich and contain 1.97 to 2.79 wt.% H_2O and 9002 to 16044 ppm CO_2 in SJ MI (Fig. 33a). MI glasses from recent (1951-2014/15) eruptions are slightly less CO_2-rich than the SJ MI glasses and contain 1.20 to 2.92 wt.% H_2O and 1239 to 9102 ppm CO_2 (Fig. 33; Table S5.1 Supplementary Material S1). CO_2 in MI glasses broadly decreases with increasing degree of melt evolution, e.g., with decreasing CaO/Al_2O_3 (Fig. 22b) and MgO (Fig. 22d) and increasing FeOt/MgO (Fig. 22c). The SJ MI glasses exhibit higher S concentrations (2676-7794 ppm) than the 1951 and 2014/15 MI (1146 to 5509 ppm) (values measured by nano-SIMS, Tables 5 and S5.1 Supplementary Material 1). Chlorine concentrations, measured by nano-SIMS, range from 947 to 1358 ppm in SJ MI and from 956 to 1415 ppm for the recent eruptions. The measured fluorine concentrations are 1285-2216 ppm in SJ MI glasses and 1617-2249 ppm in the 1951-2014/15 MI glasses. For each element, a general least-squares linear regression was calculated, along with both 95% confidence and prediction intervals. This process allowed us to extract an error associated with the estimation through the 95% confidence interval for each measurement corrected by the determined linear regression. Subsequently, this error was quadratically added to the measurement itself. The absolute and relative errors were most pronounced for very low concentrations outside the range covered by our set of standards. As we extrapolated to higher concentrations, absolute errors increased. However, for measured concentrations (on average, >2000 ppm), the relative error rose less drastically compared to lower concentrations. For further details, please refer to Table S9 in Supplementary Material S1 and Figure S2 in Supplementary Material S2. The PEC-corrected concentrations vary as follows: 1.9-2.7 wt.% (SJ MI) and 1.2-2.8 wt.% (1951 and 2014/15 eruptions) for H_2O (Fig. 33a); 2621-7718 ppm (SJ) and 1120-5250 ppm (1951-2014/15) for S; 917-1328 ppm (SJ) and 934-1415 ppm (1951-2014/15) for Cl (Fig. 34). As typical of alkaline magmas in general (Webster et al., 2018), the Fogo MI glasses are especially Cl- and F-enriched (up to 1415 and to 2249 ppm) relative to other OIB localities (Fig. 34), being only matched by the El Hierro basanitic MI (Taracsák et al., 2019). The Fogo MI have F/Cl ratios in the 1.2 to 2.4 range, i.e., higher than F/Cl values of most arc magmas, exception made for F/Cl reaching 2.5 in the Trans Mexican arc (Vigouroux et al., 2008) and in the Central American arc (Sadofsky et al., 2008; Fig. 34). This F-rich signature is a distinctive characteristic of OIB magmas in general (Kendrick et al., 2014).

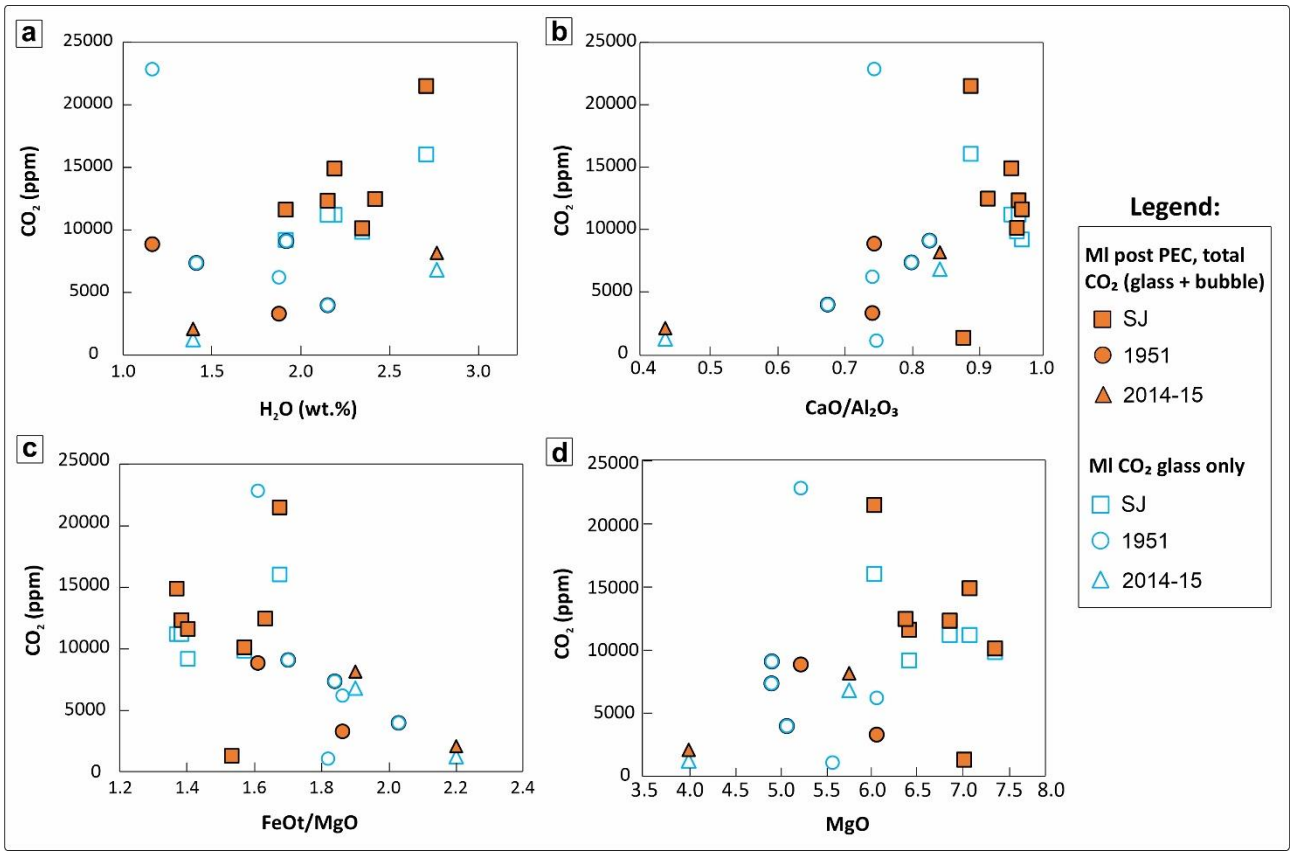

Figure 33 CO_2 concentrations vs. H_2O (**a**), CaO/Al_2O_3 (**b**) and FeOt/MgO (**c**) ratios, and MgO (**d**). The SJ MI exhibit higher H_2O and CO_2 contents than those from the more recent eruptions in 1951 and 2014-15. The orange symbols represent data related to the total CO_2 content in the MI (glass + bubble), corresponding to measurements obtained through Raman-based total CO_2 estimates (see section 5.1 for further details).

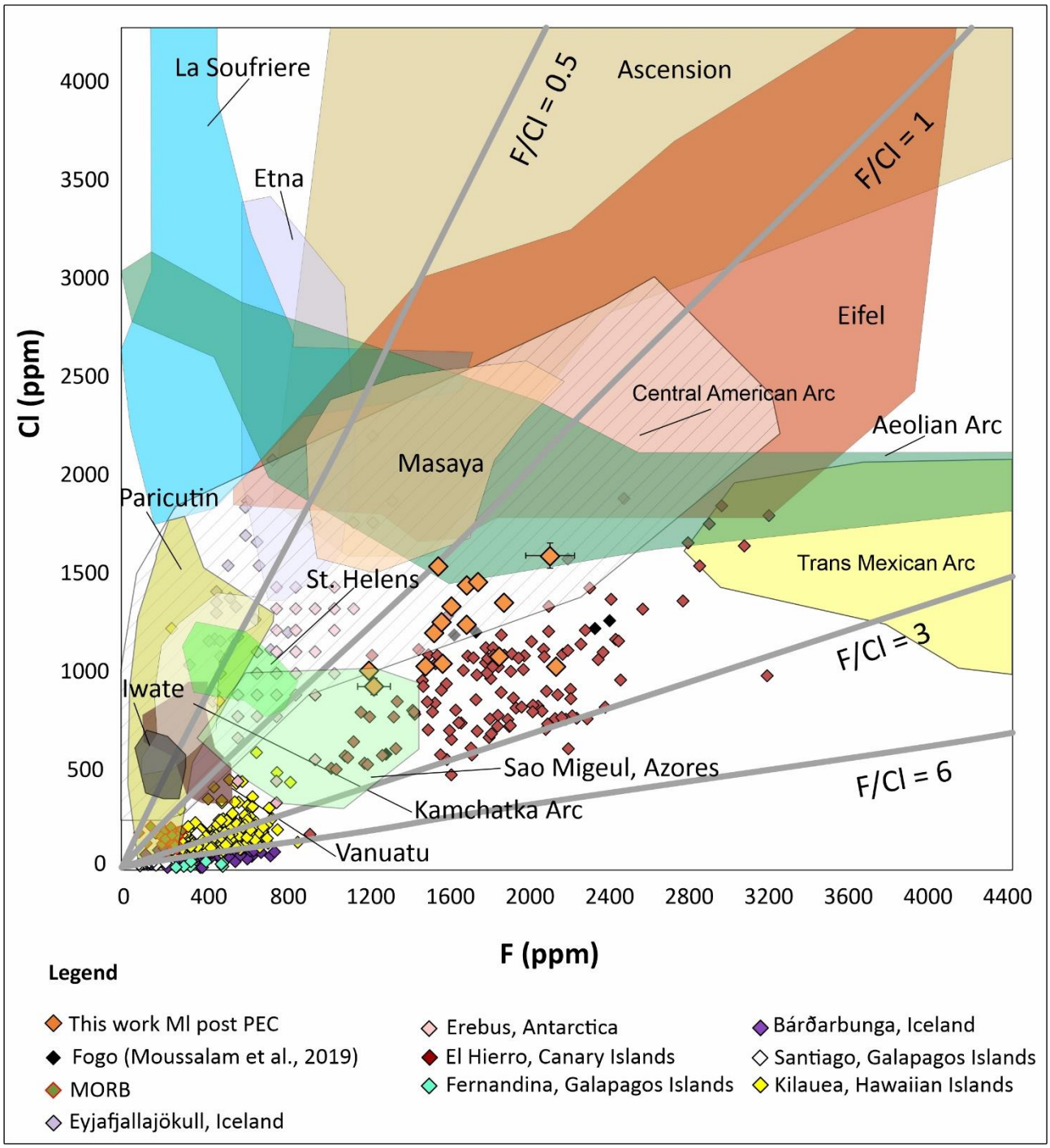

Figure 34 In the F vs. Cl plot, our data are compared to MI of different OIB localities and from volcanoes of different geodynamic contexts, such as Ascension (Webster and Rebbert, 2001), Etna (Métrich et al., 1993, 2004), La Soufriere (Heath et al., 1998), St. Helens (Blundy and Cashman, 2005), Parìcutín (Rowe et al., 2011), Trans Mexican belt (Vigouroux et al., 2008), Central American belt (Sadofsky et al., 2008), Vanuatu (Métrich et al., 2011), Eifel (Harms and Schmincke, 2000), Aeolian islands (Di Martino et al., 2011), Masaya (Pérez et al., 2020), and Kamchatka volcanoes (Portnyagin et al., 2011). The F/Cl ratios of our MI (1.16-2.41) fall in the field of OIB volcanoes and partially overlap the composition of El Hierro MI.

6.5. Discussion

6.5.1. Reconstructing the total (glass+bubble) CO_2 content in MI

Our results show that the Fogo MI glasses contain up to ~1.6 wt.% CO_2 (Fig. 22), plus ~2 wt.% H_2O and ~0.48 wt.% S, on average. However, all MI also contain CO_2-rich bubbles (Fig. 29). There is a positive relationship between total MI volumes and bubbles volumes (Fig. 35a), indicating that all MI contain similarly low bubble volumetric fractions (0.2-8.6 %). We conclude that the contemporaneous entrapment of melt and fluid inclusions is unlikely (Rasmussen et al., 2020), and therefore all fluid bubbles found are shrinkage bubbles. Hence, as recently demonstrated elsewhere (Taracsák et al., 2019), reconstructing the total MI CO_2 budget requires a procedure in which the CO_2 masses contained in (i) shrinkage bubbles and (ii) glass are both fully taken into account.

The CO_2 mass contained in the glass is initially calculated by multiplying glass mass in the MI (glass density × glass volume) by CO_2 concentration in the glass (cfr. 4.5). Glass density is derived using MIMiC (Rasmussen et al., 2020), which uses the relationships of Lesher and Spera (2015), while glass volume is estimated following the procedure of Moore et al. (2015).

Next, we quantify shrinkage bubble CO_2 using three different, independent methodologies: (i) the Raman method (Esposito et al. 2011; Hartley et al. 2014; Moore et al. 2015; Rasmussen et al. 2018); (ii) the Simulated-volume method (Rasmussen et al., 2020); and (iii) the Observed-volume method (e.g., Shaw et al., 2010; Wanless et al., 2014; Hauri et al., 2018; Tucker et al., 2019). Our aim is to use the level of agreement/disagreement of these different methods as a proxy for the level of accuracy/inaccuracy of such bubble CO_2 estimates (Fig. 35).

In the Raman method (Hartley et al., 2014; Moore et al., 2015; Moore and Bodnar, 2019; Rasmussen et al., 2020), the bubble CO_2 mass is derived as the product of bubble CO_2 density × bubble volume. Raman indicates a pure-CO_2 gas phase composition for the shrinkage bubble (Figure 29 a); we hence apply the densimeter by Wang et al. (2011) for the calculation of the bubble CO_2 density.

The other two CO_2 estimates (Simulated and Observed) are derived using the MiMiC code (Rasmussen et al., 2020). The Simulated-volume method relies on estimating bubble volumes and CO_2 contents from modelling the growth of bubbles during the cooling and quenching of the melt inclusions (rather than directly measuring bubble volumes). This bubble growth model assumes that exchange of CO_2 between melt and bubble terminates at a CO_2 closure temperature (T_c) for diffusion (generally higher than the glass-transition temperature) followed by further bubble expansion with no CO_2 loss to bubble (Rasmussen et al., 2020).

Finally, the Observed-volume method (e.g., Shaw et al. 2010; Wanless et al. 2014; Hauri et al. 2018; Tucker et al. 2019) uses directly measured bubble volumes and entails determining the CO_2 mass within the vapor bubble by applying the modified Redlich-Kwong (MRK) equation of state. The method relies on the assumption that vapor-melt equilibrium is maintained throughout the entire bubble quenching/growth history. The temperature of vapor-melt equilibrium is determined based on the calculated glass-transition temperature, which however can vary significantly by several hundred degrees Celsius, depending on factors such as melt viscosity and cooling rate (Giordano et al., 2005). All three CO_2 restoration methods have their caveats and limitations which can potentially lead to overestimation/underestimation of the total MI CO_2. Use of the Raman restoration method (e.g., Esposito et al., 2011; Moore et al., 2015), in particular, is challenged by difficulties in (i) correctly measuring melt inclusion geometry, and hence glass vs. bubble volumes (Moore et al., 2015) and (ii) quantifying the relative volumetric fractions occupied by minerals and fluid in the bubble (Schiavi et al., 2020). Determination of melt inclusion geometry (glass and bubble volumes) in principle requires accurate 3D scanning microtomographic analysis, which is rarely available. Our glass/bubble volumes (Table S7 of Supplementary Material S1) are estimated from 2D analysis, and on the assumption that the length of the third semi-axis c (normal to the polished plane) equals to the arithmetic mean of axes a and b (Moore et al., 2015); this assumption should, at least in principle, introduce a relatively minor (5%) error (Wallace et al., 2015). More problematic is to account for the carbon mass sequestered in mineral phases inside the bubble. Recent studies have found that mineral phases such as carbonates, sulphides, sulphates and native sulphur can precipitate inside bubbles during cooling (e.g., Kamenetsky et al., 2002; Hartley et al., 2014; Moore et al., 2015; Esposito et al., 2016; Robidoux et al., 2018; Guzmics et al., 2019; Tucker et al., 2019; Schiavi et al., 2020; Venugopal et al., 2020; Buso et al., 2022; Feignon et al., 2022). Precipitation of these minerals can potentially sequester large fractions of the bubble-carried CO_2, hence ignoring their presence can result in significant (up to 40%) underestimation of the total MI CO_2 (Schiavi et al., 2020). We detected the presence of carbonate phases, such as Fe-magnesite and nahcolite (Supplementary Material S2 Figure S2), and sulphates, in roughly 50 % of the Raman spectra. The proportions of the different phases are highly variable. Raman microtomography revealed significant volumes of carbonates crystallised on the walls of the MI Fog 43-6-2 bubble, amounting to ~35 vol% according to an approximate average estimate based on few 2D sections extracted from the 3D map (Supplementary Material S2 Figure S2). This corresponds to ~25% of the CO_2 sequestered in the bubble (compared with 9% reported in Table S7 of the Supplementary Material S1). We conclude that the total CO_2 content can be

underestimated (by about 15-20 % for MI Fog 43-6-2) if carbon stored in carbonates inside the bubble is neglected. However, considering the overall positive correlation observed between glass MI CO_2 and shrinkage bubble density (Fig. 35b), we conclude that precipitation of carbonates is likely to be marginal in all samples except Fog 43-8-1 and 43-6-2 (that coherently exhibit the most intense Raman peaks associated with carbonates).

The second CO_2 restoration methodology used (Simulated-volume method) overcomes some of the limitations above, as it does not rely on measured bubble volumes, but rather on estimated bubble volumes based on modelling bubble growth during MI cooling and quenching. The detailed sensitivity study of Rasmussen et al. (2020) demonstrates that the amount of cooling experienced by MI, from their entrapment temperature (T_e) to their CO_2 closure temperature (T_c), is the key parameter controlling the extent of CO_2 loss to bubbles. According to Rasmussen et al. (2020), this cooling extent ($T_e - T_c$) depends on MI dimension (measured texturally) and cooling rate, for which we unfortunately have no independent estimate. In such conditions, MIMiC adopts a calculated cooling rate derived by solving the Dodson equation for the magnesium closure temperature (T_c(MgO)); this procedure can potentially introduce a maximum error of 50% on the restored CO_2 concentrations (when the used T_c(MgO) is in excess of by one order of magnitude).

Finally, the Observed-volume method calculates the CO_2 mass in the bubble by applying an equation of state and performing a mass balance. In this approach, the observed bubble volume, measured under the microscope, used in the calculation assumes that melt-bubble equilibrium is maintained throughout the entire bubble growth history. However, if equilibrium is not maintained, the calculation based on the observed volume may not be accurate. Additionally, this method assumes the glass transition temperature (T_g) as the final melt-bubble equilibrium temperature, but precisely assessing T_g is complicated by its strong dependence on factors such as cooling rate, melt composition, melt viscosity, and volatile content (Rasmussen et al., 2020).

Ultimately, since all restoration methods have limits and caveats, a multi-method approach is advisable (Rasmussen et al., 2020). The outputs of the three restoration methods used here are compared in Figures 35c and 35d. We find that the Raman spectroscopy measurements and simulated-volume approach yield CO_2 concentrations that agree within 9.7 % on average (range: 0.4-22.6 %). The agreement between these two independent methodologies provides confidence in our restored total MI CO_2 values. The total MI CO_2 contents determined with the observed-volume method also positively correlate with those inferred from Raman analysis (Fig. 35d), but typically plot above the 1:1 line, indicating that the observed-volume approach may systematically over-estimate the MI CO_2

budget, as already suggested (Moore et al., 2018; Rasmussen et al., 2020). Rasmussen et al. (2020) also found that the concentrations reconstructed from both Raman measurements and the simulated-volume method are quantitatively consistent with those obtained by re-homogenising MI at high temperature and pressure – this latter procedure being considered as that yielding the most accurate CO_2 reconstructions. Ultimately, while we are well aware of the many existing potential sources of uncertainty, we conclude that our calculations bring nonetheless robust evidences that (i) in some cases of OIB MI, a large fraction (up to~50 %) of the MI CO_2 is contained in the bubbles (Mironov et al., 2015), and (ii) the total (glass+bubble) CO_2 content in the Fogo parental melt is certainly > 1 wt. %, and potentially as high as ~2 wt. % (the highest value obtained by the Raman and Observed-volume methods). For the sake of simplicity, in the discussion below we refer to the Raman-based bubble (and hence total) CO_2 estimates, but we note that these overlap with those derived from the bubble growth model using MiMIC by a factor of <10%.

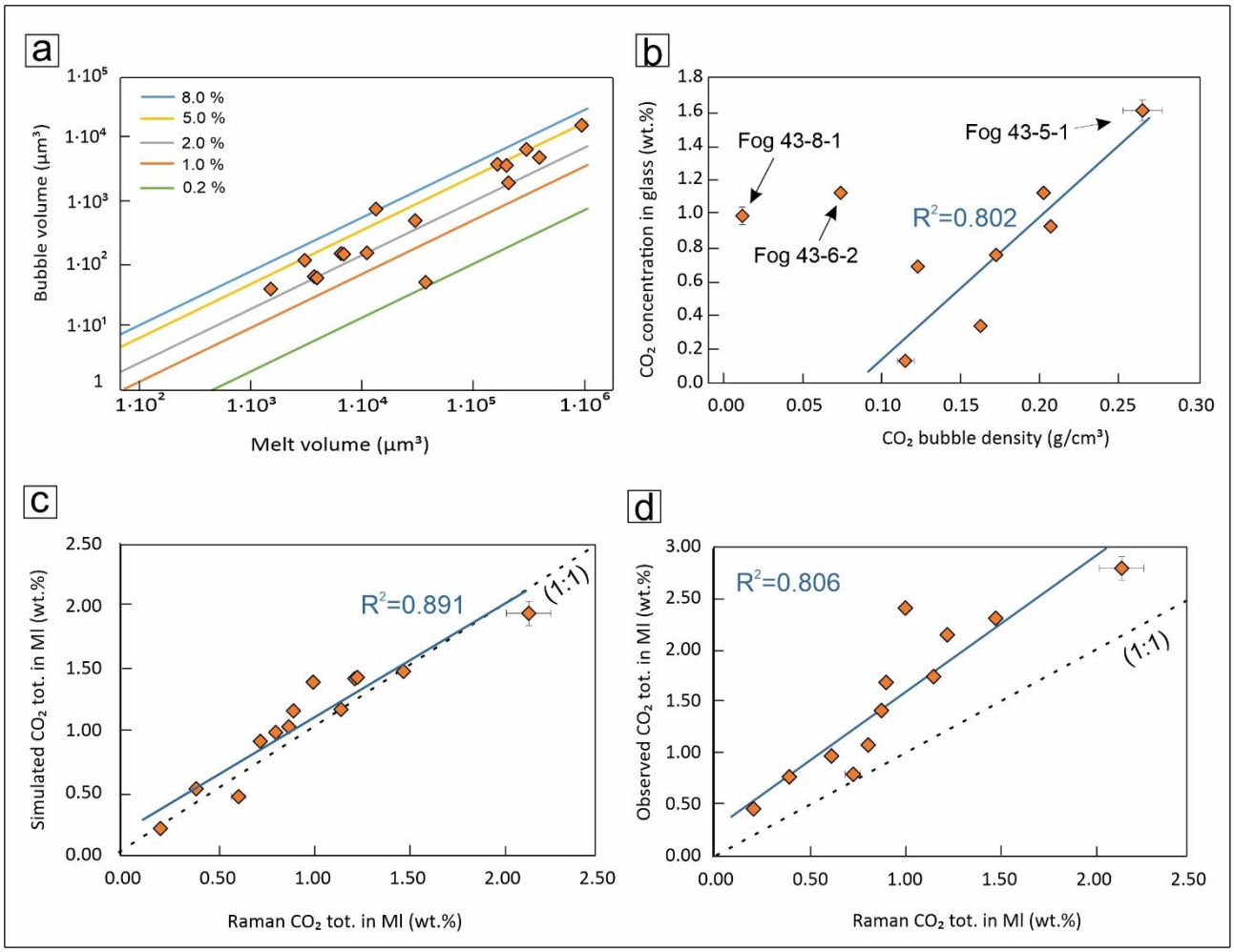

Figure 35 (**a**) Plot of bubble volumes as a function of MI volumes; isovolumetric lines corresponding to bubble/MI volume ratios of 0.2 %, 1.0 %, 2.0 %, 5.0 %, and 8.0 % are also shown. (**b**) The plot shows a positive correlation between the CO_2 calculated in the glass and the density of the shrinkage bubble, except for the two samples (Fog 43-8-1 and 43-6-2) which exhibit intense Raman peaks associated with carbonates, specifically Fe-magnesite and nahcolite crystals on the bubble wall (Fig. 2). As shown in (b), the overlooked presence of carbonates in the bubble leads to an underestimation of the total CO_2 content. Excluding these two outliers, the samples show a good correlation (R2 = 0.802). Plot of the total CO_2 concentration in MI, calculated using the Raman and Simulated methods (**c**) and the Raman and Observed methods (**d**). In plot (**c**), there is a strong correlation (R2=0.891), with CO_2 concentrations from Raman and Simulated-volume methods showing a 1:1.1 relationship. In contrast, in plot (**d**), the total CO_2 calculated using the Raman and Observed-volume methods is not strongly correlated (R2=0.806), with a ratio of 1:1.6. The dashed lines correspond to a ratio 1:1.

6.5.2. A CO_2-rich parental melt

Finally, glass CO_2 mass and shrinkage bubble CO_2 mass are summed to obtain total CO_2 mass in MI, which is ultimately converted in total CO_2 concentration in the MI. All calculations, for each MI analysed, are given in Table 4 and in Table S7 of Supplementary Material S1. Using the Raman method results described above, we find that bubbles contain 281-5546 ppm CO_2 (for the SJ MI) and 857-2920 ppm CO_2 (for the 1951 and 2014/15 MI). The total CO_2 contents thus range from 1309 to 21502 ppm for SJ MI, and from 1084 to 9102 ppm for the 1951 and 2014/15 eruptions (Fig. 33). We thus estimate that 3 to 47 % of the total MI CO_2 content is contained in the bubbles.

Table 4. Summary of the total CO_2 content (bubble + glass) calculated in the analysed melt inclusions using three different methods (Raman, Simulated, and Observed).

Sample	CO_2 wt% in MI (Raman Method)	CO_2 wt% in MI (Simulated Method)	CO_2 wt% in MI (Observed Method)
Fog 43-3-1	1.25	1.43	/
43-5-1	2.15	1.95	2.75
43-6-1	1.49	1.48	2.31
43-6-2	1.23	1.42	2.15
43-6-3	1.16	1.18	1.74
43-6-4	/	/	/
43-7-1	0.13	/	/
43-8-1	1.01	1.40	/

Fog 8-1-1	0.40	0.54	0.77
8-4-1	0.89	1.03	1.41
8-7-1	0.74	0.92	0.79
8-8-1	0.91	1.16	1.69
8-11-2	0.62	0.47	0.97
8-11-3	/	/	/
8-11-4	0.11	/	/
8-11-5	/	/	/
Fog 11-2-1	0.21	0.22	0.46
11-3-1	0.82	0.99	1.08

Our results show that the basanitic melts from Fogo are exceptionally CO_2-rich. Their volatile-rich nature is additionally demonstrated by high halogen contents (Fig. 34). The estimated CO_2 content of the parental melt (2.15 wt.%) is up to a factor 10 higher than for other OIB localities (e.g., Erebus in Antarctica, Moussallam et al., 2014; Fernandina and Santiago in the Galapagos, Koleszar et al., 2009; Piton de la Fournaise in Reunion Island, Di Muro et al., 2014 ; Kilauea in the Hawaii, Sides et al., 2014; Pico in the Azores, Métrich et al., 2014) and in the near ridge OIB localities such as Iceland (e.g., Bardabunga, Bali et al., 2018, and Laki, Hartley, 2014) (Fig. 36a). In addition to confirming that bubbles do matter if the CO_2 MI budget is to be reconstructed (Moore et al., 2015; Rasmussen et al., 2020; Buso et al., 2022), our novel results also corroborate recent work that shows that alkali rich OIB magmas are especially carbon-rich, as observed at El Hierro (CO_2 up to 4 wt.% ; Longpré et al., 2017; Moussallam et al., 2019; Taracsák et al., 2019) and La Palma (3-5 wt. % ; e.g., Burton et al., 2023) in the Canary Archipelago, and at Piton de La Fournaise in La Reunion Island (3.5 ± 1.4 wt.%, Boudoire et al., 2018) (Fig. 36a) (note that in these studies shrinkage bubble CO_2 has been accounted for with either observations or modelling). The fact that alkali rich OIB volcanoes erupted magmas richer in CO_2 than alkali poor OIBs has been documented at a global scale (Sun and Dasgupta, 2023), although we see no evidence in our MI of the extremely high (9-10 wt.%) CO_2 contents inferred by these authors for the Cape Verde archipelago parental melts. Rather, the ~2 wt. % CO_2 content we estimate for the Fogo parental melt is at the lower range of the measured/inferred (Hudgins et al., 2015; Aiuppa et al., 2021) CO_2-enriched signatures of alkaline mafic melts from continental rift context (e.g., in the East African rift system; Foley et al., 2012). This link between high CO_2

compositions and melt enrichment in alkalis (and other incompatible elements; Aiuppa et al., 2021) is further explored below (Fig. 37).

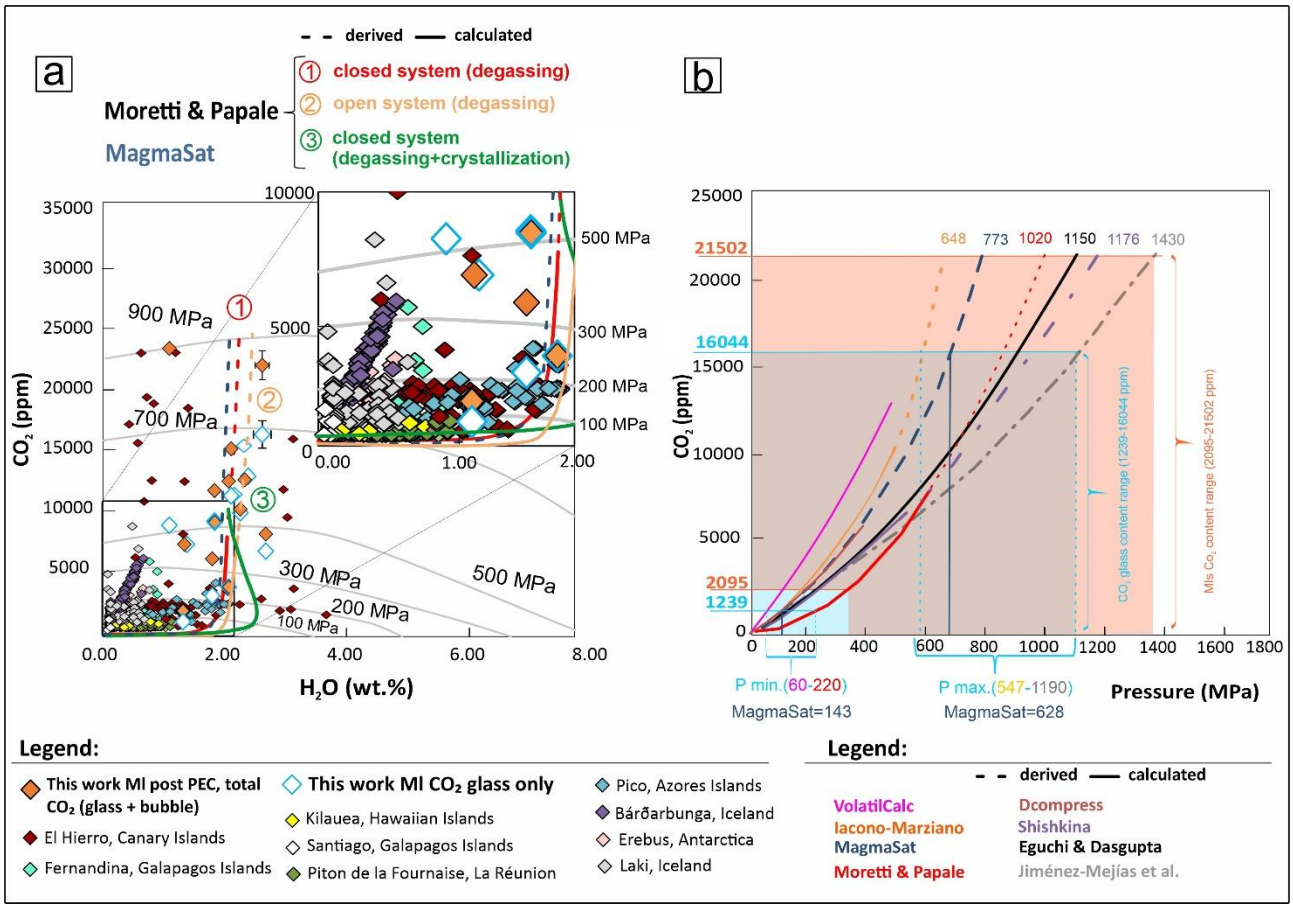

Figure 36 (**a**) H_2O and CO_2 concentration in studied MI and in other OIB occurrences. Isobars were calculated using an average composition of our MI samples at temperature of 1150 °C and an oxygen fugacity of ΔFMQ +1.5 (Moussallam et al., 2019). Degassing paths, in a closed system, were calculated using the volatile saturation models by Moretti et al. (2003) and MagmaSat (Ghiorso and Gualda, 2015), with the same input melt composition and temperature and volatile contents of 21502 ppm and 2.0 wt.% for CO_2 and H_2O respectively. (**b**) In the CO_2 content vs. Pressure graph, different saturation models are compared. The solid lines represent the outputs of the different models, instead the dashed lines represent the extrapolations of these models.

6.5.3. Clues from CO_2 vs. trace-element correlations

A potentially useful approach to test the accuracy of our reconstructed MI CO_2 content is to normalize them to the measured Nb and Ba contents in the same MI glasses (Fig. 37). These trace elements are thought to have similar bulk mineral/melt distribution coefficients to that of carbon (e.g., Rosenthal et al., 2015; Hirschmann, 2018). Hence, the CO_2/Nb and CO_2/Ba ratios should not be fractionated

during mantle melting and fractional crystallisation of mafic melts. If a mantle-sourced melt has not degassed CO_2 during crustal emplacement, it is thus expected to preserve a record of its source mantle CO_2/trace element ratio (e.g., Saal et al., 2002; Michael and Graham, 2015; Shimizu et al., 2016; Le Voyer et al., 2017; Hauri et al., 2018; Tucker et al., 2019). Following these premises, the expected range of mantle CO_2/Nb (Fig. 26a) and CO_2/Ba (Fig. 37b) have been inferred (see grey filled diagonal bands in Figure 37) from analysis of MORB that, owing to their volatile-depleted nature, are thought not to have reached volatile saturation before eruption (undegassed MORB; Michael and Graham, 2015) or entrapped as MI (e.g., Saal et al., 2002; Le Voyer et al., 2017; Moussallam et al., 2023). OIB magmas, in contrast, owing to their volatile enriched nature, do systematically reach saturation during ascent (Dixon and Stolper, 1995) and, even more significantly, form post-entrapment shrinkage bubbles that can sequester a large fraction of the MI CO_2 upon cooling and decompression (Hartley et al., 2014; Moore et al., 2015; Wallace et al., 2015; Tucker et al., 2019; Schiavi et al., 2020). As noted above, most MI results from the literature refer to glass measurements only, in which no correction for CO_2 in the bubbles has been attempted (with exceptions; Taracsák et al., 2019; Tucker et al., 2019); unsurprisingly, these plot below the mantle field in Figure 37, implying their CO_2/trace element ratios underestimate the source mantle ratios, owing to extensive CO_2 loss to bubbles, pre- and post-entrapment (e.g., Hartley et al., 2014).

Considering the highest reconstructed total CO_2 contents only, our MI exhibit a relatively narrow range of CO_2/Nb (277-283) and CO_2/Ba (26-22) (Fig. 37). This is at the lower limit (CO_2/Nb), or below (CO_2/Ba), the interval of representative ratios proposed for the upper mantle, based on the analysis of MORB MI and/or undegassed MORB glasses (Fig. 37). It is important to recall that, in their recent global compilation, Sun and Dasgupta (2023) have proposed that the mantle source of OIB volcanism is characterised by higher CO_2/Nb (~1850) and CO_2/Ba (~226) ratios than the depleted mantle source feeding MORB volcanism. Overall, Fig. 37 indicates that, in spite of our applied correction for CO_2 in shrinkage bubbles, our reconstructed total CO_2 concentrations likely still underestimate the real parental melt CO_2 contents, potentially because of early (before MI formation) CO_2 separation from melt into the vapour phase (e.g., Rosenthal et al., 2015; Le Voyer et al., 2017; Hirschmann, 2018; Aiuppa et al., 2021).

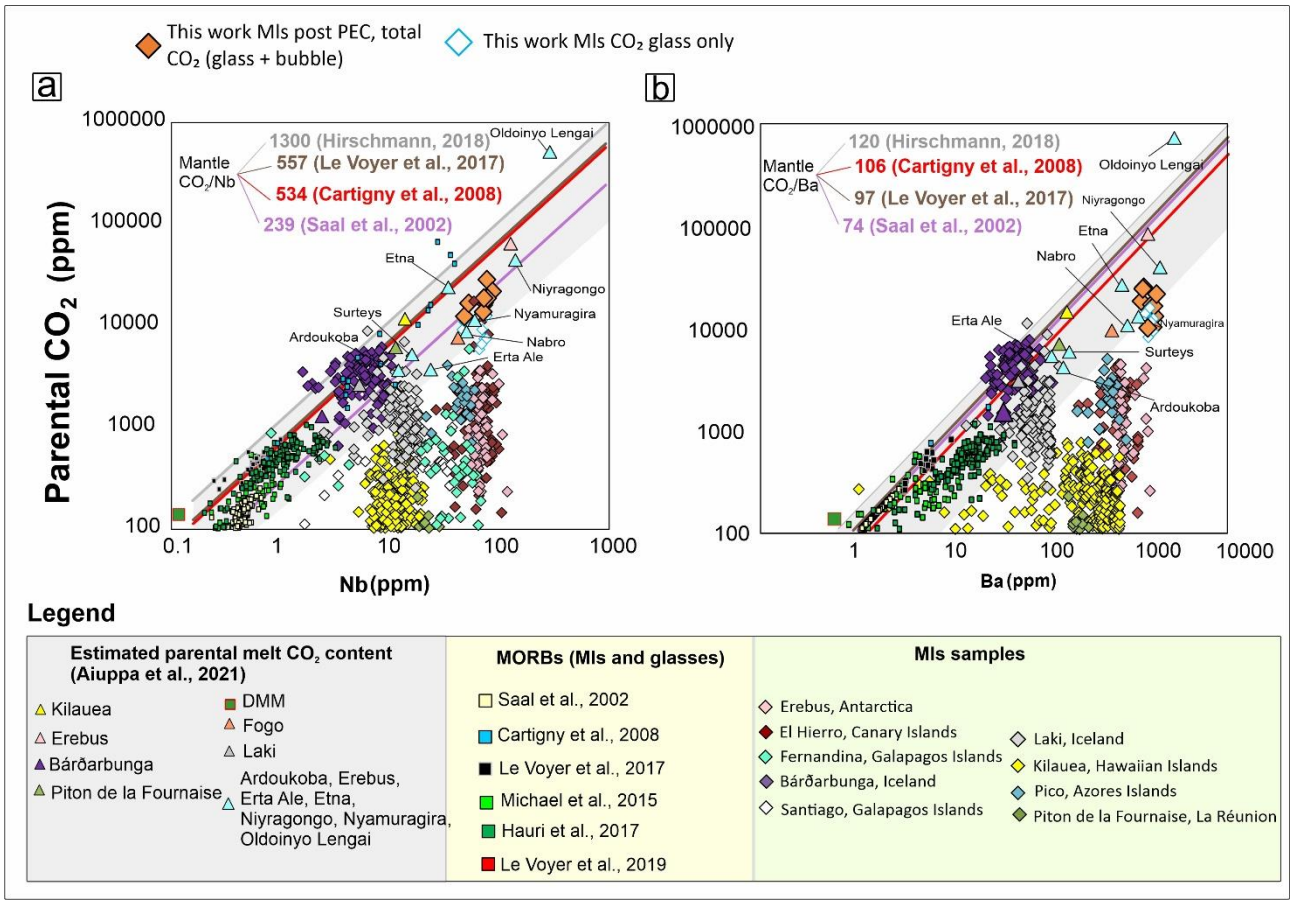

Figure 37 CO_2/trace element ratios. (**a**) In the Nb versus CO_2 plot, most of the literature "degassed" MI and our MI with the CO_2 content measured in the glass only (white diamond with light blue border) plot below the CO_2-Nb mantle array (represented by the grey area), as defined by the un-degassed MI and glasses of the MORB (characteristic upper mantle CO_2/Nb ratios from refs. Saal et al., 2002; Cartigny et al., 2008; Le Voyer et al., 2017; Hirschmann, 2018). Contrarily, our MI with the total CO_2 content (orange symbol, CO_2 glass+CO_2 bubble) fall in the mantle array field. (**b**) same as (**a**) but using Ba. Our MI with the total CO_2 content fall within the CO_2/Ba mantle range, 74-120 (Saal et al., 2002; Cartigny et al., 2008; Le Voyer et al., 2017; Hirschmann, 2018). In contrast, literature "degassed" MI and our MI with CO_2 measured only in the glass plot below the CO_2/Ba mantle array.

6.5.4. High CO_2 implies deep magma storage

The important implication of the high CO_2 contents of the studied MI is that magma must be stored deep in the Fogo plumbing system prior to eruption (Figs. 36b, 38). To demonstrate this, we use the inferred H_2O-CO_2 MI concentrations (Fig. 36a), in combination with available saturation models (Fig. 36b), to estimate the MI entrapment pressures (assuming MI are volatile saturated at the time of their entrapment). The problem that arises here is that conversion of volatile contents into pressures requires selection of one of the several saturation models existing in the literature (e.g., MagmaSat,

Ghiorso and Gualda, 2015; Iacono-Marziano et al., 2012; D-Compress, Burgisser et al., 2015; Moretti et al., 2003; VolatileCalc, Newman and Lowenstern, 2002; Jiménez-Mejías et al., 2021; Shishkina et al., 2014), all of which have been calibrated over different compositional ranges and at relatively low pressures, and hence for lower CO_2 concentrations than the concentrations considered hereby). In addition to being calibrated at relatively low pressures (< 800 MPa, the model of Eguchi and Dasgupta, 2018 being the only exception), these different volatile saturation models predict CO_2 solubilities in Fogo melts that are highly variable, and typically span a factor 2 to 4 (or more) between the least and the most conservative estimate (Fig. 35b). This implies that, for a given MI CO_2 content, a range of MI entrapment pressures can be derived, with the VolatileCalc and Iacono-Marziano et al. (2012) models typically returning the lowest entrapment pressures, and the Jiménez-Mejías et al. (2021) model the highest (Fig. 36b). It is important to remind that some of these models have been calibrated for tholeiitic compositions, and their results are therefore shown for illustrative purposes only. The MagmaSat model outputs some intermediate entrapment pressure conditions in all cases (Fig. 36b).

We focus on the range (2095-21502 ppm) of total CO_2 contents, which convert into a minimum-maximum range of entrapment pressures of 100-290 MPa (217 MPa with MagmaSat) for the most CO_2-depleted inclusion (Fog 11-2-1; 0.21 wt. %) and to 648-1430 MPa (773 MPa with MagmaSat) for the most CO_2-rich inclusion (Fog 43-5-1; 2.1 wt. %). The upper range of MI entrapment pressures is higher than the pressures obtained previously at Fogo using clinopyroxene-liquid barometry (300-750 MPa) and fluid inclusion microthermometry (200-740 MPa) (Hildner et al. 2011, 2012; Klügel et al., 2020; Lo Forte et al., 2023). Ultimately, these pressures indicate MI may have been entrapped during early olivine crystallisation at depths of 26 to 35 km, well within the lithospheric mantle (extending from ~12 to ~60 km depth underneath Fogo Island; Liu et al., 2021).

We then use the composition (major elements and volatile contents) of this deeply trapped Fog 43-5-1 MI as the starting condition for model simulations of volatile degassing upon decompression. We run two model simulations of degassing using the saturation codes of Moretti et al. (2003) and MagmaSat (Ghiorso and Gualda, 2015). Both codes have been used previously to model magma degassing in a variety of volcanic systems erupting magmas of different composition (Aiuppa et al., 2007, 2010, 2017, 2022; Edmonds et al., 2010; Marini et al., 2011; Oppenheimer et al., 2011; Pino et al., 2011; Moretti 2013a, 2013b; de Moor et al., 2016; Bamber et al., 2022; Halldórsson et al., 2022; Romero et al., 2023; Sharpe et al., 2022; Boulanger and France, 2023; Liu et al., 2023; Mitchell et al., 2023). With both volatile saturation codes, we model dissolved volatile contents in melt along a

closed-system decompression path, starting from 1200 MPa pressure (final pressure, 0.1 MPa), in isothermal conditions (T = 1150 °C), and at redox conditions of ΔFMQ +1.5. Results of our model calculations, illustrated in Figure 25a, indicate that the modelled melt volatile compositions reproduce well the range of H_2O-CO_2 contents measured in our MI (Fig. 36a), providing confidence in our choice of volatile saturation models and model output. For comparison, we also show in Figure 36 the modelled degassing path calculated for (i) isothermal decompression in open-system conditions (orange curve) and (ii) non-isothermal (temperature range, 1128-985 °C) closed-system degassing with crystallisation taken into account (green curve). The latter model trend was obtained by linking together (a) MI saturation pressures (from H_2O-CO_2 contents) with (b) MI major element compositions, and hence (by matching against the modelled LLD; Fig. 31) melt temperature and extent of crystallisation. The open system run predicts some extreme CO_2 depletions at low pressure (that are not observed in the MI dataset; see inset in Fig. 36a); while the non-isothermal closed system+crystallisation model trend predicts some larger (> 2 wt. %) H_2O enrichments at low pressure that potentially explain the composition of some more evolved El Hierro MI.

Our results (Fig. 36) suggest magma storage conditions at Fogo to be significantly deeper than previously thought. Previous work, based on fluid inclusion microthermometry (Hildner et al., 2011, 2012; Klügel et al., 2020; Lo Forte et al., 2023) and on clinopyroxene-liquid geothermobarometry (Hildner et al., 2011, 2012; Klügel et al., 2020), have revealed the existence of a complex, vertically stacked magma storage system, with a main zone at 17–25 ± 5 km depth (Fig. 38) overlain, in the 9–12 ± 2 km depth range, by a sequence of levels of temporary magma stagnation, where differentiation eventually takes place prior/during eruption (generating phono-tephritic melts, such as those erupted during the 1951, 1995 and 2014-2015 eruptions). Our volatile data, especially those of the CO_2-richest – and hence more deeply trapped – MI (2.15 wt.%, Fog 43-5-1), extend the range of magma storage conditions downward. The entrapment (saturation) pressure range, inferred for this MI, is between 648 and 1430 MPa (i.e. about 20 to 45 km depth), depending on the saturation model used (see Fig. 36b). If we concentrate on the models that account for the increase of CO_2 solubility with melt alkalinity (and silica undersaturation), the inferred MI entrapment pressures are 773 (MagmaSat) and 1020 MPa (Moretti et al., 2003), respectively. With the mantle-crust reference model previously utilised by Lo Forte et al. (2023), these pressures correspond to entrapment depths of ~27 km (MagmaSat) and ~36 km (Moretti et al., 2003). The shrinkage bubble in this MI contains a small amount of minerals (cfr. 5.1), implying its Raman-derived CO_2 bubble density (and hence bubble CO_2 content) is not severely affected by mineral precipitation. Although it is well possible that the

measured CO_2 content underestimates the real CO_2 content of the parental melt, because of pre-entrapment CO_2 loss to bubbles (cfr. 5.2), we interpret such MI saturation pressures as indicative of a deep magma storage at 31.5 ± 4.3 km depth, at (or nearby) a main geological boundary bounded by the Elastic effective Thickness (Te; located at ~30 km depth; Pim et al., 2008).

Ultimately, our data prove that pre-eruptive magma storage/ascent underneath Fogo occurs/starts within/from a deep magma storage zone at 31.5 ± 4.3 km, in the lithospheric mantle. This is right above a cluster of deep earthquakes (38-43 km depth; Leva et al. 2019) that may correspond to fracturing events during magma accumulation zone replenishment events with more deeply sourced melts, rising from the convecting mantle source (at > 60 km). Such deep pre-eruptive magma storage conditions are similar to those of other intraplate oceanic islands, e.g., El Hierro (Taracsák et al., 2019), Piton de la Fournaise (Boudoire et al., 2018), La Palma (Dayton et al., 2023), and the Azores islands (e.g., Zanon et al., 2023).

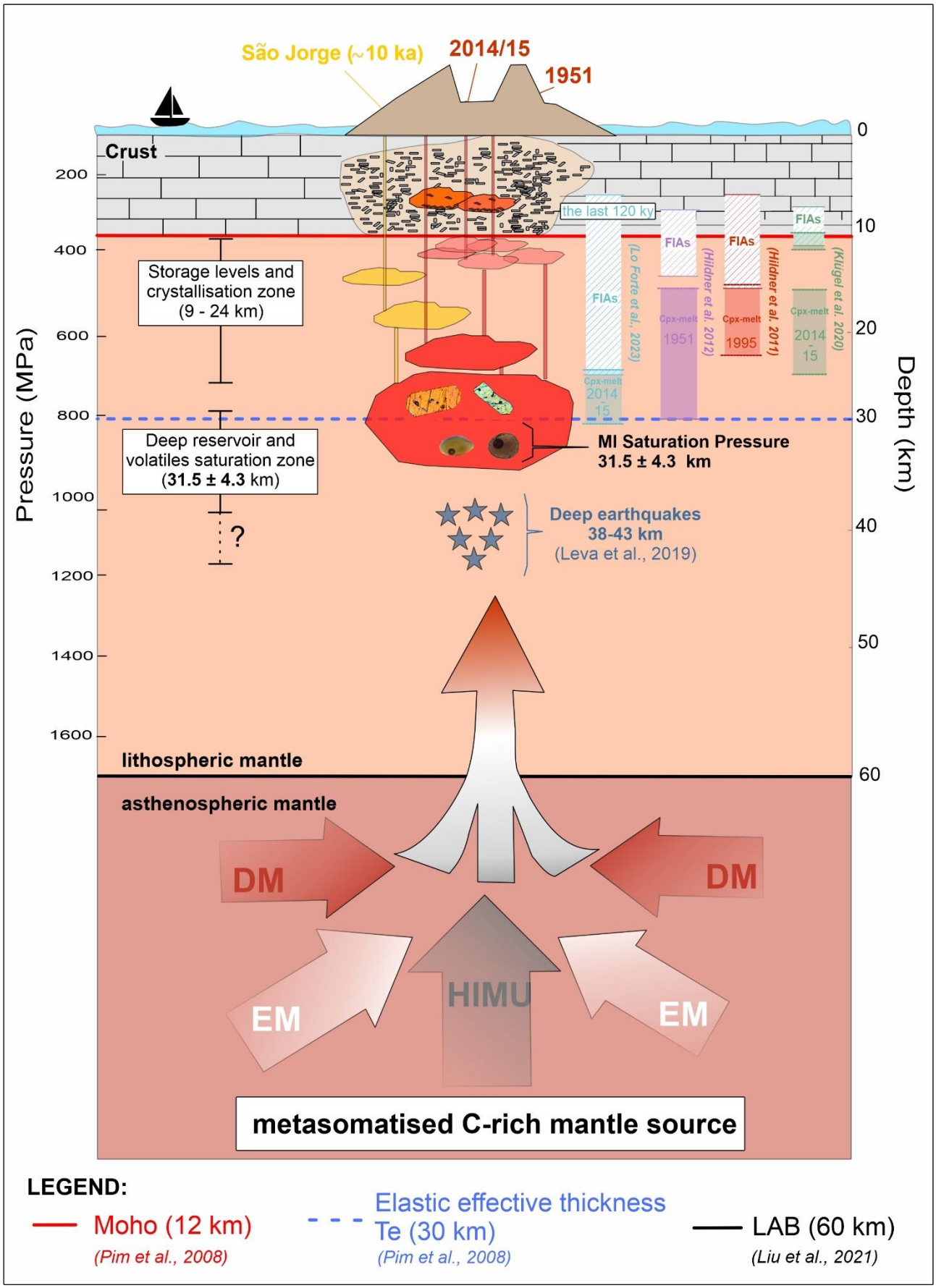
São Jorge (~10 ka)
2014/15
1951
Crust
Pressure (MPa)
Depth (km)
200
400
600
800
1000
1200
1400
1600
0
10
20
30
40
50
60
Storage levels and crystallisation zone (9 - 24 km)
Deep reservoir and volatiles saturation zone (31.5 ± 4.3 km)
?
the last 120 ky
FIAs
Cpx-melt 2014 15
(Lo Forte et al., 2023)
FIAs
Cpx-melt 1951
(Hildner et al. 2012)
FIAs
Cpx-melt 1995
(Hildner et al. 2011)
FIAs
Cpx-melt 2014 - 15
(Klügel et al. 2020)
MI Saturation Pressure 31.5 ± 4.3 km
Deep earthquakes 38-43 km (Leva et al., 2019)
lithospheric mantle
asthenospheric mantle
DM
DM
EM
HIMU
EM
metasomatised C-rich mantle source
LEGEND:
Moho (12 km)
(Pim et al., 2008)
Elastic effective thickness Te (30 km)
(Pim et al., 2008)
LAB (60 km)
(Liu et al., 2021)

Figure 38 Schematic cross-section (not to scale) showing the entire magma plumbing system of Fogo volcano. The model is based on the framework proposed by Lo Forte et al. (2023). Our data provide new constrain on the location of the roots of the volcano at 31.5 ± 4.3 km depth, which feed the upward magma storage zone at 13-25 km depth, as well as the magma stagnation zone located at 9-12 km depth. The blue stars represent the deep earthquakes recorded by Leva et al. (2019), in proximity of the deep magma accumulation zone. The right-hand side boxes present the previous barometry results. Consistent with Liu et al. (2021), the lithosphere-asthenosphere boundary (LAB) is located at 60 km depth. The three isotopic mantle components, which sign the magmatism of Cape Verde, were obtained from prior literature works (e.g., Gerlach et al., 1988; Doucelance et al., 2003; Escrig et al., 2005; Martins et al., 2010; Jackson et al., 2018a).

6.5.5. High carbon in the source mantle, and implications for the global carbon cycle

We use our parental melt CO_2 content inferred above (2.15 wt. %) to estimate the carbon content in the mantle source feeding volcanism at Fogo. To this aim, we use a modal batch-melting equation (Shaw, 1970):

$$C_{pm} = \frac{C_0}{[F+D(1-F)]} \cong C_0/F \quad (1)$$

in which C_{pm} stands for the CO_2 in mantle-derived parental melts (2.15 wt. % in our case), C_0 is the initial abundance of CO_2 in the source mantle, D is the CO_2 solid-melt partition coefficient (assumed at 0.00055; Rosenthal et al., 2015), and F is the melt fraction (0 to 1). This partial melting degree F in the Fogo mantle source is estimated at 0.06-0.07 by using MI major element composition to derive the final stage mantle-melt equilibration temperature (~1597 °C) and pressure (~4.8 GPa), and hence melting degree, according to the methodology of Sun and Dasgupta (2020, 2023). With these numbers, the 2.15 wt. % parental melt CO_2 content converts into 355-414 ppm C in the Fogo mantle source.

We caution our estimated carbon range should be considered as a conservative lower limit, since our MI potentially entrap an already partially degassed melt (see above). Also, the model is intrinsically simplistic as it assumes a homogeneous (with fixed C content) mantle, while we know the mantle is in fact spatially heterogenous. In spite of these limitations, we conclude our results unambiguously prove the CO_2-rich nature of alkali-rich mafic melts feeding intraplate volcanism at Cape Verde. Note that, given the very low D for CO_2 (~0; Rosenthal et al., 2015), the use of a fractional meting equation (in place of batch melting) would not lead to any obvious difference.

Our results, combined with recent observations at other OIB localities globally (e.g., Anderson and Poland, 2017; Longprè et al., 2017; Boudoire et al., 2018; Hauri et al., 2018; Miller et al., 2019; Taracsák et al., 2019; Tucker et al., 2019), suggest that a C enriched OIB mantle source is likely to

be the rule rather than the exception. Our estimated Fogo mantle content (355-414 ppm C) is well within the OIB mantle source range recently derived by Sung and Dasgupta (2023) (330-400 ppm), but well above the maximal C content of 164±55 ppm inferred by Rosenthal et al. (2015) for the mantle source of intraplate basalts.

This carbon-enriched nature of global OIB, and of their mantle sources, brings important consequences for our understanding of the mass/volume of deep carbon reservoirs, and of the deep carbon cycle - the transfer of carbon from the deep reservoir(s) (mantle+core) to the exosphere (ocean+atmosphere). First, our results contribute to the still open debate on the carbon content of the Bulk Silicate Earth, for which available estimates remain divergent, from ~110 ppm C (Hirschmann, 2018) to 330-450 ppm C (Marty et al., 2020) or even up to ~500 ppm C (Marty, 2012). The high C content of the OIB source mantle manifestly leans toward estimates based upon Ar (Marty, 2012) or C/N ratio (Marty et al., 2020) terrestrial inventories that require the deep convecting mantle to be C-rich, possibly >10 more enriched than the Depleted Mantle (DMM) that sustains MORB volcanism (~20-56 ppm C; Voyer et al., 2017; Hauri et al., 2019). We need to bear in mind, however, that radiogenic isotopes have clearly proven the presence of a variety of recycled (slab-related) crustal materials in the OIB mantle (Cabral et al., 2013; Ellam, 2021), and that it is therefore well possible that a substantial fraction of the high C in OIB is in fact derived from a recycled crustal carbon source (Cabral et al., 2014). Carbon isotope results for OIB magmas would be vital to test this hypothesis but are unfortunately available for only a handful set of OIB. Where available, however, results suggest a heavy (crustal) carbon signature in the mantle (Sandoval-Velasquez et al., 2021). This implies that high carbon OIB may in fact reflect local infiltration of C-enriched metasomatic fluids/melts resulting from melting of carbonated lithologies (e.g., carbon-rich sediments and/or carbonated oceanic lithosphere) entrained into the mantle during past subduction events (Dasgupta, 2018). Such a situation may indeed explain the enriched nature of Fogo magmas.

Secondly, our results with those recently obtained elsewhere (Boudoire et al., 2018; Taracsák et al., 2019) are critical to refining estimates of the OIB contribution to deep carbon flux to the atmosphere. Previous work (Dasgupta and Hirschmann, 2010; Hauri et al., 2019) has found carbon outgassing from our planet interior to be primarily controlled by the volumetrically dominant MORB volcanism, and by less voluminous but more C-rich calcalkaline volcanism. However, MORB magmas are CO_2-poor (typically <<0.1 wt.%; see Fig. 37), while calcalkaline magma CO_2 contents are though to lie somewhere between 0.1 and 1 wt % CO_2 (Plank and Manning, 2019). If the majority of OIB globally is as C-rich as Fogo, then OIB volcanism is expected to contribute disproportionally (relative to other

forms of volcanism) to the deep carbon flux to the atmosphere. Previous inventories (Dasgupta and Hirschmann, 2010) have found the carbon flux through OIB volcanism to be highly difficult to estimate, reflecting the often degassed (C-depleted) nature of OIB-carried MI (especially when no correction for shrinkage bubbles CO_2 is applied), and because of their extreme heterogeneity (in terms of depleted vs. enriched compositions). Because of these complexities, Dasgupta and Hirschmann (2010) conservatively derived their OIB carbon flux (1.2-30 Tg/yr) by assuming it to be ~10–50% of the MORB C flux. If for simplicity we assume global OIB to be dominantly alkaline in nature and to contain 2.15 wt. % CO_2 as our Fogo parental melt, then with a cumulative OIB magma extrusive output of 0.3-0.4 km^3/yr (Crisp, 1984) the global OIB carbon flux would be 16-21 Tg/yr, and > 100 Tg/yr if degassing of intrusive magma (1.5-2 km^3/yr; Crisp, 1984) is also taken into account.
These initial calculations are subject to large uncertainties. For example, tholeiitic OIB (e.g., Hawaii) or near-ridge hot-spot related OIB (e.g., Iceland) are less CO_2-poor than alkali rich OIB (Fig. 37), and the fact that all alkali rich OIB are as C-rich as Fogo (or El Hierro; Taracsák et al., 2019) is virtually untested. Ultimately, the volumetric proportions of enriched and non-enriched OIB would need to be constrained with a reasonable level of detail. Thus, our calculations here are only merely meant to indicate that the global OIB carbon flux might be significantly higher than previously thought.

6.6. Conclusions

Olivine-hosted MI from recent (≤10 ka) Fogo basanitic tephra samples exhibit some of the highest (glass + bubbles) CO_2 contents (up to 2.15 wt. %) on record. The Fogo MI are also found to additionally contain up to 2.73 wt. % H_2O, 8205 ppm S, 1459 ppm Cl and 2249 ppm F. Our results are based on the use of three independent methodologies to correct for CO_2 contained in shrinkage bubbles, whose general agreement corroborates our reconstructed total CO_2 concentrations. The inferred MI CO_2/Nb (277-283) and CO_2/Ba (26-22) ratios are lower than the characteristic mantle ratios, suggesting our MI – although exceptionally CO_2-rich - do still underestimate the real CO_2 contents in primary melts (potentially containing up to 8-9 wt % CO_2; Sun and Dasgupta, 2023) due to pre-entrapment CO_2 loss to bubbles. This notwithstanding, our results suggest that the basanitic magmas sustaining Fogo activity may originate from a metasomatized, carbon-rich mantle source containing a minimum of 355-414 ppm C, in agreement with recent estimates for global OIB mantle sources. Prior to eruption, these parental basanitic magmas would remain stored in the lithospheric

mantle in the ~27 to ~36 km depth range, deeper than previously inferred (Hildner et al., 2011, 2012; Klügel et al., 2020; Lo Forte et al., 2023).

Our results demonstrate the importance of measuring shrinkage bubble CO_2 to correctly reconstructing the architecture of magmatic plumbing systems, and confirm the exceptional carbon-rich signature of alkali rich OIB magmas and their carbon-rich mantle sources. In spite of their relatively low eruptive volumes, OIB eruptions may contribute disproportionally to global volcanic carbon outgassing from the mantle into the Earth's atmosphere. We tentatively estimate the global OIB carbon flux to potentially be as high as 17-23 Tg/yr.

REFERENCES

Aiuppa, A., Allard, P., Bernard, B., Lo Forte, F.M., Moretti, R., Hidalgo, S., 2022. Gas Leakage from Shallow Ponding Magma and Trapdoor Faulting at Sierra Negra Volcano (Isabela Island, Galápagos). Geochem. Geophys. Geosyst. 23.

Aiuppa, A., Bertagnini, A., Métrich, N., Moretti, R., Di Muro, A., Liuzzo, M., Tamburello, G., 2010. A model of degassing for Stromboli volcano. Earth and Planet. Sci. Lett. 295, 195–204.

Aiuppa, A., Bitetto, M., Francofonte, V., Velasquez, G., Parra, C.B., Giudice, G., et al., 2017. A CO_2-gas precursor to the March 2015 Villarrica volcano eruption. Geochem. Geophys. Geosyst. 18, 2120–2132.

Aiuppa, A., Casetta, F., Coltorti, M., Stagno, V., Tamburello, G., 2021. Carbon concentration increases with depth of melting in Earth's upper mantle. Nat. Geosci. 14, 697–703.

Aiuppa, A., Moretti, R., Federico, C., Giudice, G., Gurrieri, S., Liuzzo, M., Papale, P., Shinohara, H., Valenza, M., 2007. Forecasting Etna eruptions by real-time observation of volcanic gas composition. Geol. 35, 1115.

Aiuppa, A., Ronchi, A., Bitetto, M., Rizzo, A.L., Viveiros, F., Allard, P., Frezzotti, M.L., Valenti, V., Zanon, V., 2020. The fumarolic CO_2 output from Pico do Fogo volcano (Cape Verde). Ital. J. Geosci. 139, 325–340.

Anderson, A.T., 1974. Evidence for a Picritic, Volatile-rich Magma beneath Mt. J. Petrol. 15, 243–267.

Anderson, K.R, Poland, M.P., 2017. Abundant carbon in the mantle beneath Hawaii. Nat. Geosci. 10: 704-708

Ariskin, A.A., Barmina, G.S., 1999. An empirical model for the calculation of spinel-melt equilibria in mafic igneous systems at atmospheric pressure: 2. Fe-Ti oxides. Contrib. Mineral. Petrol. 134, 251–263.

Aster, E.M., Wallace, P.J., Moore, L.R., Watkins, J., Gazel, E., Bodnar, R.J., 2016. Reconstructing CO_2 concentrations in basaltic melt inclusions using Raman analysis of vapor bubbles. J. Volcanol. Geotherm. Res. 323, 148–162.

Bali, E., Hartley, M.E., Halldórsson, S.A., Gudfinnsson, G.H., Jakobsson, S., 2018. Melt inclusion constraints on volatile systematics and degassing history of the 2014–2015 Holuhraun eruption, Iceland. Contrib. Mineral. Petrol. 173, 9.

Bamber, E.C., La Spina, G., Arzilli, F., de' Michieli Vitturi, M., Polacci, M., Hartley, M.E., et al., 2022. Basaltic Plinian eruptions at Las Sierras-Masaya volcano driven by cool storage of crystal-rich magmas. Commun. Earth Environ. 3, 253.

Blundy, J., Cashman, K., 2005. Rapid decompression-driven crystallization recorded by melt inclusions from Mount St. Helens volcano. Geol. 33, 793.

Bonadiman, C., Beccaluva, L., Coltorti, M., Siena, F., 2005. Kimberlite-like Metasomatism and 'Garnet Signature' in Spinel-peridotite Xenoliths from Sal, Cape Verde Archipelago: relics of a subcontinental mantle domain within the atlantic oceanic lithosphere? J. Petrol. 46, 2465–2493.

Boudoire G., Pasdeloup G., Schiavi F**.**, Cluzel N., Rafflin V., Grassa F., et al., 2023. Magma storage and degassing beneath the youngest volcanoes of the Massif Central (France): lessons for the monitoring of a dormant volcanic province. Chem Geol., 634, 121603.

Boudoire, G., Rizzo, A.L., Di Muro, A., Grassa, F., Liuzzo, M., 2018. Extensive CO_2 degassing in the upper mantle beneath oceanic basaltic volcanoes: First insights from Piton de la Fournaise volcano (La Réunion Island). Geochim. et Cosmochim. Acta 235, 376–401.

Boulard, E., Menguy, N., Auzende, A. L., Benzerara, K., Bureau, H., Antonangeli, D., et al., 2012. Experimental Investigation of the Stability of Fe-Rich Carbonates in the Lower Mantle. J. Geophys. Res. 117, B02208.

Boulanger, M., France, L., 2023. Cumulate Formation and Melt Extraction from Mush-Dominated Magma Reservoirs: The Melt Flush Process Exemplified at Mid-Ocean Ridges. J. Petrol. 64, egad005.

Burgisser, A., Alletti, M., Scaillet, B., 2015. Simulating the behavior of volatiles belonging to the C–O–H–S system in silicate melts under magmatic conditions with the software D-Compress. Comput. Geosci. 79, 1–14.

Burton, M., Aiuppa, A., Allard, P., Asensio-Ramos, M., Confrades, A.P., La Spina., A., et al., 2023. Exceptional eruptive CO_2 emissions from intra-plate alkaline magmatism in the Canary volcanic archipelago. Commun. Earth Environ. 4, 467.

Buso, R., Laporte, D., Schiavi, F., Cluzel, N., Fonquernie, C., 2022. High-pressure homogenization of olivine-hosted CO_2-rich melt inclusions in a piston cylinder: insight into the volatile content of primary mantle melts. Eur. J. Mineral., 34, 325–349.

Cabral, R. A., Jackson, M. G., Koga, K. T., Rose-Koga, E. F., Hauri, E. H., M. J. Whitehouse et al., 2014. Volatile cycling of H_2O, CO_2, F, and Cl in the HIMU mantle: A new window provided by melt inclusions from oceanic hot spot lavas at Mangaia, Cook Islands, Geochem. Geophys. Geosyst., 15, 4445–4467.

Cabral, R. A., Jackson, M. G., Rose-Koga, E. F., Koga, K. T., Whitehouse, M. J., Antonelli, M. A., et al., 2013. Anomalous sulphur isotopes in plume lavas reveal deep mantle storage of Archaean crust. Nature 496, 490–493

Cannatelli, C., Doherty, A.L., Esposito, R., Lima, A., De Vivo, B., 2016. Understanding a volcano through a droplet: A melt inclusion approach. J. of Geochem. Explor. 171, 4–19.

Carroll, M.R., and Webster, J.D., 1994. Sulfur, noble gases, and halogens: solubility relations of the less abundant volatile species in magmas. Rev. Mineral. Geochem. 30, 231-79.

Cartigny, P., Pineau, F., Aubaud, C., Javoy, M., 2008. Towards a consistent mantle carbon flux estimate: Insights from volatile systematics (H_2O/Ce, δD, CO_2/Nb) in the North Atlantic mantle (14° N and 34° N). Earth and Planet. Sci. Lett. 265, 672–685.

Chen, Y., Provost, A., Schiano, P., and Cluzel, N., 2011. The rate of water loss from olivine-hosted melt inclusions. Contrib. Mineral. Petrol., 162(3), 625–636.

Cottrell, E., Spiegelman, M., Langmuir, C.H., 2002. Consequences of diffusive reequilibration for the interpretation of melt inclusions: reequilibration of melt inclusions. Geochem. Geophys. Geosyst. 3, 1–26.

Créon, L., Levresse, G., Remusat, L., Bureau, H., Carrasco-Nuñez, G. 2018. New method for initial composition determination of crystallized silicate melt inclusions. Chem. Geol. 483, 162-173.

Crisp, J. A. 1984. Rates of magma emplacement and volcanic output, J. Volcanol. Geotherm. Res., 20, 177 – 211.

Danyushevsky, L.V., 2001. The effect of small amounts of H_2O on crystallisation of mid-ocean ridge and backarc basin magmas. J. Volcanol. and Geother. Res. 110, 265–280.

Danyushevsky, L.V., Della-Pasqua, F.N., Sokolov, S., 2000. Re-equilibration of melt inclusions trapped by magnesian olivine phenocrysts from subduction-related magmas: petrological implications. Contrib. Mineral. Petrol. 138, 68–83.

Danyushevsky, L.V., McNeill, A.W., Sobolev, A.V., 2002. Experimental and petrological studies of melt inclusions in phenocrysts from mantle-derived magmas: an overview of techniques, advantages and complications. Chem. Geol. 183, 5–24.

Danyushevsky, L.V., Plechov, P., 2011. Petrolog3: Integrated software for modeling crystallization processes: Petrolog3. Geochem. Geophys. Geosyst. 12.

Dasgupta, R., 2018 Volatile-bearing partial melts beneath oceans and continents – where, how much, and of what compositions? Am. J. Sci. 318, 141–165.

Dasgupta, R., Chi, H., Shimizu, N., Buono, A.S., Walker, D., 2013. Carbon solution and partitioning between metallic and silicate melts in a shallow magma ocean: implications for the origin and distribution of terrestrial carbon. Geochim. Cos-mochim. Acta102, 191–212.

Dasgupta, R., Hirschmann, M.M., 2010. The deep carbon cycle and melting in Earth's interior. Earth and Planet. Sci. Lett. 298, 1–13.

Day, S.J., Heleno da Silva, S.I.N., Fonseca, J.F.B.D., 1999. A past giant lateral collapse and present-day flank instability of Fogo, Cape Verde Islands. J. Volcanol. and Geother. Res. 94, 191–218.

de Moor, J.M., Aiuppa, A., Avard, G., Wehrmann, H., Dunbar, N., Muller, C., et al., 2016. Turmoil at Turrialba Volcano (Costa Rica): Degassing and eruptive processes inferred from high-frequency gas monitoring: Turmoil at Turrialba Volcano. J. Geophys. Res. Solid Earth 121, 5761–5775.

Di Martino, C., Forni, F., Frezzotti, M.L., Palmeri, R., Webster, J.D., Ayuso, R.A., et al., 2011. Formation of cordierite-bearing lavas during anatexis in the lower crust beneath Lipari Island (Aeolian arc, Italy). Contrib. Mineral. Petrol. 162, 1011–1030.

Di Muro, A., Metrich, N., Vergani, D., Rosi, M., Armienti, P., Fougeroux, T., Deloule, E., Arienzo, I., Civetta, L., 2014. The Shallow Plumbing System of Piton de la Fournaise Volcano (La Reunion Island, Indian Ocean) Revealed by the Major 2007 Caldera-Forming Eruption. J. Petrol. 55, 1287–1315.

Dixon J.E. and Stolper E.M., 1995. An Experimental Study of Water and Carbon Dioxide Solubilities in Mid-Ocean Ridge Basaltic Liquids. Part II: Applications to Degassing. J. Petrol. 36,6,1633-1646

Doucelance, R., Escrig, S., Moreira, M., Gariépy, C., Kurz, M.D., 2003. Pb-Sr-He isotope and trace element geochemistry of the Cape Verde Archipelago. Geochim. Cosmochim. Acta 67, 3717–3733.

Edmonds, M., Aiuppa, A., Humphreys, M., Moretti, R., Giudice, G., Martin, R.S., et al., 2010. Excess volatiles supplied by mingling of mafic magma at an andesite arc volcano: excess volatiles supplied by underplating. Geochem. Geophys. Geosyst. 11.

Edmonds, M., Liu, E.J., Cashman, K.V., 2022. Open-vent volcanoes fuelled by depth-integrated magma degassing. Bull. Volcanol. 84, 28.

Edmonds M., and Wallace P.J., 2017. Volatiles and Exsolved Vapor in Volcanic Systems. Elements, 13, 29–34.

Eguchi, J. and Dasgupta, R., 2018. A CO_2 solubility model for silicate melts from fluid saturation to graphite or diamond saturation, Chem. Geol., 487, 23–38.

Ellam, R. M. 2021. Radiogenic isotopes and mantle evolution. In: Alderton, D. and Elias, S. A. (eds.) Encyclopedia of Geology. Academic Press: Amsterdam, 330-344

Escrig, S., Doucelance, R., Moreira, M., Allègre, C.J., 2005. Os isotope systematics in Fogo Island: Evidence for lower continental crust fragments under the Cape Verde Southern Islands. Chem. Geol. 219, 93–113.

Esposito, R., Bodnar, R.J., Danyushevsky, L., De Vivo, B., Fedele, L., Hunter, J., Lima, A., and Shimizu, N. 2011. Volatile evolution of magma associated with the Solchiaro Eruption in the Phlegrean Volcanic District (Italy). Journal of Petrology. 52, 2431–2460.

Esposito, R., Lamadrid, H.M., Redi, D., Steele-MacInnis, M., Bodnar, R.J., Manning, C.E., De Vivo, B., Cannatelli, C., Lima, A., 2016. Detection of liquid H_2O in vapor bubbles in reheated melt inclusions: Implications for magmatic fluid composition and volatile budgets of magmas? Am. Mineral. 101, 1691–1695.

Fall, A., Bodnar, R.J., Szabó, C., Pál-Molnár, E. 2007. Fluid evolution in the nepheline syenites of the Ditrău alkaline Massif, Transylvania, Romania. Lithos, 95, 331-345.

Feignon J.G., Cluzel N., Schiavi F., Moune S., Roche O., Clavero J., et al., 2022. High CO_2 content in magmas of the explosive andesitic Enco eruption of Mocho-Choshuenco volcano (Chile). Bull. Volcanol. 84, 40.

Foeken, J.P.T., Day, S., Stuart, F.M., 2009. Cosmogenic ^{3}He exposure dating of the Quaternary basalts from Fogo, Cape Verdes: Implications for rift zone and magmatic reorganisation. Quaternary Geochronology 4, 37–49.

Foley, S.F. 2011. A Reappraisal of Redox Melting in the Earth's Mantle as a Function of Tectonic Setting and Time, J. Petrol., 52, 7-8, 1363–1391,

Foley, S. F., Fischer, T. P. 2017. An essential role for continental rifts and lithosphere in the deep carbon cycle. Nat. Geosci. 10, 897–902.

Foley, S. F., Link, K., Tiberindwa, J. V. & Barifaijo, E. 2012. Patterns and origin of igneous activity around the Tanzanian craton. J. Afr. Earth Sci. 62, 1–18.

Foley, S.F., Yaxley, G.M., Rosenthal, A., Buhre, S., Kiseeva, E.S., Rapp, R.P., Jacob. D.E. 2009. The composition of near-solidus melts of peridotite in the presence of CO_2 and H_2O between 40 and 60 kbar. Lithos. 112S, 274-283.

French, S., and Romanowicz, B., 2015. Broad plumes rooted at the base of the Earth's mantle beneath major hotspots, Nature, 525, 95–99.

Gaetani, G.A., O'Leary, J.A., Shimizu, N., Bucholz, C.E., and Newville, M., 2012. Rapid reequilibration of H_2O and oxygen fugacity in olivine-hosted melt inclusions. Geol., 40(10), 915–918.

Gaetani, G.A., and Watson, E.B., 2000. Open system behavior of olivine-hosted melt inclusions. Earth and Planet. Sci. Lett. 183, 27–41.

Gaetani, G.A., and Watson, E.B., 2002. Modeling the major-element evolution of olivine-hosted melt inclusions. Chem. Geol. 183, 25–41.

Gerlach, D.C., Cliff, R.A., Davies, G.R., Norry, M., Hodgson, N., 1988. Magma sources of the Cape Verdes archipelago: Isotopic and trace element constraints. Geochim. et Cosmochim. Acta 52, 2979–2992.

Ghiorso, M.S., and Gualda, G.A.R., 2015. An H_2O–CO_2 mixed fluid saturation model compatible with rhyolite-MELTS. Contrib. Mineral. Petrol. 169, 53.

Giordano, D., Nichols, A.R., and Dingwell, D.B. 2005. Glass transition temperatures of natural hydrous melts: a relationship with shear viscosity and implications for the welding process. J. Volcanol. and Geother. Res. , 142 (1–2), 105–118.

Guzmics, T., Berkesi, M., Bodnar, R.J., Fall, A., Bali, E., Milke, R., Vetlényi, E., Szabó, C., 2019. Natrocarbonatites: A hidden product of three-phase immiscibility. Geol. 47, 527–530.

Halldórsson, S.A., Marshall, E.W., Caracciolo, A., Matthews, S., Bali, E., Rasmussen, M.B., et al., 2022. Rapid shifting of a deep magmatic source at Fagradalsfjall volcano, Iceland. Nature 609, 529–534.

Harms, E., ans Schmincke, H.U., 2000. Volatile composition of the phonolitic Laacher See magma (12,900 yr BP): implications for syn-eruptive degassing of S, F, Cl and H_2O. Contrib. Mineral. Petrol. 138, 84–98.

Hartley, M.E., Maclennan, J., Edmonds, M., Thordarson, T., 2014. Reconstructing the deep CO_2 degassing behaviour of large basaltic fissure eruptions. Earth and Planet. Sci. Lett. 393, 120–131.

Hauri, E., 2002. SIMS analysis of volatiles in silicate glasses, 2: isotopes and abundances in Hawaiian melt inclusions. Chem. Geol. 183, 115–141.

Hauri, E.H., Cottrell, E., Kelley, K.A., Tucker, J.M., Shimizu, K., Voyer, M.L., Marske, J., Saal, A.E., 2019. Carbon in the Convecting Mantle, in: Orcutt, B.N., Daniel, I., Dasgupta, R. (Eds.), Deep Carbon. Cambridge University Press, pp. 237–275.

Hauri, E.H., Maclennan, J., McKenzie, D., Gronvold, K., Oskarsson, N., Shimizu, N., 2018. CO_2 content beneath northern Iceland and the variability of mantle carbon. Geol. 46, 55–58.

Heath, E., Macdonald, R., Belkin, H., Hawkesworth, C., Sigurdsson, H., 1998. Magma genesis at Soufriere Volcano, St Vincent, Lesser Antilles Arc. J. Petrol. 39, 1721–1764.

Hekinian, R., and D. Walker (1987), Diversity and spatial zonation of volcanic-rocks from the East Pacific Rise near 21-degrees-N, Contrib. Mineral. Petrol., 96 (3), 265– 280

Hildner, E., Klügel, A., Hansteen, T.H., 2012. Barometry of lavas from the 1951 eruption of Fogo, Cape Verde Islands: Implications for historic and prehistoric magma plumbing systems. J. Volcanol. and Geother. Res. 217–218, 73–90.

Hildner, E., Klügel, A., Hauff, F., 2011. Magma storage and ascent during the 1995 eruption of Fogo, Cape Verde Archipelago. Contrib. Mineral. Petrol. 162, 751–772.

Hirschmann, M.M. 2006. Water, melting, and the deep Earth H_2O cycle Annu. Rev. Earth Planet. Sci. 629-653.

Hirschmann, M.M., 2018. Comparative deep Earth volatile cycles: The case for C recycling from exosphere/mantle fractionation of major (H_2O, C, N) volatiles and from H_2O/Ce, CO_2/Ba, and CO_2/Nb exosphere ratios. Earth and Planet. Sci. Lett. 502, 262–273.

Hoernle, K., Tilton, G., Le Bas, M.J., Duggen, S., Garbe-Schönberg, D., 2002. Geochemistry of oceanic carbonatites compared with continental carbonatites: mantle recycling of oceanic crustal carbonate. Contrib. Mineral. Petrol. 142, 520–542.

Holm, P. M., Wilson, J.R., Christensen B.P., Hansen, L., Hansen, S. L., Hein, K.M., et al., 2006, Sampling the Cape Verde Mantle Plume: Evolution of Melt Compositions on Santo Antão, Cape Verde Islands, J. Petrol., 47, 1, 145–189.

Hudgins, T.R., Mukasa, S.B., Simon, A.C., Moore, G., Barifaijo, E. 2015. Melt inclusion evidence for CO_2-rich melts beneath the western branch of the East African Rift: implications for long-term storage of volatiles in the deep lithospheric mantle Contrib. Mineral. Petrol., 169, 1-18.

Iacono-Marziano, G., Morizet, Y., Le Trong, E., Gaillard, F., 2012. New experimental data and semi-empirical parameterization of H_2O–CO_2 solubility in mafic melts. Geochim. Cosmochim. Acta 97, 1–23.

Jackson, M.G., Becker, T.W., Konter, J.G., 2018a. Evidence for a deep mantle source for EM and HIMU domains from integrated geochemical and geophysical constraints. Earth Planet. Sci. Lett. 484, 154-167

Jiménez-Mejías, M., Andújar, J., Scaillet, B., Casillas, R., 2021. Experimental determination of H_2O and CO_2 solubilities of mafic alkaline magmas from Canary Islands. Comptes Rendus. Géoscience 353, 289–314.

Kamenetsky, V.S., Davidson, P., Mernagh, T.P., Crawford, A.J., Gemmell, J.B., Portnyagin, M.V., Shinjo, R., 2002. Fluid bubbles in melt inclusions and pillow-rim glasses: high-temperature precursors to hydrothermal fluids? Chem. Geol. 183, 349–364.

Kawakami, Y., Yamamoto, J., Kagi, H., 2003. Micro-Raman densimeter for CO_2 inclusions in mantle-derived minerals. Appl. Spectrosc. 57,11, 1333–1339.

Kendrick, M.A., Jackson, M.G., Kent, A.J.R., Hauri, E.H., Wallace, P.J., Woodhead, J., 2014. Contrasting behaviours of CO_2, S, H_2O and halogens (F, Cl, Br, and I) in enriched-mantle melts from Pitcairn and Society seamounts. Chem. Geol. 370, 69–81.

Kent, A.J.R., 2008. Melt inclusions in basaltic and related volcanic rocks. In: Putirka, K.D., Tepley III, F.J. (Eds.) Minerals, inclusions and volcanic processes. Reviews in Mineralogy and Petrology 69, 273-332.

Klügel, A., Day, S., Schmid, M., Faria, B., 2020. Magma Plumbing During the 2014–2015 Eruption of Fogo (Cape Verde Islands). Front. Earth Sci. 8, 157.

Koleszar, A.M., Saal, A.E., Hauri, E.H., Nagle, A.N., Liang, Y., Kurz, M.D., 2009. The volatile contents of the Galapagos plume; evidence for H_2O and F open system behavior in melt inclusions. Earth and Planet. Sci. Lett. 287, 442–452.

Le Bas, M.J.L., Maitre, R.W.L., Streckeisen, A., Zanettin, B., 1986. IUGS Subcommission on the Systematics of Igneous Rocks. A Chemical Classification of Volcanic Rocks Based on the Total Alkali-Silica Diagram. J. Petrol. 27,3, 745–750.

Le Voyer, M., Hauri, E.H., Cottrell, E., Kelley, K.A., Salters, V.J.M., Langmuir, C.H., Hilton, D.R., Barry, P.H., Füri, E., 2019. Carbon Fluxes and Primary Magma CO_2 Contents Along the Global Mid-Ocean Ridge System. Geochem. Geophys. Geosyst. 20, 1387–1424.

Le Voyer, M., Kelley, K.A., Cottrell, E., Hauri, E.H., 2017. Heterogeneity in mantle carbon content from CO_2-undersaturated basalts. Nat. Commun. 8, 14062.

Lesher, C.E., Spera, F.J., 2015. Thermodynamic and Transport Properties of Silicate Melts and Magma, in: The Encyclopedia of Volcanoes. Elsevier, pp. 113–141.

Liu, B., Zhang, Z., Giuliani, A., Xie, Q., Kong, W., Wang, C., et al., 2023. A Mantle Plume Connection for Alkaline Lamprophyres (Sannaites) from the Permian Tarim Large Igneous Province: Petrological, Geochemical and Isotopic Constraints. J. Petrol. 64, egad004.

Liu, X., Zhao, D., 2021. Seismic evidence for a plume-modified oceanic lithosphere–asthenosphere system beneath Cape Verde. Geophys. J. Int.225, 872–886.

Lo Forte, F.M., Aiuppa, A., Rotolo, S.G., Zanon, V., 2023. Temporal evolution of the Fogo Volcano magma storage system (Cape Verde Archipelago): a fluid inclusions perspective. J. Volcanol. and Geother. Res. 433, 107730.

Longpré, M.-A., Stix, J., Klügel, A., Shimizu, N., 2017. Mantle to surface degassing of carbon- and sulphur-rich alkaline magma at El Hierro, Canary Islands. Earth and Planet. Sci. Lett. 460, 268–280.

Lowenstern, J.B. 1995. Applications of silicate MIs to the study of magmatic volatiles. In: Magmas, Fluids, and Ore Deposits, 23 (ed. J. F. H. Thompson). Mineralogical Society of Canada, , 71–99.

Lowenstern, J.B., 2003. Melt inclusions come of age: volatiles, volcanoes, and sorby's legacy. Develop. Volcanol. 5, 1–21.

Lowenstern, J. B., 2015. Bursting the bubble of melt inclusions, Am. Mineral., 100, 672–673.

Maclennan, J., 2017. Bubble formation and decrepitation control the CO_2 content of olivine-hosted melt inclusions: melt inclusion carbon dioxide. Geochem. Geophys. Geosyst. 18, 597–616.

Marini, L., Moretti, R., Accornero, M., 2011. Sulfur Isotopes in Magmatic-Hydrothermal Systems, Melts, and Magmas. Reviews in Mineralogy and Geochemistry 73, 423–492.

Martínez-Moreno, F.J., Monteiro Santos, F.A., Madeira, J., Pous, J., Bernardo, I., Soares, A., et al., 2018. Investigating collapse structures in oceanic islands using magnetotelluric surveys: The case of Fogo Island in Cape Verde. J. Volcanol. and Geother. Res. 357, 152–162.

Martins, S., Mata, J., Munhá, J., Mendes, M.H., Maerschalk, C., Caldeira, R., et al., 2010. Chemical and mineralogical evidence of the occurrence of mantle metasomatism by carbonate-rich melts in an oceanic environment (Santiago Island, Cape Verde). Miner. Petrol. 99, 43–65.

Marty, B., 2012. The origins and concentrations of water, carbon, nitrogen and noble gases on Earth. Earth Planet. Sci. Lett. 313, 56–66.

Marty, B., Almayrac, M., Barry, P.H., Bekaert, D.V., Broadley, M.W., Byrne, D.J., et al., 2020. An evaluation of the C/N ratio of the mantle from natural CO_2-rich gas analysis: Geochemical and cosmochemical implications. Earth Planet. Sci. Lett. 551, 116574.

Massare, D., Métrich, N., and Clocchiatti, R. 2002. High-temperature experiments on silicate melt inclusions in olivine at 1 atm: Inference on temperatures of homogenization and H_2O concentrations. Chem. Geol., 183(1–4), 87–98.

Mata, J., Martins, S., Mattielli, N., Madeira, J., Faria, B., Ramalho, R.S., et al., 2017. The 2014–15 eruption and the short-term geochemical evolution of the Fogo volcano (Cape Verde): Evidence for small-scale mantle heterogeneity. Lithos 288–289, 91–107.

Melián, G.V., Hernández, P.A., Pérez, N.M., Asensio-Ramos, M., Padrón, E., Alonso, M., et al., 2021 Insights from Fumarole Gas Geochemistry on the Recent Volcanic Unrest of Pico do Fogo, Cape Verde. Front. Earth Sci. 9:631190.

Métrich, N., Allard, P., Aiuppa, A., Bani, P., Bertagnini, A., Shinohara, H., et al., 2011. Magma and Volatile Supply to Post-collapse Volcanism and Block Resurgence in Siwi Caldera (Tanna Island, Vanuatu Arc). J. of Petrol. 52, 1077–1105.

Métrich, N., Allard, P., Spilliaert, N., Andronico, D., Burton, M., 2004. 2001 flank eruption of the alkali- and volatile-rich primitive basalt responsible for Mount Etna's evolution in the last three decades. Earth Planet. Sci. Lett. 228, 1–17.

Métrich, N., Clocchiatti, R., Mosbah, M., Chaussidon, M., 1993. The 1989–1990 activity of Etna magma mingling and ascent of H_2O, Cl, S rich basaltic magma. Evidence from melt inclusions. J. Volcanol. and Geother. Res. 59, 131–144.

Métrich, N., and Wallace, P.J., 2008. Volatile Abundances in Basaltic Magmas and Their Degassing Paths Tracked by Melt Inclusions. Reviews in Mineralogy and Geochemistry 69, 363–402.

Métrich, N., Zanon, V., Créon, L., Hildenbrand, A., Moreira, M., Marques, F.O., 2014. Is the 'Azores Hotspot' a Wetspot? Insights from the Geochemistry of Fluid and Melt Inclusions in Olivine of Pico Basalts. J. Petrol. 55, 377–393.

Michael, P.J., Graham, D.W., 2015. The behavior and concentration of CO_2 in the suboceanic mantle: Inferences from undegassed ocean ridge and ocean island basalts. Lithos 236–237, 338–351.

Miller, W.G.R., Maclennan, J., Shorttle, O., Gaetani, G.A., Le Roux, V., Klein, F., 2019. Estimating the carbon content of the deep mantle with Icelandic melt inclusions. Earth Planet. Sci. Lett. 523, 115699.

Mironov, N.L., Portnyagin, M.V., 2011. H_2O and CO_2 in parental magmas of Kliuchevskoi volcano inferred from study of melt and fluid inclusions in olivine. Russian geology and geophysics 52, 1353-1367.

Mironov, N., Portnyagin, M., Botcharnikov, R., Gurenko, A., Hoernle, K., Holtz, F., 2015. Quantification of the CO_2 budget and H_2O–CO_2 systematics in subduction-zone magmas through the experimental hydration of melt inclusions in olivine at high H_2O pressure. Earth and Planetary Science Letters 425, 1-11.

Mironov, N., Tobelko, D.P., Smirnov, S.Z., Portnyagin, M.V., Krasheninnikov, S.P., 2020. Estimation of CO_2 content in the gas phase of melt inclusions using Raman spectroscopy: Case study of inclusions in olivine from the Karymsky volcano (Kamchatka). Russian Geology and Geophysics 61, 600-610.

Mitchell, M.A., Peacock, J.R., Burgess, S.D., 2023. Imaging the magmatic plumbing of the Clear Lake Volcanic Field using 3-D gravity inversions. J. Volcanol. and Geother. Res. 435, 107758.

Moore, L.R., Bodnar, R.J., 2019. A pedagogical approach to estimating the CO_2 budget of magmas. JGS 176, 398–407.

Moore, L.R., Gazel, E., Tuohy, R., Lloyd, A.S., Esposito, R., Steele-MacInnis, M., et al., 2015. Bubbles matter: An assessment of the contribution of vapor bubbles to melt inclusion volatile budgets. Am. Mineral. 100, 806–823.

Moore, L.R., Mironov,N., Portnyagin, M., Gazel, E., Bodnar, R.J. 2018. Volatile contents of primitive bubble-bearing melt inclusions from Klyuchevskoy volcano, Kamchatka:

Comparison of volatile contents determined by mass-balance versus experimental homogenization J. Volcanol. Geotherm. Res., 358, 124-131.

Moretti, R., Arienzo, I., Civetta, L., Orsi, G., Papale, P., 2013a. Multiple magma degassing sources at an explosive volcano. Earth and Planet. Sci. Lett. 367, 95–104.

Moretti, R., Arienzo, I., Orsi, G., Civetta, L., D'Antonio, M., 2013b. The Deep Plumbing System of Ischia: a Physico-chemical Window on the Fluid-saturated and CO_2-sustained Neapolitan Volcanism (Southern Italy). J. Petrol. 54, 951–984.

Moretti, R., Papale, P., Ottonello, G., 2003. A model for the saturation of C-O-H-S fluids in silicate melts. SP 213, 81–101.

Mourão, C., Moreira, M., Mata, J., Raquin, A., Madeira, J., 2012. Primary and secondary processes constraining the noble gas isotopic signatures of carbonatites and silicate rocks from Brava Island: evidence for a lower mantle origin of the Cape Verde plume. Contrib. Mineral. Petrol. 163, 995–1009.

Moussallam, Y., Georgeais, G., Rose-Koga, E.F., Koga, K.T., Hartley, M.E., Scaillet, B., Oppenheimer, C., Peters, N., 2023. CO2 -Undersaturated Melt Inclusions From the South West Indian Ridge Record Surprisingly Uniform Redox Conditions. Geochem Geophys Geosyst 24, e2023GC011235.

Moussallam, Y., Longpré, M.-A., McCammon, C., Gomez-Ulla, A., Rose-Koga, E.F., Scaillet, B., Peters, N., Gennaro, E., Paris, R., Oppenheimer, C., 2019. Mantle plumes are oxidised. Earth and Planet. Sci. Lett. 527, 115798.

Moussallam, Y., Oppenheimer, C., Scaillet, B., Gaillard, F., Kyle, P., Peters, N., Hartley, M., Berlo, K., Donovan, A., 2014. Tracking the changing oxidation state of Erebus magmas, from mantle to surface, driven by magma ascent and degassing. Earth and Planet. Sci. Lett. 393, 200–209.

Naumov, V.B., Portnyagin, M.V., Tolstykh, M.L., Yarmolyuk, V.V., 2003. Composition of Magmatic Melts from the Southern Baikal Volcanic Region: A Study of Inclusions in Olivine from Trachybasalts. Geochemistry International. 41, 213-223.

Newman, S., Lowenstern, J.B., 2002. VolatileCalc: a silicate melt–H_2O–CO_2 solution model written in Visual Basic for excel. Computers & Geosciences 28, 597–604.

Ni, P., Zhang, Y., Guan, Y., 2017. Volatile loss during homogenization of lunar melt inclusions. Earth and Planet. Sci. Lett. 478, 214–224.

Oppenheimer, C., Fischer, T.P., Scaillet, B., 2014. Volcanic Degassing: Process and Impact, in: Treatise on Geochemistry. Elsevier, pp. 111–179.

Oppenheimer, C., Moretti, R., Kyle, P.R., Eschenbacher, A., Lowenstern, J.B., Hervig, R.L., Dunbar, N.W., 2011. Mantle to surface degassing of alkalic magmas at Erebus volcano, Antarctica. Earth and Planet. Sci. Lett. 306, 261–271.

Palme, H., & O'Neill, H. ST C. 2003. Cosmochemical estimates of mantle composition. The mantle and core, 1-38.

Pérez, W., Freundt, A., Kutterolf, S., 2020. The basaltic plinian eruption of the ~6 ka San Antonio Tephra and formation of the Masaya caldera, Nicaragua. J. Volcanol. and Geother. Res. 401, 106975.

Pim, J., Peirce, C., Watts, A.B., Grevemeyer, I., Krabbenhoeft, A., 2008. Crustal structure and origin of the Cape Verde rise. Earth Planet. Sci. Lett. 272, 422–428.

Pino, N.A., Moretti, R., Allard, P., Boschi, E., 2011. Seismic precursors of a basaltic paroxysmal explosion track deep gas accumulation and slug upraise. J. Geophys. Res. 116, B02312.

Plank, T., Manning, C.E., 2019. Subducting carbon. Nature 574, 343–352.

Portnyagin, M., Almeev, R., Matveev, S., and Holtz, F. 2008. Experimental evidence for rapid water exchange between melt inclusions in olivine and host magma. Earth and Planet. Sci. Lett., 272(3), 541–552.

Portnyagin, M., Mironov, N., Botcharnikov, R., Gurenko, A., Almeev, R.R., Luft, C., et al., 2019. Dehydration of melt inclusions in olivine and implications for the origin of silica-undersaturated island-arc melts. Earth and Planet. Sci. Lett., 517, 95–105.

Portnyagin, M.V., Naumov, V.B., Mironov, N.L., Belousov, I.A., Kononkova, N.N., 2011. Composition and evolution of the melts erupted in 1996 at Karymskoe Lake, Eastern Kamchatka: Evidence from inclusions in minerals. Geochem. Int. 49, 1085–1110.

Putirka, K.D., Perfit, M., Ryerson, F.J., Jackson, M.G., 2007. Ambient and excess mantle temperatures, olivine thermometry, and active vs. passive upwelling. Chem. Geol. 241, 177–206.

Rasmussen, D.J., Plank, T.A., Roman, D.C., Power, J.A., Bodnar, R.J., and Hauri, E.H. 2018. When does eruption run-up begin? Multidisciplinary insight from the 1999 eruption of Shishaldin volcano. Earth and Planet. Sci. Lett., 486, 1–14.

Rasmussen, D.J., Plank, T.A., Wallace, P.J., Newcombe, M.E., Lowenstern, J.B., 2020. Vapor-bubble growth in olivine-hosted melt inclusions. Am. Mineral. 105, 1898–1919.

Ribeiro O., (1954), A Ilha do Fogo e as suas erupções, Memórias da Junta de Investigação Científica do Ultramar, Série Geográfica, I, Lisboa, 327

Robidoux, P., Frezzotti, M.L., Hauri, E.H., Aiuppa, A., 2018. Shrinkage Bubbles: The C–O–H–S Magmatic Fluid System at San Cristóbal Volcano. J. Petrol. 59, 2093–2122.

Roedder, E., 1979. Origin and significance of magmatic inclusions. Bull. Mineral. 102, 467–510.

Romero, J.E., Morgado, E., Pisello, A., Boschetty, F., Petrelli, M., Cáceres, F., et al., 2023. Pre-eruptive Conditions of the 3 March 2015 Lava Fountain of Villarrica Volcano (Southern Andes). Bull. Volcanol. 85,1, 2.

Rose-Koga, E.F., Bouvier, A.-S., Gaetani, G.A., Wallace, P.J., Allison, C.M., Andrys, J.A., et al., 2021. Silicate melt inclusions in the new millennium: A review of recommended practices for preparation, analysis, and data presentation. Chem. Geol. 570, 120145.

Rose-Koga, E.F., Koga, K.T., Devidal, J.-L., Shimizu, N., Le Voyer, M., Dalou, C., et al., 2020. In-situ measurements of magmatic volatile elements, F, S, and Cl, by electron microprobe, secondary ion mass spectrometry, and heavy ion elastic recoil detection analysis. Am. Mineral. 105, 616–626.

Rose-Koga, E.F., Koga, K.T., Hamada, M., Hélouis, T., Whitehouse, M.J., Shimizu, N., 2014. Volatile (F and Cl) concentrations in Iwate olivine-hosted melt inclusions indicating low-temperature subduction. Earth, Planets and Space 66, 81.

Rose-Koga, E.F., Koga, K.T., Moreira, M., Vlastelic, I., Jackson, M.G., Whitehouse, M.J., et al., 2017. Geochemical systematics of Pb isotopes, fluorine, and sulfur in melt inclusions from São Miguel, Azores. Chem. Geol. 458, 22–37.

Rosenthal, A., Hauri, E.H., Hirschmann, M.M., 2015. Experimental determination of C, F, and H partitioning between mantle minerals and carbonated basalt, CO_2/Ba and CO_2/Nb systematics of partial melting, and the CO_2 contents of basaltic source regions. Earth and Planet. Sci. Lett. 412, 77–87.

Rowe, M.C., Peate, D.W., Ukstins Peate, I., 2011. An Investigation into the Nature of the Magmatic Plumbing System at Paricutin Volcano, Mexico. J. Petrol. 52, 2187–2220.

Saal, A.E., Hauri, E.H., Langmuir, C.H., Perfit, M.R., 2002. Vapour undersaturation in primitive mid-ocean-ridge basalt and the volatile content of Earth's upper mantle. Nature 419, 451–455.

Sadofsky, S.J., Portnyagin, M., Hoernle, K., 2008. Subduction cycling of volatiles and trace elements through the Central American volcanic arc: evidence from melt inclusions. Contrib. Mineral. Petrol. 155:433–456.

Sandoval-Velasquez, A., Rizzo, A.L., Aiuppa, A., Remigi, S., Padrón, E., Pérez, N.M., Frezzotti, M.L., 2021. Recycled crustal carbon in the depleted mantle source of El Hierro volcano, Canary Islands. Lithos 400–401, 106414. https://doi.org/10.1016/j.lithos.2021.106414

Schiano, P., 2003. Primitive mantle magmas recorded as silicate melt inclusions in igneous minerals. Earth-Sci. Rev. 63, 121–144.

Schiavi, F., Bolfan-Casanova, N., Buso, R., Laumonier, M., Laporte, D., Medjoubi, K., Venugopal, S., Gómez-Ulla, A., Cluzel, N., Hardiagon, M., 2020. Quantifying magmatic volatiles by Raman microtomography of glass inclusion-hosted bubbles. Geochem. Persp. Let. 16, 17–24.

Sharpe, M.S., Barker, S.J., Rooyakkers, S.M., Wilson, C.J.N., Chambefort, I., Rowe, M.C., Schipper, C.I., Charlier, B.L.A., 2022. A sulfur and halogen budget for the large magmatic system beneath Taupō volcano. Contrib. Mineral. Petrol. 177, 95.

Shaw, D.M., 1970. Trace element fractionation during anatexis. Geochimica et Cosmochimica Acta 34, 237-243.

Shaw, A.M., Behn, M.D., Humphris, S.E., Sohn, R.A., Gregg, P.M., 2010. Deep pooling of low degree melts and volatile fluxes at the 85°E segment of the Gakkel Ridge: Evidence from olivine-hosted melt inclusions and glasses. Earth and Planet. Sci. Lett. 289, 311–322.

Shaw, A.M., Hauri, E.H., Fischer, T.P., Hilton, D.R., Kelley, K.A., 2008. Hydrogen isotopes in Mariana arc melt inclusions: Implications for subduction dehydration and the deep-Earth water cycle. Earth and Planet. Sci. Lett. 275, 138–145.

Shimizu, K., Alexander, C.M.O'D., Hauri, E.H., Sarafian, A.R., Nittler, L.R., Wang, et al., 2021. Highly volatile element (H, C, F, Cl, S) abundances and H isotopic compositions in chondrules from carbonaceous and ordinary chondrites Geochim. Cosmochim. Acta, 301, 230-258.

Shimizu, K., Saal, A.E., Myers, C.E., Nagle, A.N., Hauri, E.H., Forsyth, D.W., Kamenetsky, V.S., Niu, Y., 2016. Two-component mantle melting-mixing model for the generation of mid-ocean ridge basalts: Implications for the volatile content of the Pacific upper mantle. Geochim. Cosmochim. Acta 176, 44–80.

Shimizu, K., Ushikubo, T., Hamada, M., Itoh, S., Higashi, Y., Takahashi, E., et al., 2017. H_2O, CO_2, F, S, Cl, and P_2O_5 analyses of silicate glasses using SIMS: Report of volatile standard glasses. Geochem. J., 51(4), 299-313.

Shishkina, T.A., Botcharnikov, R.E., Holtz, F., Almeev, R.R., Jazwa, A.M., Jakubiak, A.A., 2014. Compositional and pressure effects on the solubility of H_2O and CO_2 in mafic melts. Chemical Geology 388, 112-129.

Sides, I.R., Edmonds, M., Maclennan, J., Swanson, D.A., Houghton, B.F., 2014. Eruption style at Kīlauea Volcano in Hawai‘i linked to primary melt composition. Nature Geosciences 7, 464–469.

Spilliaert, N., Allard, P., Métrich, N., Sobolev, A.V., 2006. Melt inclusion record of the conditions of ascent, degassing, and extrusion of volatile-rich alkali basalt during the powerful 2002 flank eruption of Mount Etna (Italy). J. Geophys. Res. 111, B04203.

Sorby, H.C., 1858. On the microscopical structure of crystals, indicating the origin of minerals and rocks. Q. J. Geol. Soc. 14, 453–500.

Sun, C., Dasgupta, R., 2020. Thermobarometry of CO_2-rich, silica-undersaturated melts constrains cratonic lithosphere thinning through time in areas of kimberlitic magmatism. Earth Planet. Sci. Lett.550, 116549.

Sun, C. and Dasgupta, R., 2023. Carbon budget of Earth's deep mantle constrained by petrogenesis of silica-poor ocean island basalts. Earth and Planet. Sci. Lett. 611, 118135.

Sun, S.S. and McDonough, W.F. 1989. Chemical and Isotopic Systematics of Oceanic Basalts: Implications for Mantle Composition and Processes. In: Saunders, A.D., Norry, M.J., Eds., Magmatism in the Ocean Basins, Geological Society, London, Special Publications, 42, 313-345.

Taracsák, Z., Hartley, M.E., Burgess, R., Edmonds, M., Iddon, F., Longpré, M.-A., 2019. High fluxes of deep volatiles from ocean island volcanoes: Insights from El Hierro, Canary Islands. Geochim Cosmochim. Acta 258, 19–36.

Toplis, M.J., 2005. The thermodynamics of iron and magnesium partitioning between olivine and liquid: criteria for assessing and predicting equilibrium in natural and experimental systems. Contrib. Mineral. Petrol. 149, 22–39.

Torres, P., Silva, L.C., Munhá, J., Caldeira, R., Mata, J., Tassinari, C., 2010. Petrology and geochemistry of lavas from Sal Island: Implication for the variability of the Cape Verde magmatism. Comunicaçõe Geológicas 97, 35–62.

Tucker, J.M., Hauri, E.H., Pietruszka, A.J., Garcia, M.O., Marske, J.P., Trusdell, F.A., 2019. A high carbon content of the Hawaiian mantle from olivine-hosted melt inclusions. Geochim Cosmochim. Acta 254, 156–172.

Van Achterbergh, E., Ryan, C.G., Jackson, S.E., Griffin, W.L., 2001. Data reduction software for LA-ICP-MS. Laser-Ablation-ICPMS in the earth sciences—principles and applications Miner. Assoc. Can. (short course series) 29, 239-243.

Vigouroux, N., Wallace, P.J., Kent, A.J.R., 2008. Volatiles in High-K Magmas from the Western Trans-Mexican Volcanic Belt: Evidence for Fluid Fluxing and Extreme Enrichment of the Mantle Wedge by Subduction Processes. J. Petrol. 49, 1589–1618.

Wallace, P. J. 2005. Volatiles in subduction zone magmas: concentrations and fluxes based on melt inclusions and volcanic gas data. J. Volcanol. Geotherm. Res. 140, 217–240.

Wallace, P.J., Kamenetsky, V.S., Cervantes, P., 2015. Melt inclusion CO_2 contents, pressures of olivine crystallization, and the problem of shrinkage bubbles. Am. Mineral. 100, 787–794.

Wallace, P.J., Plan, T., Bodnar, R.J., Gaetani, G.A., Shea, T., 2021. Olivine-hosted melt inclusions: a microscopic perspective on a complex magmatic world. Annu. Rev. Earth Planet. Sci.49, 465–494.

Wang, X., Chou, I.-M., Hu, W., Burruss, R.C., Sun, Q., Song, Y., 2011. Raman spectroscopic measurements of CO_2 density: Experimental calibration with high-pressure optical cell (HPOC) and fused silica capillary capsule (FSCC) with application to fluid inclusion observations. Geochim Cosmochim. Acta 75, 4080–4093.

Wanless, V.D., Behn, M.D., Shaw, A.M., Plank, T., 2014. Variations in melting dynamics and mantle compositions along the Eastern Volcanic Zone of the Gakkel Ridge: insights from olivine-hosted melt inclusions. Contrib. Mineral. Petrol. 167, 1005.

Wanless, V.D., Shaw, A.M., Behn, M.D., Soule, S.A., Escartín, J., Hamelin, C., 2015. Magmatic plumbing at Lucky Strike volcano based on olivine-hosted melt inclusion compositions. Geochem. Geophys. Geosyst. 16, 126–147.

Weaver, B.L., 1991. The origin of ocean island basalt end-member compositions: trace element and isotopic constraints. Earth and Planet. Sci. Lett. 104, 381–397.

Webster, J.D., Baker, D.R., Aiuppa, A., 2018. Halogens in mafic and intermediate-silica content magmas. In: Harlov, D.E., Aranovich, L. (Eds.), The Role of Halogens in Terrestrial and Extraterrestrial Geochemical Processes: Surface, Crust, and Mantle. Springer International Publishing, Cham, 307–430.

Webster, J.D., Rebbert, C.R., 2001. The geochemical signature of fluid-saturated magma determined from silicate melt inclusions in Ascension Island granite xenoliths. Geochim. Cosmochim. Acta 65, 123–136.

Wedepohl, K.H., and Hartmann, G., 1994. The composition of the primitive upper earth's mantle. In: Kimberlites, related rocks and mantle xenoliths. In: Meyer, H.O.A. and Leonardos, O.H. (Eds.), Companhia de Pesquisa de Recursos Minerais, 1, 486-495. Rio de Janeiro.

Willbold, M., Stracke, A., 2006. Trace element composition of mantle end-members: Implications for recycling of oceanic and upper and lower continental crust. Geochem. Geophys. Geosyst. 7, 2005GC001005.

Zanon, V., Silva, R., & Goulart, C. (2023). The crust-mantle transition beneath the Azores region (central-north Atlantic Ocean). Contrib. Mineral. Petrol, 178 (8), 50.

CHAPTER 7.

THE HELIUM AND CARBON ISOTOPIC SIGNATURE OF OCEAN ISLAND BASALTS: CLUES FROM FOGO VOLCANO, CAPE VERDE ARCHIPELAGO

ABSTRACT

Fluid inclusions (FI) entrapped in crystals carried by Ocean Island Basalts (OIB) contain key information on volatile abundance and origin in their mantle sources. Here, we add new piece of knowledge to our understanding of volatile geochemistry in global OIB magmas, by presenting novel noble gas (He-Ne-Ar) and carbon (C) isotope results for olivine- and clinopyroxene-hosted FI from cumulates, lavas, tephra and volcanic gas samples from Fogo, the most active volcano of the Cape Verde Archipelago (eastern Atlantic). FI, in tandem with crater fumaroles, constrain the Fogo $^{3}He/^{4}He$ signature at 7.14-8.44 R_c/R_a (where R_C is the air-corrected $^{3}He/^{4}He$ isotope ratio, and R_a is the same ratio in air), which is within the typical MORB-like mantle. The carbon isotopic ratio ($\delta^{13}C$ vs. PDB) of CO_2 in FI and fumaroles range from -6.04 to -4.41‰. We identify systematic variations of $\delta^{13}C$ and He/Ar* with FI entrapment pressure (as estimated from a combination of host mineral barometers and FI densimetry/microthermometry), from which we develop a model for volatile degassing in the mantle-to-crustal magmatic plumbing system. From this model, we predict a crustal signature for carbon ($\delta^{13}C$ of ~ -0.4‰) in primary melts formed by upper mantle melting at ~2200 MPa (~77 km), which we interpret as indicative of mantle metasomatism by melts/fluids enriched in a recycled crustal carbon component. We also use our results to characterise regional and global trends in OIB C and He isotope composition. From comparison with the few other OIB localities for which $\delta^{13}C$ in FI are available, we propose that recycled crustal carbon is a common component in global OIB volcanism, although often masked by isotope fractionation during magmatic degassing. We additionally find that, at regional scale (in the Cape Verde and Canary archipelago), He isotopes in OIB scale inversely with individual islands' volumes (and, hence, with magma production rates in the source mantles), while the global OIB He isotopic signatures are primarily controlled by plume buoyancy flux and overlying plate speed. In this interpretation, the MORB-like $^{3}He/^{4}He$ (8±1 Ra) at Fogo would reflect a combination of (i) high magma productivity, (ii) relatively low plume buoyancy flux (~1.1 Mg/s), and (iii) slow average speed (~4 cm/yr) of the overlying plate.

Keywords: Oceanic Island Basalts, Fogo volcano, Cape Verde, fluid inclusions, helium and carbon isotopes.

7.1. Introduction

Ocean Island Basalts (OIB) offer invaluable insights into the geochemistry of the Earth's upper mantle, and eventually on the characteristics of deeply rooted mantle plumes (Hards et al., 1995; Kurz et al., 1996; Hoernle et al., 2000). OIB are, for example, known to exhibit highly variable radiogenic isotope (Sr-Nd-Pb) signatures, commonly interpreted as evidence of mantle heterogeneity (e.g., Jackson and Dasgupta, 2008), and to reflect the existence of several distinct mantle components interacting each other, and mixing in various proportions, in the various OIB localities (Zindler and Hart, 1986). Light noble gases (He, Ar and Ne) are especially useful tracers of mantle processes (e.g., Fisher, 1983; Sarda et al., 1988; Dunai and Porcelli, 2002; Gurenko et al., 2006; Hopp et al., 2007a, 2007b; Dickin, 2018; Boudoire et al., 2018, 2020; Rizzo et al., 2018, 2021; Day et al., 2022; Sandoval-Velasquez et al., 2023), because the different fluid components (primordial, crustal, radiogenic, atmospheric) potentially present in the OIB mantle source have distinct isotopic signatures. Noble gases in fluid inclusions (FI), tiny droplets of fluids entrapped in crystals carried by magmas (e.g. Roedder et al., 1984), are especially useful for understanding the processes that modify the characteristics of the mantle in space and time, and the nature and signature of fluids in the mantle (Frezzotti and Peccerillo, 2004; Frezzotti and Peccerillo, 2007; Frezzotti et al., 1992, 2002). Past studies identified large regional and global diversity in noble gas isotopic compositions in FI (e.g., Gautheron et al., 2005; Martelli et al., 2014; Day et al., 2015; Boudoire et al., 2018, 2020; Rizzo et al., 2018, 2021; Sandoval-Velasquez et al., 2021a, 2021b, 2023). However, the factors responsible for the observed variability are not entirely understood.

In the Cape Verde archipelago, the most studied OIB locality in eastern Atlantic, sizeable noble gas heterogeneities have been identified studying FI in crystals from magmatic rocks (Christensen et al., 2001; Doucelance et al., 2003; Mourão et al., 2011) (Figs. 39,40). He isotope data, available for seven out of the 10 main islands, span from < 1 Ra (where R is the $^{3}He/^{4}He$ isotopic ratio of the sample and Ra is the corresponding ratio in air) to > 40 Ra (Fig. 1) (Christensen et al., 2001; Doucelance, et al., 2003; Mourão et al., 2011). Large inter-island isotopic diversity and individual island heterogeneity is observed (Fig. 1), with the least radiogenic (more primitive mantle-like) He compositions observed at São Nicolau (10.5-15.7 Ra; mean, 13.3 Ra) and in the northern islands in general (3.2-42.6 Ra,

mean 11.4 Ra) (Fig. 40), and more MORB-like (8±1 Ra; Graham, 2002) compositions in the southern islands of Santiago (0.2-29.3Ra; mean 8.1 Ra) and Fogo (3.7-12.1 Ra; mean 7.9 Ra) (Christensen et al., 2001; Doucelance et al., 2003; Mourão et al., 2011; Alonso e al., 2021; Melián et al., 2021). At Fogo Island, the only with recurrent magmatic activity, the He isotope compositions measured in FI and in summit crater fumaroles range from 3.7 to 12.1 Ra (Doucelance et al., 2003; Alonso et al., 2021; Melián et al., 2021).

The carbon isotope signature of OIB (and of their mantle sources) has been even more difficult to decipher. This is because very few FI results are available (Aubaud, 2022), and because of the technical challenges in precisely measuring $\delta^{13}C$ compositions of dissolved carbon in glassy melt inclusions and in magmatic minerals. Yet we know from FI in mantle xenoliths (Deines, 2002) that the mantle has very diverse carbon isotope signatures at a worldwide scale, with $\delta^{13}C$ values ranging from -29.9‰ at Hawaii (Pineau and Mathez, 1990) to +0.9‰ at El Hierro (Canary Islands, Sandoval-Velasquez et al., 2021a). This wide range suggests the involvement of a variety of crustal carbon components [ranging from organic crustal carbon (-30‰ to -10‰) to limestone carbon (from -1‰ to +1‰)] and the mixing in various proportions with a deep Depleted MORB-like (Mid- Ocean Ridge Basalt) Mantle (DM) carbon ($\delta^{13}C$ of -4 to -8 ‰) (Sano and Marty, 1995; Deines, 2002). OIBs, especially if alkaline in nature, are carbon-rich (Sun and Dasgupta, 2023 and references therein), indicating these magmas do form by low-degree partial melting of carbon-enriched (metasomatized) mantle sources. Measuring the carbon isotope signature of alkaline OIB is thus critical to testing models (Dasgupta, 2019) that see these metasomatic agents (carbonatitic to carbonated silicate melts) to derive from melting of deeply subducted, carbon enriched crustal lithologies. The presence of recycled crustal carbon in OIB mantle has recently been identified in the Canary Islands (Sandoval-Velasquez et al., 2021a, 2023), but remains untested in most OIB localities including at Cape Verde, where carbon isotopic results are only available for Fogo fumaroles (Melián et al., 2021).

Here, we present novel FI results from crystals in lavas, tephra, and enclaves from Fogo volcano, including the first FI carbon isotopic measurements for the Cape Verde archipelago. We compare our results with the regional and global OIB context, in the attempt to refine our understating of the factors that primarily control the OIB isotopic diversity. The carbon isotope results are used to model the source-to-surface carbon isotopic evolution during magmatic degassing in the volcano plumbing system, revealing the presence of a recycled crustal carbon component in the mantle of alkaline OIB volcanism.

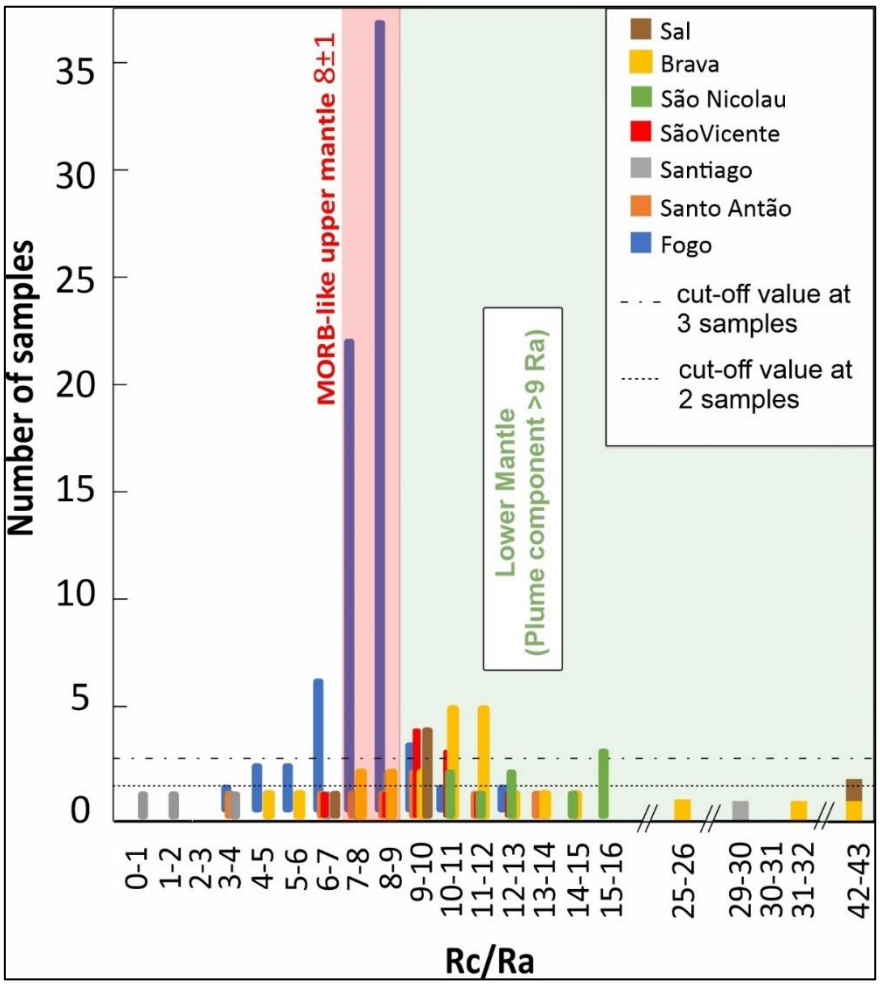

Figure 39 He isotopes (expressed as Rc/Ra values, where RC is the air-corrected He isotope composition) in FI and fumarolic gases from the different islands of Cape Verde archipelago. Data are from Christensen et al. (2002), Doucelance et al. (2003), Mourão et al. (2011), Alonso e al. (2021), Melián et al. (2021). Measurements are categorised in 19 different classes. Two different cut-off values (of 2 and 3 samples per class) are proposed (for the more and less populated classes, respectively); samples/classes below these cut-off values are considered outliers, and are not considered in the calculation of individual islands' refined ranges of Rc/Ra values, shown in Fig. 29. No data is available for Maio and Boa Vista Islands

7.2. Volcanological and geodynamical background

Fogo Island is located in the Cape Verde archipelago, in the central Atlantic Ocean (West Africa). The archipelago stands on the Cape Verde Rise, an oceanic intraplate bathymetric anomaly, interpreted to result from the interaction between a mantle plume and the quasi-stationary (~3 cm/yr, average plate speed; Hoggard et al., 2020 and reference therein) African plate (Pollitz, 1991). The archipelago consists of ten major islands divided into two main branches: the northern islands (Santo Antão, São

Vicente, Santa Luzia, São Nicolau, Sal, and Boa Vista), and the southern islands (Maio, Santiago, Fogo and Brava). The two branches exhibit contrasting isotopic (Sr-Nd-Pb) signature, with HIMU (High-μ=high $^{238}U/^{204}Pb$ ratio) and EM-I (Enriched Mantle) mantle source affinities (Gerlach et al., 1988; Doucelance et al., 2003; Mata et al., 2017). Recent melt inclusion work on Fogo volcano suggests a CO_2-rich mantle source beneath the archipelago (342-411 ppm C; Lo Forte et al., 2024). A carbon-rich, metasomatized mantle source is additionally supported by rare carbonatites, which have been erupted both in islands of Fogo (Hoernle et al., 2002), Brava (Mourão et al., 2010) and Santiago (Martins et al., 2010), in the south of the archipelago and in the island of Sal in the north of Cape Verde (Bonadiman et al., 2005).

Magmatism at Fogo Island dates back at 3-4.5 Ma and historically has been focussed at Pico do Fogo volcano (Day et al., 1999). Volcanism is dominated by silica-undersaturated magmas (Gerlach et al., 1988) and rare carbonatites (e.g., Hoernle et al., 2002; Mourão et al., 2012). Previous studies on Fogo volcano focussed on magma chemistry and on the reconstruction of the magma plumbing system, which is characterized by: (i) a deep magma reservoir at 27-36 km depth, (ii) a main magma storage zone at ~12-24 depth, (iii) and a magma stagnation zone at ~9-12 km depth, where the magma stalls during its ascent at the crustal-mantle boundary layer.(e.g., Hildner et al., 2011; 2012; Mata et al., 2017; Klügel et al., 2020; Lo Forte et al., 2023).

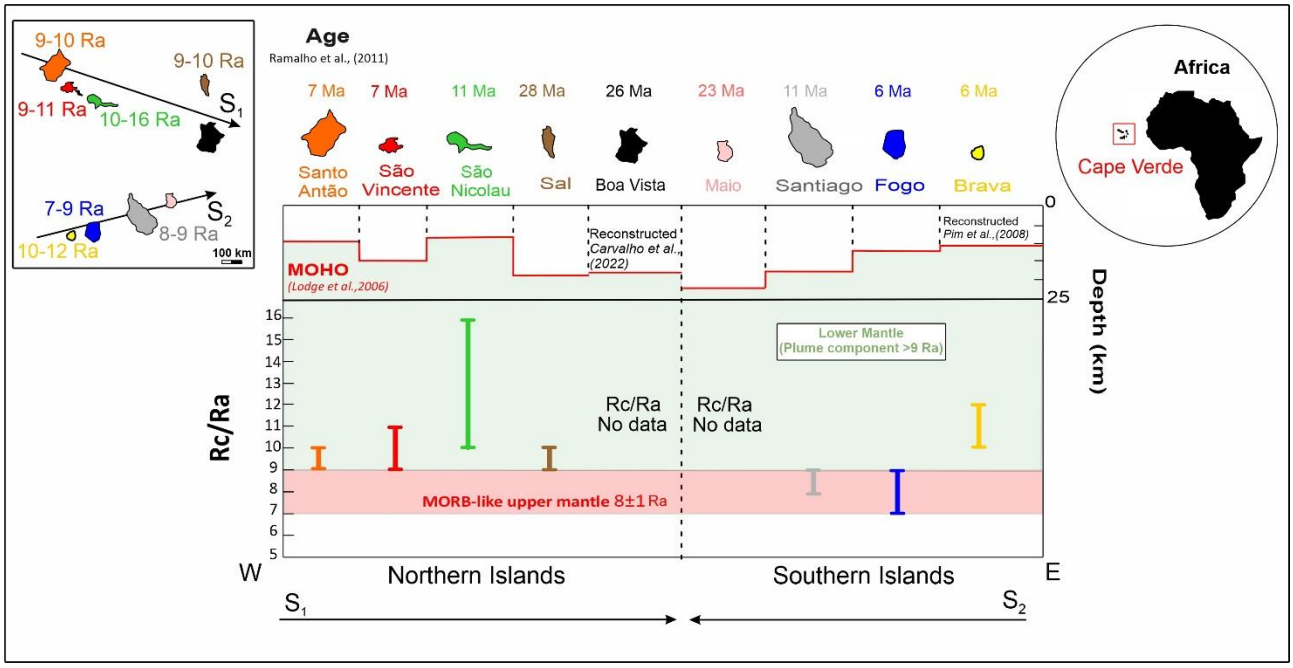

Figure 40 The $^{3}He/^{4}He$ refined range of individual islands of the Cape Verde Archipelago. We initially screened the entire dataset available (listed in Table S1 of the Supplementary material S1) and performed a data quality check that considers the noble gas extraction method used (single-step

and multi-step crushing, and melting). We discarded all results employing multi-step crushing or melting extraction methods that, in contrast to the single-step crushing (employed by Gautheron et al., 2005), are potentially affected by the release of radiogenic and cosmogenic noble gases trapped within the crystal lattice. Insets show position of the archipelago relative to Africa (right) and the southern and northern branches (left). The reported ages are the maximum ages reported for each island from (Ramalho, 2011). The solid red line is Moho depth (data from Lodge and Helffrich, 2006 except for Boa Vista, where the Moho depth is based on the reconstruction of Carvalho et al. (2022), and Brava, based on the Moho reconstruction of Pim et al. (2008)).

7.3. Methods

7.3.1. Samples

We report on the He, Ne, Ar, and CO_2 isotope signature of FI in olivine and clinopyroxene crystals from lavas, tephra and mafic enclaves from Fogo Island. Lavas and tephra samples have been already studied for bulk-rock and melt inclusion geochemistry, and FI microthermometry (Lo Forte et al., 2023a; 2023b; 2024) and their data are summarized in section 3.1. The mafic enclaves (FG1-A, FG2-A1, FG2-A3, FG3-A, FG4-A, FG4-B, FG4-D, and FG4-E) were found in lavas and tephra outcropping in the periphery of Pico di Fogo and within the Chã das Caldeira caldera (Table 5). We also report novel isotopic results for two Pico do Fogo fumarole samples (PF-1 and PF-2), whose chemical composition and SO_2 flux are reported in Aiuppa et al. (2020). Table 5 lists the studied samples and summarizes the analyses conducted. Further details on the lava, tephra, and mafic enclaves samples, as well as the analytical methods employed for the FI composition and CO_2 densimetry (Raman spectroscopy) and mineral chemistry (Electron Microprobe, EMPA), are provided in Supplementary Material S2. Based on their compositions, clinopyroxene crystals in mafic enclaves are categorised in Group Ia, Ib and II (see Supplementary Material S2).

Table 5. List of the analyzed samples. NG= Noble gases isotopes; C= carbon isotopes; R= Raman; M= Mineral chemistry. (*) Samples analysed in previous work (Lo Forte et al., 2023).

Sample name	Rock type	Rock composition	Eruption	Analyses performed	Coordinate
Fog 20 (*)	Lava	Basanite	1799	NG	14° 57’ 41.5” N 24° 17’ 39.6” W
Fog 23 (*)	Lava	Basanite	1664	NG	15° 0’ 24.9” N 24° 18’ 19.2” W
Fog 24 (*)	Lava	Basanite	1852	NG	15° 0’ 40.1” N 24° 18’ 22.8” W

Fog 27 (*)	Lava	Basanite	~60 ka	NG	14° 52’ 13.0” N 24° 22’ 7.5” W
Fog 28 (*)	Lava	/	~10 ka	NG	14° 58’ 11.8” N 24° 20’ 59.5” W
Fog 31 (*)	Lava	/	1951	NG	14° 55’ 1.2” N 24° 17’ 45.7” W
Fog 33 (*)	Lava	Basanite	1400s-1800s	NG, C	14° 57’ 3.7” N 24° 20’ 30.9” W
Fog 43 (*)	Tephra	/	~10 ka	NG	15° 0’ 53.6” N 24° 24’ 34.7” W
FG1-A	Cumulate	/	~10 ka	NG, C, R, M	14° 58’ 50.9” N 24° 22’ 11.4” W
FG2-A1	Cumulate	/	1951	NG, M	14° 58’ 50.0” N 24° 21’ 20.3” W
FG2-A3	Cumulate	/	1951	NG, R, M	14° 58’ 50.0” N 24° 21’ 20.3” W
FG3-A	Cumulate	/	1400s-1800s	NG, C, R, M	14° 57’ 6.10” N 24° 20’ 33.45” W
FG4-A	Cumulate	/	~10 ka	NG, R, M	14° 58’ 14.1” N 24° 22’ 05.4” W
FG4-B	Cumulate	/	~10 ka	NG, M	14° 58’ 14.1” N 24° 22’ 05.4” W
FG4-D	Cumulate	/	~10 ka	NG, M	14° 58’ 14.1” N 24° 22’ 05.4” W
FG4-E	Cumulate	/	~10 ka	NG, R, M	14° 58’ 14.1” N 24° 22’ 05.4” W
Pico do Fogo1	Fumarole	/	/	NG, C	14° 57' 1.6” N 24° 20’ 27.9”
Pico do Fogo 2	Fumarole	/	/	NG, C	14° 57' 2.3” N 24° 20’ 26.5”

7.3.1.1. Lavas and tephra

Lava and tephra samples (Fog 20, 23, 24, 27, 28, 31, 33, 43) are nepheline-normative (nepheline: 8.4-25.4%) basanites SiO_2 content from 41.1 to 44.3 wt% and $K_2O + Na_2O$ contents varying between 3.0 and 9.4 wt%. The typical mineral assemblage includes clinopyroxene, olivine, plagioclase, and Fe-Ti

oxides. Clinopyroxene phenocrysts are diopsides (Wo_{49} En_{32} Fs_{11} to Wo_{52} En_{40} Fs_{15}) except a single augite crystal (Wo_{33} En_{42} Fs_{26}) and exhibit a wide range of Al_2O_3 content (from 5.6 to 14.2 wt%). TiO_2 and Na_2O show relatively less variability, ranging from 2.4 to 5.9 wt.% and from 0.4 to 2.4 wt.%, respectively. Olivine phenocrysts have forsterite contents ranging from Fo_{77} to Fo_{85}, CaO ranging between 0.28 and 0.40 wt%, and NiO in the 0.03–0.15 wt% range.

Fluid inclusions (FI) are hosted in olivine and clinopyroxene phenocrysts in both lava and tephra samples from the last 120 ka of Fogo's activity. All the FI are made of pure CO_2 and are biphasic (liquid + vapor) below the temperature of homogenization with the liquid phase being more abundant than the vapor phase (L_V). FI do not contain visible daughter minerals or co-trapped minerals. Both early-stage fluid inclusions (Type I), entrapped during crystal formation and growth, and late-stage (Type II) inclusions, formed through re-equilibration processes of the fluid, have been identified by Lo Forte et al. (2023). FI homogenised to the liquid phase in a range of temperatures (Th_L) from 2.8 to 30.8 °C, corresponding to densities between 0.952 and 0.543 g/cc (uncertainty in density calculation, is on average 5 %). These CO_2 densities reflect entrapping pressure from 245 to 740 MPa (corresponding to depths of 9.2-24.3 km).

The melt inclusions (MI) were exclusively hosted within olivine phenocrysts from tephra samples of the last 10 ka of activity of Fogo volcano. All MI contain shrinkage bubbles, which occupy the 0.2-8.6 % of the total MI volume. There is no textural evidence of MI decrepitation. Part of the MI shrinkage bubbles contains mineral phases such as Fe-magnesite, nahcolite, and sulphates. MI compositions are in the ranges 39.9-45.7 wt.% SiO_2, 4.0-7.4 wt.% MgO, 3.0-5.2 wt.% Na_2O, and 8.4-11.6 wt.% FeOt. The CaO/Al_2O_3 ratios vary between 0.44 and 0.97. The volatiles contents in the measured MI range from 1.17 to 2.78 wt.%, from 0.21 to 2.15 wt.% from 1120 to 8205 ppm, from 917 to 1415 ppm, and from 1285 to 2249 ppm for H_2O, CO_2, S, Cl, and F, respectively. The MI saturation pressure derived from the most CO_2-rich melt (2.15 wt.%) range between 773 and 1020 MPa (corresponding to depths of 31.5 ± 4.3 km). Combining barometric results determined by FI microthermometry (Lo Forte et al., 2023) and MI saturation pressures (Lo Forte et al., 2024), the Fogo plumbing system consists of: (i) a deep magma reservoir at ~31.5 ± 4.3 km depth; (ii) a deeper storage zone at ~24 km depth; (iii) a main magma storage zone at 13-17 km depth, and (iv) a magma stagnation zone at 9-12 km depth.

7.3.1.2. Mafic enclaves

The mafic enclaves (FG1-A, FG2-A1, FG2-A3, FG3-A, FG4-B, FG4-D, FG4-E) analysed in this study for noble gases and carbon isotopes were embedded in lava flows and crystals were extracted by scraping. No petrological characterization of these samples was performed.

Electron microprobe analyses on mineral phases were performed by using a CAMECA SX5 (LMV, Clermont-Ferrand, France) set with 15 kV potential, 20 nA focused beam coupled with a counting time varying from 10 to 50s depending on the element. Analytical error (as 3σ) was lower than 2% of the measurement for Si-Mg-Ca (12% for Ca in clinopyroxene), lower than 4% for Fe-Al; lower than 13 % for Ti-Na in clinopyroxene and lower than 40 % and 70 % for Cr in clinopyroxene and Ni in olivine, respectively. Only values above three times the detection limit were kept. EMPA results are listed in Table S3 of the Appendix B. The composition of olivine crystals in samples FG2-A1, FG2-A3 and FG3-A is homogenous with forsterite content in the range 80.3-82.6 and mostly (> 95%) in the range 81.3-82.6. No core to rim gradient in Forsterite, CaO and NiO was observed. Clinopyroxene crystals are either Ti-rich diopside (TiO_2 from 2.0 to 4.6 wt%; Group Ia and Ib) or diopside (in samples FG1-A and FG4-B; TiO_2 from 0.5 to 1.1 wt%; Group II) without noticeable difference between crystal cores and rims (even if no detailed zoning study was performed). As previously documented in recent lavas at Fogo (Klügel et al., 2020), Ti-rich diopside crystals show two distinct behaviours (Fig. S1, Appendix B): Group Ia is richer in Si-Fe and poorer in Al-Ti than Group Ib at similar MgO content. Group Ia (FG4-A, FG4-D, FG4-E) is reminiscent of the composition of clinopyroxene crystals founded in phonotephritic lavas whereas Group Ib (FG2-A1, FG2-A3, FG3-A) rather mirrors those in tephritic lavas (Klügel et al., 2020). In this study (and in the absence of melt analysis), the clinopyroxene-only barometer of (Putirka, 2008) is used (Eq. 32a) with an averaged magma temperature of 1130°C (see Klügel et al., 2020) to obtain pressure estimates (Table S3 of the Appendix B). Fluid inclusions in clinopyroxene and olivine crystals were analysed by Raman at the Laboratoire Magmas et Volcans (LMV, Clermont-Ferrand, France) using an InVia confocal Raman micro-spectrometer manufactured by Renishaw and equipped with a 532 nm diode laser, a Peltier-cooled CDD detector of 1040x256 pixels, a motorized XY stage, and a Leica DM 2500 M optical microscope. Laser power was reduced to 10% of the nominal output power (200 mW) using filters. A 2400 grooves/mm was used for the analysis resulting in a spectral resolution better than 1 cm^{-1}. Calibration of the spectrometer was performed on a Si 520.5 cm^{-1} standard. FI in olivine

and clinopyroxene crystals from the mafic enclaves were essentially present as trails of secondary fluid inclusions (Fig. S2, Appendix B). Only rounded FI with a diameter in the range 2-6 μm were analysed. Decrepitated inclusions, or with visible secondary mineral phases (especially in the biggest FI; Frezzotti and Touret, 2014), were discarded. The targeted FI were homogenous at the Raman microscope without moving CO_2 vapor bubbles in a liquid phase. Numerous FIs were empty and only few of them were analysable in samples FG1-A, FG2-A3, FG3-A, FG4-A and FG4-E. Analysed FIs by Raman spectroscopy reveal the presence of CO_2 (Fermi doublet; Fig. S2, Appendix B) without other detectable gaseous species. Carbonate were detected in some FIs in clinopyroxene crystals from FG4-E (main peak at 1094 cm^{-1}; magnesite) (Fig. S2, Appendix B). Potential hydrated sulphates (weak peak at 1112 cm^{-1} and 1184 cm^{-1}) were detected in some FIs in clinopyroxene crystals from FG1-A.

Pressure estimates from FI were obtained by CO_2 densimetry deduced from the Fermi doublet split (Frezzotti et al., 2012) between the 1388 cm^{-1} and 1285 cm^{-1} bands (Δ). Recent study has demonstrated the sample preparation and instrumental dependence of the Fermi doublet (Hagiwara et al., 2021; Lamadrid et al., 2017; Remigi et al., 2021), limiting the use of CO_2-densimetry equations calibrated on other machines. Olivine and clinopyroxene crystals in which fluid inclusions were analysed ranges between 1 and 1.5 mm in diameter and are more than 200 μm thick. Crystal thickness was homogenized during the sample preparation (polishing). This sample preparation makes the crystal-linked heating effect of fluid inclusions negligible (Hagiwara et al., 2021). By reducing the laser power from 10% to 5%, no heating effect was observed on the Fermi doublet (Hagiwara et al., 2021). The CO_2 densimetry equation of Song et al. (2009) was used to retrieve the CO_2 density from the Fermi doublet. Measurements were obtained following the same procedure than described in Boudoire et al. (2023) with a final uncertainty of 0.054 g/cm^3 on CO_2 densities. At room temperature, H_2O vapor was not detectable by Raman spectroscopy. However, the presence of a CO_2-H_2O mixture is common in FI (Frezzotti and Touret, 2014). Later dehydratation of FI, by diffusion within the hosting crystal and by reaction with it, can lead to the formation of hydrous phases and carbonates (present in some fluid inclusions analysed in this study). FI densities were thus calculated assuming the original CO_2-rich fluid can contain up to 10 mol% of H_2O in accordance with previous results obtained at Fogo (e.g., Klügel et al., 2020). Pressure was estimated with the ISOC code (Bakker, 2003) using the equation of state of Duan et al. (1992, 1996) set for CO_2-H_2O mixture on a large range of pressure and temperature. Results are listed in Table S2 of the Appendix B. In general, CO_2 density in FI ranges from 0.19 to 0.29 g/cc (0.19 to 0.30 g/cc by adding 10 mol% of H_2O) in

clinopyroxene crystals and from 0.15 to 0.62 g/cc (0.15 to 0.65 g/cc by adding 10 mol% of H_2O) in olivine crystals.

7.3.2. Noble gases and Carbon isotopes analyses

The concentrations and isotopic compositions of noble gases (He, Ne, and Ar) and CO_2 in both (i) fluid inclusions (FI) hosted in mineral separates from lavas/tephra/cumulates and (ii) fumaroles were analysed at the INGV, Sezione di Palermo isotopic laboratories, Italy.

7.3.2.1. Isotope compositions of He, Ne, Ar, and CO_2 in fluid inclusions

The selected crystals were divided into two aliquots: a first aliquot was used for noble gas isotopes measurement, while the second one was used to determine the concentration and isotope composition of CO_2. Either noble gases or CO_2 were extracted by in vacuo single-step crushing at about 200 bars. The protocol adopted for FI purification before noble gases and carbon mass spectrometric measurements are the same reported in Rizzo et al. (2018, 2021) and Sandoval-Velasquez et al. (2021a, 2021b, 2023).

Helium isotopes (^3He and ^4He) and ^{20}Ne were measured separately using two different split-flight-tube mass spectrometers (Helix SFT, Thermo Scientific). $^3He/^4He$ ratios are expressed in units of R/Ra, where Ra represents the $^3He/^4He$ ratio of air, which is equal to 1.39×10^{-6} (Ozima and Podozek, 2002). The analytical uncertainty of the He-isotope ratio (1σ) was generally less than 1.6%. The ^{20}Ne was corrected for isobaric interferences at m/z values of 20 ($^{40}Ar^{2+}$). The ^{36}Ar, ^{38}Ar, and ^{40}Ar were analysed using a multi-collector mass spectrometer (Argus, GVI) with an analytical uncertainty (1σ) of less than 0.5%. Additional information regarding analytical procedures, adopted standards and their precision over time, can be found in Rizzo et al. (2018, 2021), and in Sandoval-Velasquez et al (2021a, 2021b, 2023).

The ^{40}Ar was corrected for air contamination ($^{40}Ar^*$) as follows:

$$^{40}Ar^* = {}^{40}Ar_{sample} - [{}^{36}Ar_{sample} \cdot (^{40}Ar/^{36}Ar)_{air}]$$

The $^3He/^4He$ ratio was corrected for atmospheric contamination (Rc/Ra) by utilizing the measured $^4He/^{20}Ne$ ratio, as follows:

$$Rc/Ra = ((R_M/Ra)(He/Ne)_M - (He/Ne)_A)/((He/Ne)_M - (He/Ne)_A)$$

where Rc stands for the air-corrected $^3He/^4He$ ratios, and subscripts M and A represent measured and atmospheric theoretical values, respectively.

Following the noble gas analysis, three aliquots with the highest CO_2 concentrations (olivines from the samples Fog33 and FG3-A, and clinopyroxene from the sample FG1A) were selected for determining the carbon isotopic composition of FI ($^{13}C/^{12}C$), which is reported as $\delta^{13}C$ in parts per mil (‰) relative to the Vienna Pee Dee Belemnite international standard (V-PDB). The CO_2 extraction and purification protocol are the same reported in Correale et al. (2015), Gennaro et al. (2017) and Rizzo et al. (2018). The analytical error, estimated as 2σ, was better than 0.3‰.

Noble gas and carbon isotope results are listed in Table S1 of Appendix B.

7.3.2.2. Isotope compositions of He, Ne, Ar, and CO_2 in fumaroles

Fumarole gas samples were collected as "dry gas" in glass and stainless-steel bottles with two stopcocks, following the procedure reported in e.g., Rizzo et al. (2015). Major gas concentrations were measured by a gas chromatograph (Clarus 500, Perkin Elmer) equipped with a 30-meter column (inner diameter = 0.32 mm; Poraplot-Q), operated at a constant temperature of 50°C using helium as the carrier gas, at the laboratory of INGV, Sezione di Palermo, Italy.

^3He, ^4He, and ^{20}Ne, as well as the $^4He/^{20}Ne$ ratios, were measured by introducing He and Ne separately into a split-flight tube mass spectrometer (GVI-Helix SFT, for He analysis) and a multi-collector mass spectrometer (Thermo-Helix MC plus, for Ne analysis) after standard purification procedures.

The carbon isotope composition of CO_2, expressed as $\delta^{13}C$ vs. V-PDB (Vienna Pee Dee Belemnite), was determined using a continuous-flow isotope-ratio mass spectrometer (Thermo Delta Plus XP, Finnigan) connected to a gas chromatograph (Trace GC) and interface (Thermo GC/C III, Finnigan). The standard deviation (SDs) for the $\delta^{13}C$ was less than 0.2‰.

Further details on the analytical procedure and adopted standards are the same reported in Rizzo et al. (2015, 2016, 2019). The chemical and isotopic compositions of dry gases are reported in Table S1 of Appendix B.

7.4. Results

The studied FI consist of pure CO_2 whose concentration in mafic enclaves range from 0.09 to $8.8 \cdot 10^{-8}$ mol/g in olivine crystals, and from 0.0008 mol/g to $6.7 \cdot 10^{-7}$ mol/g in clinopyroxene crystals. For comparison, in olivine crystals hosted in lavas and tephra, CO_2 concentrations span from 0.14 to $1.2 \cdot 10^{-8}$ mol/g. The CO_2 concentrations in the two fumaroles are >96% vol. (Table S1 of Appendix B).

The $\delta^{13}C$ isotope compositions of CO_2 in FI from crystals in mafic enclaves vary from -6.04 to -4.73‰. The most negative $\delta^{13}C$ value is obtained for FI in clinopyroxene crystals in sample FG1-A, while the most positive in the olivine crystals of sample FG3-A. The $\delta^{13}C$ of CO_2 in the two fumarolic samples are overall consistent with the FI results, ranging from -5.1 to -4.7 ‰ for PF-2 and PF-1, respectively.

The Rc/Ra values range from 7.35 to 8.18 and from 7.86 to 8.44 in olivine-hosted and clinopyroxene-hosted FI in mafic enclaves, from 7.14 to 8.25 in olivine crystals from lava and tephra samples, and from 8.06 to 8.07 in the fumaroles (Fig. 41).

In the mafic enclaves, the $^{4}He/^{20}Ne$ ratios vary between 167 and 746 in olivine-hosted FI, and between 99 and 2388 in clinopyroxene-hosted FI (Fig. 41). The $^{4}He/^{20}Ne$ ratios range from 10 to 468 for FI in crystals from lava and tephra samples, and from 37 to 104 in the fumaroles.

The $^{4}He/^{40}Ar^{*}$ ratios are 0.47-2.44 and 0.48-11.28 in FI from olivine and clinopyroxene crystals from mafic enclaves, respectively, 0.13-1.12 in olivine-hosted FI in lava and tephra, and 0.91-1.13 in fumaroles (Fig. 41).

The $^{40}Ar/^{36}Ar$ values range from 339 to 1670 and from 315 to 1174 in FI from olivine and clinopyroxene crystals from mafic enclaves, and from 354 to 1758 in olivine crystals from lava and tephra samples. The observed $^{40}Ar/^{36}Ar$ ratios in the fumaroles PF-2 and PF-1 are from 324 to 397. For the sake of simplicity, in the discussion below we do not differentiate between lava and tephra samples and mafic enclaves due to their comparable isotopic compositions.

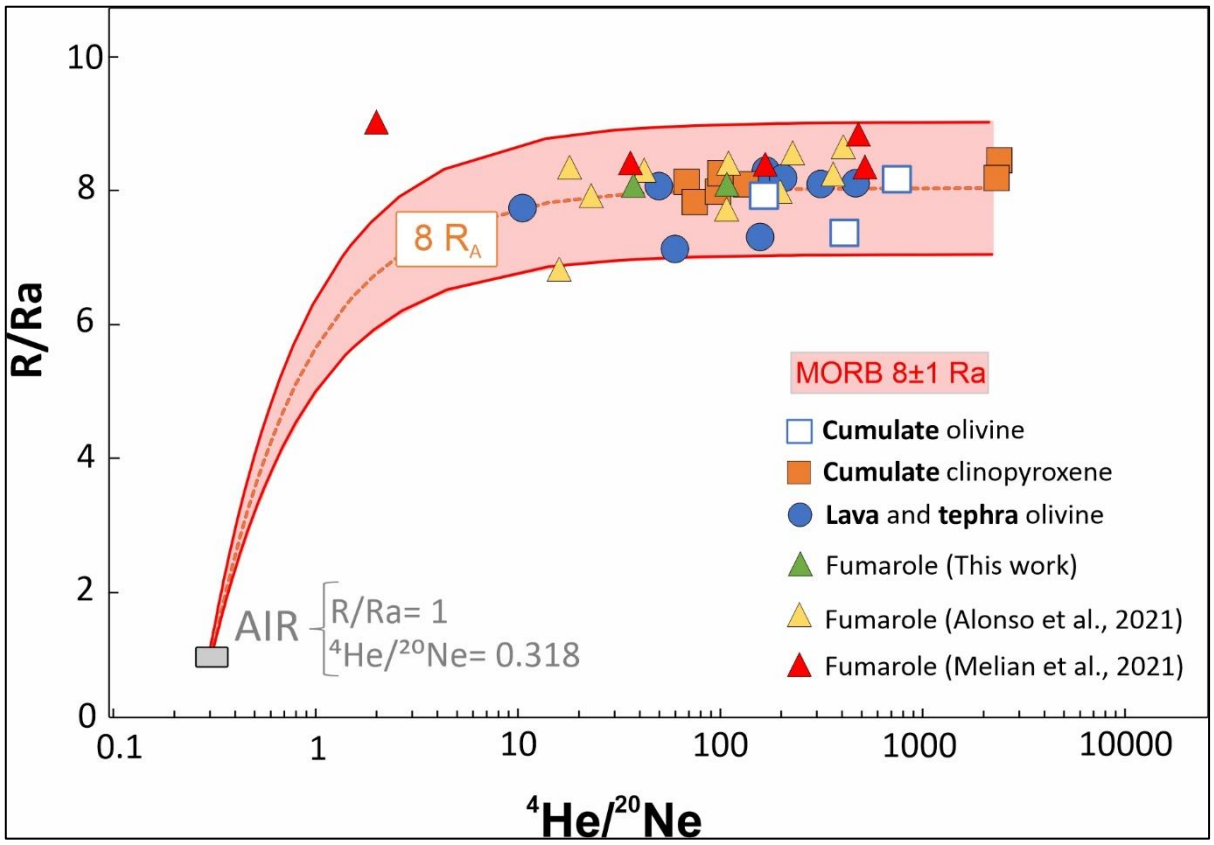

Figure 41 $^3He/^4He$ expressed as R/Ra vs. $^4He/^{20}Ne$. The binary mixing curves are between (i) air and a MORB-like (8±1 Ra) magmatic endmember (8±1).

7.5. Discussion

7.5.1. FI entrapment conditions.

The conditions of magmas storage underneath Fogo volcano have been established previously by using mineral barometers (Klügel et al., 2020), FI microthermometry (Hildner et al 2011; 2012; Lo Forte et al., 2023), and melt inclusions geochemistry (Lo Forte et al., 2024) (Fig. 42a). Based on these results, a complex, vertically stacked magma system has been reconstructed (Fig. 42b), in which (1) magmas are initially stored in a deep magma reservoir at 773-1020 MPa (27-36 km depth); (2) an intermediate magma storage zone exists at 385-740 MPa pressure (~13-26 km depth); (3) upon pre-eruptive ascent, magmas eventually reside in the crust at 250-380 MPa pressure (~9-12 km depth) (Figs. 42a and 42b).

Our novel clinopyroxene barometric results for mafic enclaves (Table S3 of the Supplementary Material S1) confirm these results (Fig. 42a). Using the average temperatures of 1050 °C and 1130°C for tephritic (Group Ia) and phonotephritic (Group Ib) melts (Klügel et al., 2020), respectively,

clinopyroxene-based barometry (Eq. 32a; Putirka, 2008) yields equilibrium pressures of 536-737 (±130) MPa (18-26 km depth, using densities from the crustal model of Pim et al., 2008) for Group Ia and 336-464 (±144) MPa (12-16 km depth) for Group Ib (Fig. S2; 42a). These estimated pressures broadly overlap with those obtained previously by applying clinopyroxene barometry to Fogo lavas (e.g., Klügel et al., 2020) (Fig. 42a). We consider the distinct pressure ranges for the two groups of clinopyroxene crystals as statistically relevant, considering the uncertainty of 260 MPa obtained from experimental calibrations (Putirka et al., 2008). Unreliable (negative) pressures are obtained for clinopyroxene crystals from Group I. The shallow origin of these clinopyroxene crystal is inferred from their elevated Ti/Al ratios (0.98±0.74, on average for Group I vs. 0.26±0.02 for Group II) that could imply lower pressures of crystallization (Boudoire et al., 2019). The presence of sulphates in fluid inclusions from this group (cf. Supplementary Material) likely reflects late-stage exsolution of SO_2-rich gas from magma and is therefore well consistent with a shallow magmatic environment.

The CO_2 densimetry of fluid inclusions in clinopyroxene crystals broadly indicates lower pressures (<135 MPa) than inferred from clinopyroxene barometry (Table S2 of Appendix B). Somewhat higher pressures (up to 350 MPa) are recorded by FI in olivine crystals (Fig. 4a), but still at the lower end of the clinopyroxene population. Previous works (Klügel et al., 2020; Boudoire et al., 2023; Lo Forte et al. 2023) documented a variety of post-entrapment processes affecting FI density (and hence the estimated entrapment pressure), including their volumetric re-equilibration, and/or the precipitation of carbonates (observed by Raman; Fig. S3b of Appendix B). Re-equilibration of FI is known to be the strongest for clinopyroxenes (Klügel et al., 2000) as caused by plastic deformation of the host crystal during magma ascent and/or in lava flow (with respect to air- quenched lapilli). This process may be even more marked for fluid inclusions entrapped in crystals from enclaves (Boudoire et al., 2023). However, we note that the highest estimated pressure (350 MPa for sample FG3-A) falls at the upper range of pressures (320-340 MPa) previously estimated by CO_2 densimetry in FI; the corresponding depth range (10.5-11.2 km) has been interpreted to reflect temporary magma storage near the Moho (Hildner et al. 2011; 2012; Lo Forte et al., 2023).

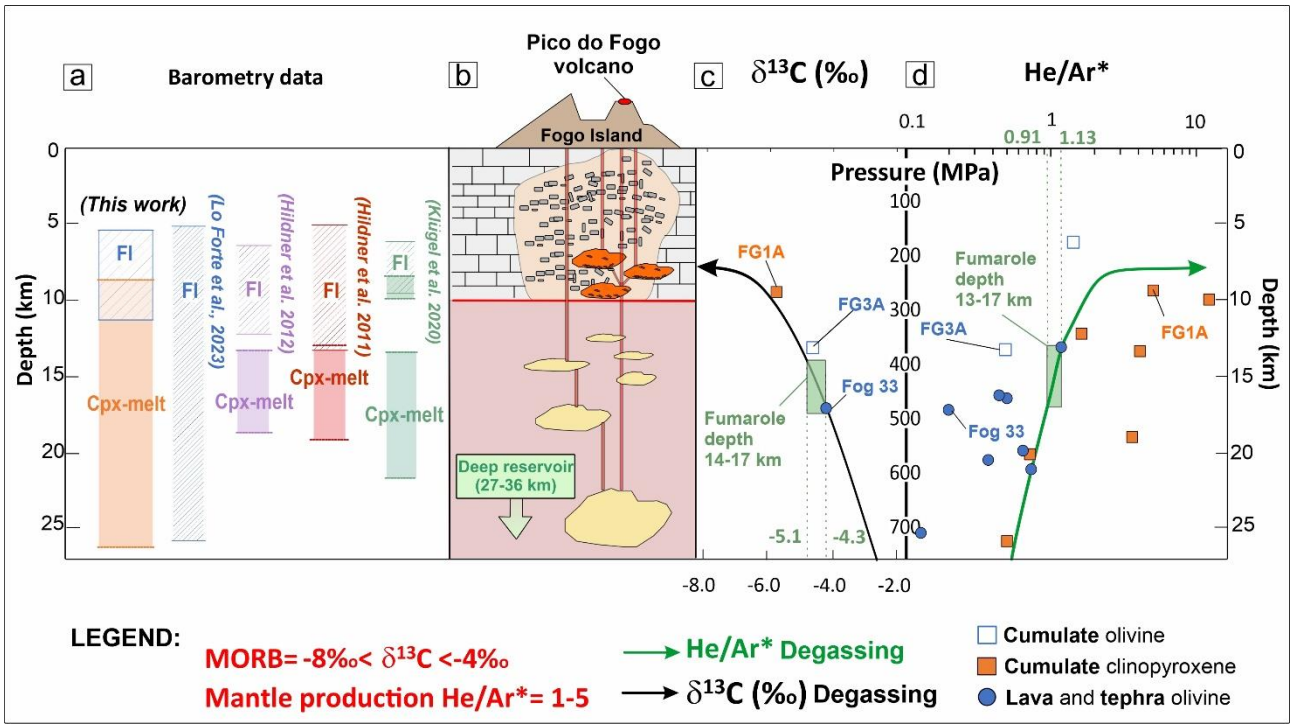

Figure 42 a) Barometric data obtained from fluid inclusions (FI) and clinopyroxene (cpx) analyses in our samples, compared with data from previous studies (Hildner et al., 2011, 2012; Klügel et al., 2020; Lo Forte et al., 2023). **b)** Schematic cross-section (not in scale) illustrating the internal structure of the Fogo plumbing system, adapted from Lo Forte et al. (2023), indicating the main magma storage zone (yellow magma pockets at 13-26 km depth) and the magma stagnation zone (orange magma pockets at 9-12 km depth). **c)** $\delta^{13}C$ values in FI vs. the corresponding pressure/depth. The modelled $\delta^{13}C$ compositions of the magmatic vapor phase (eq. 1 and 2) reproduce the observations related to a pressure-dependent isotopic fractionation due to magma degassing. See text for further details on modelling; **d)** He/Ar* ratios in FI vs. the corresponding pressure/depth. For pressure/depth, we use a combination cpx barometry for clinopyroxenes (cumulate clinopyroxenes), FI densimetry (cumulate olivines) and FI microthermometry (lava and tephra olivine). The diagram shows a broad He/Ar* ratio decrease with depressurization that is reproduced by an open-system degassing model (see text).

7.5.2. Magma degassing as revealed by C and noble gas isotopes.

The isotopic compositions of CO_2 and noble gas (i.e., He/Ar*) in FI and fumarole gases allow tracking magma degassing processes taking place during magma ascent from the mantle source (Iacono-Marziano et al., 2010; Duan, 2014), and eventually to back-calculate the composition of primary (mantle) melt and gas (Boudoire et al., 2018). This possibility is opened by the preferential partitioning of ^{13}C into a CO_2-rich vapour phase (relative to the coexisting melt) upon increasing extents of degassing, which leads to $\delta^{13}C$ of both melt and vapour to evolve towards increasingly lighter isotopic ratios (e.g., Javoy et al., 1978; Mattey, 1991; Boudoire et al., 2018; Aubaud, 2022). If samples allow, this isotopic evolution can be potentially traced (and modelled) using a suite of FI.

Helium and argon, in view of their contrasting solubilities in silicate melts, are also extremely useful to reconstruct magmatic degassing. Argon, being about 7-10 times less soluble than helium, is enriched in the early (more deeply) separated magmatic vapour phase (Iacono-Marziano et al., 2010 and references therein), while the He/Ar ratio then increases with increasing degassing extents (e.g., during magma decompression). In our samples, both $\delta^{13}C$ (CO_2) and He/Ar* exhibit marked pressure dependence (in FI from both olivine and clinopyroxene crystals FI), with the $\delta^{13}C$ (CO_2) progressively evolving toward lighter values, and He/Ar* manifestly increasing, with decreasing pressures (Figs. 42c, d).

The $\delta^{13}C$ (CO_2) carbon isotopic compositions range from -6.04‰ to -4.30‰ (Fig. 4c), within the MORB mantle range (-8‰<$\delta^{13}C$<-4‰; Sano and Marty, 1995). However, this MORB-like signature may be apparent, and needs to be verified according to models that consider isotopic fractionation during magma degassing. To quantitatively evaluate this process, we modelled the pressure-dependent evolution of both $\delta^{13}C$ (and He/Ar*) upon increasing extents of (decompression-driven) magmatic degassing, using the Fractional Equilibrium Degassing (FED) equations proposed by Macpherson and Mattey (1994) and applied by e.g., Boudoire et al. (2018) for similar purposes:

$$\delta^{13}C_{(m)} = \delta^{13}C_{(m,i)} + (\Delta \cdot lnF) \qquad \text{(eq. 1)}$$

$$\delta^{13}C_{(v)} = \delta^{13}C_{(m)} + \Delta \qquad \text{(eq. 2)}$$

$$\frac{He}{Ar}_{(g)} = \frac{He}{Ar}_{(g,i)} \cdot \frac{K_{Ar}}{K_{He}} \cdot F^{(\frac{K_{Ar}}{K_{He}}-1)} \qquad \text{(eq. 3)}$$

where F is residual fraction of gas remaining in the melt; in eq. 1 and eq. 2, $\delta^{13}C_{(m)}$, $\delta^{13}C_{(m,i)}$, and $\delta^{13}C_{(v)}$ are the carbon isotopes composition in the melt ($\delta^{13}C_{(m)}$) and in the vapour ($\delta^{13}C_{(v)}$) at each step of degassing path, and in the primary melt ($\delta^{13}C_{(m,i)}$); $\Delta = \delta^{13}C_{vapour} - \delta^{13}C_{melt}$ is the carbon isotope enrichment factor between vapour and melt, assumed at +2.74‰ as in other OIB-like melts (Boudoire et al., 2018). In eq. 3, $\frac{He}{Ar}_{(g)}$ *and* $\frac{He}{Ar}_{(g,i)}$ are the ratios in gas (g) at respectively a given step (for a given F) of the degassing path, and in the early exsolved vapour (at the initial pressure); K_{Ar} and K_{He} are Ar and He (Hernian) solubility constants (taken from Iacono-Marziano et al., 2010).

The $\delta^{13}C$-CO_2 degassing model is initialised with the following set of boundary conditions:

i) Sun and Dasgupta (2023) have shown that the primary melts at Cape Verde contain up to 9.1 wt.% of CO_2 and form by low degree of melting of a C-enriched mantle source;

ii) Eguchi and Dasgupta (2018) developed a solubility model that relate the CO_2 content of a melt with the corresponding pressure, which applied to Fogo and a primary CO_2 content of 9.1 wt.% yields a pressure of ~2200 MPa (~77 km) (Fig. 5);

iii) in FI of olivine sample FOG33, we measured a $\delta^{13}C$ of -4.41‰ and estimated an average entrapment pressure of ~480 MPa (~17 km) (Figs. 42c and 43); based on the Eguchi and Dasgupta (2018) model, at this pressure the Fogo melt would contain ~0.78 wt.% CO_2 dissolved in the melt, fixing the residual fraction (F) at ~0.08 (i.e., ~92% of the primary dissolved CO_2 was lost due to magmatic degassing). These pressures align with a region that represents the amalgamation of support from buoyancy within the lithosphere, stemming from the low-density region, and dynamic support originating from the upwelling material (Wilson et al., 2013);

iv) in our FED model of $\delta^{13}C$-CO_2, at F=0.08 the vapour CO_2 should have a $\delta^{13}C$ of ~ -4.41‰, as measured in Fog33 olivine sample (Fig. 42c).

Using the above boundary conditions, we use eq. 1 and 2 to back-calculate the $\delta^{13}C$ pressure-dependent evolution in both gas and melt (Figs. 42c and 43). For a primary melt with 9.1 wt.% of dissolved CO_2 at a pressure of ~2200 MPa (~77 km), we constrain a $\delta^{13}C$-CO_2 in the melt of -0.4‰, corresponding to a $\delta^{13}C$-CO_2 of the primary vapour of 2.3‰ (Fig. 43). Even considering in the boundary conditions of the model the other two samples for which we measured a $\delta^{13}C$ in the FI and a relative entrapment pressure (i.e., olivine crystals in Fog 33 and clinopyroxene crystals in FG1-A), the back-calculated $\delta^{13}C$ of the primary melt would vary slightly (from -0.4‰ to 0.2‰). Considering the uncertainty associated with the estimated pressure values for the samples employed in the degassing model, ± 52 MPa and ± 30 MPa for Fog 33 and FG1-A, respectively, we observe that the variability of $\delta^{13}C$ in the melt and primary vapour is < ± 1 ‰.

Similarly, for He/Ar* degassing model, we constrain the boundary conditions considering the entrapment pressure and He/Ar* value in FI from clinopyroxene crystals in the FG4-E sample (P=737 MPa and He/Ar*=0.48; Fig. 42d), which is the deepest one among our samples. Based on the model by Eguchi and Dasgupta (2018) above applied to CO_2 and $\delta^{13}C$-CO_2, a pressure of ~730 MPa would imply a CO_2 content of ~1.4 wt. % and thus a F of 0.15. Assuming that at F=0.15 the vapour phase should have a He/Ar* of ~0.5, we used eq. 3 to back-calculate the pressure-dependent evolution of the ratio in the vapour (Figs. 42d and 43). We constrain a He/Ar* of the mantle at 0.9, which is slightly lower than the U+Th/K production ratio assumed for the upper mantle (He/Ar=1-5; Marty, 2012). We point out that above ~400 MPa the model does not well reproduce the He/Ar* behaviour observed in

our data. This could be a limit at shallow depth of Eguchi and Dasgupta (2018) model when relating CO_2 content and barometry, considering that these authors inferred their relationships based upon results of experiments at high pressures. However, for the purpose of this work, this does not compromise the back-calculation of the primary conditions of CO_2 and noble gases, as the samples chosen in the boundary conditions have entrapment pressure higher than 400 MPa (Figs. 42c and 42d).

Ultimately, based on the outcomes of our $\delta^{13}C$ and He/Ar* modelling, we argue that CO_2 and noble gases in present fumarole gases of Fogo are fed by melts residing and degassing at ~13-17 km depth, in the intermediate storage zone located in the mantle (Figs. 42b, 42c). This implies that, during volcano quiescence , the main degassing and magma ponding source is below the underplating, which seems to be a common feature in many OIB volcanoes, as recently suggested for Piton de la Fournaise (Boudoire et al., 2018), El Hierro (Taracsák et al., 2019), La Palma (e.g., Sandoval-Velasquez et al., 2023), Azores Islands central volcanoes (e.g., Zanon et al., 2020; Zanon and Pimentel 2015; Zanon and Frezzotti 2013), all of which are characterized by vertically stacked magma systems down to the mantle (see Section 5.5 for further details).

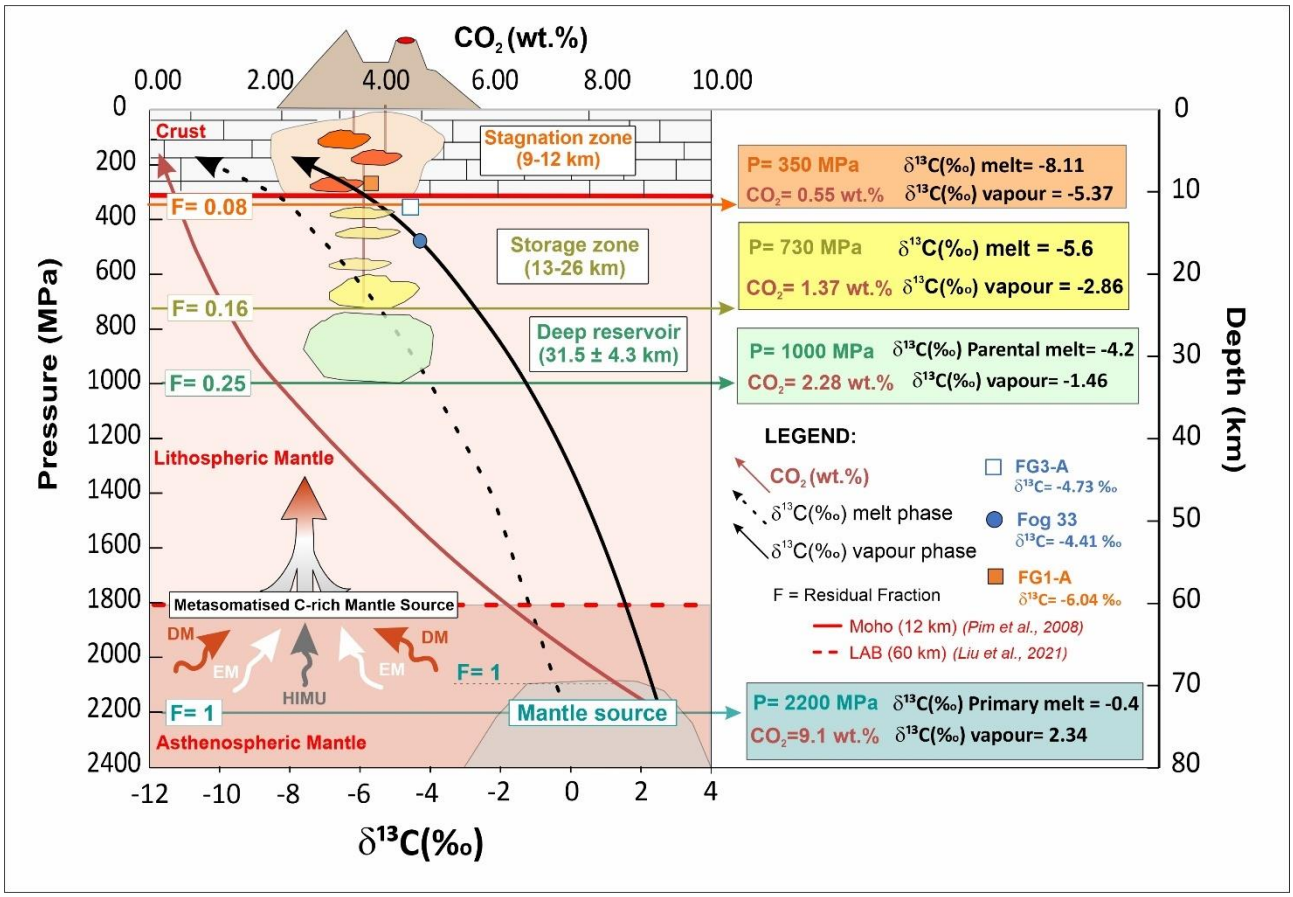

Figure 43 Conceptual model for CO_2 degassing in the Fogo plumbing system, illustrating the pressure-dependent evolution of (i) dissolved CO_2 in the melt (red line), (ii) $\delta^{13}C$ in the melt phase (dash black line), and (iii) $\delta^{13}C$ in the vapor phase (solid black line). See text for description.

7.5.3. Crustal carbon in the Cape Verde mantle source

Sun and Dasgupta (2023) reported that primary melts at Cape Verde may contain as high as 9 wt. % CO_2, converting into >400 ppm C in the mantle source (Lo Forte et al., 2024). One important corollary of this extremely high primary CO_2 content is that CO_2 saturation would be reached by magmas while deep in the mantle (at ~2200 MPa, or ~77 km, according to the model of Eguchi and Dasgupta, 2018), implying that even the most deep melts entrapped in olivine crystals as melt inclusions (at 896 ± 175 MPa, or 27-36 km), containing up to 2.3 wt.% dissolved CO_2 (Lo Forte et al., 2024), would be extremely degassed (F=0.25). Likewise, in view of our modelled $\delta^{13}C$- and He/Ar*-pressure dependences (Figs. 42c, 42d and 43), magmatic vapours entrapped in FI (at pressures ≤740 MPa, or ≤25 km) or fumarole gases would be representative of "late-exsolved" magmatic vapours, whose isotopic compositions would in no way reflect that of primary melts, and of the mantle source. In their study on La Reunion Island, Boudoire et al. (2018) similarly found that gas entrapped in FI from local underplating magmas (~13 km) displays $\delta^{13}C$ of ~-6 ‰ and He/Ar* of ~2. In this depth range, magmas have already lost ~90% of their original (primary melt) dissolved CO_2 (inferred at up to 3.5 wt. %) and are therefore isotopically depleted in ^{13}C relative to their source (characterised at $\delta^{13}C$ ~ -0.8 ‰).

In our Fogo model (Fig. 43), we obtain primary $\delta^{13}C$ values for both dissolved C ($\delta^{13}C_{melt}$ of -0.4 ‰) and coexisting (early) vapour ($\delta^{13}C_{vapour}$ of 2.34 ‰) that are extremely more positive than recorded in the gas entrapped in FI and in fumarole gases. We caution that our calculations are based on a very limited dataset of only three samples, and that a far larger dataset would therefore be required if more robust conclusions were to be reached. Yet, our calculations suggest that, if OIB magmas are as C-rich as recently suggested (Boudoire et al., 2018; Aiuppa et al., 2021; Burton et al. 2023; Sun and Dasgupta, 2023 and references therein), then FI in magmatic products (e.g., lavas, tephra, crustal/mantle cumulates, and submarine glasses) and/or in fumarole gases may hardly record the C isotopic signature at source (Boudoire et al., 2018; Aubaud et al., 2022; Sandoval Velasquez et al., 2023; this work), unless carefully modelled for degassing. It is worth mentioning that FI in mantle xenoliths should be used as a more reliable proxy for this purpose as they are generally brought to the surface from high depths in the mantle (e.g., Haggerty and Suatter, 1999). In this context, Fig. 6

highlights that our modelled primary melt/gas $\delta^{13}C$ signatures (-0.4 ‰/+2.23 ‰) match closely those inferred for El Hierro ($\delta^{13}C$= -0.96‰), La Palma ($\delta^{13}C$= -1.70‰) and Lanzarote ($\delta^{13}C$= -0.80‰) mantle sources from nearby Canary Island OIB, as determined by analysing FI in mantle xenoliths (-2.38 ‰< $\delta^{13}C$ < 0.96 ‰, Sandoval-Velasquez et al., 2021a, 2023; 2024).

A ^{13}C-enriched signature for Fogo primary melts, if confirmed by future studies, would provide decisive clues for the existence of a metasomatized (C-enriched) mantle source underneath Cape Verde, as recently indicated by melt inclusions studies (e.g., De Vitre et al., 2023; Lo Forte et al., 2024), magma petrology (Sun and Dasgupta, 2023), and by the rare carbonatites (Foeken et al., 2007). The mantle metasomatism involving carbonatitic to carbonated-silicate melts within the Cape Verde archipelago, as inferred by Bonadiman et al. (2005), may potentially reflect the recycling of old, deeply subducted (e.g., Hoernle et al., 2002) crustal materials ($\delta^{13}C \geq$ -1 ‰) into the deep mantle beneath Cape Verde (Dasgupta and Hirschmann, 2010; Dorfman et al., 2018). The HIMU affinity of many recent lavas at Fogo, and in the Cape Verde archipelago in general (Mata et al., 2017), would well be consistent with the presence of a recycled crustal component (e.g., old altered oceanic crust and oceanic lithosphere) in the local mantle.

Recent FI measurements (Fig. 44) in mantle xenoliths bring increasing evidence for the mantle source(s) of continental rift and OIB volcanism (e.g., Correale et al., 2015; Rizzo et al., 2018; Sandoval-Velasquez et al., 2021a, 2021b, 2023; Halldorsson et al., 2022; Remigi et al., 2023) to be more ^{13}C-rich than previously thought (Deines, 2002), implying a recurrent recycled crustal carbon component in the local mantle. If so, some of the light-carbon OIB signatures observed so far (e.g., Society Islands; Fig. 44) may be caused by the use of degassed lavas/glasses (that contain a fractionated ^{13}C-depleted, residual carbon fraction) rather than mantle rock specimens. We recommend that mantle xenoliths are prioritised in future $\delta^{13}C$ FI studies, and that the effects of magma degassing are modelled (and filtered out) if lavas are used instead (at localities where xenoliths are missing).

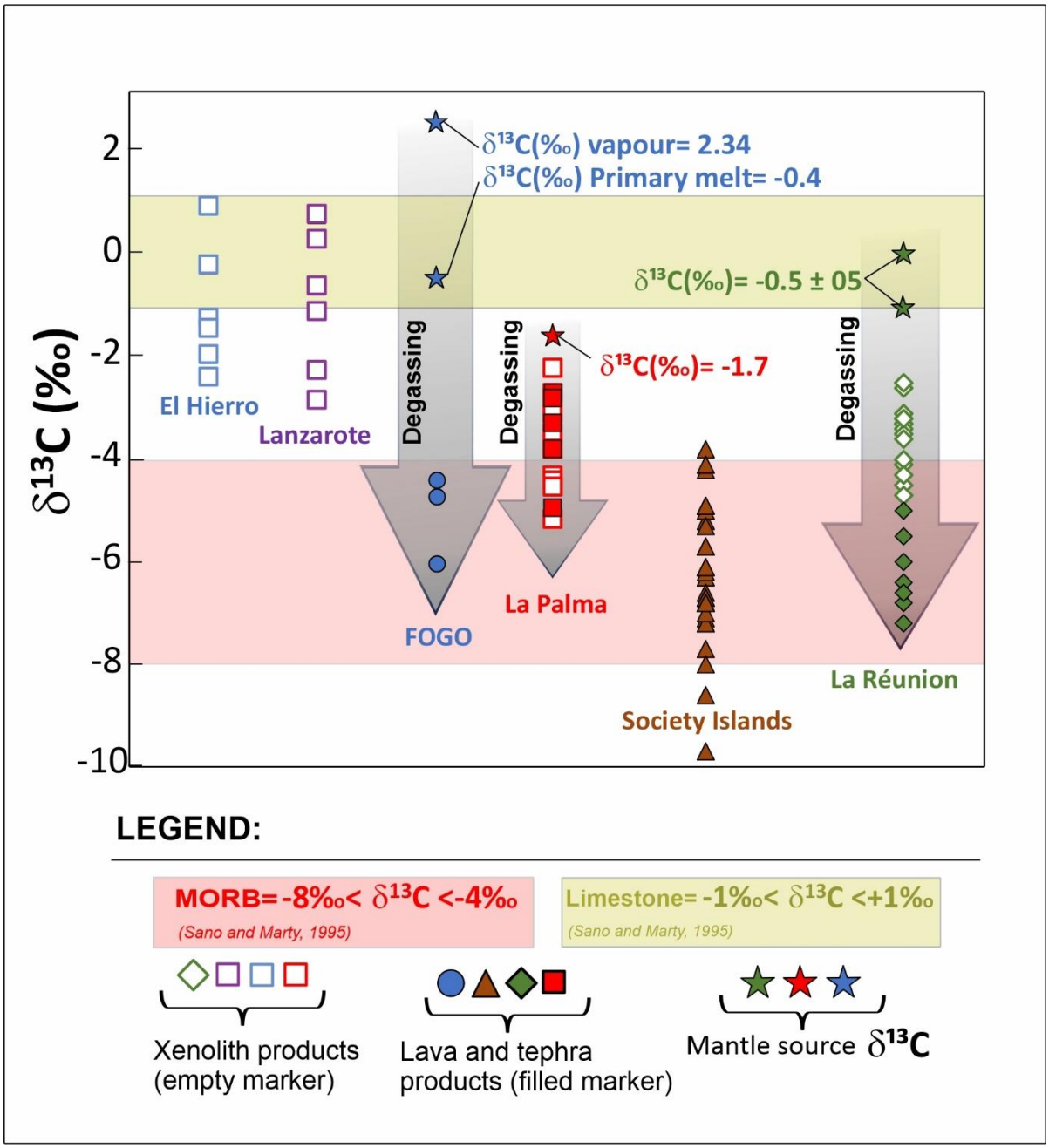

Figure 44 δ ^{13}C for Fogo, El Hierro, Lanzarote, and La Palma in the Canary archipelago (Sandoval et al., 2021a, 2023); Piton de la Fournaise in La Réunion Island (Boudoire et al., 2018); and Society Islands (Aubaud et al., 2006). The samples include xenoliths (e.g., El Hierro, Lanzarote, La Palma, La Réunion), lavas, and tephra (La Palma, La Réunion, Fogo), as well as submarine lavas (Society Islands). The black arrows indicate the degassing from the mantle source (estimated for Fogo, La Palma, and La Réunion) to MORB.

7.5.4. Regional He isotope trends

Noble gases, due to their chemical inertness, behave as strongly incompatible elements during mantle partial melting. The two helium isotopes (^{3}He and ^{4}He) have diverse (primordial vs. radiogenic) origin, and because they do not fractionate one each other during mantle melting and degassing, can – at least in principle - accurately record the signature of the mantle source (e.g., Boudoire et al., 2018; Rizzo et al., 2018; Sandoval-Velasquez et al., 2021a, b). This signature is obtained by the analysis of FI in the mineral assemblage of lavas and xenoliths (e.g., Day et al., 2022) that have not interacted with the crust, thus avoiding the overprinting of crustal fluids. The specific helium isotopic signatures of the various mantle end-member components discriminated by radiogenic isotopes (DM, HIMU, EM-1, EM-2; Garapíc et al., 2015; Jackson et al., 2017; Stracke et al., 2019) have not been fully understood.

Our data for Fogo bring no evidence of such a crustal fluid contribution (that typically shift compositions toward low R_c/R_a signatures); rather, they point to a relatively uniform MORB-type mantle source with R_c/R_a ~8±1 (Figs. 40 and 41), as inferred previously (e.g., Doucelance et al., 2003).

This agrees with recent studies in both magmatic and mantle rocks, highlighted a clear decoupling, of He and C signatures since these seem to variate independently from each other (e.g., Canary, Sandoval Velasquez et al., 2021a,b; Mexico, Sandoval-Velasquez et al., 2022). The question that remains open is how this MORB signature can be reconciled with a regional context where a ^{3}He-richer component (R_c/R_a >9) has been observed, both in northern and southern islands (Figs. 40 and 45a) (Christensen et al., 2001, Doucelance et al., 2003; Day et al., 2022).

Figure 7a explores the relationship between the La/Yb ratio, a marker of extending partial melting (e.g., Feigenson et al., 2003), and the range of measured ^{3}He/^{4}He values in each island of the Cape Verde archipelago. Additionally, we present similar observations for the Canary Islands, where ^{3}He/^{4}He in magmatic/mantle rocks and volcanic gases spans from <7 Ra (in eastern islands) to values higher than MORB (in La Palma Island) (Sandoval-Velasquez et al., 2021a, 2023; Day et al., 2022), as well as in other OIBs (e.g., Hawaii, Samoa, Galapagos, La Réunion, and the Society Islands). It is worth noting that at Cape Verde and Canary, the ^{3}He/^{4}He ratios decrease with decreasing La/Yb ratios (Fig. 45a). This suggests that any lower mantle component (^{3}He/^{4}He > 9 Ra) can only be resolved where low degrees of mantle melts prevail (i.e., high La/Yb ratio), such as Santo Antão and São Vincente. In contrast, islands where larger mantle volumes participate in the melting process (low

La/Yb ratio), such as Fogo and Santiago, are dominated by depleted upper mantle noble gas components with MORB (southern Cape Verde Islands and central-western Canary Islands) or even more radiogenic signatures (eastern Canary) (Sandoval-Velasquez et al., 2021a, 2023; Day et al., 2022). The islands of Brava and São Nicolau in Cape Verde deviate from this relationship, appearing as outliers to the trend observed within the islands of the archipelago. This deviation may suggest that (i) the mantle beneath Cape Verde is strongly heterogeneous, (ii) the geometry of the "plume" beneath Cape Verde plays a pivotal role in the He signature of each island, and (iii) the mantle is subject to different degrees of partial melting. Taking a broader perspective to provide insights into global geodynamics, it is observed that in other OIB localities worldwide, such as Hawaii, Galapagos, Society Islands, Samoa, and Reunion, where the lower mantle component (Rc/Ra > 9 Ra) is largely extended, it remains prominently evident even at high degrees of mantle partial melting, as indicated by low La/Yb ratio values (e.g., 8.8 in Hawaii, 6.0 in Fernandina in the Galapagos).

7.5.5. Implications for global OIB geodynamics

Recent studies have proven a relationship between He isotopic ratios in OIB magmas and mantle velocity, observing that high-$^{3}He/^{4}He$ (>9 Ra) signatures - indicative of a lower mantle component - are systematically associated with low-velocity mantle regions related to ascending hot mantle plumes (e.g., Jackson et al., 2017a, 2017b; Day et al., 2022; and references therein).

Figure 45b illustrates the global OIB relationship between $^{3}He/^{4}He$, plume buoyancy flux, and plate speed. For Cape Verde, we use a refined archipelago-average that considers our novel Fogo results and quality check/filtering of literature data (Figs. 39,40). Plume buoyancy fluxes (Hoggard et al., 2020) are inferred based on a volumetric approach, which is function of the (i) density of asthenospheric mantle, (ii) the density of displaced surface fluid, (iii) the volume of the swell, and (iv) a characteristic timescale of buoyancy loss.

The diagram corroborates previous evidences of Day et al. (2022) for the existence of a positive dependency between plates speed and OIB $^{3}He/^{4}He$ signatures, and suggests that OIB localities such as the Cape Verde and Canary Islands, which are thought to be associated with relatively low plume buoyancy fluxes (1-1.6 Mg/s, Hoggard et al., 2020) and plates speed, are systematically characterised by more radiogenic $^{3}He/^{4}He$ ratios than those recorded at more buoyant mantle plumes locations (e.g., Hawaii, Galapagos, Samoa). This relationship agrees with the hypothesis that (i) hot plumes are the

source of OIB with high-$^{3}He/^{4}He$ ratios (Jackson et al., 2017a, 2017b) and (ii) the plume buoyancy flux is higher in correspondence with faster moving plates (Hoggard et al., 2020). One of the factors that directly influences the plume buoyancy flux, and thus plume upwelling, is the density of the variably depleted mantle source, which decreases with increasing extents of melt extraction (Schutt and Lesher, 2006). In this context, the density difference between recycled oceanic crust and variably depleted mantle increases at high degrees of melt extraction promoting accumulation of recycled crust above the core–mantle boundary (e.g., Nakagawa et al., 2010; Stracke et al., 2019).

Interestingly, this dichotomy between high mantle flux (Hawaii, Galapagos) and low mantle flux (Cape Verde and Canary) OIB extends to the conditions of magma supply and storage. Indeed, recent results from barometric estimates indicate that magma storage conditions at OIB vary from shallow-crustal (e.g., Kilauea, Hawaii) to deep-upper mantle (e.g., Cape Verde and Canary Islands; La Réunion Island), reflecting a contrast in magma supply rate (3-4 m^3/s at Kilauea vs. 0.06 m^3/s at Fogo; see Boudoire et al., 2018; Lo Forte et al., 2023 and references therein). Taken together, evidence suggests that magma storage is consistently shallower in magmatic systems above high buoyancy flux plumes coupled to high plates speed than in off-axis systems, or above low buoyancy flux plumes coupled to low plates speed. Thus, magma supply from the underlying mantle source coupled to the $^{3}He/^{4}He$ signature represents a first-order control on the depth of magma storage beneath ocean island volcanoes (e.g., Gleeson et al., 2021).

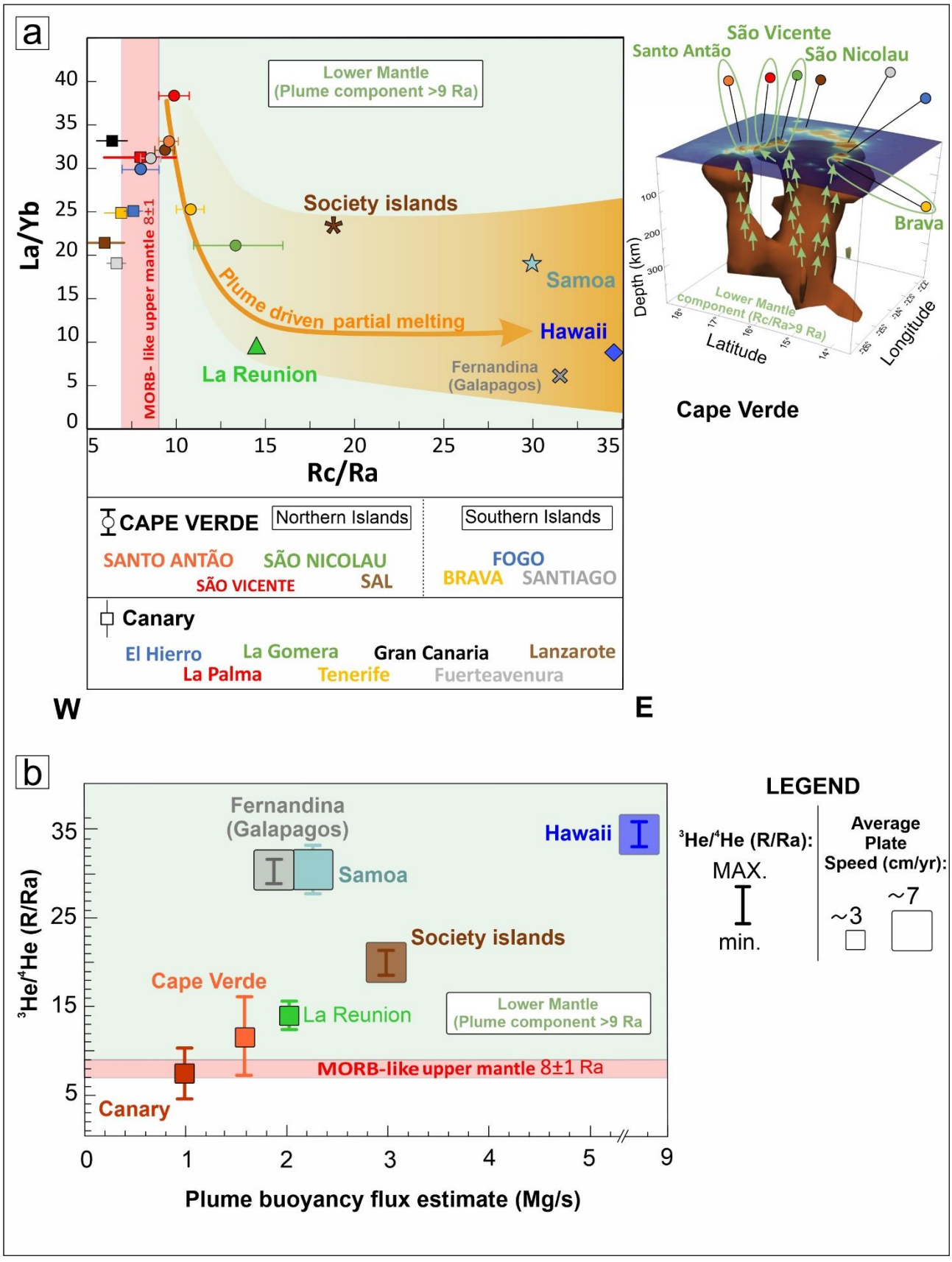
a
La/Yb
Rc/Ra
Lower Mantle
(Plume component >9 Ra)
MORB- like upper mantle 8±1
Society islands
Samoa
Plume driven partial melting
Hawaii
La Reunion
Fernandina
(Galapagos)
CAPE VERDE
Northern Islands
Southern Islands
SANTO ANTÃO
SÃO NICOLAU
SÃO VICENTE
SAL
FOGO
BRAVA
SANTIAGO
Canary
El Hierro
La Gomera
Gran Canaria
Lanzarote
La Palma
Tenerife
Fuerteavenura
W
E
São Vicente
Santo Antão
São Nicolau
Brava
Depth (km)
Lower Mantle
component (Rc/Ra>9 Ra)
Latitude
Longitude
Cape Verde
b
³He/⁴He (R/Ra)
Fernandina
(Galapagos)
Hawaii
Samoa
Society islands
Cape Verde
La Reunion
Lower Mantle
(Plume component >9 Ra
MORB-like upper mantle 8±1 Ra
Canary
Plume buoyancy flux estimate (Mg/s)
LEGEND
³He/⁴He (R/Ra):
MAX.
min.
Average
Plate
Speed (cm/yr):
~3
~7

Figure 45 **(a)** La/Yb ratio vs. $^{3}He/^{4}He$ ratio averages for Cape Verde (after the data filtering, see Section 1, Fig. 1, for further details) and other OIB localities. The He isotope compositions of Cape Verde are from this work and literature data (e.g., Christensen et al., 2001, Doucelance et al., 2003), whereas data for other islands are sourced from literature (Canary Islands, Sandoval-Velasquez et al., 2021a and references therein; Fernandina, Galapagos; Samoa; Hawaii, Jackson et al., 2014, 2017; La Réunion, Boudoire et al., 2020). The symbols (circle and square for Cape Verde and Canary, respectively) indicate the mean Rc/Ra value, whereas the bars represent the entire range of values for both Cape Verde and Canary. All the La/Yb data are from https://georoc.eu/georoc/new-start.asp. **(b)** Plume buoyancy flux vs. $^{3}He/^{4}He$ ratios vs. average plate speed in OIB localities. OIB, such as Cape Verde ($^{3}He/^{4}He$ = 7-16 Ra, plume buoyancy flux 1.6 Mg/s, and average plate speed ~3 cm/yr) and the Canary Islands ($^{3}He/^{4}He$ = 5-10 Ra, plume buoyancy flux 1.0 Mg/s, and average plate speed~3 cm/yr), are the lower end-members of the model. In contrast, OIB locations such as Galapagos and Hawaii, characterized by high $^{3}He/^{4}He$ values (>25 Ra), moderate to high plume buoyancy flux (2 Mg/s for Galapagos and 8.7 Mg/s for Hawaii), and high average plate speed (>7 cm/yr), represent the upper end-members of the model. Intermediate OIB localities, like La Réunion, fall within the ranges between these end-members, with $^{3}He/^{4}He$ ratios of 12-15 Ra, plume buoyancy flux of 2 Mg/s, and an average plate speed of~3 cm/yr. The helium isotope compositions for Cape Verde are derived from our study and literature data (e.g., Christensen et al., 2001, Doucelance et al., 2003), whereas data for other islands are sourced from literature (Canary Islands, Sandoval-Velasquez et al., 2021a and references therein; Fernandina, Galapagos; Samoa; Hawaii, Jackson et al., 2014, 2017; La Réunion, Boudoire et al., 2020). Plume buoyancy flux data are from Hoggard et al. (2020). Average plate speeds are sourced from Hoggard et al. (2020) and references therein.

7.6. Conclusions

We have presented the first carbon isotopic measurements and new noble gas (He-Ne-Ar) data in FI hosted in olivine and clinopyroxene crystals from mafic enclaves, lavas, tephra and in volcanic gas samples from Fogo, the most active volcano of the Cape Verde archipelago (eastern Atlantic). The main findings can be summarized as follows:

- He isotopic systematics in our samples (mafic enclaves, lava, tephra, and fumarole) confirm a MORB-like upper mantle signature (R_c/R_a=7.14-8.44) for the lithospheric mantle beneath Fogo, consistent with the $^{3}He/^{4}He$ signatures previously reported for fumarole (e.g., Melian et al., 2021; Alonso et al., 2021) and FI (e.g., Christensen et al., 2001; Doucelance et al., 2003).
- The carbon isotopic ratio ($\delta^{13}C$ vs. PDB) of CO_2 in FI and fumaroles range from -6.04 to -4.41‰. This variability reflects isotopic fractionation due to already high extents of magma degassing (~75-94%) at shallow depths in the Fogo plumbing system. Systematic variations of $\delta^{13}C$ and He/Ar* with FI entrapment pressure (as estimated from a combination of host mineral barometers and FI densimetry/microthermometry) allow us to develop a model for

volatile degassing in the local plumbing system. From this model, we predict a crustal signature for carbon ($\delta^{13}C$ of ~ -0.4‰) in primary melts formed by upper mantle melting at ~2200 MPa (~77 km), which we interpret as indicative of mantle metasomatism by melts/fluids enriched in a crustal carbon component.

- A ^{13}C-enriched signature for Fogo primary melts, similarly to what recently observed for Canary Islands (Sandoval-Velasquez et al., 2021a, 2023), may potentially reflect the recycling of old, deeply subducted crustal materials ($\delta^{13}C \geq -1$ ‰) into the deep mantle beneath Cape Verde, as suggested by high CO_2 contents in primary melts (Dasgupta and Hirschmann, 2010; Dorfman et al., 2018). This could imply that OIB volcanism is more ^{13}C-rich than previously thought (Deines, 2002), implying a recurrent recycled crustal carbon component in the local mantle.
- A careful review of existing $^{3}He/^{4}He$ literature in Cape Verde archipelago and other OIB localities shows that He isotopes in OIB scale vary inversely with La/Yb ratio and, hence, with magma production rates in the mantle source. Indeed, in OIBs, where a strong lower mantle component (Rc/Ra > 9 Ra) is prevalent throughout much of the mantle underlying the archipelago, a lower mantle component is also present even when high degrees of mantle partial melting occur. This does not exhibit the trend observed in Cape Verde and the Canaries, where the lower mantle ($^{3}He/^{4}He$ ratio > 9 Ra) component is evident in regions where low degrees of mantle melts prevail (i.e., high La/Yb ratio), with the only exception being Brava and São Nicolau. The MORB-like $^{3}He/^{4}He$ signature at Fogo reflects a combination of (i) relatively high magma productivity, (ii) relatively low plume buoyancy flux (~1.1 Mg/s), and (iii) slow average speed (~3 cm/yr) of the overlying plate.
- Ultimately, we propose that the dichotomy between high mantle flux (Hawaii, Galapagos) and low mantle flux (Cape Verde and Canary) OIB extends to the conditions of magma supply and storage. In detail, magma storage in OIB is consistently shallower in plumbing systems developed above high buoyancy flux plumes coupled to high plates speed than in off-axis systems, or above low buoyancy flux plumes coupled to low plates speed.

REFERENCES

Aiuppa, A., Bitetto, M., Rizzo, A.L., Viveiros, F., Allard, P., Frezzotti, M.L., Zanon, V., 2020. The fumarolic CO_2 output from Pico do Fogo Volcano (Cape Verde). Ital. J. Geosci. 139 (3), 325–340.

Aiuppa, A., Casetta, F., Coltorti, M., Stagno, V., Tamburello, G., 2021. Carbon concentration increases with depth of melting in Earth's upper mantle. Nat. Geosci. 14, 697–703.

Alonso, M., Pérez, N.M., Padrón, E., Hernández, P.A., Melián, G.V., Sumino, H., Padilla, G.D., Barrancos, J., Rodríguez, F., Dionis, S., Asensio-Ramos, M., Amonte, C., Silva, S., Pereira, J.M., 2021. Changes in the thermal energy and the diffuse ^3He and ^4He degassing prior to the 2014–2015 eruption of Pico do Fogo volcano, Cape Verde. J. Volcanol. and Geother. Res. 416, 107271.

Aubaud, C., 2022. Carbon stable isotope constraints on CO_2 degassing models of ridge, hotspot and arc magmas. Chem. Geol. 605, 120962.

Aubaud, C., Pineau, F., Hékinian, R., Javoy, M., 2006. Carbon and hydrogen isotope constraints on degassing of CO_2 and H_2O in submarine lavas from the Pitcairn hotspot (South Pacific). Geophys. Res. Lett. 33, L02308. https://doi.org/10.1029/ 2005GL024907

Boudoire, G., Brugier, Y.-A., Di Muro, A., Wörner, G., Arienzo, I., Metrich, N., Zanon, V., Braukmüller, N., Kronz, A., Le Moigne, Y., Michon, L., 2019. Eruptive Activity on the Western Flank of Piton de la Fournaise (La Réunion Island, Indian Ocean): Insights on Magma Transfer, Storage and Evolution at an Oceanic Volcanic Island. J. Petrol. 60, 1717–1752.

Boudoire, G., Pasdeloup, G., Schiavi, F., Cluzel, N., Rafflin, V., Grassa, F., ... & Rizzo, A. L., 2023. Magma storage and degassing beneath the youngest volcanoes of the Massif Central (France): Lessons for the monitoring of a dormant volcanic province. Chemical Geology, 121603.

Boudoire, G., Rizzo, A.L., Arienzo, I., Di Muro, A., 2020. Paroxysmal eruptions tracked by variations of helium isotopes: inferences from Piton de la Fournaise (La Réunion island). Sci Rep 10, 9809.

Boudoire, G., Rizzo, A.L., Di Muro, A., Grassa, F., Liuzzo, M., 2018. Extensive CO_2 degassing in the upper mantle beneath oceanic basaltic volcanoes: First insights from Piton de la Fournaise volcano (La Réunion Island). Geochim. Cosmochim. Acta 235, 376–401.

Carvalho, J., Silveira, G., Kiselev, S., Custódio, S., Ramalho, R.S., Stutzmann, E., Schimmel, M., 2022. Crustal and uppermost mantle structure of Cape Verde from ambient noise tomography. Geophys. J. Int. 231, 1421–1433.

Christensen, B.P., Holm, P.M., Jambon, A., Wilson, J.R., 2001. Helium, argon and lead isotopic composition of volcanics from Santo Antão and Fogo, Cape Verde Islands. Chem. Geol. 178, 127–142.

Clarke, W.B., Jenkins, W.J., Top, Z., 1976. Determination of tritium by mass spectrometric measurement of 3He. Int. J. Appl. Radiat. Isot. 27, 515–522.

Dasgupta, R. 2018. Volatile-bearing Partial Melts Beneath Oceans and continents–Where, How Much, and of What Compositions? Ame. J. of Sci. 318(1), 141–165.

Dasgupta, R., Hirschmann, M.M., 2010. The deep carbon cycle and melting in Earth's interior. Earth and Planet. Sci. Lett. 298, 1–13.

Day, J.M.D., Barry, P.H., Hilton, D.R., Burgess, R., Pearson, D.G., Taylor, L.A., 2015. The helium flux from the continents and ubiquity of low-$^{3}He/^{4}He$ recycled crust and lithosphere. Geochim. Cosmochim. Acta 153, 116–133.

Day, J.M.D., Jones, T.D., Nicklas, R.W., 2022. Mantle sources of ocean islands basalts revealed from noble gas isotope systematics. Chem. Geol. 587, 120626.

Deines, P., 2002. The carbon isotope geochemistry of mantle xenoliths. Earth-Sci. Rev. 58, 247–278.

Dickin, A.P., 2018. Radiogenic Isotope Geology, 3rd ed. Cambridge University Press.

DeVitre, C.L., Gazel, E., Ramalho, R.S., Venugopal, S., Steele-MacInnis, M., Hua, J., Allison, C.M., Moore, L.R., Carracedo, J.C., Monteleone, B., 2023. Oceanic intraplate explosive eruptions fed directly from the mantle. Proc. Natl. Acad. Sci. 120 (33), e2302093120.

Dorfman, S.M., Badro, J., Nabiei, F., Prakapenka, V.B., Cantoni, M., Gillet, P., 2018. Carbonate stability in the reduced lower mantle. Earth and Planet. Sci. Lett. 489, 84–91.

Doucelance, R., Escrig, S., Moreira, M., Gariépy, C., Kurz, M.D., 2003. Pb-Sr-He isotope and trace element geochemistry of the Cape Verde Archipelago. Geochim. Cosmochim. Acta 67, 3717–3733.

Dunai, T.J., Porcelli, D., 2002. Storage and Transport of Noble Gases in the Subcontinental Lithosphere. Reviews in Mineralogy and Geochemistry 47, 371–409.

Feigenson, M.D., Bolge, L.L., Carr, M.J., Herzberg, C.T., 2003. REE inverse modeling of HSDP2 basalts: evidence for multiple sources in the Hawaiian plume. Geochem. Geophys. Geosystems 4, 2.

Fisher, D.E., 1983. Rare gases from the undepleted mantle? Nature 305, 298–300.

Frezzotti, M.L., Peccerillo, A., 2004. Fluid inclusion and petrological studies elucidate reconstruction of magma conduits. Transactions of the American Geophysical Union 85 (16), 157–163.

Frezzotti, M.L., Peccerillo, A., 2007. Diamond-bearing COHS fluids in the mantle beneath Hawaii. Earth and Planet. Sci. Lett. 262, 273–283.

Frezzotti, M.L., Burke, E.A.J., De Vivo, B., Stefanini, B., Villa, I.M., 1992. Mantle fluids in pyroxenite nodules from Salt Lake Crater (Oahu, Hawaii). Eur. J. Mineral. 4, 1137–1153.

Frezzotti, M.L., Andersen, T., Neumann, E.R., Simonsen, S.L., 2002. Carbonatite melt-CO_2 fluid inclusions inmantle xenoliths from Tenerife, Canary Islands: a story of trapping, immiscibility and fluid–rock interaction in the upper mantle. Lith. 64, 77–96.

Garapíc, G., Mallik, A., Dasgupta, R., Jackson, M.G., 2015. Oceanic lavas sampling the high-$^3He/^4He$ mantle reservoir: Primitive, depleted, or re-enriched? Am. Mineral. 100, 2066–2081.

Gautheron, C., Moreira, M., Allègre, C., 2005. He, Ne and Ar composition of the European lithospheric mantle. Chem. Geol. 217, 97–112.

Gerlach, D.C., Cliff, R.A., Davies, G.R., Norry, M., Hodgson, N., 1988. Magma sources of the Cape Verdes archipelago: Isotopic and trace element constraints. Geochim. Cosmochim. Acta 52, 2979–2992.

Gleeson, M.L.M., Gibson, S.A., Stock, M.J., 2021. Upper Mantle Mush Zones beneath Low Melt Flux Ocean Island Volcanoes: Insights from Isla Floreana, Galápagos. J. Petrol. 61, egaa094.

Graham, D.W., 2002. Noble Gas Isotope Geochemistry of Mid-Ocean Ridge and Ocean Island Basalts: Characterization of Mantle Source Reservoirs. Rev. Mineral. Geochem. 47, 247–317.

Gurenko, A.A., Hoernle, K.A., Hauff, F., Schmincke, H.-U., Han, D., Miura, Y.N., Kaneoka, I., 2006. Major, trace element and Nd–Sr–Pb–O–He–Ar isotope signatures of shield stage lavas from the central and western Canary Islands: Insights into mantle and crustal processes. Chem. Geol. 233, 75–112.

Haggerty, S.E., Sautter, V., 1990. Ultradeep (greater than 300 kilometers), ultramafic upper mantle xenoliths. Science 248, 993–996.

Hards, V.L., Kempton, P.D., Thompson, R.N., 1995. The heterogeneous Iceland plume: new insights from the alkaline basalts of the Snaefell volcanic centre. JGS 152, 1003–1009.

Hilton, D.R., Fischer, T.P., Marty, B., 2002. Noble Gases and Volatile Recycling at Subduction Zones. Rev. Mineral. Geochem. 47, 319–370.

Hoernle, K., Tilton, G., Le Bas, M.J., Duggen, S., Garbe-Schönberg, D., 2002. Geochemistry of oceanic carbonatites compared with continental carbonatites: mantle recycling of oceanic crustal carbonate. Contrib. Mineral. Petrol. 142, 520–542.

Hoernle, K., Werner, R., Morgan, J.P., Garbe-Schönberg, D., Bryce, J., Mrazek, J., 2000. Existence of complex spatial zonation in the Galápagos plume. Geol. 28, 435.

Hoggard, M.J., Parnell-Turner, R., White, N., 2020. Hotspots and mantle plumes revisited: Towards reconciling the mantle heat transfer discrepancy. Earth and Planet. Sci. Lett. 542, 116317.

Hopp, J., Trieloff, M., Altherr, R., 2007a. Noble gas compositions of the lithospheric mantle below the Chyulu Hills volcanic field, Kenya. Earth and Planet. Sci. Lett.261, 635–648.

Hopp, J., Trieloff, M., Buikin, A.I., Korochantseva, E.V., Schwarz, W.H., Althaus, T., Altherr, R., 2007b. Heterogeneous mantle argon isotope composition in the subcontinental lithospheric mantle beneath the Red Sea region. Chem. Geol. 240, 36–53.

Jackson, M.G., and Dasgupta, R., 2008. Compositions of HIMU, EM1, and EM2 from global trends between radiogenic isotopes and major elements in ocean island basalts. Earth and Planet. Sci. Lett. 276, 175–186.

Jackson, M. G., Konter, J.G., Becker, T.W., 2017a. Primordial helium entrained by the hottest mantle plumes. Nature 542, 340–343.

Jackson, M.G., Price, A.A., Blichert-Toft, J., Kurz, M.D., Reinhard, A.A., 2017b. Geochemistry of lavas from the Caroline hotspot, Micronesia: Evidence for primitive and recycled components in the mantle sources of lavas with moderately elevated $^{3}He/^{4}He$. Chemical Geology 455, 385–400.

Klügel, A., Day, S., Schmid, M., Faria, B., 2020. Magma Plumbing During the 2014–2015 Eruption of Fogo (Cape Verde Islands). Front. Earth Sci. 8, 157.

Klügel, A., Hoernle, K.A., Schmincke, H., White, J.D.L., 2000. The chemically zoned 1949 eruption on La Palma (Canary Islands): Petrologic evolution and magma supply dynamics of a rift zone eruption. J. Geophys. Res. 105, 5997–6016.

Kurz, M.D., Kenna, T.C., Lassiter, J.C., DePaolo, D.J., 1996. Helium isotopic evolution of Mauna Kea Volcano: First results from the 1-km drill core. J. Geophys. Res. 101, 11781–11791.

Lo Forte, F.M., Aiuppa, A., Rotolo, S.G., Zanon, V., 2023. Temporal evolution of the Fogo Volcano magma storage system (Cape Verde Archipelago): a fluid inclusions perspective. J. Volcanol. Geotherm. Res. 433, 107730.

Lo Forte, F.M., Schiavi, F., Rose-Koga, E.F., Rotolo, S., Verdier-Paoletti, M., Aiuppa, A., et al., 2024. High CO_2 in the mantle source of ocean island basanites. Geochim. Cosmochim. Acta.

Lodge, A., and Helffrich, G., 2006. Depleted swell root beneath the Cape Verde Islands. Geol 34, 449.

Macpherson C. G. and Mattey D. P. (1994) Carbon isotope variations of CO_2 in Lau Basin basalts and ferrobasalts. Earth Planet. Sci. Lett. 121, 263–276.

Martelli, M., Rizzo, A.L., Renzulli, A., Ridolfi, F., Arienzo, I., Rosciglione, A., 2014. Noble-gas signature of magmas from a heterogeneous mantle wedge: the case of Stromboli volcano (Aeolian Islands, Italy). Chem. Geol. 368, 39–53.

Martins, S., Mata, J., Munhá, J., Mendes, M.H., Maerschalk, C., Caldeira, R., Mattielli, N., 2010. Chemical and mineralogical evidence of the occurrence of mantle metasomatism by carbonate-rich melts in an oceanic environment (Santiago Island, Cape Verde). Miner Petrol 99, 43–65.

Marty, B., 2012. The origins and concentrations of water, carbon, nitrogen and noble gases on Earth. Earth and Planet. Sci. Lett. 313–314, 56–66.

Mata, J., Martins, S., Mattielli, N., Madeira, J., Faria, B., Ramalho, R.S., Silva, P., Moreira, M., Caldeira, R., Moreira, M., Rodrigues, J., Martins, L., 2017. The 2014–15 eruption and the short-term geochemical evolution of the Fogo volcano (Cape Verde): Evidence for small-scale mantle heterogeneity. Lithos 288–289, 91–107.

Melián, G.V., Hernández, P.A., Pérez, N.M., Asensio-Ramos, M., Padrón, E., Alonso, M., Padilla, G.D., Barrancos, J., Sortino, F., Sumino, H., Rodríguez, F., Amonte, C., Silva, S., Cardoso, N., Pereira, J.M., 2021. Insights from Fumarole Gas Geochemistry on the Recent Volcanic Unrest of Pico do Fogo, Cape Verde. Front. Earth Sci. 9, 631190.

Mourão, C., Moreira, M., Mata, J., Raquin, A., Madeira, J., 2012. Primary and secondary processes constraining the noble gas isotopic signatures of carbonatites and silicate rocks from Brava Island: evidence for a lower mantle origin of the Cape Verde plume. Contrib Mineral Petrol 163, 995–1009.

Nakagawa, T., Tackley, P.J., Deschamps, F., Connolly, J.A.D., 2010. The influence of MORB and harzburgite composition on thermo-chemical mantle convection in a 3-D spherical shell with self-consistently calculated mineral physics. Earth and Planet. Sci. Lett. 296, 403–412.

Ozima, M., and Podosek, F.A. 2002. Noble gas geochemistry. Cambridge Univ. Press, Cambridge, ed. 2,

Pim, J., Peirce, C., Watts, A.B., Grevemeyer, I., Krabbenhoeft, A., 2008. Crustal structure and origin of the Cape Verde Rise. Earth and Planet. Sci. Lett. 272, 422–428.

Pineau, F., Mathez, E.A., 1990. Carbon isotopes in xenoliths from the Hualalai Volcano, Hawaii, and the generation of isotopic variability. Geochim. Cosmochim. Acta 54, 217–227

Pollitz, F.F., 1991. Two-stage model of African absolute motion during the last 30 million years. Tectonophysics 194, 91–106. https://doi.org/10.1016/0040-1951(91)90274-V

Putirka, K.D., 2008. Thermometers and Barometers for Volcanic Systems. Reviews in Mineralogy and Geochemistry 69, 61–120.

Ramalho, R.A.S., 2011. Building the Cape Verde Islands. Springer Berlin Heidelberg, Berlin, Heidelberg.

Remigi, S., Frezzotti, M.L., Rizzo, A.L., Esposito, R., Bodnar, R. J., Sandoval-Velasquez, A., et al. 2023. Spatially resolved CO_2 carbon stable isotope analyses at the microscale using Raman spectroscopy. Sci. Rep. 13, 18561.

Rizzo, A.L., Barberi, F., Carapezza, M.L., Di Piazza, A., Francalanci, L., Sortino, F., D'Alessandro, W., 2015. New mafic magma refilling a quiescent volcano: Evidence from He-Ne-Ar isotopes during the 2011-2012 unrest at Santorini, Greece. Geochem. Geophys. Geosyst. 16, 798–814.

Rizzo, A.L., Pelorosso, B., Coltorti, M., Ntaflos, T., Bonadiman, C., Matusiak-Małek, M., Italiano, F., Bergonzoni, G., 2018. Geochemistry of Noble Gases and CO_2 in Fluid Inclusions from Lithospheric Mantle Beneath Wilcza Góra (Lower Silesia, Southwest Poland). Front. Earth Sci. 6, 215.

Roedder, Edwin. Fluid inclusions, Berlin, Boston: De Gruyter, 1984.

Sandoval-Velasquez, A., Rizzo, A.L., Aiuppa, A., Remigi, S., Padrón, E., Pérez, N.M., Frezzotti, M.L., 2021a. Recycled crustal carbon in the depleted mantle source of El Hierro volcano, Canary Islands. Lithos 400–401, 106414.

Sandoval-Velasquez, A., Rizzo, A.L., Frezzotti, M.L., Saucedo, R., Aiuppa, A., 2021b. The composition of fluids stored in the central Mexican lithospheric mantle: Inferences from noble gases and CO_2 in mantle xenoliths. Chem. Geol. 576, 120270.

Sandoval-Velasquez, A., Rizzo, A.L., Casetta, F., Ntaflos, T., Aiuppa, A., Alonso, M., Padrón, E., Pankhurst, M.J., Mundl-Petermeier, A., Zanon, V., Pérez, N.M., 2023. The noble gas signature of the 2021 Tajogaite eruption (La Palma, Canary Islands). J. Volcanol. Geotherm. Res. 443, 107928.

Sandoval-Velasquez, A., Casetta, F., Ntaflos, T., Aiuppa, A., Coltorti, M., Frezzotti, M.L., et al., 2024. 2021 Tajogaite eruption records infiltration of crustal fluids within the upper mantle beneath La Palma, Canary Islands. Front. Earth Sci. 12:1303872.

Sano, Y., and Marty, B., 1995. Origin of carbon in fumarolic gas from island arcs. Chem. Geol. 119, 265–274.

Sarda, P., Staudacher, T., Allegre, C., 1988. Neon isotopes in submarine basalts. Earth and Planet. Sci. Lett. 91, 73–88.

Schutt, D.L., Lesher, C.E., 2006. Effects of melt depletion on the density and seismic velocity of garnet and spinel lherzolite: Melt Depletion. J. Geophys. Res. 111, n/a-n/a.

Stracke, A., Genske, F., Berndt, J., Koornneef, J.M., 2019. Ubiquitous ultra-depleted domains in Earth's mantle. Nat. Geosci. 12, 851–855.

Sun, C., and Dasgupta, R., 2023. Carbon budget of Earth's deep mantle constrained by petrogenesis of silica-poor ocean island basalts. Earth and Planet. Sci. Lett. 611, 118135.

Zanon, V., Pimentel, A., Auxerre, M., Marchini, G., Stuart, F. M. 2020. Unravelling the magma feeding system of a young basaltic oceanic volcano. Lith. 352-353.

Zanon, V., and Pimentel, A. 2015. Spatio-temporal variations of magma storage and ascent conditions in an extensional tectonic setting. The case of the Terceira Island, Azores (Portugal). Amm Mineral. 100, 795-805.

Zanon, V., and Frezzotti, M. L. 2013. Magma storage and ascent conditions beneath Pico and Faial islands (Azores Islands). A study on fluid inclusions. Geochemistry, Geophysics, Geosystems 14, 3494-3514.

Zindler, A., Hart, S., 1986. Chemical Geodynamics. Annu. Rev. Earth Planet. Sci. 14, 493–571.

CHAPTER 8.

CONCLUDING REMARKS

In this dissertation, I have investigated the geochemistry of FI and MI hosted in olivines and clinopyroxenes from lavas, tephra, and mafic enclaves of some selected eruptions of the recent (<120 ka) activity of Fogo Volcano, in the Cape Verde Archipelago. FI have been characterised by microthermometry, as well as for the isotope composition of noble gases and carbon. Additionally, MI were investigated for major, trace, and volatile elements.

Interpretation of the results has been aimed at: (i) characterising the current architecture of the magma plumbing system, and how it has evolved in time during the recent volcano history; (ii) quantifying the parental melt volatile contents, and understanding volatile evolution (degassing) during magma ascent through/storage within the different levels of the magma plumbing system; (iii) constraining the magmatic source and the rates/modes of magma ascent prior to and during eruption; (iv) testing the presence of recycled crustal carbon in the Cape Verde mantle source.

The main outcomes of this study are summarised as follows:

- The plumbing system has undergone several variations over the last 120 ka of activity. Although our results are only representative of a few spot events in the volcano history, the following conclusions can be drawn: (i) the ~120 ka eruption, predating the collapse event of Mt. Amarelo, emitted basanitic magma stored at 19-22 km depth; (ii) following the collapse event, results for a ~60 ka eruption provide evidence for direct magma withdrawal from the deeper storage system at ~ 24 km depth, suggesting that post-collapse, magma extraction bypassed the shallower magma system; (iii) finally, Holocene/historical eruptions indicate slower magma ascent rates and a more prolonged magma storage at ~13-17 km depth (as indicated by early-stage fluid inclusions, Type I). Additionally, at a depth of ~9-12 km, near the Moho, a magma stagnation zone exists, as indicated by surface re-equilibration of fluid inclusions (late-stage fluid inclusions, Type II). In this shallow stagnation zone, magma crystallises and differentiates, as demonstrated by the evolved nature (phono-tephritic) composition of lavas erupted during the 1951 to 2014-2015 eruptions;
- The plumbing system of Fogo exhibits similarities with other oceanic volcanoes (e.g., Piton de la Fournaise, La Reunion; El Hierro and Cumbre Vieja, Canary), wherein small-volume

magma pockets exist within a well-established crystal mush zone, overall giving rise to a vertically extended trans-crustal magmatic system;

- Results for the most recent eruptions (1951, 1995 and 2014-2015) suggest an upward shift of the magma storage conditions. Furthermore, these three eruptions exhibit relatively more abundant Type II inclusions, implying longer residence times, more larger extents of FI re-equilibration events, at depth less than 12 km, compared to older analysed samples. The prolonged residence times within the oceanic crust align with the somewhat evolved composition (SiO_2 > 42 wt%; FeO/MgO > 2.0 wt.%) of the erupted lavas in contrast to volcanic activity in the 1600s-1800s. Shallow crustal processing of magmas is therefore becoming more and more important with time, potentially caused by progressive modifications in the thermal characteristics of the ocean crust as result of Fogo's frequent activity since the 1400s;
- Olivine-hosted melt inclusions from recent basanitic tephra samples indicate that the recent (<10 ka) basanitic Fogo magmas exhibit some of the highest ever recorded parental melt CO_2 contents, reaching up to 2.15 wt.%. Recovery of these high CO_2 level was made possible using three independent methodologies to correct for CO_2 within shrinkage bubbles. The volatile-rich nature of the Fogo parental melt is further demonstrated by the high H_2O (up to 2.73 wt.%), S (up to 8200 ppm), Cl (up to 1400 ppm), and F (up to 2200 ppm) contents;
- Although exceptionally CO_2-rich, our melt inclusions still underestimate the actual CO_2 contents in primary melts. This is supported by our observed MI CO_2/Nb ratios (277-283) and CO_2/Ba ratios (26-22) been lower than the characteristic mantle ratios, and suggests pre-entrapment CO_2 loss to bubbles;
- The basanitic magmas feeding Fogo's activity are suggested to originate from a metasomatized, carbon-rich mantle source, containing a minimum of 355-414 ppm C. Our results confirm recent indications for a carbon-rich signature of alkali-rich OIB magmas worldwide. In spite of their comparatively modest eruptive volumes, OIB eruptions may disproportionately contribute to the global release of volcanic carbon from the mantle into the Earth's atmosphere. We cautiously infer the global carbon flux from OIB to be as high as 17-23 Tg/yr;
- The measured H_2O-CO_2 concentrations in MI, combined with available saturation models, are used to estimate MI entrapment pressures. The saturation pressures obtained from the most CO_2-rich melt inclusions range from 773 to 1020 MPa. Consequently, our results indicate that

Fogo parental melt is stored within the lithospheric mantle, at depths of 27-36 km, from where, magma is eventually injected (prior to eruption) into a vertically stacked magma ponding system, situated between 13-25 km;

- The isotopic systematics of He in mafic cumulate, lava, tephra, and fumarole samples confirm a MORB-like upper mantle signature (Rc/Ra=7.14-8.44) for the lithospheric mantle beneath Fogo. A thorough examination of the existing $^{3}He/^{4}He$ literature in the Cape Verde Archipelago and other OIB volcanoes, reveals that the $^{3}He/^{4}He$ ratio in OIB exhibit an inverse relationship with La/Yb ratio and, hence, with magma production rates in the mantle source. This suggests that any lower-mantle component ($^{3}He/^{4}He$ ratio > 9 Ra) can only be resolved in islands when high degrees of mantle partial melting occur (e.g., low La/Yb). Indeed, in OIBs, where a strong lower mantle component (Rc/Ra > 9 Ra) is prevalent throughout much of the mantle underlying the archipelago (e.g., Hawaii, Galapagos, Samoa, Societies), a lower mantle component is also present even when high degrees of mantle partial melting occur. Additionally, the global OIB helium isotopic signatures are predominantly influenced by the buoyancy flux of the plume and the speed of the overlying plate. Indeed, the MORB-like $^{3}He/^{4}He$ signature observed at Fogo (more broadly in the Cape Verde and in the Canary Islands) indicates: (i) elevated magma productivity, (ii) a relatively low plume buoyancy flux, and (iii) a slow average speed of the overlying plate;
- We propose magma storage in OIB consistently occurs at shallower depths in systems associated with high buoyancy flux plumes (Hawaii, Galapagos) than in off-axis systems, or in OIBs associated with low buoyancy flux plumes coupled and low plate speeds (Cape Verde and Canary);
- Using FI carbon isotopic results, we developed a model for carbon degassing within the mantle-to-crustal magmatic plumbing system. This model predicts a crustal signature for carbon (with a $\delta^{13}C$ value of a -0.4‰) in primary melts (8-9 wt. % CO_2) generated through upper mantle melting at ~ 2200 MPa (~77 km). We interpret this signature as indicative of mantle metasomatism by melts/fluids enriched with a recycled crustal carbon component. Considering that the carbon isotopic ratio ($\delta^{13}C$ vs. PDB) of CO_2 in FI and fumaroles ranges from -6.04 to -4.41‰, we interpret this variability as indicative of isotopic fractionation resulting from substantial magma degassing (~75-94%) occurring at relatively shallow depths within the Fogo plumbing system. A ^{13}C-enriched signature observed in primary melts from

Fogo is tentatively interpreted as reflecting the recycling of ancient, deeply subducted crustal materials ($\delta^{13}C \geq -1$ ‰) into the deep mantle beneath Cape Verde.

APPENDIX A. SUPPLEMENTARY MATERIAL

In Appendix A, supplementary materials are provided, referencing Chapters 5 and 6 of the thesis, which have already been published in the Journal of Volcanology and Research (Chapter 5) and in the Mendeley data repository (Chapter 6).

The supplementary materials for Chapter 5 are available online at the following link:
https://doi.org/10.1016/j.jvolgeores.2022.107730

The supplementary materials for Chapter 6 are available online at the following link:
https://data.mendeley.com/datasets/gr2dy9grdn/2

APPENDIX B. SUPPLEMENTARY MATERIAL

In Appendix B, supplementary materials (tables and figures) are provided, referencing Chapter 7 of this thesis.

TABLE S1. NOBLE GAS AND CO_2 ISOTOPIC COMPOSITIONS REPORTED IN THE LITERATURE FOR THE CAPE VERDE ARCHIPELAGO. REPORTED ERRORS ARE 2Σ UNCERTAINTIES

Locality	Sample ID	Rock	Phase	Reference	Extraction Method (FI)	Age (ka)	T (°C)
Fogo	FG3A > 1	Cumulate	Olv	This work	Single step crushing	1400s-1800s	
Fogo	FG2 A1 > 1 (2)	Cumulate	Olv	This work	Single step crushing	1951	
Fogo	FG2 A3 >1 (2)	Cumulate	Olv	This work	Single step crushing	1951	
Fogo	Fog 43	Tephra/?	Olv	This work	Single step crushing	10 ka	
Fogo	Fog 28	Lava/?	Olv	This work	Single step crushing	10 ka	
Fogo	Fog 31	Lava/?	Olv	This work	Single step crushing	1951	
Fogo	Fog 27	Lava/Basanite	Olv	This work	Single step crushing	60 ka	
Fogo	Fog 20	Lava/Basanite	Olv	This work	Single step crushing	1799	
Fogo	Fog 23	Lava/Basanite	Olv	This work	Single step crushing	1664	

Fogo	Fog 24	Lava/Basanite	Olv	This work	Single step crushing	1852	
Fogo	Fog 33	Lava/Basanite	Olv	This work	Single step crushing	1400s-1800s	
Fogo	FOGO 4E	Cumulate	Cpx	This work	Single step crushing	10 ka	
Fogo	FOGO 4D	Cumulate	Cpx	This work	Single step crushing	10 ka	
Fogo	FOGO 4A	Cumulate	Cpx	This work	Single step crushing	10 ka	
Fogo	FG2 A3 >1	Cumulate	Cpx	This work	Single step crushing	10 ka	
Fogo	FG4B (2)	Cumulate	Cpx	This work	Single step crushing	10 ka	
Fogo	FG2 A1 > 1 (2)	Cumulate	Cpx	This work	Single step crushing	10 ka	
Fogo	FG1A (2)	Cumulate	Cpx	This work	Single step crushing	10 ka	
Fogo	Pico do Fogo 1	/	Fumaroles	This work	/	/	226
Fogo	Pico do Fogo 1	/	Fumaroles	This work	/	/	226
Fogo	Pico do Fogo 1	/	Fumaroles	This work	/	/	226
Fogo	Pico do Fogo 2	/	Fumaroles	This work	/	/	315
Fogo	Pico do Fogo 2	/	Fumaroles	This work	/	/	315
Fogo	Pico do Fogo 2	/	Fumaroles	This work	/	/	315
Fogo	F-106403	Ankaramite ?	olv	Christensen et al. 2001	crushing	870 ka-historic	
Fogo	F-106403	Ankaramite ?	cpx	Christensen et al. 2001	crushing	870 ka-historic	
Fogo	F-106444	Ankaramite ?	olv	Christensen et al. 2001	crushing	870 ka-historic	
Fogo	F-106444	Ankaramite ?	cpx	Christensen et al. 2001	crushing	870 ka-historic	
Fogo	F-01	/	olv	Doucelance et al. 2003	crushing	/	
Fogo		/	cpx	Doucelance et al. 2003	crushing	/	
Fogo	F-02	Basanite	olv	Doucelance et al. 2003	crushing	/	
Fogo		Basanite	cpx	Doucelance et al. 2003	crushing	/	
Fogo		Basanite	powder	Doucelance et al. 2003	melting	/	
Fogo	F-05	/	olv	Doucelance et al. 2003	crushing	/	
Fogo		?	cpx	Doucelance et al. 2003	crushing	/	
Fogo	F-07	Basanite	olv	Doucelance et al. 2003	crushing	/	
Fogo		Basanite	powder	Doucelance et al. 2003	melting	/	
Fogo	F-08	Basanite	olv	Doucelance et al. 2003	crushing	/	
Fogo		Basanite	powder	Doucelance et al. 2003	melting	/	

Fogo	F-11	/	olv	Doucelance et al. 2003	crushing	/
Fogo		/	powder	Doucelance et al. 2003	melting	/
Fogo		/	olv	Doucelance et al. 2003	crushing	/
Fogo		/	re-crushed	Doucelance et al. 2003	crushing	/
Fogo		/	olv	Doucelance et al. 2003	crushing	/
Fogo	F-13	/	olv	Doucelance et al. 2003	crushing	/
Fogo		/	re-crushed	Doucelance et al. 2003	crushing	/
Fogo		/	cpx	Doucelance et al. 2003	crushing	/
Fogo		/	powder	Doucelance et al. 2003	melting	/
Fogo		/	cpx	Doucelance et al. 2003	crushing	/
Fogo	F-15	Basanite	olv	Doucelance et al. 2003	crushing	/
Fogo	F-16	/	olv	Doucelance et al. 2003	crushing	/
Fogo	F-18	/	olv	Doucelance et al. 2003	crushing	/
Fogo	F-20	Foidite	olv	Doucelance et al. 2003	crushing	/
Fogo	F-21	/	olv	Doucelance et al. 2003	crushing	/
Fogo	F-24	Basanite	olv	Doucelance et al. 2003	crushing	/
Fogo	F1	/	Fumaroles	Alonso et al. 2021	/	/
Fogo	F1	/	Fumaroles	Alonso et al. 2021	/	/
Fogo	F1	/	Fumaroles	Alonso et al. 2021	/	/
Fogo	F1	/	Fumaroles	Alonso et al. 2021	/	/
Fogo	F1	/	Fumaroles	Alonso et al. 2021	/	/
Fogo	F1	/	Fumaroles	Alonso et al. 2021	/	/
Fogo	F1	/	Fumaroles	Alonso et al. 2021	/	/
Fogo	F1	/	Fumaroles	Alonso et al. 2021	/	/
Fogo	F1	/	Fumaroles	Alonso et al. 2021	/	/
Fogo	F1	/	Fumaroles	Alonso et al. 2021	/	/
Fogo	F1	/	Fumaroles	Alonso et al. 2021	/	/
Fogo	F1	/	Fumaroles	Alonso et al. 2021	/	/
Fogo	F1	/	Fumaroles	Alonso et al. 2021	/	/
Fogo	F1	/	Fumaroles	Alonso et al. 2021	/	/
Fogo	F2	/	Fumaroles	Melian et al. 2021	/	/

Fogo	F2	/	Fumaroles	Melian et al. 2021	/	/
Fogo	F2	/	Fumaroles	Melian et al. 2021	/	/
Fogo	F2	/	Fumaroles	Melian et al. 2021	/	/
Fogo	F2	/	Fumaroles	Melian et al. 2021	/	/
Fogo	F2	/	Fumaroles	Melian et al. 2021	/	/
Fogo	F3	/	Fumaroles	Melian et al. 2021	/	/
Fogo	F4	/	Fumaroles	Melian et al. 2021	/	/
Santo Antão	SA-110062	Ankaramite ?	olv	Christensen et al. 2001	crushing	870 ka-historic
Santo Antão	SA-1118222	Ankaramite ?	olv	Christensen et al. 2001	crushing	870 ka-historic
Santo Antão	SA-111827a	Ankaramite ?	olv	Christensen et al. 2001	crushing	870 ka-historic
Santo Antão	SA-111827b	Ankaramite ?	olv	Christensen et al. 2001	crushing	870 ka-historic
Santo Antão	SA-111832a	Ankaramite ?	olv	Christensen et al. 2001	crushing	870 ka-historic
Santo Antão	SA-111832b	Ankaramite ?	olv	Christensen et al. 2001	crushing	870 ka-historic
Santo Antão	SA-111837	Ankaramite ?	olv	Christensen et al. 2001	crushing	870 ka-historic
Santo Antão	SA-111940	Ankaramite ?	olv	Christensen et al. 2001	crushing	870 ka-historic
Santiago	ST-02	Basanite	olv	Doucelance et al. 2003	crushing	?
Santiago	ST-06	Foidite	olv	Doucelance et al. 2003	crushing	?
Santiago		Foidite	re-crushed	Doucelance et al. 2003	crushing	?
Santiago		Foidite	powder	Doucelance et al. 2003	melting	?
Santiago	ST-08	Basanite	olv	Doucelance et al. 2003	crushing	?
Santiago		Basanite	powder	Doucelance et al. 2003	melting	?
Santiago	ST-09	Foidite	cpx	Doucelance et al. 2003	crushing	?
Santiago		Foidite	powder	Doucelance et al. 2003	melting	?
SãoVicente	SV-01	Basanite	olv	Doucelance et al. 2003	crushing	?
SãoVicente		Basanite	re-crushed	Doucelance et al. 2003	crushing	?
SãoVicente	SV-02	Basanite	olv	Doucelance et al. 2003	crushing	?
SãoVicente		Basanite	cpx	Doucelance et al. 2003	crushing	?
SãoVicente		Basanite	re-crushed	Doucelance et al. 2003	crushing	?

SãoVicente	SV-03	Basanite	olv	Doucelance et al. 2003	crushing	?
SãoVicente	SV-05	Foidite	olv	Doucelance et al. 2003	crushing	?
SãoVicente		Foidite	re-crushed	Doucelance et al. 2003	crushing	?
SãoVicente	SV-09	Foidite	olv	Doucelance et al. 2003	crushing	?
SãoVicente	SV-10	Foidite	olv	Doucelance et al. 2003	crushing	?
SãoVicente	SV-12	Picro-Basalt	olv	Doucelance et al. 2003	crushing	?
São Nicolau	SN-02	Basanite	olv	Doucelance et al. 2003	crushing	?
São Nicolau		Basanite	powder	Doucelance et al. 2003	melting	?
São Nicolau	SN-03	Picro-Basalt	olv	Doucelance et al. 2003	crushing	?
São Nicolau		Picro-Basalt	re-crusehd	Doucelance et al. 2003	crushing	?
São Nicolau	SN-05	Foidite	olv	Doucelance et al. 2003	crushing	?
São Nicolau	SN-10	Foidite	olv	Doucelance et al. 2003	crushing	?
São Nicolau		Foidite	re-crushed	Doucelance et al. 2003	crushing	?
São Nicolau	SN-11	Basanite	olv	Doucelance et al. 2003	crushing	?
São Nicolau	SN-13	Basanite	olv	Doucelance et al. 2003	crushing	?
Sal	S-03	Foidite	olv	Doucelance et al. 2003	crushing	?
Sal	S-06	Foidite	olv	Doucelance et al. 2003	crushing	?
Sal	S-07	Foidite	olv	Doucelance et al. 2003	crushing	?
Sal		Foidite	re-crushed	Doucelance et al. 2003	crushing	?
Sal		Foidite	powder	Doucelance et al. 2003	melting	?
Sal		Foidite	olv	Doucelance et al. 2003	crushing	?
Brava	CY7	Mafic Rock	olv	Mourão et al. 2011	single crushing	
Brava	CY11 step 1	Mafic Rock	olv	Mourão et al. 2011	multi step crushing	
Brava	CY25	Mafic Rock	olv	Mourão et al. 2011	single crushing	
Brava	CY82	Mafic Rock	olv	Mourão et al. 2011	single crushing	
Brava	CY83	Mafic Rock	olv	Mourão et al. 2011	single crushing	
Brava	CY98	Mafic Rock	olv	Mourão et al. 2011	single crushing	
Brava	CY200	Mafic Rock	olv	Mourão et al. 2011	single crushing	
Brava	CY247	Mafic Rock	olv	Mourão et al. 2011	single crushing	
Brava	CY110	Carbonatite	apatite	Mourão et al. 2011	single crushing	
Brava	CY111	Carbonatite	apatite	Mourão et al. 2011	single crushing	
Brava	CY112	Carbonatite	apatite	Mourão et al. 2011	single crushing	

Brava	CY113	Carbonatite	apatite	Mourão et al. 2011	single crushing
Brava	CY161	Carbonatite	apatite	Mourão et al. 2011	single crushing
Brava	CY23	Carbonatite	calcite	Mourão et al. 2011	single crushing
Brava	CY56	Carbonatite	calcite	Mourão et al. 2011	single crushing
Brava	CY 116	Carbonatite	calcite	Mourão et al. 2011	single crushing
Brava	CY 144	Carbonatite	calcite	Mourão et al. 2011	single crushing
Brava	CY 156	Carbonatite	calcite	Mourão et al. 2011	single crushing
Brava	CY 161	Carbonatite	calcite	Mourão et al. 2011	single crushing
Brava	CY7	Mafic Rock	powder	Mourão et al. 2011	melting
Brava	CY11 tot	Mafic Rock	powder	Mourão et al. 2011	melting
Brava	CY 25	Mafic Rock	powder	Mourão et al. 2011	melting
Brava	CY 82	Mafic Rock	powder	Mourão et al. 2011	melting
Brava	CY 83	Mafic Rock	powder	Mourão et al. 2011	melting

Table S1. Continued

Locality	Sample ID	3He (mol/g)	4He (mol/g)	20Ne (mol/g)	40Ar (mol/g)	38Ar (mol/g)	36Ar (mol/g)	40Ar* (mol/g)
Fogo	FG3A > 1	9.06E-18	8.85E-13	2.23E-15	2.31E-12	2.86E-16	1.43E-15	1.89E-12
Fogo	FG2 A1 > 1 (2)	1.16E-17	1.09E-12	6.49E-15	3.79E-12	2.07E-15	1.13E-14	4.46E-13
Fogo	FG2 A3 >1 (2)	1.60E-17	1.45E-12	1.95E-15	2.19E-12	7.81E-16	3.81E-15	1.06E-12
Fogo	Fog 43	4.37E-18	3.90E-13	7.87E-15	3.09E-12	1.29E-15	6.78E-15	1.09E-12
Fogo	Fog 28	2.69E-17	2.38E-12	7.44E-15	5.94E-12	7.30E-16	3.49E-15	4.91E-12
Fogo	Fog 31	9.95E-18	8.77E-13	4.29E-15	2.47E-12	1.10E-15	5.70E-15	7.83E-13
Fogo	Fog 27	4.97E-18	4.65E-13	4.42E-14	2.30E-11	1.07E-16	6.53E-14	3.71E-12
Fogo	Fog 20	1.17E-17	1.02E-12	6.06E-15	4.85E-12	1.53E-13	8.30E-15	2.40E-12
Fogo	Fog 23	1.11E-17	1.10E-12	6.97E-15	1.93E-12	2.53E-16	1.23E-15	1.56E-12
Fogo	Fog 24	1.45E-17	1.29E-12	2.76E-15	3.31E-12	7.64E-16	4.12E-15	2.09E-12
Fogo	Fog 33	4.28E-18	4.33E-13	7.26E-15	3.54E-12	8.39E-16	4.54E-15	2.20E-12
Fogo	FOGO 4E	2.68E-17	2.40E-12	2.41E-14	1.03E-11	3.21E-15	1.78E-14	5.00E-12

Fogo	FOGO 4D	1.72E-17	1.51E-12	1.47E-14	4.69E-12	2.60E-15	1.44E-14	4.44E-13
Fogo	FOGO 4A	8.68E-18	7.66E-13	1.13E-14	3.71E-12	1.59E-15	8.78E-15	1.11E-12
Fogo	FG2 A3 >1	4.70E-18	4.18E-13	3.22E-15	1.56E-12	8.18E-16	4.34E-15	2.74E-13
Fogo	FG4B (2)	7.86E-16	6.71E-11	2.81E-14	1.94E-11	1.05E-15	1.76E-14	1.42E-11
Fogo	FG2 A1 > 1 (2)	8.67E-18	8.20E-13	1.08E-14	4.22E-12	2.47E-15	1.36E-14	2.14E-13
Fogo	FG1A (2)	1.32E-15	1.16E-10	5.01E-14	3.25E-11	1.43E-14	7.51E-14	1.03E-11
Fogo	Pico do Fogo 1		3.20E-08	8.00E-08	7.57E-08	2.70E-08	1.89E-08	1.99E-08
Fogo	Pico do Fogo 1		2.40E-08					
Fogo	Pico do Fogo 1		3.20E-08					
Fogo	Pico do Fogo 2		3.20E-08	2.20E-08	2.67E-08	1.62E-08	8.21E-08	2.39E-08
Fogo	Pico do Fogo 2		3.20E-08					
Fogo	Pico do Fogo 2		2.40E-08					
Fogo	F-106403		7.14E-12		1.15E-03			
Fogo	F-106403		1.41E-11		/			
Fogo	F-106444				1.95E-04			
Fogo	F-106444		8.08E-12		/			
Fogo	F-01		3.12E-13					
Fogo			1.07E-13					
Fogo	F-02		1.47E-13					
Fogo			3.35E-13					
Fogo			1.83E-13					
Fogo	F-05		3.08E-13					
Fogo			4.51E-13					
Fogo	F-07		2.28E-12					
Fogo			8.61E-13					
Fogo	F-08		1.19E-12					
Fogo			7.14E-14					
Fogo	F-11		4.46E-14					
Fogo			5.80E-14					
Fogo			5.35E-14					
Fogo			1.78E-14					
Fogo			1.70E-13					

Fogo	F-13	1.34E-13
Fogo		2.23E-14
Fogo		3.97E-13
Fogo		1.96E-13
Fogo		6.47E-13
Fogo	F-15	1.96E-12
Fogo	F-16	2.04E-12
Fogo	F-18	6.65E-13
Fogo	F-20	1.61E-13
Fogo	F-21	6.11E-13
Fogo	F-24	5.49E-13
Fogo	F1	
Fogo	F1	
Fogo	F1	
Fogo	F1	
Fogo	F1	
Fogo	F1	
Fogo	F1	
Fogo	F1	
Fogo	F1	
Fogo	F1	
Fogo	F1	
Fogo	F1	
Fogo	F1	
Fogo	F1	
Fogo	F2	
Fogo	F2	
Fogo	F2	
Fogo	F2	
Fogo	F2	
Fogo	F2	
Fogo	F3	
Fogo	F4	
Santo Antão	SA-110062	1.63E-12
Santo Antão	SA-1118222	2.99E-12
Santo Antão	SA-111827a	2.74E-12
Santo Antão	SA-111827b	2.31E-12
Santo Antão	SA-111832a	4.24E-12
Santo Antão	SA-111832b	3.48E-13
Santo Antão	SA-111837	9.82E-13
Santo Antão	SA-111940	6.29E-13
Santiago	ST-02	7.58E-14

Santiago	ST-06	1.78E-14
Santiago		8.92E-15
Santiago		2.14E-13
Santiago	ST-08	8.48E-14
Santiago		2.59E-13
Santiago	ST-09	4.91E-14
Santiago		6.82E-12
SãoVicente	SV-01	4.51E-13
SãoVicente		2.68E-14
SãoVicente	SV-02	2.68E-13
SãoVicente		1.12E-13
SãoVicente		4.02E-14
SãoVicente	SV-03	4.10E-13
SãoVicente	SV-05	2.68E-14
SãoVicente		8.92E-15
SãoVicente	SV-09	2.86E-13
SãoVicente	SV-10	1.92E-13
SãoVicente	SV-12	6.29E-13
São Nicolau	SN-02	2.23E-12
São Nicolau		2.05E-12
São Nicolau	SN-03	1.83E-13
São Nicolau		8.92E-15
São Nicolau	SN-05	8.39E-13
São Nicolau	SN-10	1.04E-12
São Nicolau		1.29E-13
São Nicolau	SN-11	6.20E-13
São Nicolau	SN-13	1.20E-13
Sal	S-03	4.00E-09
Sal	S-06	1.03E-08
Sal	S-07	9.40E-09
Sal		3.40E-09
Sal		2.52E-08

Sal		1.56E-08						
Brava	CY7	8.83E-15						
Brava	CY11 step 1	1.02E-13						
Brava	CY25	2.69E-13						
Brava	CY82	2.33E-13						
Brava	CY83	2.17E-13						
Brava	CY98	1.74E-12						
Brava	CY200	3.11E-12						
Brava	CY247	4.31E-14						
Brava	CY110	5.94E-15					1.96E-15	
Brava	CY111	3.19E-13					3.44E-15	
Brava	CY112	1.35E-14					3.39E-15	
Brava	CY113	5.50E-15					5.80E-15	
Brava	CY161	1.85E-14					5.80E-15	
Brava	CY23	4.67E-15					1.95E-14	
Brava	CY56	4.41E-14					1.93E-14	
Brava	CY 116	3.19E-14					2.45E-14	
Brava	CY 144	7.00E-16					6.73E-14	
Brava	CY 156	2.56E-14					3.48E-14	
Brava	CY 161	7.99E-15					1.47E-14	
Brava	CY7	2.17E-13						
Brava	CY11 tot	2.04E-13						
Brava	CY 25	1.73E-13						
Brava	CY 82	7.23E-15						
Brava	CY 83	3.47E-13						

Table S1. Continued

Locality	Sample ID	CO_2 (mol/g)	$^{4}He/^{20}Ne$	$^{4}He/^{40}Ar^{*}$	R/Ra	Rc/Ra	Error (+/-)	$^{40}Ar/^{36}Ar$
Fogo	FG3A > 1	8.78E-08	396.64	0.47	7.35	7.35	0.13	1670.94
Fogo	FG2 A1 > 1 (2)	5.83E-09	167.52	2.44	7.92	7.93	0.10	339.19

Fogo	FG2 A3 >1 (2)	9.71E-10	745.60	1.37	8.18	8.18	0.11	597.09
Fogo	Fog 43	4.58E-10	49.56	0.36	8.05	8.10	0.17	462.55
Fogo	Fog 28	5.52E-09	319.49	0.48	8.06	8.06	0.11	1758.11
Fogo	Fog 31	1.64E-09	204.28	1.12	8.17	8.18	0.11	440.43
Fogo	Fog 27	1.36E-09	10.50	0.13	7.69	7.91	0.16	354.32
Fogo	Fog 20	1.44E-09	167.85	0.42	8.24	8.25	0.11	592.39
Fogo	Fog 23	8.78E-09	157.11	0.70	7.29	7.30	0.14	1657.13
Fogo	Fog 24	1.17E-08	467.69	0.62	8.09	8.09	0.10	818.22
Fogo	Fog 33	9.84E-09	59.59	0.20	7.11	7.14	0.15	793.14
Fogo	FOGO 4E	4.51E-09	99.53	0.48	8.00	8.02	0.09	585.43
Fogo	FOGO 4D	/	102.35	3.39	8.21	8.24	0.09	329.56
Fogo	FOGO 4A	8.30E-11	67.57	0.69	8.12	8.16	0.09	427.82
Fogo	FG2 A3 >1	2.87E-10	129.94	1.52	8.08	8.10	0.15	363.15
Fogo	FG4B (2)	2.92E-08	2388.42	4.71	8.44	8.44	0.09	1173.98
Fogo	FG2 A1 > 1 (2)	1.81E-08	76.04	3.83	7.83	7.86	0.10	315.09
Fogo	FG1A (2)	6.74E-07	2314.89	11.28	8.22	8.23	0.09	440.83
Fogo	Pico do Fogo 1		103.83	1.13	8.05	8.07		397.36
Fogo	Pico do Fogo 1							
Fogo	Pico do Fogo 1							
Fogo	Pico do Fogo 2		37.26	0.91	8.00	8.06		323.72
Fogo	Pico do Fogo 2							
Fogo	Pico do Fogo 2							
Fogo	F-106403				6.90			3.56E+02
Fogo	F-106403				7.60			/
Fogo	F-106444							6.39E+02
Fogo	F-106444				12.10			/
Fogo	F-01				8.53			
Fogo					6.88			
Fogo	F-02				7.90			
Fogo					7.91			
Fogo					4.89			
Fogo	F-05				7.53			
Fogo					8.56			
Fogo	F-07				8.28			
Fogo					7.90			
Fogo	F-08				8.06			
Fogo					4.66			

Fogo	F-11		6.31		
Fogo			8.44		
Fogo			7.23		
Fogo			9.54		
Fogo			8.04		
Fogo	F-13		7.76		
Fogo			6.90		
Fogo			7.74		
Fogo			5.90		
Fogo			7.96		
Fogo	F-15		8.15		
Fogo	F-16		8.24		
Fogo	F-18		7.91		
Fogo	F-20		8.40		
Fogo	F-21		8.04		
Fogo	F-24		7.76		
Fogo	F1	1.23E+02	8.09	8.11	
Fogo	F1	3.62E+02	8.22	8.23	
Fogo	F1	2.30E+01	7.81	7.91	
Fogo	F1	2.28E+02	8.53	8.54	
Fogo	F1	9.40E+01	8.23	8.25	
Fogo	F1	4.20E+01	8.23	8.29	
Fogo	F1	1.94E+02	7.93	7.94	
Fogo	F1	1.80E+01	8.20	8.33	
Fogo	F1	4.06E+02	8.63	8.64	
Fogo	F1	1.10E+02	8.37	8.39	
Fogo	F1	3.60E+01	8.33	8.40	
Fogo	F1	1.06E+02	7.66	7.68	
Fogo	F1	1.60E+01	6.69	6.81	
Fogo	F1				
Fogo	F1				
Fogo	F2	2.00E+00	7.73	9.00	
Fogo	F2	5.19E+02	8.33	8.33	
Fogo	F2	1.00E+00	8.28	11.67	
Fogo	F2	4.81E+02	8.82	8.83	
Fogo	F2	1.67E+02	8.36	8.37	
Fogo	F2	3.60E+01	8.33	8.40	
Fogo	F3				
Fogo	F4				
Santo Antão	SA-110062		11.70		6.08E+02
Santo Antão	SA-1118222		3.20		1.25E+03
Santo Antão	SA-111827a		6.10		8.37E+02
Santo Antão	SA-111827b		7.90		/
Santo Antão	SA-111832a		9.70		1.23E+03
Santo Antão	SA-111832b		8.70		/
Santo Antão	SA-111837		13.80		4.48E+02
Santo Antão	SA-111940		9.10		1.26E+03
Santiago	ST-02		8.24		
Santiago	ST-06		3.90		
Santiago			7.66		
Santiago			29.20		
Santiago	ST-08		8.31		
Santiago			6.36		
Santiago	ST-09		1.38		
Santiago			0.18		

SãoVicente	SV-01		9.07	
SãoVicente			6.45	
SãoVicente	SV-02		9.95	
SãoVicente			9.07	
SãoVicente			9.82	
SãoVicente	SV-03		10.83	
SãoVicente	SV-05		10.70	
SãoVicente			10.81	
SãoVicente	SV-09		11.08	
SãoVicente	SV-10		12.27	
SãoVicente	SV-12		8.41	
São Nicolau	SN-02		12.94	
São Nicolau			12.87	
São Nicolau	SN-03		14.03	
São Nicolau			10.87	
São Nicolau	SN-05		15.24	
São Nicolau	SN-10		15.73	
São Nicolau			15.58	
São Nicolau	SN-11		10.47	
São Nicolau	SN-13		12.00	
Sal	S-03		9.55	
Sal	S-06		6.98	
Sal	S-07		9.97	
Sal			9.74	
Sal			42.64	
Sal			9.98	
Brava	CY7 CY11		7.1	
Brava	step 1		13.35	
Brava	CY25		10.61	
Brava	CY82		12.03	
Brava	CY83		10.35	
Brava	CY98		9.32	
Brava	CY200		10.27	
Brava	CY247		11.02	
Brava	CY110	2.46	8.07	418
Brava	CY111	1.12	4.01	379
Brava	CY112	5.25	9.67	371
Brava	CY113	0.97	8.63	393
Brava	CY161	5.64	5.22	352
Brava	CY23	1.18	7.4	316
Brava	CY56	0.81	11.73	577
Brava	CY 116	0.3	10.69	730
Brava	CY 144	0.33	11.8	610
Brava	CY 156	1.65	11.62	340
Brava	CY 161	0.43	10.03	421
Brava	CY7 CY11		11.94	
Brava	tot		31.76	
Brava	CY 25		25.48	
Brava	CY 82		14.62	
Brava	CY 83		42.28	

Table S1. Continued

Locality	Sample ID	Error (%)	$^{38}Ar/^{36}Ar$	Error (%)	$\delta^{13}C$ (‰)
Fogo	FG3A > 1	0.12	1.94E-01	0.19	-4.73
Fogo	FG2 A1 > 1 (2)	0.06	1.81E-01	0.19	
Fogo	FG2 A3 >1 (2)	0.09	1.84E-01	0.19	
Fogo	Fog 43	0.06	1.84E-01	0.18	
Fogo	Fog 28	0.09	1.90E-01	0.19	
Fogo	Fog 31	0.06	1.82E-01	0.18	
Fogo	Fog 27	0.11	1.81E-01	0.18	
Fogo	Fog 20	0.04	1.86E+01	19.04	
Fogo	Fog 23	0.09	1.73E-01	0.18	
Fogo	Fog 24	0.06	1.77E-01	0.18	
Fogo	Fog 33	0.06	1.78E-01	0.18	-4.41
Fogo	FOGO 4E	0.06	1.80E-01	0.18	
Fogo	FOGO 4D	0.06	1.81E-01	0.18	
Fogo	FOGO 4A	0.06	1.80E-01	0.18	
Fogo	FG2 A3 >1	0.06	1.88E-01	0.19	
Fogo	FG4B (2)	0.13	1.92E-01	0.20	
Fogo	FG2 A1 > 1 (2)	0.05	1.80E-01	0.19	
Fogo	FG1A (2)	0.06	1.84E-01	0.19	-6.04
Fogo	Pico do Fogo 1		1.90E-01		-4.73
Fogo	Pico do Fogo 1				-4.72
Fogo	Pico do Fogo 1				-4.9
Fogo	Pico do Fogo 2		1.89E-01		-5
Fogo	Pico do Fogo 2				-4.34
Fogo	Pico do Fogo 2				-5.11
Fogo	F-106403				
Fogo	F-106403				
Fogo	F-106444				
Fogo	F-106444				
Fogo	F-01				
Fogo					
Fogo	F-02				
Fogo					
Fogo					

Fogo	F-05	
Fogo		
Fogo	F-07	
Fogo		
Fogo	F-08	
Fogo		
Fogo	F-11	
Fogo		
Fogo		
Fogo		
Fogo		
Fogo	F-13	
Fogo		
Fogo		
Fogo		
Fogo		
Fogo	F-15	
Fogo	F-16	
Fogo	F-18	
Fogo	F-20	
Fogo	F-21	
Fogo	F-24	
Fogo	F1	
Fogo	F1	
Fogo	F1	
Fogo	F1	- 4.07E+00
Fogo	F1	- 4.22E+00
Fogo	F1	- 4.10E+00
Fogo	F1	- 4.26E+00
Fogo	F1	- 4.48E+00
Fogo	F1	- 4.37E+00
Fogo	F1	- 4.62E+00
Fogo	F1	- 3.88E+00
Fogo	F1	- 4.29E+00
Fogo	F1	/
Fogo	F1	- 3.61E+00
Fogo	F1	- 4.62E+00
Fogo	F2	/
Fogo	F2	- 2.00E+01
Fogo	F2	- 4.28E+00
Fogo	F2	- 4.06E+00
Fogo	F2	- 4.54E+00
Fogo	F2	- 3.90E+00
Fogo	F3	- 4.44E+00
Fogo	F4	- 3.78E+00

Santo Antão	SA-110062
Santo Antão	SA-1118222
Santo Antão	SA-111827a
Santo Antão	SA-111827b
Santo Antão	SA-111832a
Santo Antão	SA-111832b
Santo Antão	SA-111837
Santo Antão	SA-111940
Santiago	ST-02
Santiago	ST-06
Santiago	
Santiago	
Santiago	ST-08
Santiago	
Santiago	ST-09
Santiago	
SãoVicente	SV-01
SãoVicente	
SãoVicente	SV-02
SãoVicente	
SãoVicente	
SãoVicente	SV-03
SãoVicente	SV-05
SãoVicente	
SãoVicente	SV-09
SãoVicente	SV-10
SãoVicente	SV-12
São Nicolau	SN-02
São Nicolau	
São Nicolau	SN-03
São Nicolau	
São Nicolau	SN-05
São Nicolau	SN-10
São Nicolau	
São Nicolau	SN-11
São Nicolau	SN-13
Sal	S-03
Sal	S-06
Sal	S-07
Sal	
Sal	
Sal	
Brava	CY7

	CY11	
Brava	step 1	
Brava	CY25	
Brava	CY82	
Brava	CY83	
Brava	CY98	
Brava	CY200	
Brava	CY247	
Brava	CY110	0.1877
Brava	CY111	0.1879
Brava	CY112	0.1881
Brava	CY113	0.1884
Brava	CY161	0.1878
Brava	CY23	0.1876
Brava	CY56	0.1877
Brava	CY 116	0.1882
Brava	CY 144	0.1885
Brava	CY 156	0.1885
Brava	CY 161	0.1881
Brava	CY7	
Brava	CY11 tot	
Brava	CY 25	
Brava	CY 82	
Brava	CY 83	

TABLE S2. RAMAN SPECTROSCOPY OF FLUID INCLUSIONS AND CO_2 DENSIMETRY.

Sample		*Petrography*			*Raman analysis*					*Pressure (MPa)*		
Name	***Host***	***Nature***	***Morphology***	***Diameter (μm)***	***Number***	***Δmin (cm^{-1})***	***Δmax (cm^{-1})***	***Δavg (cm^{-1})***	***Mineral detected***	***Min***	***Max***	***Avg***
FG1-A	Clinopyroxene	Secondary	Rounded	2-3	4	103.34	103.56	103.47	Hydrated sulfates?	99	135	130
FG2-A3	Olivine	Secondary	Rounded	2-3	2	103.00	103.63	103.31	-	43	162	103
FG3-A	Olivine	Secondary	Rounded	1-2	3	104.11	104.22	104.17	-	305	350	326
FG4-A	Clinopyroxene	Secondary	Rounded	2-5	2	103.28	103.41	103.35	-	91	121	106
FG4-E	Clinopyroxene	Secondary	Rounded	3-6	5	103.28	103.41	103.33	Carbonates	91	121	101

TABLE S3. EMPA ANALYSIS AND CLINOPYROXENE-ONLY BAROMETRY.

Sample	Label	Host	Zone	SiO2	Al2O3	TiO2	CaO	Na2O	K2O	MnO	MgO	FeO	Cr2O3	NiO	Total
FG4D	FG4D-cpx2	clinopyroxene	core	46.56	7.62	2.61	23.62	0.82		0.14	11.61	6.79			99.78
FG4D	FG4D-cpx2	clinopyroxene	core	45.98	7.97	3.13	23.34	0.88		0.12	11.27	7.13			99.82
FG4D	FG4D-cpx3	clinopyroxene	core	45.96	7.07	3.14	23.49	0.75		0.17	11.65	7.42			99.65
FG4D	FG4D-cpx3	clinopyroxene	core	47.34	6.14	2.75	23.33	0.87		0.16	11.69	7.97			100.25
FG4D	FG4D-cpx4	clinopyroxene	core	46.73	5.94	2.45	22.85	0.90		0.20	11.00	8.97			99.04
FG4D	FG4D-cpx4	clinopyroxene	core	46.52	6.60	2.87	23.27	0.88		0.19	10.86	8.29			99.45
FG4D	FG4D-cpx5	clinopyroxene	core	51.80	2.56	1.12	23.14	0.80		0.25	13.26	7.54			100.46
FG4D	FG4D-cpx5	clinopyroxene	core	48.50	5.52	2.73	23.46	0.78		0.18	12.61	7.13			100.90
FG4D	FG4D-cpx2	clinopyroxene	rim	46.26	6.83	3.00	23.28	0.80		0.19	11.84	7.24			99.44
FG4D	FG4D-cpx2	clinopyroxene	rim	47.77	6.41	2.90	23.54	0.70		0.13	12.64	6.58			100.66
FG4D	FG4D-cpx3	clinopyroxene	rim	46.48	6.64	2.92	22.83	1.02		0.22	10.91	8.90			99.89
FG4D	FG4D-cpx3	clinopyroxene	rim	46.25	6.79	2.97	23.01	0.92		0.23	10.98	8.26			99.41
FG4D	FG4D-cpx4	clinopyroxene	rim	48.37	5.05	2.11	22.90	0.95		0.31	11.37	8.73			99.78
FG4D	FG4D-cpx4	clinopyroxene	rim	47.63	6.08	2.80	23.60	0.72		0.15	12.00	7.05			100.02
FG4D	FG4D-cpx5	clinopyroxene	rim	47.76	6.21	2.83	23.41	0.69		0.18	12.49	6.94			100.51
FG4E	FG4E-cpx1	clinopyroxene	core	45.96	6.50	2.59	22.87	0.94		0.38	10.40	9.66			99.29
FG4E	FG4E-cpx2	clinopyroxene	core	46.43	6.14	2.65	22.80	0.94		0.30	10.44	9.62			99.32
FG4E	FG4E-cpx3	clinopyroxene	core	44.78	7.29	3.17	22.50	0.96		0.31	9.70	10.46			99.16
FG4E	FG4E-cpx3	clinopyroxene	core	46.64	6.12	2.41	22.87	0.96		0.30	10.28	9.95			99.53

FG4E	FG4E-cpx5	clinopyroxene	core	46.04	6.94	2.69	22.91	1.02	0.03	0.33	10.17	9.70			99.82
FG4E	FG4E-cpx5	clinopyroxene	core	45.97	6.92	2.80	22.72	0.95		0.27	10.30	9.84			99.76
FG4E	FG4E-cpx1	clinopyroxene	rim	45.97	6.74	2.42	22.67	1.05		0.33	9.82	10.57			99.59
FG4E	FG4E-cpx1	clinopyroxene	rim	45.78	6.90	2.57	22.46	1.10		0.35	9.58	11.11			99.83
FG4E	FG4E-cpx3	clinopyroxene	rim	45.77	7.03	2.77	22.63	0.97		0.23	10.11	9.89			99.40
FG4E	FG4E-cpx4	clinopyroxene	rim	45.82	7.49	3.21	22.90	0.91		0.26	10.29	9.29			100.17
FG4E	FG4E-cpx4	clinopyroxene	rim	46.24	7.27	3.18	22.88	0.87		0.31	10.63	9.32			100.72
FG4E	FG4E-cpx5	clinopyroxene	rim	45.75	7.25	2.96	22.79	0.91		0.27	10.30	9.72			99.95
FG4E	FG4E-cpx5	clinopyroxene	rim	46.00	7.13	2.75	22.85	1.00		0.26	10.15	9.74			99.88
FG1A	FG1A-cpx2	clinopyroxene	core	53.72	1.08	0.58	23.96	0.67		0.20	15.44	4.68			100.31
FG1A	FG1A-cpx2	clinopyroxene	core	53.23	1.27	0.56	24.50	0.47		0.14	15.54	4.11			99.80
FG1A	FG1A-cpx3	clinopyroxene	core	52.93	1.38	0.72	23.88	0.70	0.02	0.18	15.29	4.51			99.61
FG1A	FG1A-cpx3	clinopyroxene	core	53.29	1.37	0.67	24.05	0.71		0.17	14.92	4.84			100.01
FG1A	FG1A-cpx2	clinopyroxene	rim	54.25	0.92	0.61	24.22	0.59		0.15	15.86	4.13	0.14		100.88
FG1A	FG1A-cpx2	clinopyroxene	rim	53.78	0.88	0.56	24.05	0.74		0.14	15.56	4.52	0.14		100.39
FG1A	FG1A-cpx3	clinopyroxene	rim	54.25	0.30	0.29	24.20	0.59		0.21	16.06	3.97			99.86
FG1A	FG1A-cpx3	clinopyroxene	rim	53.34	0.78	0.62	24.15	0.53	0.02	0.15	15.48	4.14			99.22
FG2-A1	FG2-A1-ol3	olivine	core	38.98			0.35			0.30	43.10	16.76		0.15	99.63
FG2-A1	FG2-A1-ol4	olivine	core	38.85			0.34			0.28	42.95	16.91		0.12	99.44
FG2-A1	FG2-A1-ol4	olivine	core	39.16		0.09	0.36			0.26	43.19	16.64		0.15	99.85
FG2-A1	FG2-A1-ol5	olivine	core	38.91	0.04		0.38			0.21	42.90	16.82		0.14	99.41

FG2-A1	FG2-A1-ol5	olivine	core	38.81	0.03		0.34		0.26	42.67	16.85		0.14	99.11
FG2-A1	FG2-A1-ol6	olivine	core	38.81	0.03		0.38		0.27	43.07	16.74		0.14	99.44
FG2-A1	FG2-A1-ol6	olivine	core	38.95	0.04		0.35		0.15	42.69	16.73		0.12	99.03
FG2-A1	FG2-A1-ol3	olivine	rim	39.25			0.36		0.29	43.31	16.76		0.08	100.05
FG2-A1	FG2-A1-ol3	olivine	rim	39.14	0.03		0.36		0.25	43.37	16.84		0.13	100.13
FG2-A1	FG2-A1-ol4	olivine	rim	39.24			0.37		0.25	43.30	16.83		0.06	100.05
FG2-A1	FG2-A1-ol4	olivine	rim	39.28	0.04		0.38		0.26	43.01	16.48		0.10	99.53
FG2-A1	FG2-A1-ol5	olivine	rim	38.52	0.06		0.33		0.29	42.32	16.99		0.11	98.60
FG2-A1	FG2-A1-ol6	olivine	rim	38.69	0.04		0.38		0.30	43.21	16.74		0.12	99.46
FG2-A1	FG2-A1-ol6	olivine	rim	38.99	0.04		0.35			43.10	16.65		0.11	99.24
FG2-A1	FG2-A1-cpx1	clinopyroxene	core	47.27	6.55	2.22	23.25	0.36		13.05	6.21	0.38		99.28
FG2-A1	FG2-A1-cpx1	clinopyroxene	core	47.26	6.51	2.35	23.43	0.37	0.07	13.07	6.11	0.35		99.52
FG2-A1	FG2-A1-cpx2	clinopyroxene	core	45.44	8.14	3.41	23.27	0.43	0.09	12.35	6.80			99.91
FG2-A1	FG2-A1-cpx2	clinopyroxene	core	45.69	7.94	3.45	23.24	0.48	0.13	12.19	6.69			99.80
FG2-A1	FG2-A1-cpx3	clinopyroxene	core	43.84	8.81	4.16	23.24	0.41	0.11	11.57	7.15			99.29
FG2-A1	FG2-A1-cpx3	clinopyroxene	core	45.49	7.63	3.58	23.18	0.41	0.11	12.24	7.05			99.69
FG2-A1	FG2-A1-cpx1	clinopyroxene	rim	46.90	6.67	2.49	23.33	0.39		13.17	6.25	0.27		99.45
FG2-A1	FG2-A1-cpx1	clinopyroxene	rim	47.24	6.15	2.39	23.27	0.30	0.07	13.15	6.07	0.40		99.04
FG2-A1	FG2-A1-cpx2	clinopyroxene	rim	45.09	8.09	3.54	23.18	0.44	0.08	12.12	6.95			99.48
FG2-A1	FG2-A1-cpx2	clinopyroxene	rim	44.23	9.28	3.70	23.31	0.45	0.08	11.58	7.15			99.78
FG2-A1	FG2-A1-cpx3	clinopyroxene	rim	46.36	7.26	2.88	23.48	0.37	0.09	12.93	6.82			100.20

FG2-A1	FG2-A1-cpx3	clinopyroxene	rim	44.92	7.79	3.23	23.44	0.45	0.08	12.39	6.96			99.26
FG2-A3	FG2-A3-ol1	olivine	core	38.77			0.39		0.31	43.44	16.64		0.14	99.68
FG2-A3	FG2-A3-ol1	olivine	core	39.16			0.36		0.28	43.53	16.66		0.12	100.10
FG2-A3	FG2-A3-ol2	olivine	core	38.69			0.36		0.30	43.07	16.31		0.10	98.82
FG2-A3	FG2-A3-ol2	olivine	core	38.81			0.36		0.24	43.39	16.18		0.12	99.09
FG2-A3	FG2-A3-ol3	olivine	core	39.15			0.39		0.26	43.23	16.80		0.09	99.91
FG2-A3	FG2-A3-ol3	olivine	core	38.63			0.40		0.27	43.26	16.93		0.10	99.58
FG2-A3	FG2-A3-ol4	olivine	core	38.30			0.32		0.33	42.49	17.64			99.09
FG2-A3	FG2-A3-ol4	olivine	core	38.40			0.35		0.30	42.47	17.68			99.20
FG2-A3	FG2-A3-ol5	olivine	core	38.90			0.40		0.19	43.18	16.75		0.15	99.58
FG2-A3	FG2-A3-ol5	olivine	core	38.91			0.38		0.26	43.05	16.94		0.14	99.69
FG2-A3	FG2-A3-ol6	olivine	core	39.01	0.06		0.37		0.25	43.73	16.56		0.11	100.08
FG2-A3	FG2-A3-ol6	olivine	core	39.01	0.05		0.35		0.31	43.32	16.66		0.12	99.82
FG2-A3	FG2-A3-ol2	olivine	rim	38.37	0.04		0.36		0.32	42.77	16.69		0.09	98.65
FG2-A3	FG2-A3-ol3	olivine	rim	39.15	0.05		0.40		0.19	42.95	17.00		0.08	99.82
FG2-A3	FG2-A3-ol3	olivine	rim	38.73	0.03		0.37		0.25	43.40	16.75		0.09	99.62
FG2-A3	FG2-A3-ol5	olivine	rim	38.59			0.39		0.31	42.63	16.81		0.09	98.81
FG2-A3	FG2-A3-ol5	olivine	rim	39.04	0.03		0.39		0.25	42.69	16.57		0.12	99.08
FG2-A3	FG2-A3-cpx1	clinopyroxene	core	47.39	6.82	2.30	23.14	0.45	0.14	13.11	6.68			100.02
FG2-A3	FG2-A3-cpx1	clinopyroxene	core	47.87	6.33	2.29	23.16	0.37		13.49	5.76	0.50		99.77
FG2-A3	FG2-A3-cpx2	clinopyroxene	core	46.73	6.89	2.71	23.32	0.39		13.08	6.02	0.18		99.32

FG2-A3	FG2-A3-cpx2	clinopyroxene	core	46.57	6.68	2.86	23.49	0.38		12.98	6.32	0.21	99.49
FG2-A3	FG2-A3-cpx3	clinopyroxene	core	45.92	7.35	3.37	23.14	0.45	0.14	12.37	6.89		99.63
FG2-A3	FG2-A3-cpx3	clinopyroxene	core	46.71	6.80	3.21	23.03	0.54	0.17	12.45	6.68		99.59
FG2-A3	FG2-A3-cpx4	clinopyroxene	core	46.47	7.16	2.92	23.61	0.35	0.10	12.81	6.60		100.02
FG2-A3	FG2-A3-cpx4	clinopyroxene	core	46.92	6.86	2.89	23.59	0.36	0.11	13.04	6.38	0.21	100.36
FG2-A3	FG2-A3-cpx1	clinopyroxene	rim	48.15	6.24	2.33	23.30	0.40	0.10	13.81	5.72	0.51	100.55
FG2-A3	FG2-A3-cpx1	clinopyroxene	rim	48.32	6.31	2.19	23.28	0.33	0.12	13.66	5.80	0.50	100.49
FG2-A3	FG2-A3-cpx2	clinopyroxene	rim	46.54	6.61	2.87	23.39	0.36	0.11	12.89	6.03	0.26	99.05
FG2-A3	FG2-A3-cpx3	clinopyroxene	rim	45.42	8.96	3.79	22.81	0.64	0.17	11.74	6.85		100.38
FG2-A3	FG2-A3-cpx3	clinopyroxene	rim	47.53	6.63	3.01	23.24	0.44	0.10	12.96	6.52		100.43
FG2-A3	FG2-A3-cpx4	clinopyroxene	rim	45.65	7.18	2.89	23.49	0.34		12.87	6.71		99.13
FG2-A3	FG2-A3-cpx4	clinopyroxene	rim	46.40	7.11	2.97	23.51	0.33		12.83	6.53		99.68
FG3-A	FG3-A-cpx5	clinopyroxene	core	46.79	6.86	2.67	23.33	0.36	0.09	13.02	6.64	0.13	99.89
FG3-A	FG3-A-cpx5	clinopyroxene	core	47.35	6.26	2.54	23.30	0.38	0.12	13.08	6.58		99.61
FG3-A	FG3-A-cpx4	clinopyroxene	core	45.02	8.29	3.63	23.27	0.45	0.10	12.12	6.89		99.76
FG3-A	FG3-A-cpx4	clinopyroxene	core	44.38	8.96	3.75	23.30	0.45	0.11	11.76	7.18		99.89
FG3-A	FG3-A-cpx3	clinopyroxene	core	45.65	8.09	3.50	22.79	0.58	0.22	11.82	7.04		99.68
FG3-A	FG3-A-cpx2	clinopyroxene	core	46.35	7.09	3.16	23.00	0.42	0.08	12.35	7.16		99.61
FG3-A	FG3-A-cpx2	clinopyroxene	core	44.49	9.39	3.86	23.07	0.61	0.03	10.95	7.01		99.53
FG3-A	FG3-A-cpx5	clinopyroxene	rim	46.49	6.45	2.95	23.12	0.47	0.18	12.55	6.85		99.05
FG3-A	FG3-A-cpx4	clinopyroxene	rim	44.15	8.81	3.72	23.54	0.42	0.14	11.84	7.24		99.84

FG3-A	FG3-A-cpx4	clinopyroxene	rim	45.15	8.05	3.29	23.08	0.41		0.10	12.23	7.10		99.40
FG3-A	FG3-A-cpx3	clinopyroxene	rim	46.11	7.69	3.38	23.04	0.55		0.12	12.09	6.85		99.82
FG3-A	FG3-A-cpx2	clinopyroxene	rim	43.28	10.51	4.59	22.92	0.65		0.18	10.94	7.24		100.32
FG3-A	FG3-A-ol5	olivine	core	39.09	0.05		0.32			0.27	43.08	16.51	0.16	99.48
FG3-A	FG3-A-ol5	olivine	core	39.10	0.07	0.10	0.35			0.28	43.14	16.64	0.12	99.79
FG3-A	FG3-A-ol4	olivine	core	38.94			0.36			0.33	42.27	17.83	0.07	99.80
FG3-A	FG3-A-ol4	olivine	core	37.64	0.03		0.39			0.56	37.47	23.85	0.11	100.05
FG3-A	FG3-A-ol3	olivine	core	39.04	0.04		0.33			0.33	43.82	16.35	0.11	100.01
FG3-A	FG3-A-ol3	olivine	core	39.32	0.03		0.32			0.21	43.61	16.11	0.15	99.76
FG3-A	FG3-A-ol2	olivine	core	38.80	0.03		0.35			0.25	43.48	16.95	0.10	99.96
FG3-A	FG3-A-ol5	olivine	rim	38.84	0.05		0.35			0.28	43.17	16.39	0.09	99.16
FG3-A	FG3-A-ol5	olivine	rim	39.25	0.04		0.34			0.30	43.12	16.55	0.09	99.69
FG3-A	FG3-A-ol4	olivine	rim	38.47	0.04		0.34			0.38	41.32	18.08	0.08	98.71
FG3-A	FG3-A-ol4	olivine	rim	38.25	0.05		0.35			0.35	41.92	17.88	0.11	98.90
FG3-A	FG3-A-ol3	olivine	rim	39.24			0.33			0.28	43.25	15.92	0.15	99.17
FG3-A	FG3-A-ol3	olivine	rim	39.23			0.31			0.26	43.69	15.98	0.13	99.61
FG3-A	FG3-A-ol2	olivine	rim	38.38			0.35			0.24	43.30	16.89	0.11	99.27
FG3-A	FG3-A-ol2	olivine	rim	39.05	0.03		0.34			0.22	42.79	16.44	0.10	98.98
FG4-A	FG4-A-cpx1	clinopyroxene	core	47.51	6.13	2.56	23.77	0.65		0.16	12.46	6.21		99.42
FG4-A	FG4-A-cpx1	clinopyroxene	core	46.94	6.55	2.80	23.67	0.66		0.11	12.45	6.34		99.51
FG4-A	FG4-A-cpx2	clinopyroxene	core	47.50	6.32	2.54	23.19	0.72	0.05	0.15	12.65	6.36		99.47

FG4-A	FG4-A-cpx2	clinopyroxene	core	46.88	6.58	2.76	23.45	0.67		0.11	12.38	6.56		99.38
FG4-A	FG4-A-cpx3	clinopyroxene	core	48.79	5.18	2.02	23.57	0.76		0.21	12.05	7.82		100.38
FG4-A	FG4-A-cpx3	clinopyroxene	core	46.72	6.71	2.78	23.26	0.88		0.24	11.15	8.39		100.11
FG4-A	FG4-A-cpx4	clinopyroxene	core	47.19	6.34	2.57	23.00	0.98		0.19	10.99	8.86		100.12
FG4-A	FG4-A-cpx4	clinopyroxene	core	46.41	6.47	2.81	22.90	0.86		0.24	10.91	8.78		99.38
FG4-A	FG4-A-cpx5	clinopyroxene	core	48.28	5.71	2.07	23.24	0.86		0.14	11.82	7.09	0.48	99.70
FG4-A	FG4-A-cpx5	clinopyroxene	core	47.63	5.95	2.13	23.23	0.91		0.21	11.77	7.10	0.52	99.45
FG4-A	FG4-A-cpx1	clinopyroxene	rim	47.42	6.43	2.61	23.14	0.79	0.03	0.22	11.71	7.12		99.45
FG4-A	FG4-A-cpx1	clinopyroxene	rim	47.33	6.44	2.51	23.40	0.78		0.20	12.03	7.11		99.79
FG4-A	FG4-A-cpx2	clinopyroxene	rim	47.07	6.33	2.71	23.59	0.72		0.09	12.49	6.18		99.17
FG4-A	FG4-A-cpx3	clinopyroxene	rim	46.27	6.60	3.00	22.78	0.92		0.27	10.51	9.17		99.51
FG4-A	FG4-A-cpx3	clinopyroxene	rim	46.49	6.58	2.74	22.76	0.89		0.31	10.77	9.14	0.13	99.81
FG4-A	FG4-A-cpx4	clinopyroxene	rim	46.64	6.00	2.35	22.51	1.12		0.37	10.10	10.17		99.25
FG4-A	FG4-A-cpx4	clinopyroxene	rim	46.28	6.22	2.59	22.49	1.00		0.32	10.17	10.09		99.17
FG4-A	FG4-A-cpx5	clinopyroxene	rim	47.41	5.82	2.17	23.25	0.92		0.23	11.46	7.77	0.39	99.40
FG4-A	FG4-A-cpx5	clinopyroxene	rim	46.69	6.50	2.64	23.25	0.90		0.17	10.98	7.93	0.47	99.53
FG4-B	FG4-B-cpx4	clinopyroxene	core	54.61	0.14	0.27	24.31	0.45		0.13	16.57	3.52		100.00
FG4-B	FG4-B-cpx4	clinopyroxene	core	55.06	0.15	0.33	24.31	0.43		0.16	16.77	3.55		100.76
FG4-B	FG4-B-cpx3	clinopyroxene	core	52.68	1.16	0.89	23.93	0.59		0.17	15.18	4.64		99.23
FG4-B	FG4-B-cpx3	clinopyroxene	core	52.05	1.42	1.11	23.85	0.64	0.02	0.16	14.86	5.03		99.15
FG4-B	FG4-B-cpx2	clinopyroxene	core	54.99	0.09	0.29	24.42	0.56		0.12	16.55	3.70		100.71

FG4-B	FG4-B-cpx2	clinopyroxene	core	54.57	0.16	0.36	24.17	0.51	0.15	16.56	3.82		100.29
FG4-B	FG4-B-cpx1	clinopyroxene	core	55.31	0.09	0.25	24.55	0.45	0.17	16.69	3.26		100.76
FG4-B	FG4-B-cpx1	clinopyroxene	core	55.32	0.05	0.21	24.65	0.38	0.12	16.69	3.20	0.17	100.79
FG4-B	FG4-B-cpx4	clinopyroxene	rim	54.36	0.30	0.32	24.81	0.31	0.09	16.46	2.73		99.38
FG4-B	FG4-B-cpx4	clinopyroxene	rim	54.62	0.34	0.36	25.09	0.33	0.17	16.64	2.87		100.43
FG4-B	FG4-B-cpx3	clinopyroxene	rim	54.10	0.57	0.64	24.50	0.44	0.19	15.59	4.08		100.11
FG4-B	FG4-B-cpx3	clinopyroxene	rim	53.99	0.50	0.49	24.39	0.44	0.19	15.52	4.07		99.58
FG4-B	FG4-B-cpx2	clinopyroxene	rim	54.83	0.11	0.22	24.93	0.30	0.16	16.69	3.19		100.43
FG4-B	FG4-B-cpx1	clinopyroxene	rim	55.48	0.06	0.24	24.43	0.42	0.09	16.68	3.54		100.94

Table S3. Continued

Sample			Clinopyroxene barometry					
			Ti/Al ratio		*P (MPa) Eq. 32a*		*P (MPa) Fit*	
Name	*Group*	*Number*	*Average*	*σ*	*Average*	*σ*	*Average*	*σ*
FG4-D	Gr. Ia	15	0.28	0.02	536	130	-	-
FG4-E	Gr. Ia	13	0.26	0.02	737	60	-	-
FG4-A	Gr. Ia	19	0.26	0.02	569	117	-	-
FG2-A1	Gr. Ib	12	0.26	0.02	370	84	-	-
FG2-A3	Gr. Ib	15	0.26	0.02	336	109	-	-
FG3-A	Gr. Ib	12	0.27	0.01	464	144	-	-
FG1-A	Gr. II	8	0.4	0.11	-	-	<270	14
FG4-B	Gr. II	14	1.32	0.74	-	-	<245	17

TABLE S4. BAROMETRIC DATA FROM THIS WORK (SUMMARY OF TABLES S2 AND S3) AND FROM PREVIOUS STUDY OF THE SAME SUITE OF SAMPLES

Sample	Method	Pressure (MPa)	Depth (km)	References
FG1-A	Raman CO_2 densimetry	130	4.6	This work (Table S2)
FG2-A3	Raman CO_2 densimetry	103	3.6	This work (Table S2)
FG3-A	Raman CO_2 densimetry	326	11.5	This work (Table S2)
FG4-A	Raman CO_2 densimetry	106	3.7	This work (Table S2)

FG4-E	Raman CO_2 densimetry	101	3.6	This work (Table S2)
Fog 43	Microthermometry of FI	442	15.5	Lo Forte et al., 2023
Fog 28	Microthermometry of FI	457	16.1	Lo Forte et al., 2023
Fog 31	Microthermometry of FI	407	14.3	Lo Forte et al., 2023
Fog 27	Microthermometry of FI	720	25.3	Lo Forte et al., 2023
Fog 20	Microthermometry of FI	432	15.2	Lo Forte et al., 2023
Fog 23	Microthermometry of FI	590	20.7	Lo Forte et al., 2023
Fog 24	Microthermometry of FI	457	16.1	Lo Forte et al., 2023
Fog 33	Microthermometry of FI	487	17.1	Lo Forte et al., 2023
FG4-E	Clinopyroxene barometry	737	25.9	This work (Table S3)
FG4-D	Clinopyroxene barometry	536	18.8	This work (Table S3)
FG4-A	Clinopyroxene barometry	569	20.0	This work (Table S3)
FG2-A3	Clinopyroxene barometry	336	11.8	This work (Table S3)
FG2-A1	Clinopyroxene barometry	370	13.0	This work (Table S3)

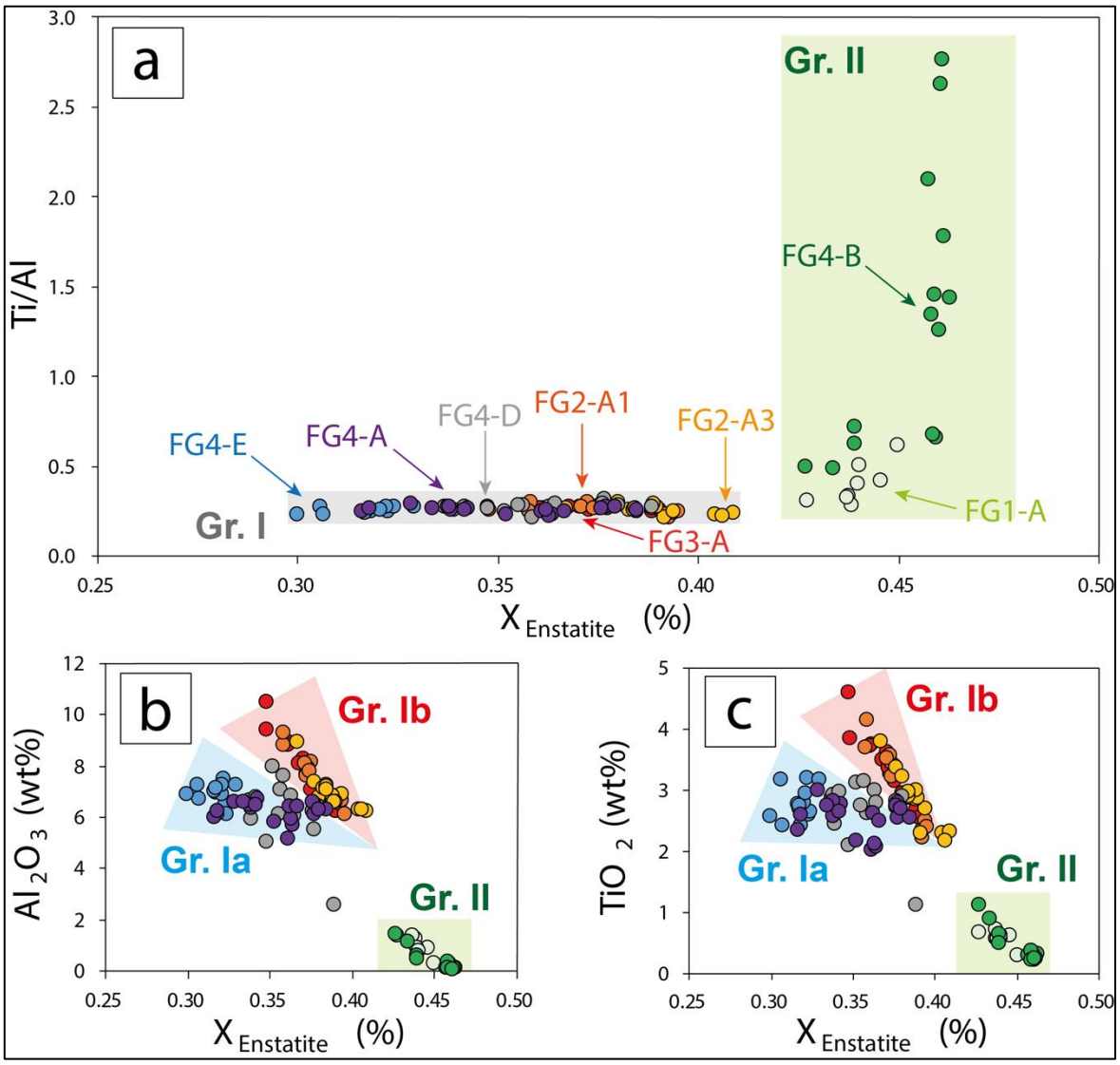

Figure S1 Composition of clinopyroxene crystals in all the samples. Percentage of enstatite (pole) vs. (a) Ti/Al, (b) Al_2O_3 and (c) TiO_2. Gr. Ia, Ib and II are the three groups of clinopyroxene crystals distinguished on the basis of their composition and discussed in the text.

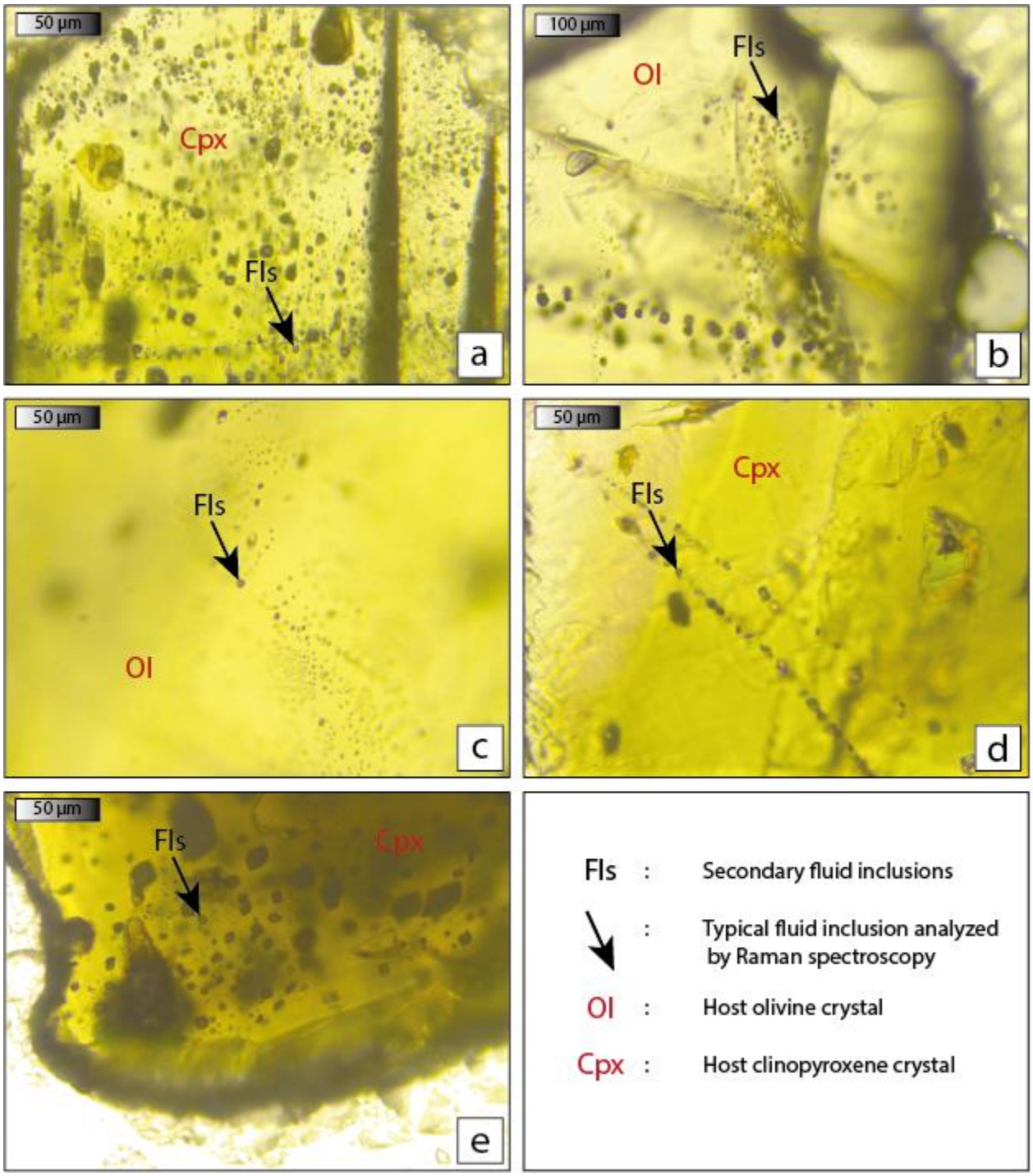

Figure S2 Microphotographs of analysed FI in olivine and clinopyroxene crystals from samples (a) FG1-A, (b) FG2-A3, (c) FG3-A, (d) FG4-A and (e) FG4-E. Only no optically-resolvable or empty FI were observed/analysed in the other samples (FG2-A1, FG4-B et FG4-D).

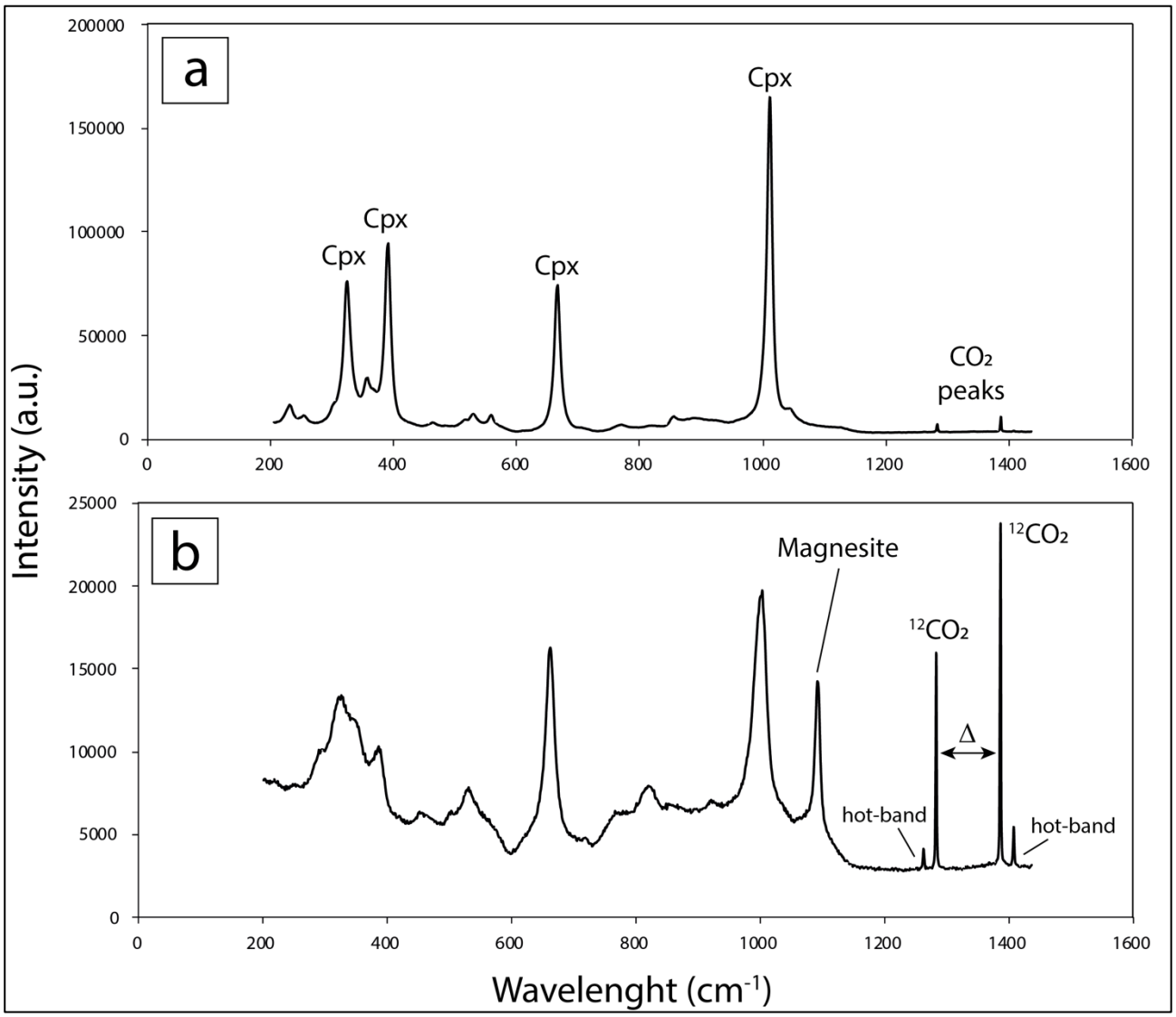

Figure S3 Raman spectra of FI in clinopyroxene crystals from (a) FG1-A et (b) FG4-E mafic enclave, showing the CO_2 peaks, the Fermi doublet (Δ) and sometimes the presence of carbonates. The petrographic description, the Fermi doublet and the estimated pressures are reported for each family of FI per sample in Table S2 of the Supplementary Material S1.

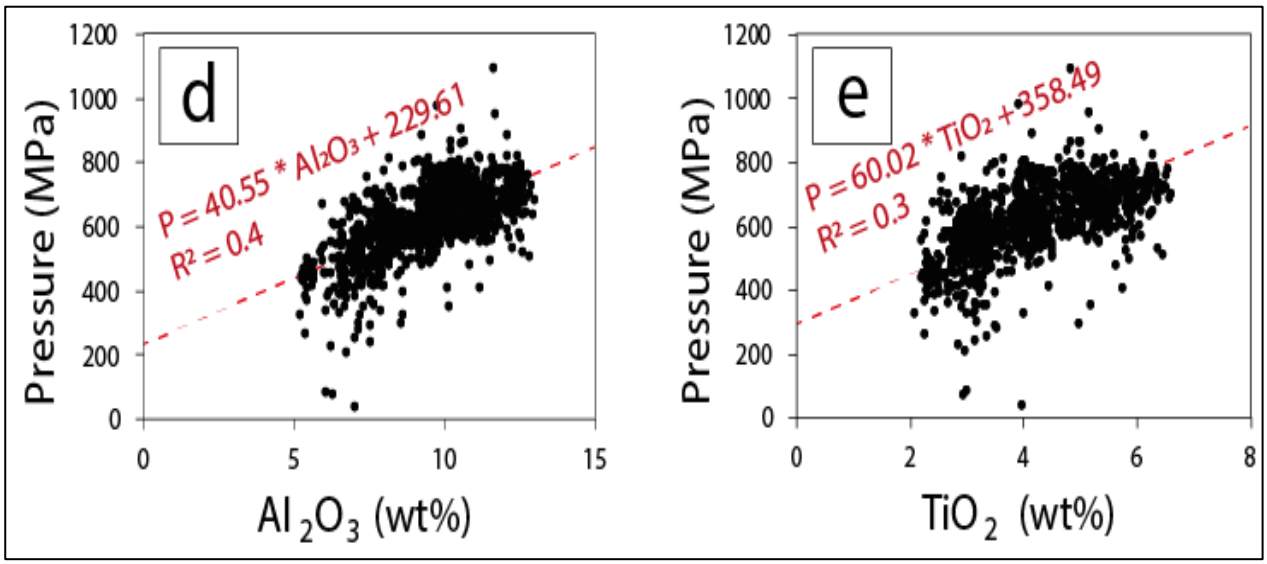

Figure S4 Composition of clinopyroxene crystals in all the samples. Percentage of enstatite (pole) vs. Al_2O_3 and (d) TiO_2. (e) Correlation between the composition of the clinopyroxene crystals previously analyzed in recent lavas at Fogo and the estimated pressure based on the clinopyroxene-melt barometer (see Klügel et al., 2020). In this study (and in the absence of melt analysis), the clinopyroxene-only barometer of Putirka (2008) is used (Eq. 32a) with an averaged magma temperature of 1130°C (see Klügel et al., 2020). For analysis where clinopyroxene-only barometer fails to provide a positive value (-), a barometric estimation is proposed based on the correlation between the pressure and the Al_2O_3 content of the clinopyroxene crystals analyzed previously. Gr. Ia, Ib and II are the three groups of clinopyroxene crystals distinguished on the basis of their composition and discussed in the text. **N.B.** Al_2O_3 et TiO_2 dependence of clinopyroxene barometry (P_Fit) at Fogo from Klügel et al. (2020)